

Technische Universität München
Institut für Energietechnik

Lehrstuhl für Thermodynamik

Impact of fuel supply impedance and fuel staging on gas turbine combustion stability

Andreas Huber

Vollständiger Abdruck der von der Fakultät für Maschinenwesen der
Technischen Universität München zur Erlangung des akademischen Grades
eines

DOKTOR – INGENIEURS

genehmigten Dissertation.

Vorsitzender:

Univ.-Prof. Dr.-Ing. habil. Hartmut Spliethoff

Prüfer der Dissertation:

1. Univ.-Prof. Wolfgang H. Polifke, Ph.D. (CCNY)
2. Prof. Dr. Franck Nicoud (Universität Montpellier II,
Frankreich)

Die Dissertation wurde am 18. Mai 2009 bei der Technischen Universität München
eingereicht und durch die Fakultät für Maschinenwesen am 3. September 2009
angenommen.

Danksagung

Die vorliegende Arbeit entstand am Lehrstuhl für Thermodynamik der Technischen Universität München im Rahmen des Verbundprogramms COOR-EFF - "CO₂ Reduktion durch Effizienz" der Arbeitsgemeinschaft AG Turbo. Sie wurde vom Bundesministerium für Wirtschaft und Technologie und der Firma Siemens Power Generation gefördert.

Mein ganz besonderer Dank gilt meinem Doktorvater, Herrn Professor Wolfgang H. Polifke, Ph.D. (CCNY) nicht nur für die fachliche Betreuung sondern auch für sein in mich gesetztes Vertrauen sowie für die Freiheit in der Bearbeitung der mir gestellten Aufgabe. Besonders dankbar bin ich für die vielen anregenden, mitunter auch spontanen Diskussionen im Bereich der Thermoakustik, die massgeblich zum Gelingen dieser Arbeit beigetragen haben.

Herrn Professor Dr. Franck Nicoud danke ich für die freundliche Übernahme des Koreferates und dafür, dass er die weite Anreise aus dem sonnigen Montpellier auf sich genommen hat. Herrn Professor Dr.-Ing. habil. Hartmut Splithoff danke ich für den Vorsitz bei der mündlichen Prüfung.

Mein Dank gilt auch allen meinen Kolleginnen und Kollegen am Lehrstuhl. Das kollegiale Betriebsklima aber auch die gemeinsamen Aktivitäten werden mir immer in guter Erinnerung bleiben. Viele Erkenntnisse und so manches Ergebnis resultieren aus Anregungen und Diskussionen vor allem innerhalb der Gruppe der Strömungsinstabilitäten. Besonderer Dank gilt meinen langjährigen Bürokollegen Ludovic Durand und später Martin Lauer für die überaus schöne Zeit, die freundschaftliche Atmosphäre und die vielen wertvollen Diskussionen.

Weiterhin danke ich den Semestranten, Diplomanten und wissenschaftlichen Hilfskräften, die im Rahmen des Projekts wichtige Beiträge geleistet haben, für ihren motivierten Einsatz und die tatkräftige Unterstützung. Danken möchte ich auch meiner Kollegin Jutta Pieringer, Helga Bassett und meiner Freundin Anne Schulz, die diese Arbeit Korrektur gelesen haben.

Meiner Freundin möchte ich zudem für ihre Unterstützung, ihr Verständnis

und ihre Geduld besonders für die vielen Wochenenden danken, an denen ich mich mit dem Anfertigen dieser Dissertation beschäftigt habe. Zuletzt möchte ich mich bei meiner Familie für ihre Unterstützung während meiner gesamten Ausbildungszeit bedanken, die damit die Voraussetzung für diese Arbeit geschaffen haben.

München, im Oktober 2009

Andreas Huber

Abstract – Zusammenfassung

Due to the environment-friendly lean premixed combustion gas turbines exhibit an increased risk in generating thermo-acoustically induced combustion oscillations. These oscillations can cause damage of combustor parts and limit the stable operating range. The present work analyses the influence of fuel supply impedance, the distance between fuel injection and flame and fuel staging on the thermo-acoustic stability of a combustion system. The flame-acoustic interactions are represented in form of a “multiple-input single-output” (MISO) model. The model coefficients are determined using transient Computational Fluid Dynamics (CFD) simulations with acoustic broadband excitation and system identification. The results obtained are implemented into an acoustic network model of the combustion system to analyze the different impacts on the thermo-acoustic stability, especially the fluctuating mixture of fuel and air and the flame front kinematics.

Stationäre Gasturbinen mit emissionsarmer, magerer Vormischverbrennung neigen zu thermoakustisch induzierten Brennkammerschwingungen, die zur Zerstörung von Bauteilen führen können. In der vorliegenden Arbeit wird der Einfluss der akustischen Impedanz der Brennstoffleitungen, der relativen Lage der Brennstoffeindüsung zur Flamme, und der Brennstoffstufung auf das thermoakustische Verhalten eines Verbrennungssystems untersucht. Die Wechselwirkungen von Flamme und Akustik werden als ”multiple-input single-output” (MISO) Modell dargestellt, die Modellkoeffizienten werden mittels numerischer Strömungssimulation mit akustischer Breitbandanregung und Systemidentifikation ermittelt. Die Ergebnisse werden in ein akustisches Netzwerkmodell des Verbrennungssystems integriert, um die Auswirkungen der verschiedenen Effekte, insbesondere Schwankungen des Brennstoff-Luftgemisches und Flammenkinematik, auf die Systemstabilität zu untersuchen.



Contents

1	Introduction	1
1.1	Technology background: Electrical energy, efficiency and environmental protection	1
1.2	Thermo-acoustic instabilities	3
1.3	Control of thermo-acoustic instabilities	7
1.4	Intention and structure of this work	10
1.5	Terminology and specification of the present work	12
2	Numerical analysis of thermo-acoustic instabilities	17
2.1	Overview of methods for thermo-acoustic stability analysis . . .	17
2.2	Flame dynamics of a practical premixed combustion system . .	24
2.2.1	Flame response to velocity fluctuations	25
2.2.2	Flame response to equivalence ratio fluctuations	28
2.2.3	MISO model structure for practical premixed flames . . .	30
2.3	Identification of flame transfer functions	33
2.3.1	Overview of methods to determine flame transfer functions	34
2.3.2	Identification strategy	37
3	Acoustics	43
3.1	Basic acoustic equations	43
3.2	Linear acoustic equations	46
3.2.1	Sound propagation in a quiescent medium	47
3.2.2	Sound propagation in a moving medium	50
3.3	Acoustic network model	51
3.3.1	Matrices and functions of acoustic elements	53
3.3.1.1	Simple ducts or tubes	55
3.3.1.2	Compact elements	55

3.3.1.3	Boundary conditions	62
3.3.2	Numerical solutions of the acoustic network model	64
4	Modeling of turbulent reactive flows using CFD	69
4.1	Theory and numerical modeling of turbulence	69
4.1.1	Basic equations of turbulent flows	69
4.1.2	Modeling turbulence with RANS	71
4.2	Theoretical and numerical combustion	74
4.2.1	Combustion theory	74
4.2.2	Practical premixed combustion model	77
5	System Identification	81
5.1	Model structures and response filters	82
5.2	System Identification	85
5.3	Excitation signals	86
5.4	A posteriori validation of identification results	89
5.5	Proof of concept for the identification of the MISO flame model	92
5.5.1	Impact of model structure on identification results	95
5.5.2	Impact of excitation signal types in the presence of noise	96
5.5.3	Impact of the measured time series length	102
6	Numerical simulation	105
6.1	Practical premixed combustor configuration	105
6.1.1	Design of the fuel injector	108
6.1.2	Numerical setup of the combustion system	110
6.2	Steady-state simulations of the combustor configurations	115
6.3	Identification of the flame transfer functions	119
6.3.1	Combustor configuration with two fuel injection stages .	120
6.3.2	Combustor configuration with three fuel injection stages	124
6.3.3	Analysis and interpretation of identification results	128
6.4	Identification of the acoustic characteristics of the swirler	134
7	Acoustic analysis	139
7.1	Setup of the acoustic network model	139
7.2	Acoustic network model results	143
7.2.1	Impact of the fuel injection stage impedance	144

7.2.2	Impact of the fuel injection nozzle location	158
7.2.3	Impact of fuel staging	162
8	Summary and Conclusions	167
A	Appendix	186
A.1	Transformation of pu, fg transfer matrix and scattering (sr) matrix notation	186
A.2	Estimation of the optimum number of circumferential injection holes	187
A.3	Main flow parameters and structure of the acoustic network models	187

Nomenclature

Latin letters

A	area [m ²]
aCFL	acoustic Courant-Friedrichs-Lewy number [-]
c	speed of sound [m/s]
c	reaction progress variable [-]
ci	confidence intervall [-]
c_p	specific heat capacity (constant pressure) [J/kg-K]
c_v	specific heat capacity (constant volume) [J/kg-K]
C	cross-correlation vector [-]
C_r	crest factor [-]
CI	cycle increment [-]
CFL	Courant-Friedrichs-Lewy number [-]
d	diameter of burner mouth [m]
d_j	diameter of fuel injection tube [m]
D	diffusion coefficient [m ² /s]
Da	Damköhler number [-]
e	internal energy per unit mass [J/kg]
e_n	noise term [-]
f	Riemann invariant (in positive direction) [m/s]
f	frequency [1/s]
f_c	cut-off frequency [1/s]
f_N	Nyquist frequency [1/s]
F_w	weighted reaction progress [-]
F	flame transfer function [-]
g	Riemann invariant (in negative direction) [m/s]

G	stretch factor [-]
h	unit impulse response vector [-]
h_s	specific enthalpy per unit mass [J/kg]
h_t	total enthalpy per unit mass [J/kg]
He	Helmholtz number [-]
ΔH	enthalpy per unit mass [J/kg]
J	impulse ratio of the fuel and main stream [-]
k	turbulent kinetic energy [m^2/s^2]
k_b	Boltzmann constant [J/K]
k_x	wave number (in x-direction) [1/m]
Ka	Karlowitz number [-]
l_f	laminar flame thickness [m]
L	length [m]
L_f	axial distance between fuel injection and burner mouth [m]
L_R	length of resonator tube [m]
l_t	turbulent integral length scale [m]
Le	Lewis number [-]
m	mass [kg]
M	molar mass [kg/kmol]
n	interaction index [-]
\mathcal{N}_A	Avogadro number [-]
p	static pressure [Pa]
Pr	Prandtl number [-]
R	specific gas constant [J/K-mol]
R_f	reflection coefficient [-]
q	heat flux [W/m^2]
\dot{q}	rate of heat release (per unit mass) [J/kg]
Q	measure of identification quality [%]
\dot{Q}	rate of heat release (per unit area) [$\text{J}/\text{s}\cdot\text{m}^2$]
\dot{Q}_V	heat production (per unit volume) [$\text{J}/\text{s}\cdot\text{m}^3$]
s	entropy [J/K]
s	signal [-]
s_{st}	mass stoichiometric ratio [-]
s_L	laminar flame speed [m/s]

Nomenclature

s_t	turbulent flame speed [m/s]
S_c	reaction source term [kg/m ² -s]
S_{sr}	Scattering matrix [-]
$Sc_{c,t}$	turbulent Schmidt number [-]
t	time [s]
t_n	sampling instant [s]
T	temperature [K]
T_{fg}	Transfer matrix described by f and g [-]
T_{per}	oscillation period [s]
T_c	cycle time [s]
Δt	sampling interval [s]
T_t	simulation time [s]
u	velocity [m/s]
\mathbf{u}	velocity vector [m/s]
u	absolute velocity [m/s]
u_i	velocity component i or vector \mathbf{u} [m/s]
V	volume [m ³]
x	input signal [-]
X	axial distance from point of fuel injection [m]
y	output signal (response) [-]
\hat{y}	predictor [-]
Y	radial distance from point of fuel injection [m]
Y	mass fraction [-]
Z	acoustic impedance [-]
Z_M	mixture fraction [-]

Greek letters

α	[-]
ϵ	prediction error [-]
ϵ_t	turbulent dissipation [m ² /s ³]
γ	ratio of specific heats [-]
Γ	auto-correlation matrix [-]

λ	air-fuel ratio [-]
λ_t	thermal conductivity [W/m-K]
λ_w	wavelength [m]
η_k	Kolmogorov length scale [m]
φ	regression vector [-]
φ_u	velocity potential [1/s]
ϕ	equivalence ratio [-]
μ_t	turbulent dynamic viscosity [kg/m-s]
ρ	density [kg/m ³]
Σ	flame surface per unit volume [m ⁻¹]
τ	stress tensor [Pa]
τ_c	chemical time scale [s]
τ_k	Kolmogorov time [s]
τ_t	turbulent time scale [s]
$\hat{\theta}$	least-square estimate [-]
ω	angular frequency [1/s]
ω_t	turbulent frequency [1/s]
$\dot{\omega}$	reaction rate [kg/m ³ -s]
χ_u	thermal diffusivity [W/m-K]
ζ	pressure loss coefficient [-]

Operators

$(.)'$	acoustic fluctuation
$(.)''$	turbulent fluctuation
$\bar{(\cdot)}$	mean value (Reynolds average)
$\tilde{(\cdot)}$	mass-weighted average (Favre average)

Indices

0	ambient state
<i>A</i>	air stream
<i>b</i>	burner exit (flame holder)
<i>cc</i>	combustion chamber
DS	downstream
<i>fl</i>	flame / flame front
<i>F</i>	fuel, fuel stream
FS	fuel supply
im	imaginary part of a complex quantity
<i>O</i>	oxidiser
real	real part of a complex quantity
<i>u</i>	unburnt
<i>s</i>	along streamlines
US	upstream

1 Introduction

1.1 Technology background: Electrical energy, efficiency and environmental protection

In times of a worldwide increasing demand for electricity, the power industry faces the challenge of ensuring the supply of economic and sustainable supply of energy. According to the International Energy Agency [3] the global primary energy demand will rise by about 50% between now and 2030. Over 70% of the increase will come from the emerging countries, with China alone accounting for 30%. Fossil fuels will still form the backbone of the electrical energy supply and remain the dominant source of energy. Their share of the worldwide electrical energy demand will slightly increase from 80% to 81% in 2030 [3]. Considering the limited reserves of raw material, the goal of an economic supply of electrical energy becomes a challenging task, assuming that fossil fuel prices will increase in the long run. Also an sustainable production of electricity is difficult to achieve given that burning fossil fuels raises the concentration of greenhouse gas carbon dioxide (CO_2) and other air pollutants such as unburnt hydrocarbons (UHC), sulfur oxide (SO_x), carbon monoxide (CO) and nitrogen oxide (NO_x), especially nitric oxide (NO). The effects of the pollutants include, among others, global warming and acid rain (see e.g. Turns [128]).

Protecting the climate and natural resources will therefore play an increasing role in the prospective utilization of fossil fuels. The European Union has recently decided to reduce greenhouse gases by 20% until 2020 (compared to 1990). To achieve high supply dependability, cost effectiveness and environmental sustainability, the German power generation industry, for instance, focuses on an energy mix. The energy mix consists of coal, nuclear power, natural gas and renewable energies. In this context, electrical power production using combined-cycle plants plays an increasing role. According to the "Ver-

band der Elektrizitätswirtschaft" (VDEW) [1], their share in Germany doubled from 5% in 1995 to 10% in 2005, whereas the net electrical energy production increased from 437×10^6 kWh to almost 536×10^6 kWh. An advantage of combined-cycle plants burning natural gas is the low emission of CO_2 ¹. Enormous progress has been made in this area in terms of emissions and efficiency in the past few decades. With an achieved increase of the degree of efficiency by about 20%, the required amount of fuel has been decreased to achieve the same power with a reduction in corresponding emissions.

As a consequence to tighter emission legislation the development of gas turbine combustion systems is mainly driven by the aim to reduce NO_x and CO emissions and to further increase efficiency. A high degree of thermal efficiency can be reached with a high and uniformly distributed temperature of the exhaust gases at the inlet of the turbine. However, to reduce the amount of NO_x [66] it is favorable to realize a minimum possible combustion temperature. The ideal flame temperature would therefore lie above but close to the lean extinction level, which corresponds to a lean air/fuel mixture. In addition to the dependence on temperature, the NO_x and CO production depends also on the residence time in the combustor. Low emissions can be ensured by low residence times. This can be achieved by increasing the burning velocity, which in turn results in compact combustion chambers.

State-of-the-art gas turbines are therefore equipped with low-emission lean premixed and compact combustors with flame temperatures far below the stoichiometric flame temperature. A drawback of these combustion systems is that they exhibit an increased risk in generating thermo-acoustically induced combustion oscillations. Such oscillations, which have been a well-known problem since the early days of gas turbine development, are due to the strong coupling between fluctuations of heat release rate and pressure and can cause mechanical and thermal damage and limit the operating range. The prevention of this phenomenon has become an important design target for gas turbine combustors.

¹ SO_x , for example, does not play a role as these emissions presume a combustion of fuels with a higher sulfur-content, such as coal or low-quality oils.

1.2 Thermo-acoustic instabilities

The interaction between acoustics and the combustion process has been known for a long time. John LeConte [67] described his observations during a visit of a private musical entertainment in 1858. He noticed that the flame of two "fish-tail" gas burners exhibited pulsations in height, which were synchronous with the audible beats. In his publication, he mentioned that even "*a deaf man might have seen the harmony*".

In terms of gas turbine combustion the mechanisms of the interaction between the flame and an acoustic wave are manifold. The physical mechanism responsible for thermo-acoustic instabilities is the transformation of fluctuating energy released in unsteady combustion into acoustic energy. The basis for this process is the flame, which transforms the internal enthalpy of the cold fresh gas to the internal enthalpy of the products. The enthalpy difference between products and educts is released in form of heat. In other words the flame expands the volume thermally and thus acts as a *volume source*. As a consequence a fluctuating flame is a fluctuating source of volume and therefore an *acoustic source*.

A fluctuating flame can be caused by natural flow phenomena – turbulent flow field or natural coherent structures – and by the acoustics of the entire combustion system. The turbulent reacting flow field induces a fluctuating heat release rate and emits broadband noise. Natural coherent structures in the shear layers at the burner outlet lead to a modulation of the convective transport of fresh gas to the flame, which also results in a fluctuating heat release rate. Nevertheless, the dominant mechanisms of combustion oscillations are due to the acoustic field, which depends on the design of the entire gas turbine, including the compressor, the combustion chamber and the turbine. Figure 1.1 presents a simplified model of a practical premixed swirl-stabilized combustion system and the corresponding acoustic perturbations which affect the heat release rate of the flame.

The model, shown in the upper part of Fig. 1.1, contains the plenum, the mixing section, the fuel supply, the swirler and the combustion chamber. The upstream (US) and downstream (DS) part, the compressor and the turbine, and

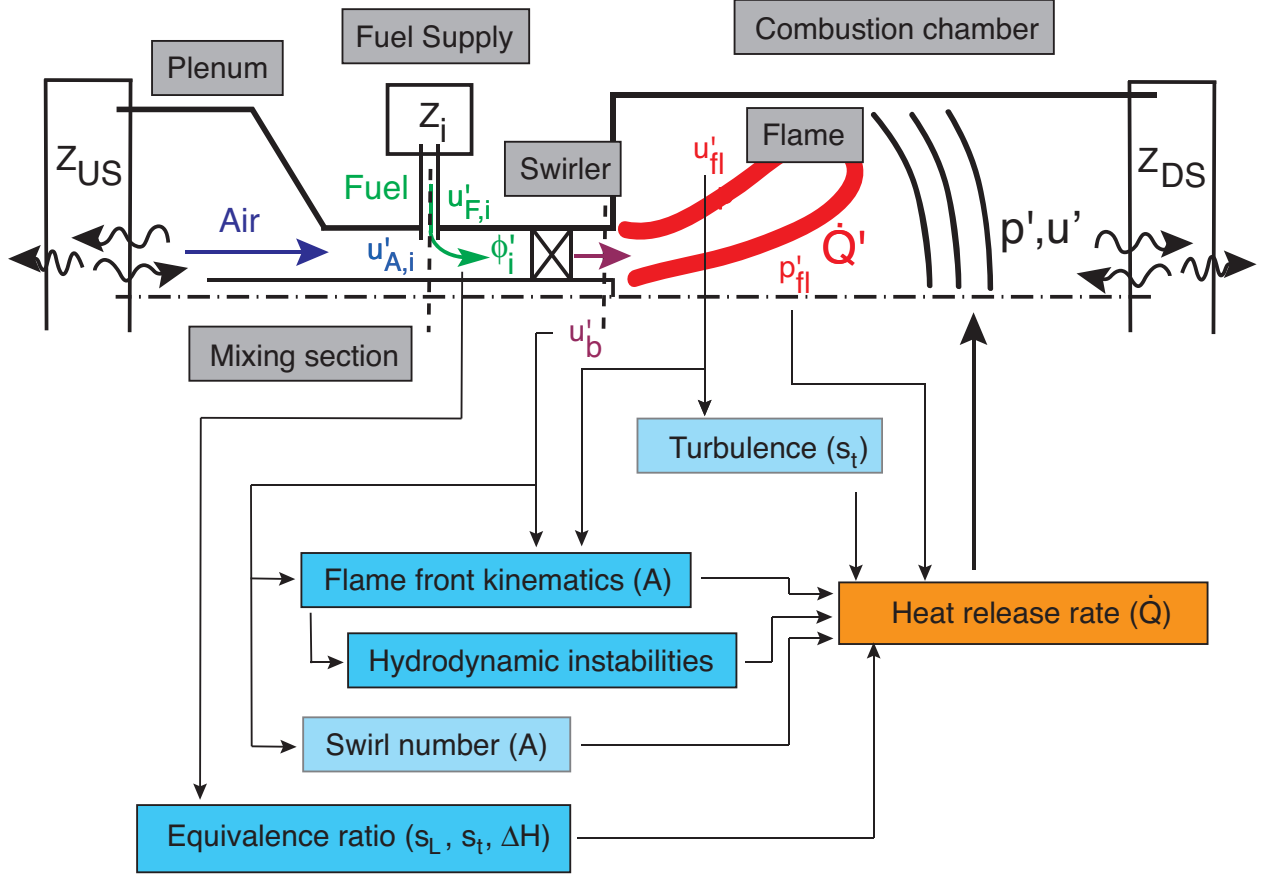


Figure 1.1: Overview of the acoustic interaction of the flame

the fuel injection stages i , $i = 1, \dots, N$, where N denotes the total number of fuel injectors in the system, are represented by their acoustic characteristics in form of the acoustic impedances Z_{US} , Z_{DS} and Z_i ². The downstream part of the figure presents an overview over the different impacts of the acoustics on the heat release rate. Following Ducruix et al. [27], Fleifil et al. [29] or Lawn and Polifke [65] the overall heat release rate is expressed as

$$\dot{Q} = \int \rho_u \Delta H \Sigma s_t dV, \quad (1.1)$$

where ρ_u is the unburnt gas density, ΔH the enthalpy or heat of reaction per unit mass of the mixture, Σ the flame surface per unit volume, s_t the turbulent flame speed and V the volume. The heat release rate fluctuations can be

²The acoustic impedance Z is defined as the ratio of acoustic pressure and velocity and is a description of the local acoustic field.

decomposed in the linear regime into separate contributions of fluctuating unburnt density, heat of reaction, flame area and flame speed:³

$$\frac{\dot{Q}'}{\bar{\dot{Q}}} \approx \frac{\rho'_u}{\bar{\rho}_u} + \frac{\Delta H'}{\Delta \bar{H}} + \frac{A'}{\bar{A}} + \frac{s'_t}{\bar{s}_t}. \quad (1.2)$$

Here, A denotes the total flame front area. The total heat release rate can thus be described as a superposition of the individual effects. The fluctuations of the unburnt density in Eqn. (1.2) can usually be neglected in typical lean-premixed combustion systems burning hydrocarbon fuels at low Mach numbers.

For practical premixed flames, two dominant interaction mechanisms between heat release rate and acoustic fluctuations have been identified:

- 1) *flame front kinematics*, i.e. the time-delayed adjustment of flame shape, flame surface area and flame position to a change in the velocity of the flow through the burner u'_b . These fluctuations result in kinematic perturbations, which are convected along the flame front [11, 13, 22, 29, 65, 68, 121]. The acoustic velocity fluctuation u'_b also influences the local turbulent flow field, especially in the shear layer within and beyond the burner, which can modulate the turbulent burning velocity and thus the fuel consumption rate [76, 90]. At large amplitudes, vortical disturbances of the flow, induced by acoustic oscillations, can manifest themselves as *large-scale vortex structures*. They strongly influence the mixing of fresh fuel/air mixture and hot combustion products and thereby the heat release rate. Vortices observed during combustion oscillations can also be due to hydrodynamic instabilities [94]. They have an impact on the local turbulent burning velocity and can enhance or reduce the combustion process or even lead to local quenching of the flame.

³Acoustic fluctuations are throughout this work denoted by an apostrophe ', whereas mean values are represented by an overbar $\bar{\cdot}$.

- 2) *equivalence ratio fluctuations* (ϕ'_i): they are created by fluctuations of the air mass flow past the injector i or of the pressure at the injector i . These inhomogeneities are transported convectively to the flame, where they lead to a modification of the enthalpy of reaction per unit volume of the mixture (ΔH), laminar (s_L) and turbulent burning velocity (s_t), flame position and hot gas temperature ("entropy waves") [14, 31, 53, 71, 99, 101, 107, 112].

The acoustic pressure (p'_{fl}) and velocity (u'_{fl}) at the flame front could also modify the heat release rate. Their influence is rather small in practical applications like gas turbines or domestic heaters and can therefore be neglected. Other effects, like a fluctuating swirl, which changes mainly the flame area, can also play a role but are not considered explicitly in the present work.

All effects mentioned lead to fluctuations in the heat release rate and thus to a fluctuating volume expansion, which result in acoustic fluctuations (p' , u'). As shown in Fig. 1.1, the acoustic waves caused by the flame travel through the combustion system and are partly reflected at the gas turbine parts, which are located upstream and downstream of the combustion chamber. The amplitude and phase of the reflection are determined by the acoustic characteristics in terms of the impedance at the outlet of the compressor or at the inlet of the turbine. The reflected waves are causing acoustic fluctuations at the flame front, at the burner outlet and at the location of fuel injection, which give rise to a direct or time-delayed response of the flame. The acoustic pressure fluctuations in the vicinity of the flame and the fluctuating heat release rate form therefore a thermodynamic feedback cycle, which is closed by the acoustics of the combustion system. Whether the cycle excites or damps possible combustion oscillations depends on the phase shift between the two characteristics and is known as the Rayleigh criterion. According to Lord Rayleigh [105], who discovered this correlation in the 19th century, the conditions for the occurrence of instabilities are met, when heat is released at the moment of greatest compression. In other words a combustion oscillation can occur if pressure and heat release rate fluctuations are in phase, i.e. the integral of the product of pressure and heat release rate fluctuations over a oscillation period T_{per} is

positive:

$$\oint_t^{t+T_{per}} \int_{V_{cc}} p'(x, y, z, t) \dot{Q}'(x, y, z, t) dV dt > 0. \quad (1.3)$$

The integration in Eqn. (1.3) is performed spatially over the combustion chamber volume V_{cc} . A positive Rayleigh integral is a necessary, but not sufficient condition for the occurrence of combustion instabilities. The generated energy of the thermo-acoustic process has to outweigh the acoustic losses in the system and the radiation of the oscillation energy over the boundaries.

To realize a low-oscillation combustion chamber three main possible approaches can be deduced from the latter consideration:

- Increase of the damping characteristics of the combustion system
- Reduction of the heat release rate fluctuations in the combustion chamber
- Favorable modification of the phase relationship between fluctuations of pressure and heat release rate

1.3 Control of thermo-acoustic instabilities

Beside the fact that many different methods were developed to suppress thermo-acoustic oscillations, the prediction of these instabilities in the early design stage is still a challenging task. Following the three approaches mentioned, the manifold strategies to reduce unwanted pressure oscillations and to control possible thermo-acoustic oscillations can be divided into active and passive control mechanism.

Active feedback control involves an actuator, which modifies certain parameters of the system in response to a measured signal. In many cases the fuel mass flow is modulated to counteract the heat release rate perturbation that

drives oscillations [17, 123]. Shcherbik et al., for example, applied harmonic modulation of the fuel injection rate with an open-loop active control system consisting of a pressure sensor and a fast response actuating valve [123]. A general overview about different methods is given by Dowling and Morgan [25]. Most active control methods belong therefore to the third approach in modifying the relationship between pressure and heat release rate. A possibility to reduce the heat release rate fluctuations is to enhance flame stabilization. This can be achieved using pilot flames, which are adjusted to the conditions of the different operation regimes. The method of using pilot flames is often a compromise between stability and reduced emission performance. An example of this approach, which comprises an actuator in the pilot gas system and a control algorithm, is described in Seume et al. [122]. A disadvantage of active control methods is the requirement of significant numbers of sensors and actuators and a robust control algorithm, which has an impact on complexity, cost and geometry of the gas turbine system.

Passive methods focus on the design optimization of different parts of the combustion system. A reduction of high pressure oscillations can be achieved by simply damping the amplitudes in the combustion chamber by Helmholtz resonators or $\lambda/4$ tubes [8, 70, 109]. The performance of these devices depends on their geometrical dimensions, their number and their arrangement in the system. As in other passive control devices, the damping performance is limited to a certain frequency range. Generally speaking, it can be stated, that a damper acting on a wider frequency band width has a lower damping performance.

To reduce the response of the flame various researchers use elliptic burner exit cross-sections [9, 89, 99]. According to Paschereit and Gutmark [89] the changed burner exit design mainly reduced the evolution of large-scale coherent structures in their combustor test rig. In the same work they reported also the positive effect of miniature vortex generators in separating shear layers, which were used in the range of high and low frequency instabilities to suppress small-scale vortices produced at the burner exit by the Kelvin-Helmholtz instability. Berenbrink and Hoffman [9] used asymmetric burner outlets (ABO), which showed a similar behavior. ABOs cause asymmetric flow

fields and shear layer distribution and reduce the feedback of symmetric ring vortices. In addition Polifke et al. [99] mentioned that a wider distribution of the time lags – a larger standard deviation – generated by an elliptical burner outlet could reduce combustion oscillations.

Other passive methods focus on a phase change of various characteristics of the thermo-acoustic feedback loop. Following Berenbrink and Hoffmann [9], detuning of multiple fuel injector combustors can improve the performance of a full-scale gas turbine in preventing coherent feedback from all combustion zones. This was realized by introducing cylindrical burner extensions (Cylindrical Burner Outlet (CBO)) with different lengths and thus different mean convective time delays to suppress possible burner-to-burner interactions. Using CBOs the formation point of coherent structures was shifted to a downstream location. In addition, the time lag from the fuel injection port to the flame was increased. They stated that both, CBOs and ABOs, could be used to substitute a certain amount of standard burners in an annular combustion chamber and shift stable operation conditions to higher power outputs.

Instead of changing the burner design different convective time lags from the point of fuel injection to the flame can be obtained by re-locating the point of axial fuel injection, as described by Straub and Richards [125], Richards and Straub [109] or Steele et al. [124]. Splitting the fuel between two or more injection positions is also a common approach to extend the stable operation regime [74, 117]. Scarinci and Halpin [117] showed that axial staging of the heat release rate inside a Rolls-Royce industrial Trent gas turbine, which was realized by an adjustment of the fuel splits, allows a wide turn down of the flame temperatures and thus a direct influence on the amplitudes and frequencies of combustion oscillations.

Richards et al. [106], Hobson et al. [43], Goldmeier et al. [37] and Lieuwen and Zinn [72] demonstrated that the stability characteristics of the combustion system could also be a strong function of the acoustic impedance of the fuel supply. Richards et al. [106] showed that a change in the phase of the equivalence ratio fluctuations, which can be achieved by adjusting the resonant characteristics of the fuel supply system, could reduce pressure oscillations. In a further analytical and experimental study [108] two fuel injectors having a variable geometry were used to produce a different dynamic response

of the flame. The resulting impedance mismatch prevents the injectors from strongly coupling to the same acoustic mode and allows a further reduction of occurring oscillations.

1.4 Intention and structure of this work

The idea to use multiple, staged fuel injectors with appropriately tuned injector impedances represents a promising passive design strategy to reduce unwanted combustion oscillations and to extend the stable operation range. Fuel staging also allows a flexible operating method regarding fuel quality and partial load requirements. An example of such a "practical premixed combustion system" with two fuel injection stages with impedances Z_i , $i = 1, 2$ is shown in Fig. 1.2.

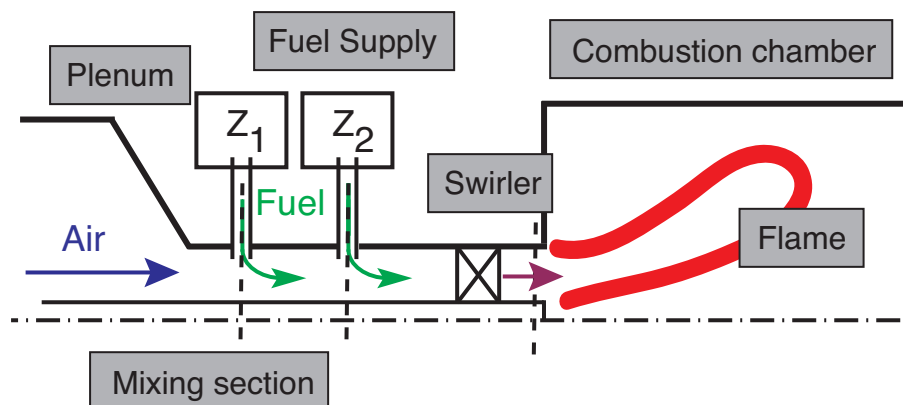


Figure 1.2: Sketch of a combustion configuration with two fuel injectors

Although there are quite a few numerical and experimental studies, which verify the impact of this passive control possibility, experience has shown that it is difficult to adjust the injector locations, impedances or both such that all possible modes of instability in a combustor are suppressed. Quantitative tools to devise such a passive control strategy for gas turbine combustors are, up to now, still missing.

In terms of thermo-acoustic analysis a physical understanding and an accurate description of the flame dynamics is essential. The flame dynamics of a

practical combustion system is mainly influenced by fluctuations of the mass flow at the burner exit (flame front kinematics) and equivalence ratio, as described in chapter 1.2. In the literature, both effects have often been discussed separately. A significant body of work is concerned with the dynamics of perfectly premixed flames, where equivalence ratio fluctuations are absent, while some of the early works on thermo-acoustic instabilities in practical premixed combustors consider only equivalence ratio fluctuations. However, it should be clear that several of the interaction mechanisms between flow, mixing, heat release and acoustics will be active simultaneously. The overall flame response is therefore a superposition of individual contributions (see Eqn. 1.2).

Retrospective of the mentioned issues, it becomes obvious that for the development of such a passive control strategy a design tool is required which accounts for the effect of multiple fuel injectors. The overall motivation and aim of this work is therefore to develop a numerical design method and to determine design guidelines for combustion systems using multiple, staged fuel injectors with tuned injector impedances.

A numerical investigation has the advantage that there is no need for a time consuming and expensive test rig and the required measurement devices. In addition, the experimental measurement of the flame dynamics of a practical premixed combustion system is rather challenging as many of the flow parameters of interest can not be measured easily. An example is the determination of the heat release rate fluctuations of a practical premixed flame using OH^* or CH^* chemiluminescence signals. According to [64], the integral heat release rate can be monitored by chemiluminescence only if an empirical correlation between both exists, which implies a known integral heat release rate of the flame. Another problem concerns the independent excitation of the air mass flow and the mass flows in the fuel injection systems. On the other hand, the disadvantage of numerical methods is that they rely on how well the physics are described by the numerical models. This is especially disadvantageous if the physics are as complex as the combustion - turbulence - acoustic interaction.

To achieve the aims mentioned the following tasks can be deduced, which reflect the organization and structure of the present work:

The work starts with an **overview and discussion of the available numerical methods** (chapter 2) to determine the thermo-acoustic characteristics of combustion systems and the chosen strategy, which is a hybrid approach using Computational Fluid Dynamics, system identification and acoustic network modelling.

On this basis, the following chapter deals with the **basic equations of the acoustics** (chapter 3) and the simplifications used in this work.

Chapter 4 describes the **basics of Computational Fluid Dynamics**, including turbulence and combustion models. It is followed by the presentation of the **system identification method** for flame dynamics responding to more than one disturbance signal (chapter 5).

The **numerical combustion test rig** used is then described with two and three fuel injection stages in chapter 6, including the **results of the numerical simulations** and the **identification of the flame dynamics**. Furthermore, the **acoustic network model** of the test rig and the **parameter study** analyzing the different influences on the combustion stability is presented in chapter 7.

The work is completed with a short **summary and conclusion** (chapter 8).

1.5 Terminology and specification of the present work

Before the possible numerical calculation methods are evaluated in terms of the tasks presented, the terminology and the main general specifications are first reviewed.

In general, the field of gaseous combustion can be subdivided into three different technical processes, which are related to the mixing process of fuel and air: premixed, non-premixed, or partial premixed combustion.

A combustion process is called premixed if the fuel and oxidizer are mixed by turbulence for a sufficient time before the mixture is ignited. In a non-premixed process, the oxidizer and fuel are injected separately into the combustion chamber. The mixing and combustion process are directly coupled

and combustion takes place in regions of stoichiometric mixture. The partial premixed process is therefore a combination of both. The diesel engine is a good example, where several liquid fuel sprays are injected into hot compressed air. Before auto-ignition occurs, the fuel evaporates and mixes partially with the air. Thus, the beginning chemical reaction can be seen as a premixed process whereas the final burnout occurs mainly under non-premixed conditions.

In the present work a so-called "practical premixed combustion system" is analyzed. It is characterized by inhomogeneous lean premixed conditions, where natural gas is injected at one or multiple locations in the mixing section as shown in Fig. 1.2. As in real gas turbines there is no choke between fuel injectors and flame. In such a configuration and in contrast to perfect premixed conditions, local and temporal fluctuations of the fuel concentration may be induced by acoustic fluctuations and must be taken into account. The difference between perfect premixed, non-premixed and practical premixed combustion systems is also shown in Fig. 1.3.

The fuel injectors of the practical premixed combustion system considered in the present work are acoustically non-stiff. In other words, the pressure drop between fuel plenum and mixing section is not sufficient to decouple the acoustics of the fuel supply system from the acoustics of the entire combustion system. This means the fuel mass flow through the fuel injectors may be influenced by the acoustics and can vary in time. The flame of such a system can therefore respond to equivalence ratio fluctuations, which are caused by acoustic fluctuations in the mixing section at the location of fuel injection *and* fluctuations in the fuel stream in the injector, *and* by mass flow fluctuations at the vicinity of the burner exit.

The main motivation to develop a design tool and design guidelines for practical premixed combustion systems is to demonstrate how fuel staging and differently tuned fuel impedances influences the overall thermo-acoustic behavior. Therefore a linear stability analysis is sufficient to accomplish the task. A non-linear analysis, which is required to predict limit cycle amplitudes or non-linear instability limits, is out of the scope of the present work.

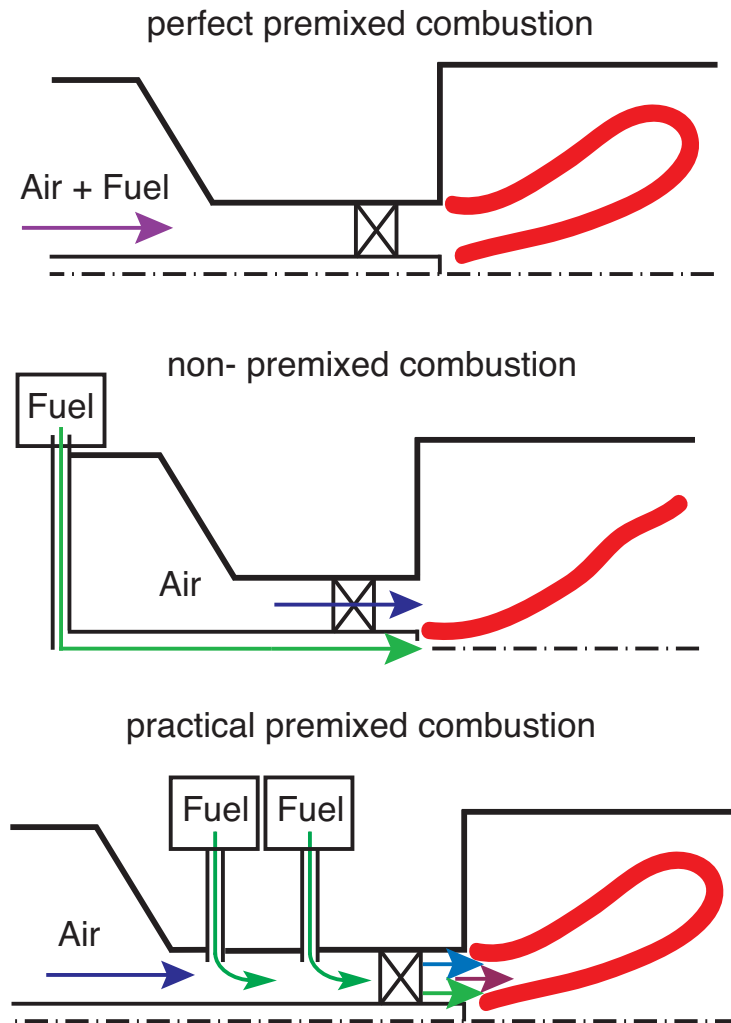


Figure 1.3: Sketch of premixed, non-premixed and practical premixed combustion systems

A general "condition" arises from the geometric extensions of the considered combustion system in relation to the wavelength of interest. The flame response exhibits low pass filter behavior in the frequency domain with a cut-off frequency. For the combustion system analyzed, this frequency lies between 400 Hz and 800 Hz. The maximum frequency can then be restricted to 1000 Hz in the present work. In addition, the burner configuration examined exhibits small radial and circumferential extensions compared to the wavelength. The problem can therefore be reduced to one-dimensional acoustics.

A design tool should deliver results of various configurations in an adequate time frame. An investigation about the impact of several parameters requires multiple calculations or simulations. The overall computational effort of the methods should be minimized and is considered as another specification.

2 Numerical analysis of thermo-acoustic instabilities

2.1 Overview of methods for thermo-acoustic stability analysis

The analytical analysis of thermo-acoustic oscillations has first been developed to explain combustion instabilities of solid-propellant and liquid-propellant rockets [18, 19]. In the area of gaseous fuels Merk [79] created a comprehensive and universal basis for the analysis of thermo-acoustic oscillations. He was the first one, who developed a mathematical approach in defining a transfer function, which relates the unsteady heat release rate to fluctuating fluid properties. Merk demonstrated for several applications, such as the Rijke tube or for premixed flames, that, with the help of the transfer function, it is possible to determine the stability of combustion systems.

Thermo-acoustic phenomena can be described by the conservation equations – the mass and species conservation or the so-called continuity equation, the momentum and the energy equation. The possible mathematical methods to determine the thermo-acoustic behavior of a system differ in having a different degree of simplification of the conservation equations in the time or frequency domain.

The most complex and expensive method is the numerical simulation of compressible, turbulent and reactive flow using Navier-Stokes equations, which is commonly associated with the term "*Computational Fluid Dynamics (CFD)*". CFD simulations are, in general, based on a finite-volume method, which discretizes, like the finite-difference method, the differential quotient in the differential equations. The advantage of this procedure, compared to other ap-

proaches, is that the representative physical processes are only slightly simplified. This is especially advantageous because the coupling between the acoustics and the dynamics of the combustion process does not need to be modeled. It follows implicitly from the solution of the non-linear partial differential equations.

The field of CFD can be characterized by three different modelling approaches. They range from the *Direct Numerical Simulation (DNS)*, which solves the Navier-Stokes equations explicitly on a very fine mesh, to methods, which simplify the equations by dividing the physical properties into resolved and modeled quantities (*Large Eddy Simulation (LES)*) or rather in mean and fluctuating quantities (*Reynolds-averaged Navier-Stokes Equations (RANS)*). Whereas the LES still resolves large scale turbulent eddies and filters the small scale ones, the RANS approach computes primarily average values, without solving any turbulent quantities. In both methods closure models are required to calculate the unresolved turbulent structures. In the case of combustion further simplifications and models are necessary to simulate the complex chemical process as well as the interaction between chemical kinetics and turbulence.

In the past a multitude of publications demonstrating the possibilities to simulate combustion oscillations using RANS or LES were published¹. To name a few, there are Murota and Ohtsuka [83], for example, for the determination of instabilities of a premixed burner, Hantschk and Vortmeyer [39] for the analysis of self-excited oscillations in a non-premixed burner, Angelberger and Veyante [4] for LES simulations of combustion instabilities of premixed flames in consideration of mass flow and equivalence ratio fluctuations and Roux et al. [111] for the comparison of experimental results, acoustic analysis and LES simulation.

Using CFD it would be possible to determine the acoustic characteristics of the combustion system – including the flame dynamics – with one method. However, to obtain meaningful results, the geometry of the combustion system has to be computed up to the point where, according to Schönfeld

¹The use of DNS is, because of its immense computational effort, until now restricted to small and simple simulation cases and not feasible for industrial and most scientific applications.

and Poinso [118], well defined boundary conditions can be defined. If the impedance of the boundaries is known, it can be implemented using an approach which is described e.g. by Huber et al. [50]. For these cases the method is suitable to predict the physically meaningful dominant eigenfrequencies and limit cycle amplitudes. Also, the method has the advantage in not being restricted to the linear behavior of the flame nor to the compactness assumption², which often applies for flame transfer functions and matrices in the frame of analytical or network models. On the other hand, a change of the combustor design, e.g. of the fuel supply impedances, has an impact on the flame response and the acoustics of the entire system. The method would therefore require one simulation for every geometrical change.

Further simplifications regarding the physical phenomena always result in the demand for an explicit model to include the coupling between acoustics and combustion. The first step in simplifying the Navier-Stokes equations is to neglect viscous effects and to linearize the main physical parameters such as density, pressure, velocity and heat release rate. This means a decomposition of the flow into a steady mean flow and small perturbations. Subtracting the mean part and neglecting higher order terms of fluctuating variables yields the *linearized Euler equations* for pressure, velocity and density. Combining the linearized Euler equations and neglecting mean flow effects, which is a feasible assumption in the low Mach number regime, leads to the *inhomogeneous wave equation*.

The inhomogeneous wave equation is commonly solved using a *finite element method*, which is based on the discretization in terms of the ansatz functions. These functions are defined on individual elements in the domain and approximate the solution. Pankiewicz and Sattelmayer have shown in several publications [87, 88] that this approach can be applied to analyze the thermo-acoustic behavior of large and complex geometries, such as annular combustion chambers. Another advantage is the fact that the method does not require any assumptions about the coupling of different modes. When non-linearities, such as saturation effects in the combustion process, are

²An acoustic element can be considered as compact if its geometrical length l is much smaller than the shortest wavelength λ_w , $l \ll \lambda_w$.

included it is possible to reproduce limit cycle oscillation. The difficulty of the method lies in the description of the source term of the reaction rate. Additional flow effects or driving mechanisms for oscillations, like equivalence ratio fluctuations, can only be determined indirectly. Pankiewicz therefore suggested a hybrid approach using a finite element method to simulate the pure acoustics of the combustion system while the flame behavior is provided externally through experiments or CFD. Furthermore, pressure losses or damping in the system cannot be realized in a straightforward manner.

The *Galerkin method* or the *Green's function technique* are further numerical approaches to solve the inhomogeneous wave equation. In the first method the acoustic pressure can be expanded in a Galerkin series of trial functions. The elements of the trial functions are commonly represented by the amplitudes of the pressure perturbations and the acoustic eigenfunctions of the homogeneous wave equation. Thus, the detailed knowledge of the mode shapes and geometry without mean flow and heat release has to be known a priori. This could be done by calculating the analytical solution or by using software tools for more complex geometries. The calculation of the acoustic pressure field reduces to solve a set of ordinary differential equations. The solution tracks in time whether the amplitude of each mode will grow or decay. Dowling and Stow [26] and Dowling [21] demonstrated that the form of the coupling between the heat input and the unsteady flow has a critical effect on the frequency of oscillations. They suggested a multiple-term Galerkin series expansion to determine the frequency shift for unsteady combustion. Also, Krebs et al. [59] used the Galerkin method to analyze the thermo-acoustic behavior of annular combustors and stated that by using this method even the coupling of different modes could be taken into account. In the second technique mentioned, the harmonic heat perturbation term is represented by a Green's function. If formal coupling between flow perturbations and heat release rate fluctuations is considered, the use of the Green's function simplifies the inhomogeneous partial differential equation to an integral equation, which can be solved iteratively. To determine the one-dimensional pressure perturbation generated by unsteady combustion Hedge et al. [41] calculated the resonance frequencies by minimizing the magnitude of the

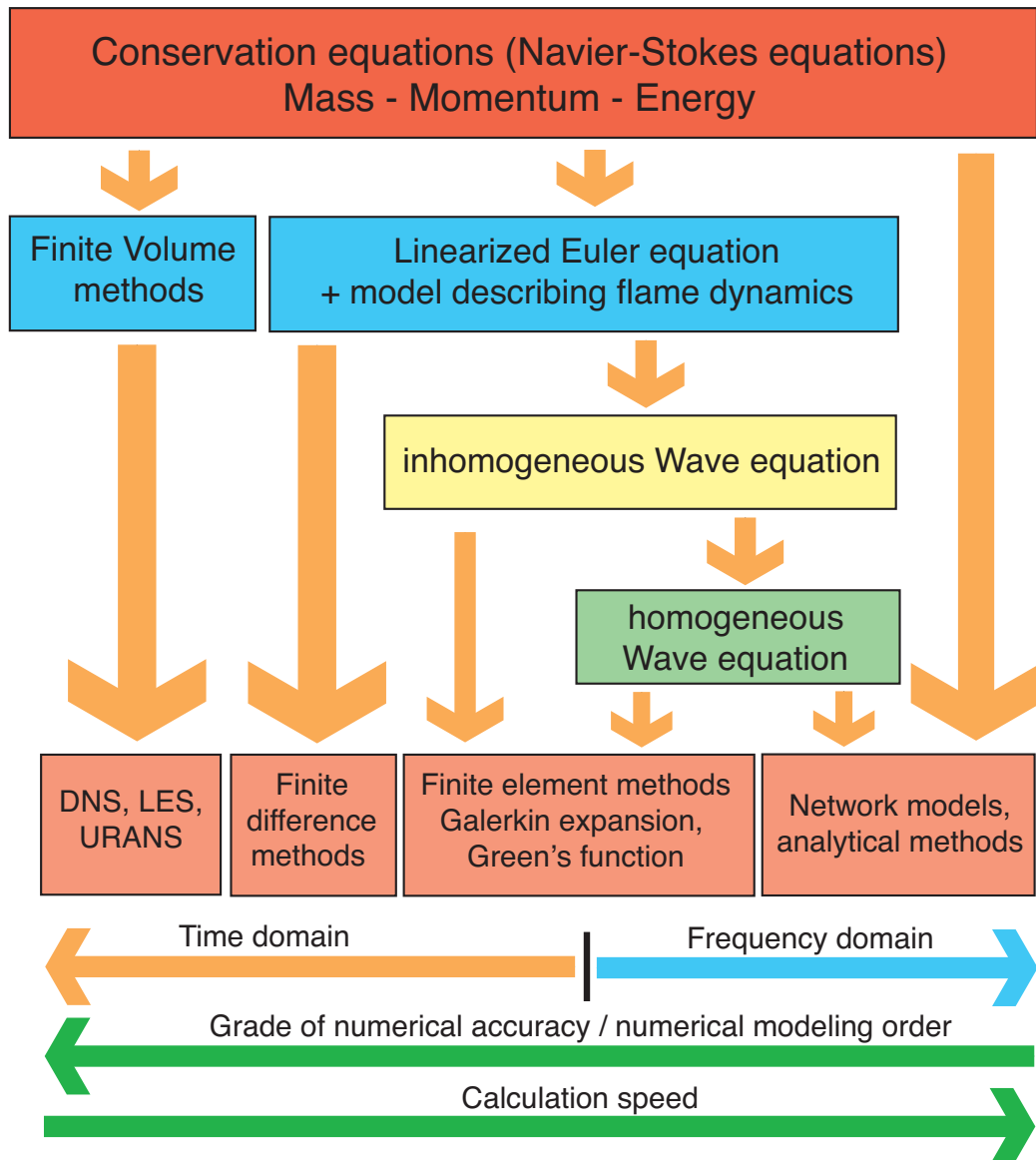


Figure 2.1: Overview of common numerical thermo-acoustic calculation methods

denominator in the Green's function. Peracchio and Proscia [91] also took advantage of the Green's function in developing a non-linear parametric heat release rate/acoustic model.

A further simplification comes from technical acoustics. Munjal [82] proposed

to divide a complex system into a network consisting of simple elements. Deuker [20] transferred this approach to the thermo-acoustic problem in the field of gas turbines. Nowadays, the *acoustic network model technique* is a widely used design tool and allows a fast and robust estimation of the thermo-acoustic behavior for a multitude of combustion systems [23,46,58,61,70,101]. In the network model approach the acoustic behavior of each element is commonly described by a transfer matrix. A transfer matrix relates the acoustic pressure and the velocity or the Riemann Invariants f and g between inlet and outlet of the element. The superposition of the two Riemann Invariants f and g , which travel in opposite directions, are a general solution of the wave equation in the one- or two-dimensional case. A further limitation to plane and harmonic waves and the presumption of certain mode shapes enables the determination of the acoustic field and analysis of an acoustic system. The connection of the elements finally results in an algebraic eigenvalue problem, which can be solved analytically or numerically. As shown e.g. by Sattelmayer and Polifke [113, 114], the dynamics of such a system can also be analyzed using methods derived from control theory. The latter approach enables the determination of eigenfrequencies in the real frequency domain, which is necessary when experimentally determined acoustic elements are used. In network models the flame is commonly assumed to be a discontinuity of negligible thickness and can be represented by simple flame models. Flame transfer functions obtained by experiment or CFD can also be implemented as a single network element via the linearized Rankine-Hugoniot relations. Hubbard and Dowling [47, 48] used network-like models to analyze the effect of different analytical flame models or the impact of a Helmholtz resonator attached to the plenum of a Rolls-Royce gas turbine. A model investigating some generic aspects in relation to fuel supply impedances is reported by Hobson et al. [43]. Here, a CFD simulation was performed to obtain a time delay to optimize the description of the flame response. Polifke et al. [101] investigated the interaction between combustor acoustics and entropy waves using a network model. The authors were able to verify that entropy waves at the exit nozzle can enhance or reduce thermo-acoustic stability of a combustor. The network model technique was also successfully applied by Evesque and Polifke [28] and Koppitz et al. [58] to two-dimensional geometries as annular combustion cham-

bers. In the latter work, Kopitz et al. implemented an experimentally measured flame transfer function into a network model.

Another common approach is the use of *analytical methods* to analyze the thermo-acoustic behavior of combustion systems. The developed models are similar to the network technique but usually comprise very simplified estimates of the geometry, the combustion mechanism and the flow physics. Basic physical effects on the combustion process using analytical approximations are the focus of various publications. Examples can be found in Fleifil et al. [29], Lieuwen and Zinn [72], Hubbart and Dowling [48], Polifke et al. [101], Sattelmayer [112], Cho and Lieuwen [15] and Richards et al. [106, 108].

A schematic classification of the methods presented is shown in Fig. 2.1. The main differences between the described calculation methods lie in the various degrees of simplification regarding the description of physical phenomena and the calculation routine to find appropriate solutions. Generally it can be stated that a higher degree of simplification corresponds to a reduced computational effort and a reduced modelling accuracy. Another difference is the fact that only CFD is able to model the acoustic-combustion interaction – all other methods presented require a description of the flame dynamics either through an analytical model or models derived from CFD simulations or experiments (e.g. flame transfer functions).

The CFD simulation of the entire combustion system including plenum, mixing section, injectors, swirler and combustion chamber, would therefore be straightforward in the sense that only a method is sufficient to determine the thermo-acoustic behavior of the system. As every design change requires a new simulation, it is also the computational most expensive variant. The computational effort for a parameter study, which is required for the present work (see chapter 1.5), is unacceptable and therefore not considered any further.

Finite element methods, Galerkin or Green's functions, which are useful tools to analyze complex three-dimensional acoustic fields, do not have more advantages compared to acoustic network models, as the present work is restricted to one-dimensional acoustics. They are also not taken into account

in the following.

Simple approaches, however, which are based on analytical derivations, can hardly be achieved because of the complexity of the combustion test rig acoustics. In contrast to the latter, network models proved to be quite useful in terms of calculation speed and flexibility to perform parameter studies. They are therefore chosen in the present work to calculate the acoustics of the practical premixed combustion system.

The network model approach requires a description of the flame dynamics. A physically meaningful description of the practical premixed flame is essential to determine the overall thermo-acoustic behavior of a combustion system. The flame dynamics and its implementation into the acoustic network model are discussed in detail in the following sections.

2.2 Flame dynamics of a practical premixed combustion system

The flame dynamics of a practical premixed combustion system can be described in the linear regime using a general analytical relation (see Eqn. (1.2)):

$$\frac{\dot{Q}'}{\bar{Q}} \sim \frac{\Delta H'}{\Delta \bar{H}} + \frac{A'}{\bar{A}} + \frac{s'_t}{\bar{s}_t} = \frac{\phi'}{\bar{\phi}} + \frac{A'}{\bar{A}} + \frac{s'_t}{\bar{s}_t}. \quad (2.1)$$

The individual terms on the right hand side can be related to the dominant acoustic-combustion interaction mechanisms, which cause heat release fluctuations immediately or after a certain time delay. Assuming that the flame response to acoustic fluctuation of pressure at the flame can be neglected the main mechanisms are due to acoustic fluctuations at the flame holder and at the location of fuel injection as discussed in chapter 1.2. A sketch of a practical premixed combustion system with one fuel injector is shown in Fig. 2.2 to clarify important parameters and locations in the following.

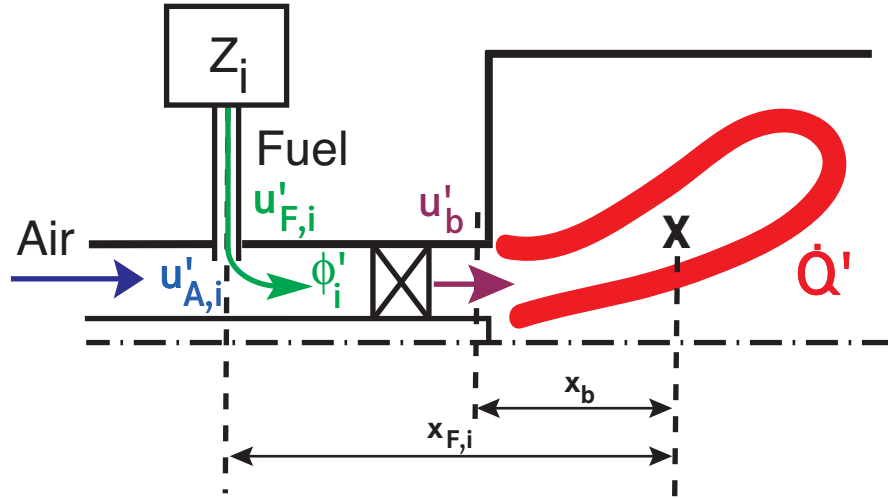


Figure 2.2: Sketch of a practical premixed combustion system, indicating important parameters and dimensions

2.2.1 Flame response to velocity fluctuations

The response of the flame to fluctuations of mass flow or velocity u'_b at a reference location, i.e. the burner exit (see e.g. [13, 22, 29, 121])

$$\frac{\dot{Q}'}{\bar{Q}} \sim \frac{u'_b}{\bar{u}_b} \quad (2.2)$$

is commonly rewritten in the frequency domain in terms of a *flame transfer function*, F_u . The flame transfer function relates a fluctuating "signal", in this case, the velocity u'_b , to its "response", i.e. the resulting fluctuation of the heat release rate \dot{Q}' :

$$F_u \equiv \frac{\dot{Q}'(\omega)}{\bar{Q}(\omega)} / \frac{u'_b(\omega)}{\bar{u}_b(\omega)} \quad (2.3)$$

$$\Rightarrow \frac{\dot{Q}'(\omega)}{\bar{Q}(\omega)} = F_u \frac{u'_b(\omega)}{\bar{u}_b(\omega)}. \quad (2.4)$$

The latter relation represents a single-input single-output (SISO) system with

input u'_b and output \dot{Q}' as shown in Fig. 2.3. The flame response of a perfect premixed combustion system, in which no equivalence ratio fluctuations exist, is completely described by such a SISO system.

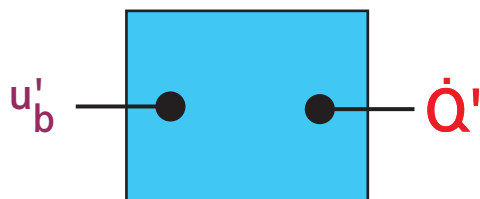


Figure 2.3: SISO system representing a perfect premixed flame

A proper choice of the reference location " b " for the velocity fluctuation u'_b is crucial to obtain a flame transfer function which is independent of the acoustic impedance at the burner. The acoustic impedance at the burner is characterized by the acoustic properties and the acoustic boundary conditions of the combustion system. As the flame dynamics is mainly controlled by the flame front kinematics, the proper reference location is the burner exit. At this location acoustic fluctuations generate vortical perturbations in the flow field (shear layer), which are transported with the speed of the flow to and through the flame, modulating the flame area and turbulent flame speed. The strength of the disturbance is directly related to the amplitude of the velocity fluctuation at this position. A velocity signal, which is taken at a different location, may be influenced in a spurious manner by the acoustics of the combustion system. If the distance between burner exit (x_b) and the reference location ($x_{\tilde{b}}$) is not much smaller than a acoustic wave length (speed of sound divided by frequency), the acoustic velocities at both locations differ in terms of amplitude and phase. If now the acoustics of the system is changed, e.g. by changing the upstream boundary condition, the amplitude and phase difference between the acoustic velocities at both locations is modified. This is clarified in Fig. 2.4, which shows the spatial amplitude of the acoustic velocity of two cases a) and b) with a different upstream boundary condition Z_1 and Z_2 . As the velocity fluctuation at x_b is the driving parameter, a high velocity value at x_b would result in almost no heat release rate fluctuation in case a). However, the contrary is demonstrated in case b), in which a low value at $x_{\tilde{b}}$ corresponds to a strong response of the flame. The modification of the system changes there-

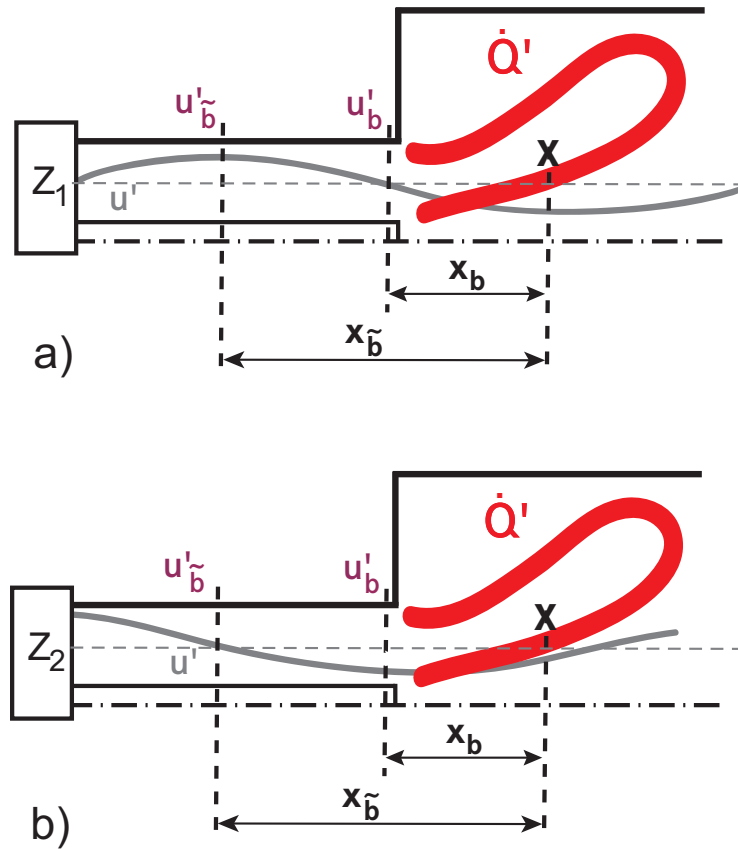


Figure 2.4: Impact of the combustion system acoustics on the choice of the reference location

fore also the relation – the transfer function – between the velocity fluctuation at $x_{\tilde{b}}$ and the heat release rate fluctuation. A transfer function using the reference location $x_{\tilde{b}}$ is thus not independent of the acoustics of the combustion system. It is therefore not a useful description of the flame dynamics. Indeed, the latter was demonstrated by Truffin and Poinso [127]. In their work they showed that the values of phase and gain of the flame response depend significantly on the combustor outlet reflection coefficient, if a reference location far upstream is selected. Here, Truffin and Poinso proposed, that the distance $x_{\tilde{b}} - x_b$, expressed as a Helmholtz number, should not exceed 0.01 to obtain consistent results. This limit is a surprisingly strict criterion, indicating that already a distance of a few millimeter can have a noticeable effect on the results.

2.2.2 Flame response to equivalence ratio fluctuations

In a practical premixed combustion system, where fuel is injected at a location with non-negligible acoustic fluctuations of pressure or velocity, the equivalence ratio ϕ_i will also fluctuate, see Fig. 2.2. When the fluctuations, which are transported convectively with the flow, arrive at the flame front, they affect the heat release rate through a change of heat of reaction per unit mass of pre-mixture, burning velocity and flame area. All these processes can be captured by another transfer function, which describes the impact of equivalence ratio fluctuation ϕ_i to heat release rate fluctuations

$$F_{\phi,i}(\omega) \equiv \frac{\dot{Q}'(\omega)/\bar{Q}}{\phi'_i(\omega)/\bar{\phi}}, \quad (2.5)$$

where $\bar{\phi}$ denotes the mean equivalence ratio of the entire system. ϕ_i represents the nominal equivalence ratio fluctuations, which is measured at the point of injection. The transfer function represents again a SISO system with input ϕ'_i and output \dot{Q}' . Similar to the discussion above the point of injection is the physical correct reference location as equivalence ratio fluctuations are the result of acoustic velocity fluctuations at this location. At the point of injection the equivalence ratio fluctuations can be expressed in terms of the acoustic velocity fluctuations of the main air mass flow and the fuel mass flow, which is a very useful relationship. It provides in conjunction with the transfer function $F_{\phi,i}$ a closure relation for stability analysis of the combustion system using e.g. a low-order network model as in the present work or a finite-element model for a generalized Helmholtz-Equation [53, 84, 96, 101]. The derivation of the relationship is represented below. Care has to be taken if equivalence ratio fluctuations are determined at a different position as the convectively transported equivalence ratio fluctuations are dispersed on the way to the flame. The dispersion of the fuel depends on the geometry of and on the turbulent flow field in the mixing section or swirler. Additionally, in jet-in-cross flow injector configurations for example, as shown in Fig. 2.2, the depth of penetration can, depending on the fluctuations, also change. A different depth of penetration results in a different radial fuel-air composition at the burner exit. This may have an influence on the local heat release rate fluctuation and thus on the transfer function as indicated by Armitage et al. [7]

for example. The reference location can therefore only be chosen arbitrarily if a perfect fuel-air mixture is achieved at the burner exit. However, for many practical applications this is not the case.

Determination of equivalence ratio fluctuations

The nominal equivalence ratio fluctuations can be expressed as a function of the acoustic velocities in the main air and fuel stream at the point of injection, which is presented in the following. The overall equivalence ratio ϕ is defined by the mass flow rate of air and the sum of the fuel mass flow rates at the different injectors "i",

$$\phi = s_{st} \frac{\sum_{i=1}^N \dot{m}_{F,i}}{\dot{m}_A}, \quad (2.6)$$

where N represents the number of injectors and s_{st} denotes the stoichiometric factor.

At each injector "i", the nominal equivalence ratio ϕ_i is increased in the presence of acoustic fluctuations, if the velocity of the flow past the injector is reduced (by a negative velocity fluctuation $u'_{A,i}$) or the mass flow rate through the fuel nozzle is increased (by a positive velocity fluctuation $u'_{F,i}$), see Fig. 2.2 [75, 101].

Dividing the equivalence ratio at injector "i = k" into the contributions which are injected upstream "i = 1, ..., k - 1" of and at "i = k", it follows:

$$\begin{aligned} \phi_k &= s \frac{(\bar{m}_{E,k} + \dot{m}'_{F,k})}{(\bar{m}_A + \dot{m}'_A)} + \frac{\sum_{i=1}^{k-1} \bar{m}_{F,i}}{\bar{m}_A} = \\ &= s \frac{\rho_F A_F (\bar{u}_{F,k} + u'_{F,k})}{\rho_A A_A (\bar{u}_{A,k} + u'_{A,k})} + s \frac{\sum_{i=1}^{k-1} \bar{m}_{F,i}}{\bar{m}_A}, \end{aligned} \quad (2.7)$$

where $\dot{m}_{F,i}$, \dot{m}_A denote the fuel mass flow in the fuel line of injector "i" and the air mass flow, respectively. With series expansion of the first order of the term $(\bar{u}_A + u'_A)$ with respect to u'_A around \bar{u}_A (higher orders are neglected) one

obtains:

$$\frac{(\bar{u}_{F,k} + u'_{F,k})}{(\bar{u}_{A,k} + u'_{A,k})} = \frac{\bar{u}_{F,k}}{\bar{u}_{A,k}} \left(1 + \frac{u'_{F,k}}{\bar{u}_{F,k}} - \frac{u'_{A,k}}{\bar{u}_{A,k}} \right). \quad (2.8)$$

Equation (2.7) can be rewritten to:

$$\phi_k = s \frac{\sum_{i=0}^k \bar{m}_{F,i}}{\bar{m}_A} + s \frac{\bar{m}_{F,k}}{\bar{m}_A} \left(\frac{u'_{F,k}}{\bar{u}_{F,k}} - \frac{u'_{A,k}}{\bar{u}_{A,k}} \right), \quad (2.9)$$

where the first part on the right side represents the mean value $\bar{\phi}_k$ and the second the fluctuating variable ϕ'_k . Taking Eqn. (2.9), a general equation for the ratio of the equivalence ratio fluctuations at each injector "i" to the overall mean value $\phi'_i/\bar{\phi}$ can be derived:

$$\frac{\phi'_i}{\bar{\phi}} = \left(\frac{u'_{F,i}}{\bar{u}_{F,i}} - \frac{u'_{A,k}}{\bar{u}_{A,k}} \right) \frac{\bar{m}_{F,i}}{\underbrace{\sum_{i=1}^N \bar{m}_{F,i}}_{K_i}}. \quad (2.10)$$

2.2.3 MISO model structure for practical premixed flames

Combining the results obtained so far, the overall fluctuations of heat release rate for a practical premix burner with N fuel injection stages – see figure 1.2 – are determined as a superposition of the responses to velocity and equivalence ratio perturbations, respectively:

$$\begin{aligned} \frac{\dot{Q}'(\omega)}{\bar{Q}} &= F_u(\omega) \frac{u'_b(\omega)}{\bar{u}_b} + \sum_{i=1}^N F_{\phi,i} \frac{\phi'_i(\omega)}{\bar{\phi}} \\ &= F_u(\omega) \frac{u'_b(\omega)}{\bar{u}_b} + \sum_{i=1}^N F_{\phi,i}(\omega) \left(\frac{u'_{F,i}(\omega)}{\bar{u}_{F,i}} - \frac{u'_{A,i}(\omega)}{\bar{u}_{A,i}} \right) \frac{\bar{m}_{F,i}}{\sum_{i=1}^N \bar{m}_{F,i}}. \end{aligned} \quad (2.11)$$

Comparing the latter relation with Eqn. (2.4) or (2.5), the flame is described as a multiple-input single-output (MISO) system with input signals u'_b and ϕ'_i , where ϕ'_i can be expressed in terms of the velocity fluctuations $u'_{F,i}$ and $u'_{A,i}$

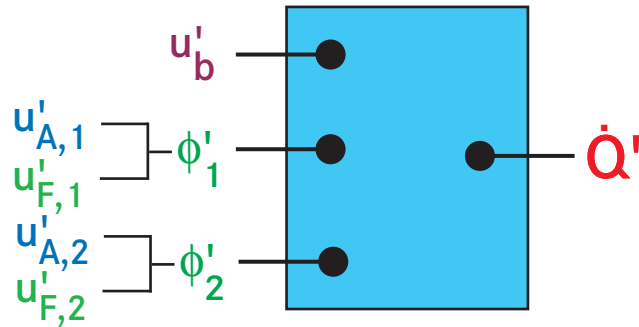


Figure 2.5: Sketch of a MISO system with two fuel injectors.

at the injectors $i = 1, \dots, N$. For a burner with two fuel injectors ($N = 2$) the corresponding block diagram is shown in figure 2.5.

A simple SISO model structure or use of inappropriate reference locations will lead to significant errors in the description of the practical premixed flame dynamics. This is demonstrated in Fig. 2.6, which shows a practical premixed combustion system with different upstream boundary conditions Z_1 and Z_2 . For simplicity an acoustically "stiff" fuel injector with a large pressure drop across the fuel injector is assumed. In this case the fluctuations of fuel mass flow induced by acoustic fluctuations will be very small, and signal variables $u'_{F,i}$ may be neglected. The acoustic field of the combustor is represented in Fig. 2.6 in terms of the acoustic velocity u' . A SISO model based on the flame transfer function F_u and the velocity fluctuations at the burner exit u'_b would result in almost no heat release rate fluctuations in case a) as the amplitude of the acoustic velocity u'_b exhibits a minimum. Heat release rate fluctuations, which are due to equivalence fluctuations generated at the point of injection, are not taken into account. The SISO model would therefore not be a proper description of the flame. An exception is the case, in which the fuel injector is located very close ("acoustically compact" distance) to the reference location "b". In this case the acoustic velocity $u'_{A,i}$ has, independent of the boundary conditions, almost the same amplitude and phase as u'_b . It can therefore be replaced by u'_b . In case b) the amplitude of the velocity fluctuations at the fuel injection $u'_{A,i}$ is now zero, whereas the amplitude of velocity fluctuations at the burner exit exhibits a maximum. The SISO model based on F_u would only in

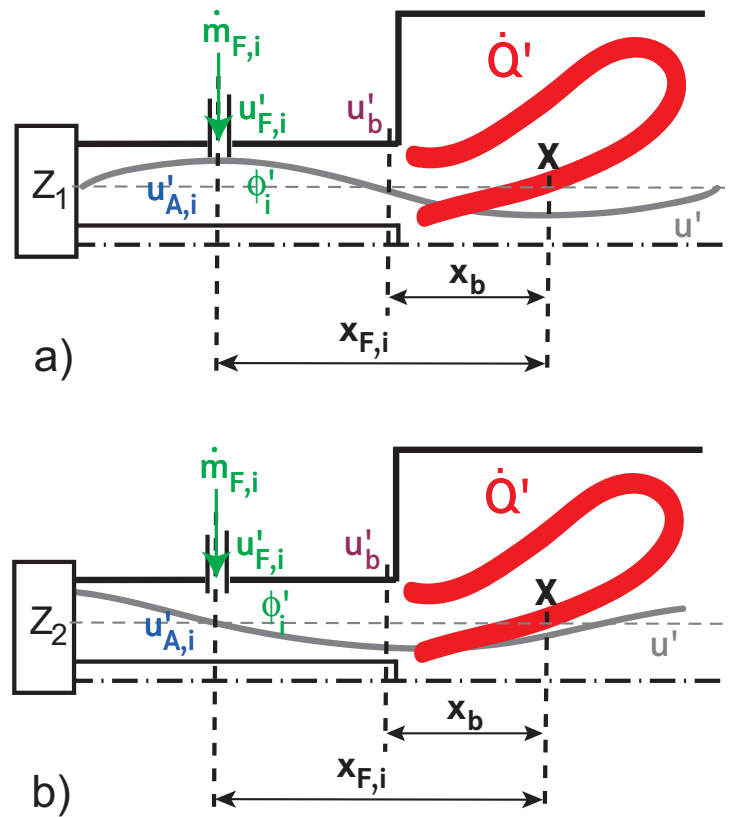


Figure 2.6: Impact of the combustion system acoustics on the description of the flame dynamics

this case reflect the flame dynamics correctly. If the assumption of the "stiff" fuel injector does not hold, the SISO model would again neglect the influence of equivalence ratio fluctuations, which result from velocity fluctuations in the fuel injector $u'_{F,i}$. If the flame is described, on the other hand, by a SISO model based on equivalence ratio fluctuations, the same considerations can be obtained.

A SISO model can finally not describe the practical premixed flame dynamics properly as it clearly depends on the acoustics of the entire combustion system. It can only be represented by such a model if the fuel injectors are placed at the burner exit and if they are acoustically "stiff". This is not the case for most practical premixed combustion systems. The only physically meaningful description of the flame is therefore the MISO model based on velocity

fluctuations at the burner exit and equivalence fluctuations at the point of injection.

The fact, that the flame has to be described by a MISO system with signals u'_b and ϕ'_i , is not always addressed in work on combustion dynamics of practical premixed combustors. Many studies neglect the influence of the flame front kinematics completely. In the field of fuel staging or tuned fuel impedances examples can be found in Lieuwen and Zinn [72], Richards et al. [106, 108] or Scarinci et al. [115, 116]. Comprehensive models, which take the significant interaction mechanisms into account, have been developed so far by e.g. [14, 48, 65, 101, 119, 133].

2.3 Identification of flame transfer functions

After the model structure of the practical premixed flame has been derived, the question arises how the required flame transfer functions F_u and $F_{\phi,i}$ can be determined. Flame transfer functions can be obtained using experiments, numerical simulation or analytical relations. As the present work focuses on numerical design methods, experimental methods are out of the scope and not addressed in the following. In terms of numerical methods a wide range of approaches exists ranging from simple analytical relations to transient CFD simulations combined with a post-processing step to extract the flame behavior. These approaches are shortly reviewed in the following. Furthermore, the flame transfer functions obtained have to be implemented into an acoustic network model, which is based on acoustic variables u' , p' or Riemann invariants f and g . Here, it has to be defined how the input and output signals of the identified flame model can be related to an equivalent flame model in the network model. The coupling between flame dynamics and network model has thus an influence on the identification procedure in terms of the signals, which can be practically determined by the chosen method. Different coupling strategies are therefore discussed in the second part of the chapter.

2.3.1 Overview of methods to determine flame transfer functions

The flame transfer function F can basically be described in the frequency domain by amplitude A and phase ϕ , which determines the time lag of the flame response:

$$F(\omega) = A(\omega)e^{i\phi(\omega)}. \quad (2.12)$$

Various researchers derived a multitude of analytic relations describing the amplitude and phase of the flame transfer function (e.g. [13, 15, 29, 48, 72, 101, 112]). In many cases they are not only restricted to single effects, like the flame front kinematics or the influence of equivalence ratio fluctuations, but also to laminar combustion cases or simple laboratory configurations. An exception is the derivation of e.g. Lawn and Polifke [65], who consider a swirl stabilized turbulent flame. However their model lacks in the low frequency range where it does not exhibit the correct limiting behavior. A simple description of the flame transfer function, which is widely used, is the so-called $n - \tau$ model, which was developed by Crocco and Chen [19]. Here, the amplitude and phase are replaced by an frequency independent acoustic-combustion interaction index n , which accounts for the influences as turbulent flame speed, flame area or enthalpy and time lag τ :

$$F(\omega) = ne^{-i\omega\tau}. \quad (2.13)$$

The $n - \tau$ model and many other analytical models are restricted to one specific time delay without any time delay distribution. The idea to characterize the flame response with one global time delay, which ignores the convective dispersion of fuel inhomogeneities, is only adequate for the low frequency regime as pointed out by Sattelmayer [112]. Turbulent fluctuations, boundary layers and recirculation zones induce a non-uniform velocity field both at the location of fuel injection and in the combustion chamber. The consequence is a non-uniform distribution of the fuel. The same consideration holds for the combustion process, which is affected by velocity fluctuations at the burner exit. Therefore, many researchers agree that models based on a time delay distribution represent the flame response significantly better [31, 99, 112].

Regarding the present work Richards et al. [106], for example, used a reduced order model to include the influence of different fuel injector impedances.

The developed flame model focuses mainly on the fluctuation of equivalence ratio with a fixed single time delay, but neglects any flame front kinematics, turbulence, change in shear layers, etc. The turbulent mixing process, which naturally damps this kind of fluctuation as shown in Scarinci and Freeman [115], is also not considered. But even Scarinci and Freeman [115] used a simplified approach in form of a spatio-temporal mixing model, which is comparable to the prediction of the atmospheric dispersion of a pollutant emitted from a plant stack over an open field. It determines the average fuel concentration at a certain position based on a Lagrangian formulation.

An alternative method to identify the flame behavior at relatively low costs is the use of Computational Fluid Dynamics. With steady state simulations an accurate time-lag distribution can be obtained using a Lagrangian approach with injected particles as described by Flohr et al. [30, 31]. To save computational time the authors injected the particles shortly downstream of the injection plane and measured their traveling times until they hit the flame front. Alternatively Krebs et al. [59, 60] performed transient simulations and calculated the instationary dispersion of injected passive scalars in a statistically stationary flow field. Compared to the Lagrangian approach the Eulerian approach enables a determination of time lags not only at a predefined surface but also in the entire combustion chamber. The distribution obtained can then be used to improve the time lag description in the $n - \tau$ model. In a further extension of the Eulerian approach the time lags could be weighted with the corresponding local heat release rate in relation to the overall heat release rate to incorporate the local characteristics of the flame. However, the latter method requires a solution for recirculation zones to avoid multiple counts of the time lags passing the flame.

To obtain not only the time lag distribution but also the transfer function amplitude as a function of frequency, many methods based on transient CFD simulations analyze the response of the flame to harmonic forcing of the acoustic variables at one specific frequency. Using harmonic forcing is especially a common procedure in experiments. This approach is particularly suitable to determine the kinematic response $F_u(\omega)$ of the flame front to flow

perturbations. Hettel et al. [42] studied the response of a premixed turbulent axial methane jet flame using unsteady RANS simulation with a sinusoidal modulation of the inlet mass flow. A LES simulation of a double swirler premixed burner was performed by Giauque et al. [36] at three different frequencies. The simulation was able to identify two main flow structures, namely a toroidal structure and a precessing vortex core attached to the center of the axial swirler, which modulates the global heat release rate. The obvious drawback of these approaches is that numerous simulations are necessary to obtain a transfer function over a wide range of frequencies. To reduce the computational effort Bohn et al. [12] used a sudden increase of the inlet mass flow as excitation signal, which contains by design multiple frequencies. A Laplace transformation of the resulting unit function response represents the flame dynamics in the frequency domain. Polifke et al. [102] proposed an advanced system identification method (CFD/SI) based on digital signal theory to post-process time series data generated by transient CFD simulation with broadband excitation. The method uses auto- and cross-correlations of time series of "signals" and "responses" and the Wiener-Hopf-Inversion to identify unit impulse responses (UIR). The acoustic transfer function or transfer matrix is obtained by a z -transform of the unit impulse responses. In their work they successfully obtained the acoustic transfer matrix of a gauze in a Rijke tube. Gentemann et al. applied the approach to determine the transfer matrix of a sudden jump in cross-section in compressible flow [34] and a flame transfer function of a perfect premixed combustion system [35]. In the latter case [35] the "signal" is the velocity fluctuation close to the burner exit, whereas the heat release rate fluctuation caused downstream is regarded as the "response". A similar method was developed by Zhu et al. [6, 135], which describes the flame response as an infinite impulse response (IIR) filter model. The model coefficients are determined by a least square estimation of the signals. As in [35], the "outputs" of the IIR model are fluctuations of heat release rate, while the "inputs" are fluctuations of the flow variable. A different method, based on steady state simulations, is proposed by van Kampen et al. [129]. The authors calculated the transfer function using a linear coefficient method in combination with an efficient order reduction algorithm.

To determine the flame transfer function, which is the key element in analyzing the thermo-acoustic behavior of combustion systems, an advanced and accurate method should be chosen. Analytic descriptions can hardly be used in the area of realistic gas turbine combustion chambers because of their limitation and accuracy. Even semi-analytical approaches using a time lag distribution obtained by CFD can only improve simple flame models like the $n - \tau$ model for example. The amplitude of the impact of these fluctuations in terms of the interaction n is still unsolved. Most methods based on transient CFD account only for a SISO model of the flame dynamics using the velocity fluctuations at the flame holder *or* equivalence ratio fluctuations at the location of injection as input signal. Therefore they can not be used, at least not in their original form, in the present context. However, the mentioned combination of CFD and system identification used by Polifke et al. [102] or Gentemann et al. [35], [34] is also suitable for more complex structures. It was originally developed in the thermo-acoustic context to obtain acoustic transfer matrices, i.e. multiple-input multiple-output (MIMO) systems. It represents a flexible and powerful method and is chosen in the following as a starting basis. In the present work the method has to be extended to identify the practical premixed flame behavior, which has to be described by a MISO system.

The chosen hybrid approach combining CFD simulations, system identification and acoustic network modeling represents an optimal solution. The numerical CFD simulations and system identification enable an accurate determination of the complex acoustic behavior of the flame. The network model, on the other hand, is suitable to analyze the impact of a wide range of parameters and geometries on the thermo-acoustic stability of the combustion system.

2.3.2 Identification strategy

No matter, which combination of analysis and identification method is chosen, the question arises how the flame transfer function $F_{\phi,i}$ is determined practically and how the signal and responses of the flame model can be re-

lated to an equivalent element in the acoustic network model.

The identification of flame transfer functions by CFD/SI requires an excitation of the flow variables to cause a system response. As the flame responds to mass flow and equivalence ratio fluctuations two independent excitation signals are required to discern the individual effects in the post-processing identification step. The excitation in such a simulation should be provided by the boundary conditions or adequate sources inside the CFD domain. A meaningful coupling between CFD/SI and acoustic network model has to take into account that the network model describes the system characteristics in terms of acoustic variables. Therefore equivalence ratio fluctuations have to be expressed in a suitable way as, e.g. described in Eqn. (2.10).

The excitation, the signal and its location, which will be used as the input to identify $F_{\phi,i}$, determine the size of the simulated domain and therefore the computational effort. It also affects the interface between CFD/SI and network model and the corresponding network flame element. The kinematic flame response F_u , on the other hand, can be included in a straightforward manner extracting the acoustic velocity fluctuations at the burner exit. Its identification only requires the simulation of the combustion chamber if a proper inlet boundary condition is set, which takes the flow conditions upstream into account (e.g. swirling flow).

In the following different possibilities are discussed, which are denoted as A, B, C and D. The comparison between the possibilities is shown in Fig. 2.7. The columns present the computational domain required, the excitation and signals extracted and their locations and the corresponding network flame element.

In case A the combustor, including swirler vanes, mixing section and part of the fuel injectors is resolved as shown in the first row and first column. The length of the fuel injectors, which have to be modeled, should be long enough to ensure a well developed velocity profile at the entry to the mixing section. For this option, the fuel mass flow and the air mass flow are excited at the inlet boundary condition of the fuel line and of the mixing section, respectively. Here, the mass flow averaged velocity fluctuations upstream the fuel injec-

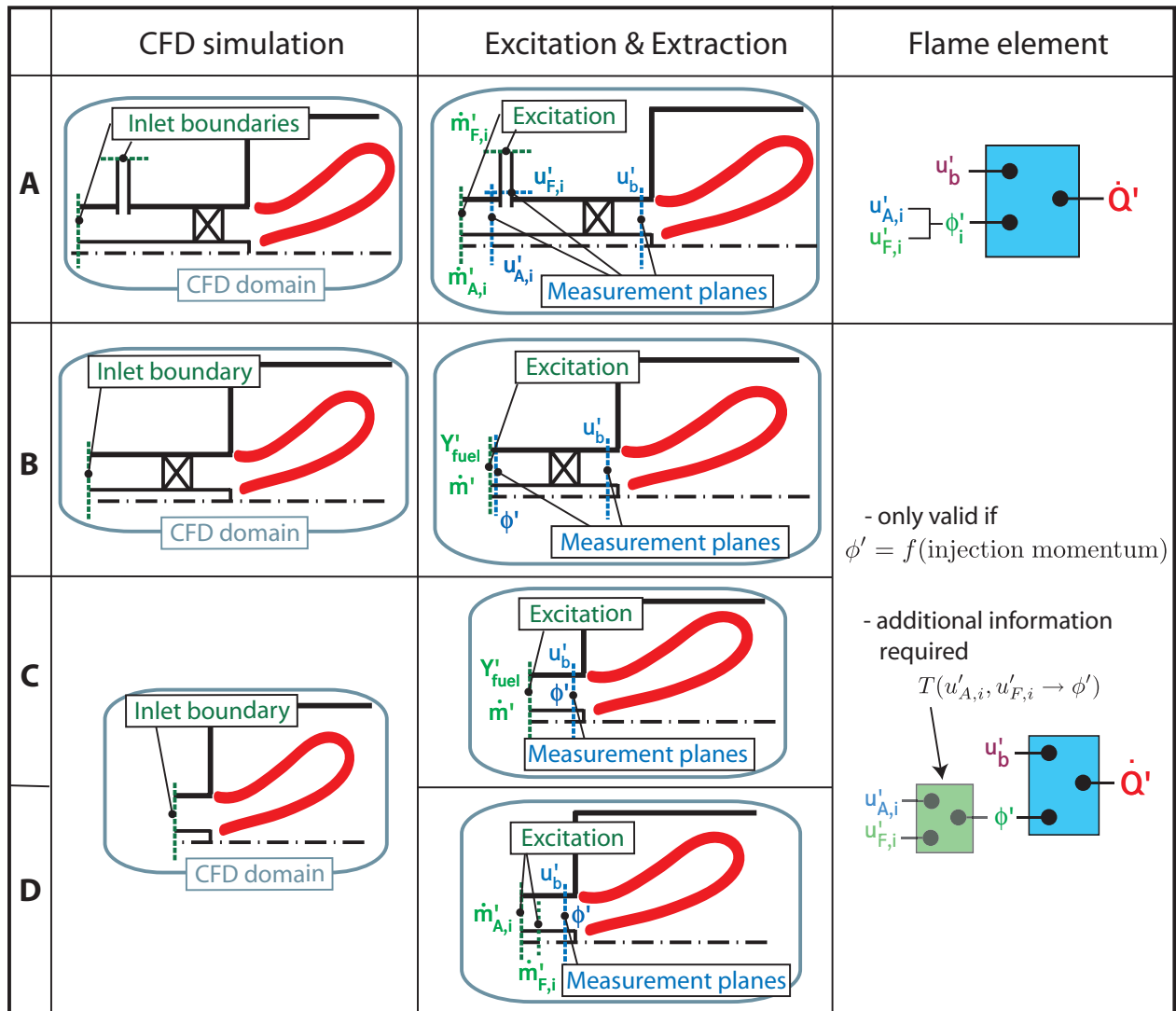


Figure 2.7: Comparison of possibilities to identify the flame transfer functions and to couple the transfer functions to the acoustic network model

tion and in the mixing section upstream of the burner exit are taken as the input signals for the post-processor. They are extracted at the "measurement" planes, which are shown in the second column. The heat release fluctuations due to equivalence ratio fluctuations can thus be determined by combining Eqn. (2.10) and (2.5). The total heat release rate fluctuations can be obtained by the summation of the two flame transfer functions:

$$\frac{\dot{Q}'}{\bar{\dot{Q}}} = F_{\phi,i} \left(\frac{u'_{F,i}}{\bar{u}_{F,i}} - \frac{u'_{A,k}}{\bar{u}_{A,k}} \right) \frac{\bar{\dot{m}}_{F,i}}{\sum_{i=1}^N \bar{\dot{m}}_{F,i}} + F_u \frac{u'_b}{\bar{u}_b}. \quad (2.14)$$

This flame model structure can be directly transferred to the acoustic network model environment as the input for both models are the velocity fluctuations $u'_{F,i}$, $u'_{A,i}$ and u'_b . A sketch of the flame element is shown in the third column³.

Alternatively, the fuel mass flow can be excited downstream the fuel injector in applying fuel mass fraction fluctuations at the inlet boundary. The mass fraction Y is defined as the ratio of the mass m_k of a particular species k and the total mass of the fluid m :

$$Y = \frac{m_k}{m}. \quad (2.15)$$

To obtain the flame response to velocity fluctuations at the burner exit the total mass flow rate is in addition excited at the inlet. This is shown in the second row (case B). Here, the CFD domain contains a part of the mixing section, the swirler and the combustion chamber. The input signal for the identification of $F_{\phi,i}$ would be the equivalence ratio fluctuations ϕ' at the inlet, which can be calculated using (see also Eqn. (2.6))

$$\phi' = s_{st} \frac{Y'_F}{Y'_O}, \quad (2.16)$$

where Y_F and Y_O denote the fuel mass fraction of fuel and oxidizer mass fraction, respectively. However, this possibility is based, as discussed in chapter 2.2.2, on the assumption that the spatial distribution of equivalence ratio fluctuations does not vary with injection momentum. This is not the case for all

³The response \dot{Q}' of the network flame element has still to be expressed as a function the acoustic variables downstream of the flame, which can be done using e.g. the Rankine-Hugoniot relations.

injection systems. Examples are jet-in-cross flow injector configurations, in which a strong dependence on momentum ratio between air and fuel stream is observed. In this case, an increased fuel velocity results in increased penetration of the fuel stream into the air stream and thus in a different fuel distribution, which may influence the heat release rate. As the equivalence ratio fluctuations are generated at the location of injection, a transfer function T has to be defined in the network model environment, which connects the acoustic velocities at this location to the equivalence ratio fluctuations at the "measurement" plane in the CFD simulation. Here, the equivalence ratio fluctuations do not have to be extracted. They can be directly calculated using the excitation signals at the inlet boundary. The corresponding network elements are shown in the third column. In simple configurations a constant time delay model can be chosen, which accounts for the convective transport of the fuel between both locations. If the inlet boundary and the "measurement" plane is taken very close to the injection point, the same relation for the flame transfer function and the same network flame element can be used as in case A.

The CFD domain could be further reduced in considering the combustor downstream of the fuel injection and swirler vanes, which is shown in the third and fourth row of Table 2.7. Here, the swirler and fuel injection are not modeled. The excitation can be provided by

- C) a fuel mass fraction fluctuation and a fluctuation of the total mass flow rate, which are applied at the inlet boundary
- D) introducing a fluctuating mass source function inside the computational domain and a fluctuation of the air mass flow rate at the inlet boundary

In both cases the equivalence ratio fluctuations can be calculated using Eqn. (2.16). In case C the excitation signals can be used directly for the calculation. In case D only one "measurement" plane at the burner exit is necessary to extract the fuel and oxidizer mass fractions as well as velocity fluctuations. The network flame model for both cases require again a transfer function T to express the equivalence ratio in terms of the acoustic fluctuations at the location of fuel injection. In contrast to case B such a transfer function should

ideally also account for the dispersion due to the turbulent flow field in the mixing section and swirler.

In the present work jet-in-cross flow injectors are used. In consideration of the modeling uncertainties associated with cases B, C and D, case A is chosen, which has the advantage of a straightforward and exact implementation.

Therefore the mixing section, a part of the injection tubes, the swirler and the combustion chamber are simulated in the following. The velocity fluctuations at the location of injection and at the burner exit, which can be directly coupled to the corresponding flame element in the network model, are used as input signals for the identification routine. Except the acoustic characteristics of the swirler, which will be also determined using CFD/SI, the acoustic network elements representing all other parts of the combustion system can be derived analytically. The acoustic network model obtained can then be used to analyze the acoustic behavior of practical premixed combustion systems using multiple, staged fuel injectors with tuned impedances.

The next chapters describe the theory and the models, which are required for the present purpose. Chapter 3 describes the basic acoustic relations of the network model. The introduction of Computational Fluid Dynamics with the chosen numerical turbulence and combustion models is discussed in chapter 4. The system identification method with its extension to determine multiple-input single-output systems is addressed in chapter 5.

3 Acoustics

Before analyzing the acoustic behavior of a combustion system, the basic theory of the propagation of sound in gaseous media has to be understood. This section presents the main relevant mathematical equations and their simplifications, as they are appropriate in the present context. The later sub-chapters deal with the relations used in the acoustic network model. All relations can be found in various books and publications about basic acoustics and aeroacoustics, especially in Dowling and Ffowcs Williams [24], Morse and Ingard [81], Pierce [93], Rienstra and Hirschberg [110], Goldstein [38] or Munjal [82].

3.1 Basic acoustic equations

The basis for the following derivations are the conservation equations for mass, momentum and energy. The conservation equation for momentum reduces to the *Euler equation* in absence of body forces and neglecting viscosity:

conservation of mass:

$$\frac{D\rho}{Dt} + \rho(\nabla \cdot \mathbf{u}) = 0, \quad (3.1)$$

conservation of momentum:

$$\rho \frac{D\mathbf{u}}{Dt} + \nabla p = 0, \quad (3.2)$$

conservation of energy:

$$\rho \frac{D}{Dt} \left(e + \frac{1}{2} |u|^2 \right) = -\nabla q - \nabla \cdot (p\mathbf{u}) + \dot{Q}_V. \quad (3.3)$$

The term $\frac{D}{Dt} = \frac{\partial}{\partial t} + \mathbf{u} \cdot \nabla$ is the material derivative. ρ denotes the density, t the time, u the velocity, p the pressure and e is the internal energy per unit of mass¹. In the energy equation (3.3) $1/2|u|^2$ is the kinetic energy where $|u|$ denotes the absolute value of the velocity vector \mathbf{u} . q represents the heat flux and \dot{Q}_V the heat production per unit of volume which can be caused by chemical reactions or electrical heating. The energy equation can be replaced by the equation for the entropy s , which is derived by a combination of the energy equation with the second law of thermodynamics. If the heat transfer and dissipation are negligible the entropy equation can be written as

$$\rho T \frac{Ds}{Dt} = \dot{Q}_V, \quad (3.4)$$

where T denotes the temperature. In the following it is assumed that the flow is homentropic except in the region where the flame is located. Homentropy implies, that the flow is adiabatic, reversible ($\frac{Ds}{Dt} = 0$) and uniform ($\nabla s = 0$). The combustion process adds heat to the system, which does not result in a uniform temperature distribution – especially if equivalence ratio fluctuations are present. The flame is therefore treated as a discontinuity. If the flow is uniform, entropy waves, which are caused by equivalence ratio fluctuations at the flame, propagate independently with the mean flow speed and may also be coupled to the acoustics of the system at boundaries, at which the flow faces strong velocity gradients². As these boundaries, e.g. nozzles or choked cross sections, are not considered in the present work, entropy waves are neglected and the assumption of homentropy for the flow field upstream and downstream the flame is valid.

The conservation laws (3.1), (3.2), (3.3) do not form a complete set of equations. Additional information is required which is provided by the constitutive equations. Assuming that the flow is homogeneous and in a state of local thermodynamic equilibrium, two intrinsic state variables are sufficient to specify the thermodynamic state of the fluid. It is common to use the density ρ and the entropy s as the basic state variables. The pressure can then be expressed

¹The internal energy is also called the *specific internal energy* or simply *the energy*.

²Here, a temperature fluctuation results in a volume flux fluctuation and can generate expansion waves propagating upstream.

as a function of the state variables $p = p(\rho, s)$ (equation of state). In differential form this equation yields

$$dp = \left(\frac{\partial p}{\partial \rho}\right)_s d\rho + \left(\frac{\partial p}{\partial s}\right)_\rho ds, \quad (3.5)$$

where

$$\left(\frac{\partial p}{\partial \rho}\right)_s \equiv c^2. \quad (3.6)$$

Equation (3.6) is a definition of the thermodynamic variable $c = c(\rho, s)$ and is a measure for the speed of sound. In the present work, air at atmospheric pressure is considered as the main fluid, which behaves like an ideal gas. The equation of state can therefore be simplified to

$$p = \rho RT, \quad (3.7)$$

where R denotes the specific gas constant, which is defined by the Boltzmann constant k_b and the Avogadro number \mathcal{N}_A divided by the molar mass M of the gas ($R = k_b \mathcal{N}_A / M$). For an ideal gas R can be expressed also as $R = c_p - c_v$, where c_p and c_v are the specific heat at constant pressure and volume, respectively. The ratio of the specific heats is defined by $\gamma \equiv c_p / c_v$.

A further useful relation is the combining of the first and second law of thermodynamics³:

$$T ds = de + pd\frac{1}{\rho}. \quad (3.8)$$

Using this equation, the equation of state (3.7) for an ideal gas and assuming that $e = c_v T$, which is a valid assumption for most ideal gases over a wide range of temperatures, one obtains a further formulation of the equation of state relating pressure and density:

$$\frac{p}{p_0} = \left(\frac{\rho}{\rho_0}\right)^\gamma \exp\left(\frac{s - s_0}{c_v}\right). \quad (3.9)$$

³which is also called the *fundamental equation of thermodynamics*

If the flow is homentropic the pressure p is proportional to ρ^γ . With the same relations and assumptions an equation for the energy and the specific enthalpy, which is defined as $h_s = e + p/\rho$, can be defined:

$$e = \frac{1}{\gamma - 1} \frac{p}{\rho}, \quad (3.10)$$

$$h_s = \frac{\gamma}{\gamma - 1} \frac{p}{\rho}. \quad (3.11)$$

Beside the conservation equations, which are the basis for the following derivation of the wave equations and its simple d'Alembert's solutions, an additional equation, the *Bernoulli equation* plays an important role in describing the acoustic characteristics of compact elements. The bases for its derivation are the Euler equations. Considering an irrotational flow and the equations derived for the homentropic flow, the Bernoulli equation for compressible flow can be written as

$$\frac{\partial \varphi_s}{\partial t} + \frac{1}{2} u_s^2 + \frac{\gamma}{\gamma - 1} \frac{p}{\rho} = g(t), \quad (3.12)$$

which is valid along streamlines. φ_s denotes the scalar velocity potential, which is defined as $\nabla \varphi_s = u_s$. $g(t)$ is a function which is determined by the boundary conditions. Equation (3.12) can be further simplified in the case of incompressible steady flow to

$$\frac{1}{2} |u| \cdot |u| + \frac{p}{\rho} = \text{const.} \quad (3.13)$$

3.2 Linear acoustic equations

In the present work, it is assumed that the sound-induced fluctuations of pressure p and density ρ are small compared to their ambient state values:

$$\frac{p'}{\rho_0} \ll 1, \quad \frac{\rho'}{\rho_0} \ll 1. \quad (3.14)$$

Here, the apostrophe ' stands for the fluctuation of the acoustic variable while the subscript 0 refers to the ambient state in absence of acoustic fluctuations. The ambient state is comparable to the introduced mean values (denoted by the overbar $\bar{}$) and defines, in general, the medium through which the sound waves propagate. The velocity fluctuation u' of the fluid associated with the acoustic wave propagation $u' = p' / (\rho c)$ is therefore also considered to be small. The assumptions made above justify a linear approximation of the conservation equations. However, this implies that the following derivations are restricted to the application of linear acoustics. It follows from Eqn. (3.14) that the flow variables at location x and time t can be expressed in terms of the state value superposed by the fluctuating part⁴:

$$\begin{aligned} p(x, t) &= p_0 + p'(x, t), \\ \rho(x, t) &= \rho_0 + \rho'(x, t), \\ u(x, t) &= u_0 + u'(x, t). \end{aligned} \tag{3.15}$$

3.2.1 Sound propagation in a quiescent medium

Assuming that the medium is quiescent, in which the ambient quantities are independent of time and the flow is stagnant ($u_0 = 0$), the relations (3.15) can be used to simplify the conservation equation for mass and momentum. The result are the *linear acoustic equations*⁵

$$\frac{\partial \rho'}{\partial t} + \rho_0 \nabla \cdot \mathbf{u}' = 0, \tag{3.16}$$

$$\rho_0 \frac{\partial \mathbf{u}'}{\partial t} + \nabla p' = 0, \tag{3.17}$$

where second- and higher-order terms are neglected. A first order approximation for the pressure fluctuations (see also the constitutive equations (3.5) and

⁴Here, it is assumed that no other fluctuations are present, e.g. imposed by turbulence.

⁵Again, entropy fluctuations and their impact on the acoustics are not considered in the present work.

(3.6)) yields:

$$p' = c^2 \rho'. \quad (3.18)$$

The wave equation can be derived by subtracting the time derivative of the mass conservation equation (3.16) from the divergence of the momentum equation (3.17) and using the constitutive equation (3.18):

$$\frac{\partial^2 p'}{\partial t^2} - c^2 \nabla^2 p' = 0. \quad (3.19)$$

Equation (3.19) describes the three-dimensional propagation of the pressure waves with propagation speed c . The direction of the wave propagation is normal to the wave front, which is defined as the surface of all points featuring the same pressure amplitude and phase.

In most gas turbine combustion systems the thermo-acoustic instabilities occur in the frequency range up to 1000 Hz. The radial and circumferential dimensions of the combustion system considered are much shorter than any wavelength in this range as already discussed in chapter 1.5. Here, the *cut-off frequency* of possible two- or three-dimensional modes is higher than the maximum frequency. This implies that these modes are exponentially damped in the direction of propagation. Therefore, the wave propagation can be restricted to one-dimensional duct acoustics with plane waves⁶.

The wave equation (3.19) can then be simplified to:

$$\frac{\partial^2 p'}{\partial t^2} - c^2 \frac{\partial^2 p'}{\partial x^2} = 0. \quad (3.20)$$

Simple and important solutions of the one-dimensional wave equation are the d'Alembert's solutions, which result by substitution of the variables $\xi = x - ct$, $\eta = x + ct$:

⁶Multi-dimensional wave fields, on the other hand, have only to be considered in combustion systems, in which the circumferential or radial dimensions are of the order of the occurring wavelength [28, 58, 62, 88, 101]

$$\frac{p'}{\rho_0 c} = f(\xi) + g(\eta) = f(x - ct) + g(x + ct). \quad (3.21)$$

The solution p' of the latter equation is, in general, normalized by the characteristic impedance $\rho_0 c$. f and g are the so-called *Riemann Invariants* and are determined by boundary or initial conditions. The Riemann Invariants represent physically waves, which are traveling with speed of sound c in the right or positive x -direction (f) or rather in the left or negative direction (g) as shown in Fig. 3.1.

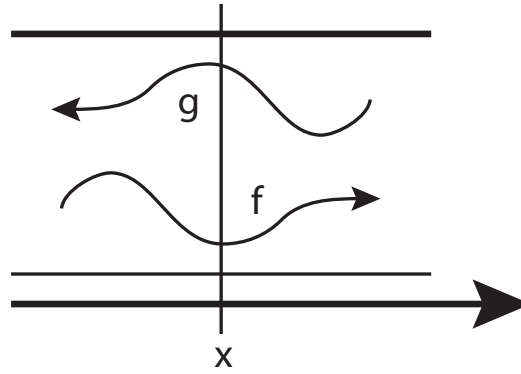


Figure 3.1: Riemann Invariants f and g traveling in positive and negative x -direction

The acoustic velocity u' can be obtained from the acoustic pressure p' (Eqn. (3.21)) and the linearized momentum equation (3.17):

$$u' = f(x - ct) - g(x + ct). \quad (3.22)$$

Using Eqn. (3.21) and (3.22), the Riemann Invariants can be conversely expressed in terms of p' and u' :

$$f = \frac{1}{2} \left(\frac{p'}{\rho_0 c} + u' \right), \quad (3.23)$$

$$g = \frac{1}{2} \left(\frac{p'}{\rho_0 c} - u' \right). \quad (3.24)$$

In case of time-harmonic plane waves, the acoustic pressure and velocity can be written in complex form as a function of the angular frequency of oscillation ($\omega = 2\pi f$):

$$p'(x, t), u'(x, t) \sim \exp(i\omega t - ikx), \quad (3.25)$$

where $k = \omega/c$ denotes the wave number with direction normal to the wave front of a plane wave. Using the latter relation Eqn. (3.21) and (3.22) can be rewritten in the following form:

$$\frac{p'(x, t)}{\rho_0 c} = \exp(i\omega t) (f \exp(-ikx) + g \exp(+ikx)), \quad (3.26)$$

$$u'(x, t) = \exp(i\omega t) (f \exp(-ikx) - g \exp(+ikx)). \quad (3.27)$$

3.2.2 Sound propagation in a moving medium

In the presence of an uniform mean flow the convective wave equation can be obtained by performing a transformation of coordinates from the system moving with the fluid to the laboratory system

$$x' = x + u_0 t, \quad t' = t, \quad u_0 = \text{const.}, \quad (3.28)$$

and yields

$$\left(\frac{\partial}{\partial t} + u_0 \frac{\partial}{\partial x} \right)^2 - c^2 \frac{\partial^2}{\partial x^2} p' = 0, \quad (3.29)$$

where $\frac{\partial}{\partial t} + u_0 \frac{\partial}{\partial x}$ denotes a time derivative moving with the mean flow. The wave number vector k is the same in the laboratory system as it is in the co-moving system. Therefore, the wave number considering mean flow can be written as:

$$k_{\pm} = \pm \frac{\omega/c}{1 \pm M}. \quad (3.30)$$

Similar to Eqn. (3.26) and (3.27) the following solution for the convective wave equation can be found:

$$\frac{p'(x, t)}{\rho_0 c} = \exp(i \omega t) (f \exp(-i k_+ x) + g \exp(+i k_- x)), \quad (3.31)$$

$$u'(x, t) = \exp(i \omega t) (f \exp(-i k_+ x) - g \exp(+i k_- x)). \quad (3.32)$$

The term $\exp(i\omega t)$ is omitted in the following as the harmonic time dependence is the same for every location in space.

3.3 Acoustic network model

An acoustic low-order network model is a fast, flexible and useful tool to analyze the dynamic properties of a complex system. In a network model the entire system is divided into discrete acoustic elements. In this way a complex system becomes easy to handle. The acoustic characteristics of each element are usually represented by its transfer matrix. A transfer matrix describes the relationship of the acoustic pressure and the velocity or the Riemann Invariants f and g between the inlet and the outlet of the element. Acoustic network models are widely used in the context of thermo-acoustic analysis of gas turbines and are described in many publications [10, 20, 23, 46, 58, 61, 70] (see also chapter 2.1). The presented network model approach is based on the work by Keller [53] and Polifke et al. [101, 103]. Applications of this approach can be found in Huber and Polifke [49]. A sketch of a network model representing a combustion system is shown in Fig. 3.2.

The mathematical bases of acoustic network models are the linear acoustic relations derived in the last section, especially the wave equation, the solutions of d'Alembert and the Bernoulli equation. The elements of the acoustic system in the present work are mainly characterized by two in-ports and two out-ports, whereas the boundary conditions possess one in- and one out-port. An exception are "T-junctions" in form of a "joint" or "fork" with altogether four in-ports and two out-ports or two in-ports and four out-ports, respectively. A "joint" represents an intersection, in which two ducts are combined into one, whereas a "fork" is an intersection, in which a duct is divided into two. The in- and out-ports of an element are connected by the Riemann Invariants f and

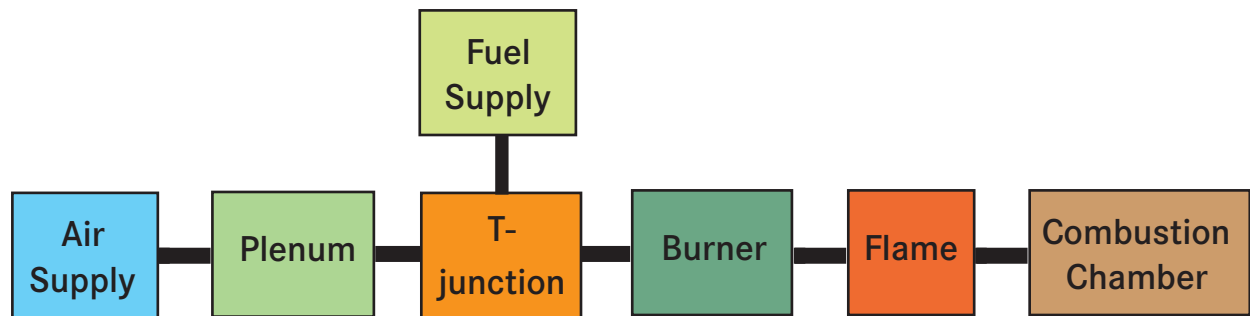


Figure 3.2: Simplified sketch of a network model representing a combustion system

g . The out-port of one element is the in-port of the following for the f -wave and vice versa for the g -wave as shown in Fig. 3.3.

The structure of the network model is organized by different port numbers, which define also the number of the Riemann Invariants f and g . The characteristics between two ports are determined by the acoustic behavior of the element. It can be described by the acoustic transfer matrix in case of a two in-port, two out-port element, by transfer functions in case of boundary conditions and by three equations resulting in a 3x3 transfer matrix in case of "T-junctions". The elements and boundary conditions form a system of linear equations. The system can be split into a system matrix containing the

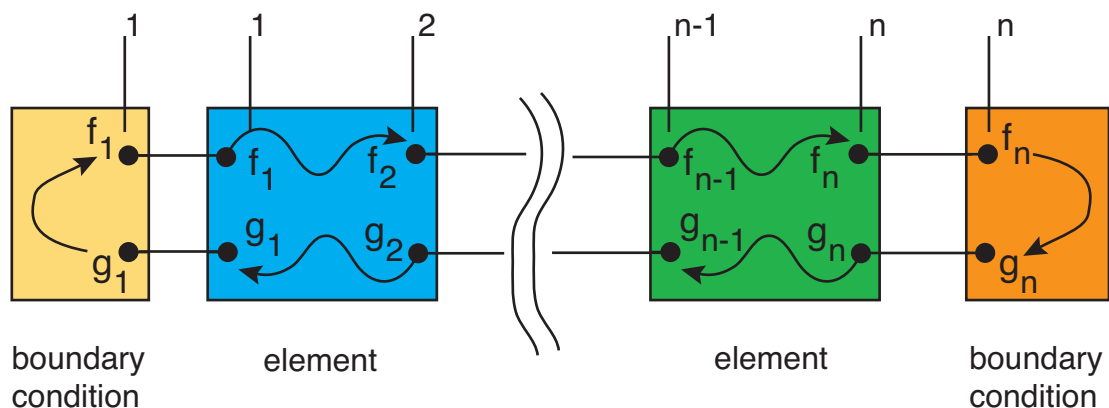


Figure 3.3: Structure of a network model with connected elements

matrix elements and the transfer functions, a vector containing the unknown Riemann Invariants and a source term vector. The next subsection 3.3.1 describes the matrices and functions of basic acoustic elements and boundary conditions. Subsection 3.3.2 deals with methods solving the entire acoustic system.

3.3.1 Matrices and functions of acoustic elements

The acoustic characteristics of an individual network element is described by a 2×2 acoustic transfer matrix or 1×1 transfer function. "T-junctions" can, in principle, also be characterized by a transfer matrix. For the sake of simplicity they are described using three different matrices for each pair of ports resulting in three linear equations.

In the following the upstream end of the transfer matrix element is denoted by i , and the downstream end by j . The relationship between Riemann Invariants f and g of both sides of the element, which is described by a 2×2 transfer matrix, are presented in Fig. 3.4 and are mathematically described as:

$$\begin{bmatrix} f_j \\ g_j \end{bmatrix} \equiv \underbrace{\begin{bmatrix} T_{11} & T_{12} \\ T_{21} & T_{22} \end{bmatrix}}_{\text{Transfer matrix } T_{fg}} \begin{bmatrix} f_i \\ g_i \end{bmatrix}. \quad (3.33)$$

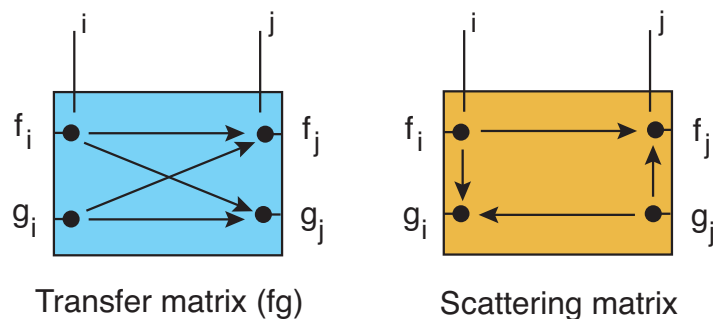


Figure 3.4: Transfer matrix (fg) and scattering matrix

Beside the transfer matrix for variables f and g , the scattering matrix and the transfer matrix characterized by p and u are widely used. Considering the pu -notation, f and g are replaced by the normalized acoustic pressure $p'/(\rho_0 c)$ and the velocity u' . The scattering matrix, on the other hand, describes the acoustic behavior of an element in a pure causal way. The relationship between the Riemann Invariants f and g is determined by the direction of wave propagation (see Fig. 3.4):

$$\begin{bmatrix} f_j \\ g_i \end{bmatrix} \equiv [S_{sr}] \begin{bmatrix} f_i \\ g_j \end{bmatrix}. \quad (3.34)$$

Here, f_i and g_j denote the input or the signal whereas f_j and g_i represent the output or the response. All different forms of matrices can be mathematically transformed into each other as described in appendix A.1.

In some cases it is useful for a better understanding to split the transfer matrix in matrices for each pair of ports. This is applied in the following to the "T-junction", the flame and area change element.

Transfer functions, on the other hand, connect one acoustic variable with another as in the causal input-output relationship of the flame transfer function or of the causal (reflection coefficient R_f) and non-causal (acoustic impedance Z) description of the boundary conditions. Mathematically the impedance is defined as the acoustic pressure p' divided by the acoustic velocity component normal to a surface u'_n :

$$Z(\omega) = \frac{p'(\omega)}{u'_n(\omega)}. \quad (3.35)$$

The impedance is commonly used to characterize the propagation (transmission, absorption) of sound through a medium, or the reflection of sound at the boundary of two materials having different acoustic impedances. In the present work it is used to describe the acoustic characteristics of the fuel injection stages. The reflection coefficient describes the relationship between the reflected acoustic wave and the incident wave traveling towards a surface. For the downstream side, for example, it yields:

$$R_f(\omega) = \frac{g(\omega)}{f(\omega)}. \quad (3.36)$$

The impedance can be related to the reflection coefficient for the downstream side

$$R_f(\omega) = \frac{Z(\omega) - \rho_0 c}{Z(\omega) + \rho_0 c}, \quad (3.37)$$

or vice versa

$$Z(\omega) = \rho_0 c \frac{1 + R_f(\omega)}{1 - R_f(\omega)}. \quad (3.38)$$

The factor $\rho_0 c$ in the last equations is referred to as the characteristic impedance.

Beside the classification of the acoustic elements in matrices and transfer functions, they can also be divided into three different groups, which are described in the following subsections:

- elements with a certain geometrical extension (simple ducts and tubes)
- compact elements (e.g. area change, "T-junction", flame)
- boundary conditions (e.g. closed end, open end, loudspeaker).

3.3.1.1 Simple ducts or tubes

In simple ducts or tubes with constant cross section and length L the acoustic waves propagate undisturbed. Neglecting any acoustic losses, e.g. in the boundary layer of the duct walls, it can be easily shown that according to Eqn. (3.26), (3.27) or Eqn. (3.31), (3.32) only a phase change will appear between the upstream end and the downstream end of the duct. The transfer function of a simple duct can then be described by:

$$\begin{bmatrix} e^{-ik_+L} & 0 \\ 0 & e^{-ik_-L} \end{bmatrix} \begin{bmatrix} f_i \\ g_i \end{bmatrix} = \begin{bmatrix} f_j \\ g_j \end{bmatrix}. \quad (3.39)$$

3.3.1.2 Compact elements

In regions or elements – for example at boundaries, area changes, "T-junctions" or the flame – where the corresponding geometrical length L is

much smaller than the shortest wavelength λ_w ($\lambda_w = 2\pi c/\omega$), the acoustic flow can locally be approximated as an incompressible flow. In contrast to simple ducts or tubes the phase change over the length is negligible. Such elements or regions can be called *compact*. A criterion for compactness is the Helmholtz number defined as:

$$\text{He} = \frac{L}{c\tau} = \frac{\omega L}{c} = \frac{2\pi L}{\lambda_w}. \quad (3.40)$$

Similar to L , τ represents in this context a typical time scale. An element can be seen as compact if

$$\text{He} \ll 1. \quad (3.41)$$

The element may thus be regarded as a discontinuity, which has to fulfill the mass conservation equation. In addition the Bernoulli equation for instationary, incompressible flow (Eqn. (3.13) + $\partial\varphi/\partial t$) can be used to analyze the acoustic change of the flow state between the two sides of the element. Considering again an uniform one-dimensional flow the velocity potential may be written as $\int u dx$. A pressure loss between the upstream and downstream location is considered, which is commonly defined as

$$\Delta p_{i \rightarrow j} = \zeta \frac{1}{2} \rho_0 u_j^2, \quad (3.42)$$

and corresponds to the downstream mean velocity u_j . Linearizing the Bernoulli equation, using the relations derived above and neglecting terms of higher order (e.g. products of acoustic quantities) an equation over the geometrical extension of the element ($i \rightarrow j$) can be derived:

$$\frac{d}{dt} \int_{x_i}^{x_j} u' dx + \left[\frac{p'}{\rho} + u_0 u' \right]_i^j + u_{0j} \zeta u'_j = 0. \quad (3.43)$$

The remaining integral can be simplified using the continuity of flux ($A_i u'_i = A(x) u'(x)$) to

$$u'_i \int_{x_i}^{x_j} \frac{A_i}{A(x)} dx \approx u' l_{\text{eff}}, \quad (3.44)$$

where A denotes the cross-sectional area of the element. Considering a time-harmonic dependence of the acoustic variables (Eqn. (3.25)) Eqn. (3.43) yields:

$$i \omega l_{\text{eff}} u'_i + \left[\frac{p'}{\rho_0} + u_0 u' \right]_i^j + u_{0j} \zeta u'_j = 0. \quad (3.45)$$

The second necessary relation for a compact element can be derived using the integral mass conservation equation:

$$\frac{d}{dt} \int \rho dV + \int \rho u dA = 0. \quad (3.46)$$

Considering one-dimensional flows and linearizing this equation results in:

$$\frac{d}{dt} \int_{x_i}^{x_j} \rho' A dx + [(\rho' u_0 + \rho_0 u')]_i^j = 0. \quad (3.47)$$

Again a time-harmonic dependence (Eqn. (3.25)) of the acoustic variables is assumed. If the speed of sound is constant one obtains introducing $\int_{x_i}^{x_j} A(x)/A_j \equiv l_{\text{red}}$ and using Eqn. (3.18)

$$\frac{i \omega p'_i}{c_i c_i} l_{\text{red}} A_j + \left[\left(\frac{p'}{c} M + \rho_0 u' \right) A \right]_i^j = 0, \quad (3.48)$$

where M denotes the Mach number ($M = u_0/c$). The values of the first term of the left hand side of Eqn. (3.48) and Eqn. (3.45) are in case of compact elements small and are omitted in the following. A further simplification can be made if the speed of sound and the density are assumed to be constant over the element ($c_i = c_j = c$, $\rho_{0i} = \rho_{0j} = \rho_0$). Dividing Eqn. (3.45) by c and Eqn. (3.48) by ρ_0 leads to the following relations for compact elements:

$$\begin{aligned} & \left[A \left(\frac{p'}{\rho_0 c} M + u' \right) \right]_i^j = 0, \\ & \left[\frac{p'}{\rho_0 c} + M u' \right]_i^j + \zeta_j M_j u'_j = 0. \end{aligned} \quad (3.49)$$

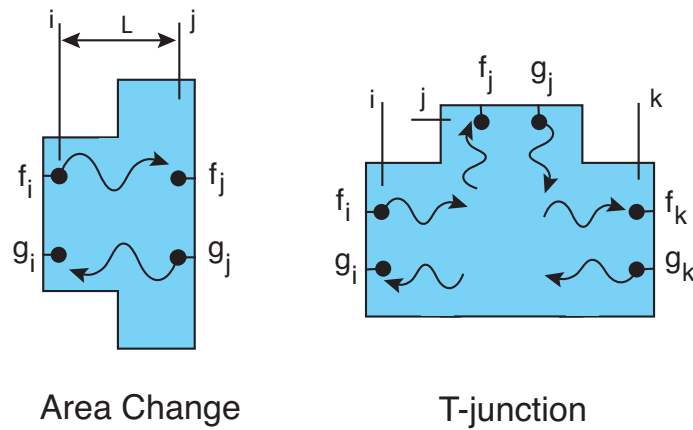


Figure 3.5: Sketch of an area change and a "T-junction"

Area changes

Using Eqn. (3.49) the acoustic characteristics of an area change can be described in terms of the Riemann Invariants as:

$$\begin{bmatrix} 1 + M_i & 1 - M_i \\ A_i(1 + M_i) & A_i(M_i - 1) \end{bmatrix} \begin{bmatrix} f_i \\ g_i \end{bmatrix} = \begin{bmatrix} (1 + M_j(1 + \zeta)) & (1 - M_j(1 + \zeta)) \\ A_j(1 + M_j) & A_j(M_j - 1) \end{bmatrix} \begin{bmatrix} f_j \\ g_j \end{bmatrix}. \quad (3.50)$$

A sketch of an area change is presented in Fig. 3.5.

T-junction

The relation of the matrices for the "T-junction" is an extension of Eqn. (3.45) and Eqn. (3.48). In the present work only joints are of special interests, in which a second upstream port is added (four in-ports and two out-ports). Here, i and j denote the upstream ports and k the downstream ones as shown in Fig. 3.5. As the "T-junction" is a part of the fuel injection stage, the describing matrices have to take the different speed of sound and density at the in-

coming connections into account⁷:

$$\begin{aligned}
 & \begin{bmatrix} c_i(1 + M_i(1 - \zeta_i)) & c_i(1 - M_i(1 - \zeta_i)) \\ 0 & 0 \\ \rho_{0i}A_i(1 + M_i) & \rho_{0i}A_i(M_i - 1) \end{bmatrix} \begin{bmatrix} f_i \\ g_i \end{bmatrix} + \\
 & \begin{bmatrix} 0 & 0 \\ c_j(1 + M_j(1 - \zeta_j)) & c_j(1 - M_j(1 - \zeta_j)) \\ \rho_{0j}A_j(1 + M_j) & \rho_{0j}A_j(M_j - 1) \end{bmatrix} \begin{bmatrix} f_j \\ g_j \end{bmatrix} = \\
 & \begin{bmatrix} c_k(1 + M_k) & c_k(1 - M_k) \\ c_k(1 + M_k) & c_k(1 - M_k) \\ \rho_{0k}A_k(1 + M_k) & \rho_{0k}A_k(M_k - 1) \end{bmatrix} \begin{bmatrix} f_k \\ g_k \end{bmatrix}. \quad (3.51)
 \end{aligned}$$

Practical premixed flame element

A special case of the compact element is the flame element. According to [16,54], the flame can be considered as a discontinuity of negligible thickness, where heat is added uniformly distributed over the chamber cross-section to the otherwise isentropic flow of an ideal gas. A detailed derivation can be found in Polifke et al. [101]. In the following only the basic relations are explained.

In the steady case the energy equation over the flame sheet can be rewritten to connect the cold and fresh gas side (i) and the hot gas side (j) with a given rate of heat addition. Using Eqn. (3.11) and the definition of the speed of sound ($c^2 = \gamma p / \rho_0$), the energy equation yields

$$\left[\frac{c^2}{\gamma - 1} + \frac{1}{2} u^2 \right]_i^j = \dot{q}, \quad (3.52)$$

where \dot{q} is the rate of heat addition per unit mass. The latter equation can be rearranged, neglecting terms of higher order, as:

⁷The simplification of the integral of Eqn. (3.48) assumes a constant speed of sound over the element, which is violated in the equations used. Because of the compactness of the element, the value of the integral is rather small and can therefore be neglected.

$$\frac{c_j^2}{c_i^2} = 1 + \frac{\gamma - 1}{\gamma} \frac{\dot{Q}}{p_i u_i}. \quad (3.53)$$

$\dot{Q} = \rho_i u_i \dot{q}$ in this context denotes the heat addition per unit area. With the equation of state of an ideal gas (Eqn. (3.7)), the ratio c_j^2/c_i^2 can be expressed as a function of T_j/T_i , where T_j and T_i are the corresponding temperatures. Thus Eqn. (3.53) can be written as $T_j/T_i - 1 = (\gamma - 1)/(\gamma) \cdot \dot{Q}/(p_i u_i)$. The momentum equation can be reformulated in the same way and one obtains two new relations for the velocity and pressure upstream and downstream the flame:

$$\frac{u_j}{u_i} = 1 + \frac{\gamma - 1}{\gamma} \frac{\dot{Q}}{p_i u_i}, \quad (3.54)$$

$$\frac{p_j}{p_i} = 1 - (\gamma - 1) \frac{\dot{Q}}{p_i u_i} M_i^2. \quad (3.55)$$

After linearization of the last equations the linearized Rankine-Hugoniot relations can be derived connecting the acoustic velocity and pressure between the cold and hot side:

$$\begin{aligned} u'_j &= u'_i + \left(\frac{T_j}{T_i} - 1 \right) u_{0i} \left(\frac{\dot{Q}'}{\bar{Q}} - \frac{p'_i}{\bar{p}_i} \right), \\ p'_j &= p'_i - \left(\frac{T_j}{T_i} - 1 \right) \rho_{0i} u_{0i}^2 \left(\frac{u'_i}{\bar{u}_i} + \frac{\dot{Q}'}{\bar{Q}} \right). \end{aligned} \quad (3.56)$$

As described in chapter 2.2.3, the normalized heat release fluctuations \dot{Q}'/\bar{Q} for a practical premixed combustion system depend on the acoustics at the burner exit and the fuel injection stages. The corresponding flame element has therefore to take the acoustics at the additional locations into account. In the following one fuel injection stage ($N = 1$) is considered. 3×2 more ports have therefore to be included into the flame element. Here, the location m represents the burner exit and k and l the fuel injection, where k corresponds to the acoustic conditions in the fuel injector and l to the conditions

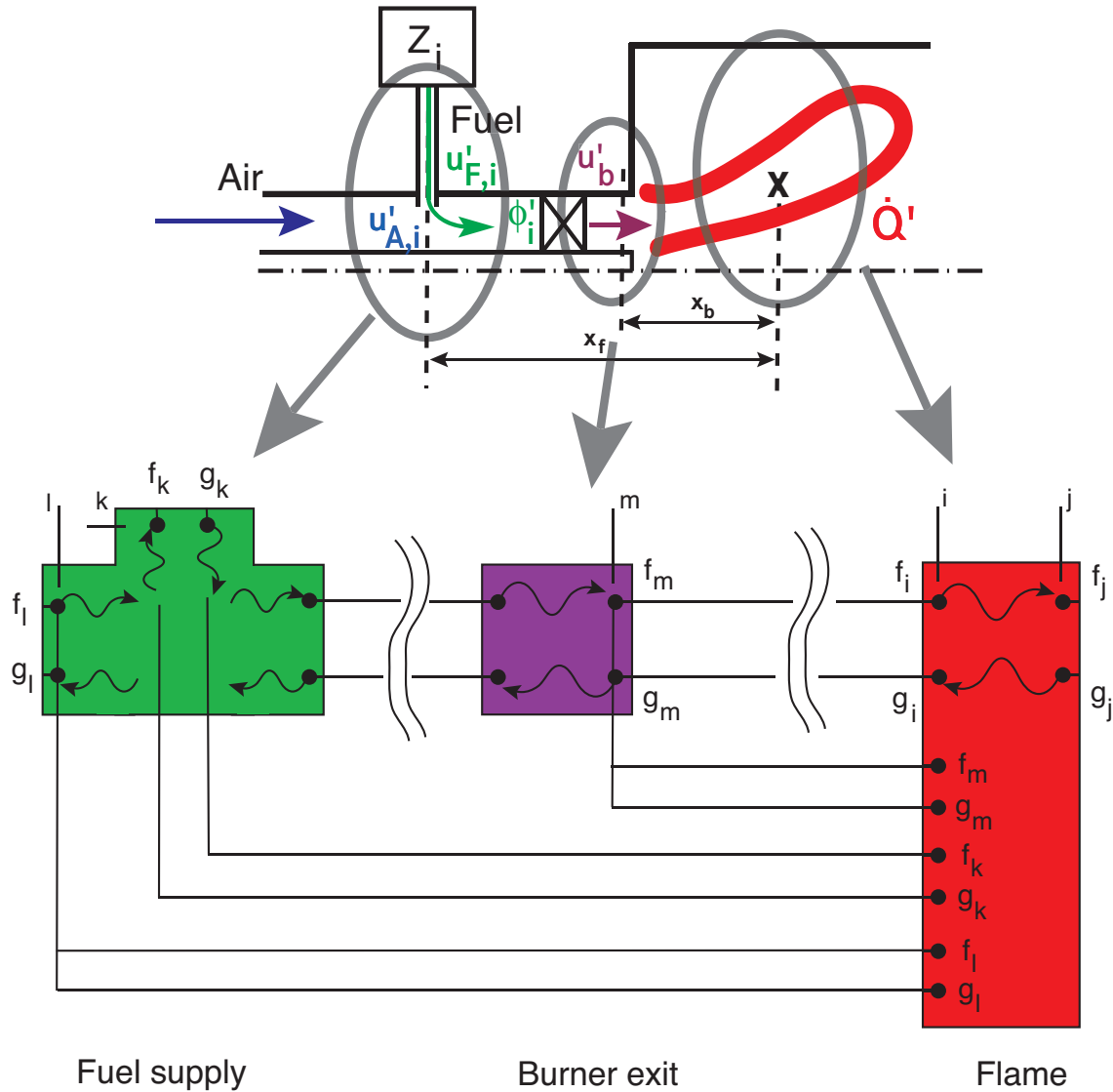


Figure 3.6: Sketch and structure of a practical premixed flame element with one fuel injection stage

in the main flow upstream of the injection location. The different locations, the structural set-up of the flame element considering one fuel injection stage and a sketch of the corresponding practical premixed combustion system are shown in Fig. 3.6. The normalized heat release rate fluctuations (Eqn. (2.11))

can be rewritten in terms of the additional ports as follows

$$\frac{\dot{Q}'(\omega)}{\bar{Q}} = F_u(\omega) \frac{u'_m(\omega)}{\bar{u}_m} + F_\phi(\omega) \left(\frac{u'_k(\omega)}{\bar{u}_k} - \frac{u'_l(\omega)}{\bar{u}_l} \right) K, \quad (3.57)$$

where K denotes the ratio between the fuel injected at this fuel injection stage and the entire injected fuel in the combustion system (see Eqn. (2.10), (2.11)). Using Eqn. (3.57) and the equation of state (Eqn. (3.7)), Eqn. (3.56) can be transformed into relations for the Riemann Invariants upstream and downstream of the flame

$$\begin{aligned} & \begin{bmatrix} 1 - r_T M_i & 1 + r_T M_i \\ 1 - r_T \gamma M_i & -1 - r_T \gamma M_i \end{bmatrix} \begin{bmatrix} f_i \\ g_i \end{bmatrix} + \\ & \begin{bmatrix} -r_T M_i \frac{u_{0i}}{u_{0k}} F_\phi K & r_T M_i \frac{u_{0i}}{u_{0k}} F_\phi K \\ r_T \frac{u_{0i}}{u_{0k}} F_\phi K & -r_T \frac{u_{0i}}{u_{0k}} F_\phi r_m \end{bmatrix} \begin{bmatrix} f_k \\ g_k \end{bmatrix} + \\ & \begin{bmatrix} r_T M_i \frac{u_{0i}}{u_{0l}} F_\phi K & -r_T M_i \frac{u_{0i}}{u_{0l}} F_\phi K \\ -r_T \frac{u_{0i}}{u_{0l}} F_\phi K & r_T \frac{u_{0i}}{u_{0l}} F_\phi K \end{bmatrix} \begin{bmatrix} f_l \\ g_l \end{bmatrix} + \\ & \begin{bmatrix} -r_T M_i \frac{u_{0i}}{u_{0m}} F_u & r_T M_i \frac{u_{0i}}{u_{0m}} F_u \\ r_T \frac{u_{0i}}{u_{0m}} F_u & -r_T \frac{u_{0i}}{u_{0m}} F_u \end{bmatrix} \begin{bmatrix} f_m \\ g_m \end{bmatrix} = \begin{bmatrix} \frac{\rho_{0j} c_j}{\rho_{0i} c_i} & \frac{\rho_{0j} c_j}{\rho_{0i} c_i} \\ 1 & -1 \end{bmatrix} \begin{bmatrix} f_j \\ g_j \end{bmatrix}, \quad (3.58) \end{aligned}$$

where $r_T = \left(\frac{T_j}{T_i} - 1 \right)$. Equation (3.58) can, of course, be extended easily to combustion systems with more fuel injection stages.

3.3.1.3 Boundary conditions

To complete an acoustic network model appropriate boundary conditions are required. In a combustion test rig the air or the fuel enter the plenum in many cases through small holes, which generate a considerable pressure loss. If the

pressure drop across the inlet is high enough, the supply lines upstream of the inlet are acoustically decoupled from the remaining system. This kind of inlet condition can therefore be seen as a "hard wall" or a "closed end", where the acoustic velocity disappears⁸:

$$\begin{bmatrix} 1 + M_i & M_i - 1 \end{bmatrix} \begin{bmatrix} f_i \\ g_i \end{bmatrix} = 0. \quad (3.59)$$

The end or outflow boundary condition of gas turbine systems is usually described by an "open end", an reflecting exit or by a choked exit. A choked flow may occur in a convergent nozzle for a subsonic inflow where the flow reaches $M = 1$ at the location of smallest cross-sectional area. On the other hand an "open end" is an outlet where the fluid enters into the atmosphere, which is often true for many simple combustion test rigs. In this case the acoustic pressure must vanish at the combustion chamber outlet. Thus the "open end" condition can be applied:

$$\begin{bmatrix} 1 + M_i & 1 - M_i \end{bmatrix} \begin{bmatrix} f_i \\ g_i \end{bmatrix} = 0. \quad (3.60)$$

The "open end" implies that the downstream traveling acoustic waves are fully reflected at the combustion chamber end. In the analyzed configuration a part of the waves are leaving the outlet without being reflected. To account for the reflection Eqn. (3.61) can be rewritten in the following way:

$$\begin{bmatrix} 1 + M_i & 1 - M_i \end{bmatrix} \begin{bmatrix} f_i \\ g_i \end{bmatrix} = -|R_f|. \quad (3.61)$$

In terms of the frequency response analysis, explained in the next section, the acoustic system has to be excited at a boundary condition. This is done, similar to experiments, in using a loudspeaker to produce certain amplitudes of

⁸The equations for the boundaries are adjusted to include the mean flow effect and to conserve the acoustic energy.

velocity fluctuations. The loudspeaker has the same characteristics as a closed end boundary condition (Eqn. (3.59)), where, in addition, a fluctuation of velocity ϵ is imposed:

$$\begin{bmatrix} 1 + M_i & M_i - 1 \end{bmatrix} \begin{bmatrix} f_i \\ g_i \end{bmatrix} = \epsilon. \quad (3.62)$$

3.3.2 Numerical solutions of the acoustic network model

To analyze the acoustic behavior of a network model representing a practical premixed combustion system two different mathematical techniques are applied in the present work: The calculation of the response of the inhomogeneous system, which is excited over a certain range of frequencies or the determination of the eigenfrequencies of the unexcited homogeneous system. The individual elements of the entire acoustic network model are combined in one matrix equation with the quadratic system matrix S , which consists of the matrix coefficients, the system vector with the Riemann Invariants and the source term vector on the right hand side

$$\begin{bmatrix} T_{11}(\omega) \cdots T_{1(2n)}(\omega) \\ \vdots \\ T_{(2n)1}(\omega) \cdots T_{(2n)(2n)}(\omega) \end{bmatrix} \begin{bmatrix} f_1 \\ g_1 \\ \vdots \\ f_n \\ g_n \end{bmatrix} = \begin{bmatrix} \epsilon_1 \\ \vdots \\ \epsilon_{2n} \end{bmatrix}. \quad (3.63)$$

Here, n is the number of interfaces of the system which implies $2 \times n$ Riemann Invariants. In case of a homogeneous system the source term vector $[\epsilon_1 \dots \epsilon_{2n}]$ is zero. If the system is excited at one or more boundaries the corresponding ϵ refers to the amplitude of the excitation which leads to an inhomogeneous system. In the latter case the frequency response of the linear inhomogeneous system can be calculated for a desired, fixed range of frequencies using a simple algorithm based on LU decomposition with partial pivoting.

The eigenvalues of the homogeneous system are determined by calculating the roots of the determinant of the system matrix S :

$$\det(S) = \det \left(\begin{bmatrix} T_{11}(\omega) \cdots T_{1(2n)}(\omega) \\ \vdots \\ T_{(2n)1}(\omega) \cdots T_{(2n)(2n)}(\omega) \end{bmatrix} \right) = 0. \quad (3.64)$$

If the system considers damping effects or acoustic sources like the flame, the determinant of the system matrix becomes zero for complex eigenfrequencies ($\omega = \omega_{\text{real}} + i\omega_{\text{im}}$). Inserting the complex eigenfrequency into the assumed harmonic time dependence, the time dependence can be written as:

$$\exp(i\omega t) = \exp(i(\omega_{\text{real}} + i\omega_{\text{im}})t) = \exp(i\omega_{\text{real}}t)\exp(-\omega_{\text{im}}t). \quad (3.65)$$

If the imaginary part of the eigenfrequency has a negative value ($\omega_{\text{im}} < 0$) the oscillation will grow exponentially in time. On the other hand, a positive imaginary part ($\omega_{\text{im}} > 0$) will dampen possible oscillations. While the real part of the eigenfrequency determines the frequency of the eigenmode, the imaginary part is thus an indication for the stability of the system at this frequency. The stability can also be described by the cycle increment of the eigenmode, which is defined by the imaginary and real part as:

$$CI = \exp\left(-2\pi \frac{\omega_{\text{im}}}{\omega_{\text{real}}}\right). \quad (3.66)$$

The cycle increment can be considered as a growth rate per period of the oscillation. It is usually reduced by one to shift the stability border from one to zero. A cycle increment of $CI < 1$ or $(CI - 1) < 0$ accounts therefore for a stable eigenmode, whereas a cycle increment $CI > 1$ ($(CI - 1) > 0$) indicates an unstable eigenmode and would thus amplify an oscillation. In the following the term $CI - 1$ is used.

The routine to find frequencies ω , where $|\det(S(\omega_{\text{real}}, \omega_{\text{im}}))| \rightarrow 0$, is based on the Nelder-Mead simplex method [63], which is a direct search method and finds the minimum of a scalar function of several variables. Especially as the determinant exhibits large changes in its value over small frequency steps, the

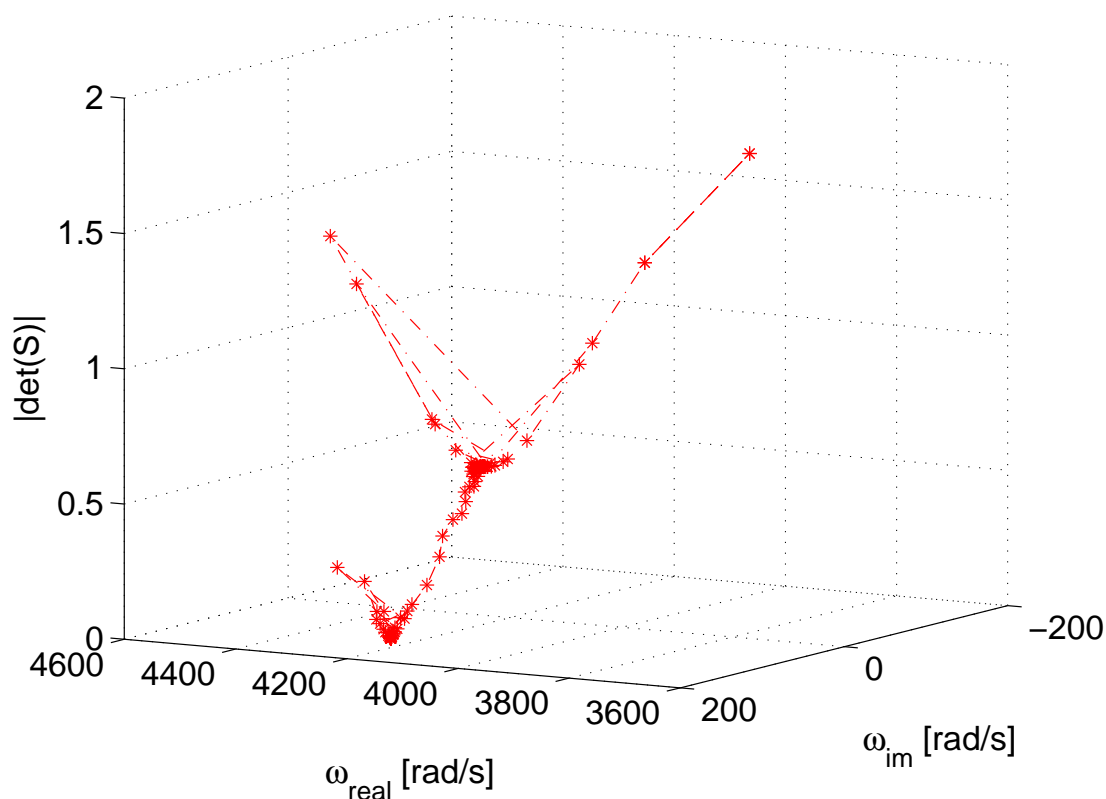


Figure 3.7: Example of a search path with one initial estimate to determine the minimum of $|\det(S)| \rightarrow 0$

advantage of this unconstrained non-linear optimization is that it does not require numerical or analytical gradients. The method requires an initial estimate of the variables, the real and imaginary part of the frequency ($\omega_{\text{real}}, \omega_{\text{im}}$), and calculates the corresponding starting simplex. For each new iteration a point close to the current simplex is determined. If the function value of this new point is smaller than the value of the current simplex it is replaced by the new one. The search is stopped by reaching a user-defined tolerance level. Figure 3.7 shows the calculation from one starting point. For a wide frequency range several initial estimates and therefore several calculations have to be performed. The amount of calculations depends on the estimated number of eigenfrequencies of the system. Here, care has to be taken in choosing good initial estimates to ensure that every eigenfrequency can be found by the rou-

tine. To roughly locate all eigenfrequencies of the system it is helpful to generate a plot of the absolute values of the determinant for a fixed range of complex frequencies. Figure 3.8 shows for example the determinant of a fuel supply system consisting of a closed end, a duct, an area change including pressure losses and an open end. The black line at $CI - 1 = 0$ indicates the stability limit according Eqn. (3.65). Possible eigenfrequencies can be found at the local minima indicated by the black colour.

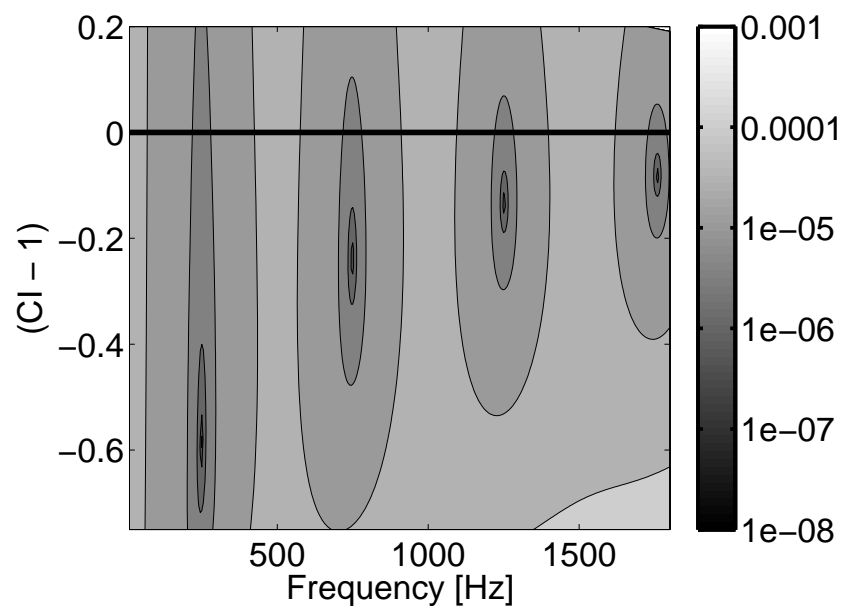


Figure 3.8: Stability map of a fuel supply system

The eigenfrequency analysis can only be applied if all elements of the network model are defined in the complex frequency domain. Transfer matrices or flame transfer functions obtained by experiments can therefore not be used in their original formulation. To avoid this problem a method proposed by Sattelmayer and Polifke [113, 114], which is based on control theory could be used instead. The CFD/SI method, however, determines the acoustic characteristics of transfer matrices and transfer functions in the time and frequency domain. The time domain information obtained can be easily transformed into the real or complex frequency domain as shown in chapter 5.

4 Modeling of turbulent reactive flows using CFD

In the present work transient Computational Fluid Dynamics simulations are used to analyze quantitatively the response of a practical premixed flame to acoustic fluctuations at the flame holder and in the vicinity of the fuel injection. The dynamics of the flame is determined in a post-processing step using the exported transient CFD data and the system identification method presented in chapter 5. This section describes the basic concepts of the numerical methods used in this work to model the turbulent reactive flow. For a more detailed information the reader is referred to Pope [104], Friedrich [33] or Tennekes and Lumley [126] regarding the description of turbulence and to Poinot and Veynante [94], Turns [128], Peters [92], Fox [32] and Williams [132] in terms of turbulent reacting flows. As the CFD simulations are performed using the commercial software package ANSYS CFX, the equations presented below are similar to those described in [5].

4.1 Theory and numerical modeling of turbulence

4.1.1 Basic equations of turbulent flows

The numerical simulation of a turbulent reacting flow is based on the conservation of mass, momentum and energy. As the conservation equations contain more unknowns than equations, further simplifications have to be made to obtain a closed system of equations. These simplifications include the introduction of the equation of state for an ideal gas (Eqn. (3.7)), the caloric constitutive equation $de = c_v dT$ and a relation for the stress tensor. The resulting system of equations is called the unsteady *Navier-Stokes equations*, which can

be written in their conservation form:

conservation of mass:

$$\frac{\partial \rho}{\partial t} + \frac{\partial \rho u_i}{\partial x_i} = 0. \quad (4.1)$$

conservation of momentum:

$$\frac{\partial(\rho u_i)}{\partial t} + \frac{\partial \rho u_i u_j}{\partial x_j} = -\frac{\partial p}{\partial x_i} + \frac{\partial \tau_{ij}}{\partial x_j}, \quad (4.2)$$

where τ_{ij} denotes the stress tensor, which is related to the strain rate by $\tau_{ij} = 2\mu \left(\frac{1}{2} \left(\frac{\partial u_i}{\partial x_j} + \frac{\partial u_j}{\partial x_i} \right) - \frac{1}{3} \frac{\partial u_i}{\partial x_i} \right)$. The energy equation in ANSYS CFX is formulated in terms of the total enthalpy h_t , where $h_t = h_s + \frac{1}{2} \mathbf{u}^2$:

conservation of energy:

$$\frac{\partial \rho h_t}{\partial t} - \frac{\partial p}{\partial t} + \frac{\partial}{\partial x_i} (\rho h_t u_i) = \frac{\partial}{\partial x_i} \left(\lambda_t \frac{\partial T}{\partial x_i} \right) + \frac{\partial \tau_{ij} u_j}{\partial x_i}. \quad (4.3)$$

Here, λ_t denotes the thermal conductivity. The static enthalpy $h_s(T, p)$ is related to the internal energy e by $h_s = e + p/\rho$ as mentioned in chapter 3. $(\partial \tau_{ij} u_j) / \partial x_i$ is the viscous work term and represents the work due to viscous stresses. Analytical solutions of the *Navier-Stokes equations* are known only for simple flows under ideal conditions. In case of real flows they are, due to the multi-dimensional and non-linear differential equations, rather difficult. Therefore, a numerical approach must be adopted whereby the equations are replaced by algebraic approximations, which can be solved using numerical methods. The phenomenon of *turbulence*, which occurs at sufficiently large Reynolds numbers², complicates the efforts of solving the equations. Turbulence is a complex three-dimensional unsteady process, which consists of fluctuations in time and space over a wide range of scales. It has a significant effect on the characteristics of the flow, especially if, as in the present work, mixing and combustion problems are involved. The combustion process itself increases the complexity of the problem, since an accurate resolution of

¹As the present study focuses on adiabatic conditions, convective enthalpy fluxes and radiative heat losses are neglected.

²The Reynolds number relates the impact of the inertia forces to the viscous forces in the fluid.

the reactive flow would require a resolution of elementary chemical reactions. Even in rather simple reaction processes this would imply to take an immense number of species and their corresponding transport equations into account.

The Navier-Stokes equations are able to describe turbulent reactive flows without any additional information. But to resolve even the smallest eddies at realistic Reynolds numbers an extremely fine finite volume mesh is required. Therefore, a high computational effort is necessary to apply such a simulation, which is known as the *Direct Numerical Simulation (DNS)*. As a consequence, DNS is far beyond the scope of industrial and many research problems and is therefore not considered in the following. First simplifications result in the *Large Eddy Simulation (LES)*, which resolves the largest turbulent scales up to a certain cut-off scale. The cut-off scale is commonly determined by the size of the mesh, which acts as a low pass filter. The effects of turbulent fluctuations, which are smaller than this limit, are modeled. In looking at time scales, which are larger than the time scales of turbulent fluctuations, a turbulent flow quantity (f_t) can be divided into an averaged (\bar{f}_t) and a time-varying fluctuating part (f_t''). This idea is exploited in the *Reynolds averaged Navier-Stokes equations (RANS)*, which determine the averaged flow quantities and model the entire turbulence spectrum. Due to the applied statistically averaging procedure the turbulence models based on the RANS formulation are known as statistical turbulence models.

The question of choosing either LES or RANS is always a compromise between numerical accuracy, computational resources and physical simulation time. For performing transient simulations Reynolds averaged Navier-Stokes equations are used in the present work because they offer satisfactory results in an acceptable time frame.

4.1.2 Modeling turbulence with RANS

In the RANS approach turbulence models solve a modified set of equations by introducing a mean and fluctuating part, which results in additional unknown terms containing products of fluctuations. To avoid further unknowns the mass-weighted averages (*Favre averages*) are usually preferred over Reynolds

averaged quantities. Every quantity can then be described as

$$f_t = \tilde{f}_t + f_t'', \quad \widetilde{f_t''} = 0, \quad (4.4)$$

where

$$\tilde{f}_t = \frac{\overline{\rho f_t}}{\bar{\rho}}. \quad (4.5)$$

Using the above definition the Reynolds averaged Navier-Stokes equations are written as follows:

conservation of mass:

$$\frac{\partial \bar{\rho}}{\partial t} + \frac{\partial \bar{\rho} \tilde{u}_i}{\partial x_i} = 0. \quad (4.6)$$

conservation of momentum:

$$\frac{\partial(\bar{\rho} \tilde{u}_i)}{\partial t} + \frac{\partial \bar{\rho} \tilde{u}_i \tilde{u}_j}{\partial x_j} = -\frac{\partial \bar{p}}{\partial x_i} + \frac{\partial \tilde{\tau}_{ij}}{\partial x_j} - \frac{\partial \bar{\rho} \widetilde{u_i'' u_j''}}{\partial x_j}, \quad (4.7)$$

conservation of energy:

$$\frac{\partial \bar{\rho} \tilde{h}_t}{\partial t} - \frac{\partial \bar{p}}{\partial t} + \frac{\partial}{\partial x_i} (\bar{\rho} \tilde{u}_i \tilde{h}_t) = \frac{\partial}{\partial x_i} (\lambda \nabla T - \bar{\rho} \widetilde{u_i'' h_t''}) + \frac{\partial \overline{u_i \tau}}{\partial x_i}. \quad (4.8)$$

Compared to the Navier-Stokes equations the latter relations exhibit additional terms in form of products of fluctuations. Two classes of terms can be identified: The Reynolds stresses $\widetilde{u_i'' u_j''}$ and the turbulent fluxes, e.g. of the enthalpy $\bar{\rho} \widetilde{u_i'' h_t''}$. The introduction of an additional equation for the combustion process (see chapter 4.2.1) results in another turbulent flux of the species or progress variable. The objective of turbulence models is now to derive closure relations for these unknown quantities.

Following the classical turbulence viscosity assumption proposed by Bussinesq, the Reynold stresses can be related to the mean velocity gradients and turbulent eddy viscosity by the gradient diffusion hypothesis

$$\bar{\rho} \widetilde{u_i'' u_j''} = -\mu_t \left(\frac{\partial \tilde{u}_i}{\partial x_j} + \frac{\partial \tilde{u}_j}{\partial x_i} - \frac{2}{3} \frac{\partial \tilde{u}_i}{\partial x_i} \right) + \frac{2}{3} \bar{\rho} k, \quad (4.9)$$

where μ_t is the turbulent dynamic viscosity, which has to be modeled. k denotes the turbulent kinetic energy, which is defined as:

$$k = \frac{1}{2} \overline{(u_i'' u_i'')}. \quad (4.10)$$

A similar solution can be found for the turbulent fluxes. The diffusivity hypothesis states that the fluxes of a scalar ϕ (species, enthalpy, progress variable) can be related linearly to the mean scalar gradient

$$-\bar{\rho} \overline{u_i'' \phi_k''} = \frac{\mu_t}{\text{Pr}_t} \frac{\partial \widetilde{\phi}_k}{\partial x_i}, \quad (4.11)$$

where Pr_t represents the turbulent Prandtl number.

A variety of methods exist to model the closure for the turbulent viscosity. The methods range from simple *mixing length* or *no-equation models* over *one or two equation models* up to computational expensive *Reynolds stress models*. Whereas the no- to two-equations models assume isotropy and homogeneity of turbulence, the Reynolds stress model solves the individual stress components resulting in six additional transport equations. As the computational effort related to the Reynolds stress models is too high, the performed simulations use the so-called *Shear Stress Transport (SST) model* to account for the complex flow field of a swirled stabilized combustion. The SST model combines the advantages of the *Wilcox $k - \omega$* [131] and the *$k - \epsilon$* model. *$k - \omega$* and *$k - \epsilon$* models solve two equations accounting for the turbulent kinetic energy k and the turbulent frequency ω_t , in case of the *$k - \omega$* model, and the turbulent dissipation ϵ_t , in case of the *$k - \epsilon$* model. The turbulent viscosity can then be determined by the relations

$$\mu_t = \rho \frac{k}{\omega_t} \quad \text{or} \quad \mu_t = c_\mu \rho \frac{k^2}{\epsilon_t}, \quad (4.12)$$

where c_μ is a constant. The main advantage of the *$k - \omega$* model is the near wall treatment. According to [5] it is even more robust and accurate, because it does not involve the complex non-linear damping functions of the *$k - \epsilon$* model. On the other hand the Wilcox formulation is known to have a strong sensitivity

to free-stream conditions [77]. The *Baseline (BSL) $k-\omega$* model tries to solve the problem in combining a transformed $k-\epsilon$ and the $k-\omega$ model. The transition between both approaches is realized near the surface and in the outer region with a blending function, which was developed by Menter [78]. The author also demonstrated [78] that the BSL $k-\omega$ model still fails to properly detect the onset and the amount of flow separation from smooth surfaces, because the model does not consider the transport of the turbulent shear stress. This results in an over-prediction of the eddy viscosity. The SST model, which is based on the BSL $k-\omega$ formulation, uses therefore a limiter for the eddy viscosity and an improved blending function. According to [5] the SST model is able to accurately predict the onset and the amount of flow separation under adverse pressure gradients. In terms of accuracy and computational effort the SST model is an adequate solution for the present work considering reactive swirling flows and is chosen in the following.

4.2 Theoretical and numerical combustion

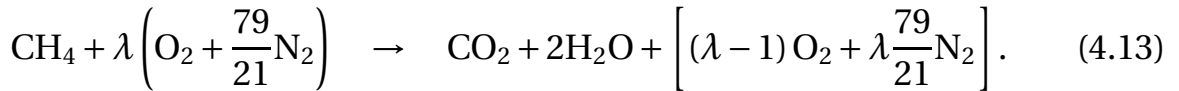
4.2.1 Combustion theory

Similar to the problems mentioned above, the description and modeling of the complex combustion process is also a challenge. Beside the basic governing conservation equations of species, energy, fluid mass and momentum, it is of importance to understand the complex interaction between the fluid flow and the combustion process. As mentioned in chapter 1.5 the field of gaseous turbulent combustion can be subdivided in premixed, non-premixed, or partial premixed combustion.

Furthermore, the combustion process can be characterized by the flow regime. In laminar combustion the process is mainly driven by chemical and molecular diffusion processes and is not affected by the flow field itself. Turbulence, on the other hand, changes completely the character of the combustion process. In presence of turbulence, each eddy can, depending on its size, wrinkle the flame front or even enter the flame and can thus modify its in-

trinsic structure. As the flow field is turbulent in most practical applications, laminar flames do not play an important role. However, the computation of laminar premixed flames is the first step towards more complex combustion models.

In terms of chemical combustion processes the global chemical reaction of natural gas can be written as follows:



Here, λ denotes the air-fuel ratio, which describes the relation of the amount of air, which is effective available and which is stoichiometric required. The reciprocal of λ is the commonly used equivalence ratio ϕ , which was defined in chapter 2.2.2 and 2.3.2. Depending on the equivalence ratio the combustion can be divided in several regimes:

$$\phi = \begin{cases} < 1 & \text{lean} \\ = 1 & \text{stoichiometric} \\ > 1 & \text{rich.} \end{cases} \quad (4.14)$$

The conservation of a species k can be derived analogously to the conservation equations (Eqn. (4.1), (4.2), (4.3))

$$\frac{\partial(\rho Y_k)}{\partial t} + \frac{\partial(\rho Y_k u_i)}{\partial x_i} = \frac{\partial}{\partial x_i} \left(\rho D_k \frac{\partial Y_k}{\partial x_i} \right) + \dot{\omega}_k, \quad (4.15)$$

where D accounts for the molecular diffusion according to Fick's law and denotes the diffusion coefficient of species k . $\dot{\omega}_k$ is the reaction rate of species k . Even in simple cases the combustion process involves many species. To accurately resolve this process various species transport equations have to be solved. This is computationally expensive and not feasible in most technical applications. Therefore, the reaction mechanism has to be reduced and is commonly represented by a few main species (like the global mechanism shown in Eqn. (4.13)). In case of perfect premixed flames, an alternative approach has been established, which replaces the species conservation equations by a transport equation of a so-called reaction progress variable. The

reaction progress variable, denoted by the scalar c , represents the probability for the instantaneous state of the fluid being reacted. It is defined in the range from:

$$c = \begin{cases} 0 & \text{unburnt mixture / fresh gas} \\ 1 & \text{burnt products.} \end{cases} \quad (4.16)$$

The species composition of the fluid can, for the special case of $(Le = 1)^3$, be computed by the following relation:

$$Y = (1 - c) Y_{\text{fresh}} + c Y_{\text{burnt}}. \quad (4.17)$$

If the combustion configuration is not premixed perfectly, an additional transport equation for the mixture fraction Z_M has to be solved to account for the mixing process of fuel and air. The mixture fraction measures the fuel-oxidizer ratio and is normalized such that $Z_M = 0$ in the oxidizer stream and $Z_M = 1$ in the fuel stream:

$$Z_M = \frac{s Y_F - Y_O + Y_O^0}{s Y_F^0 + Y_O^0}. \quad (4.18)$$

Y_F^0 and Y_O^0 denote the fuel and oxidizer mass fractions in pure fuel and oxidizer streams, respectively. Z_M is a passive or conserved scalar and alters only because of diffusion and convection processes and, in contrast to Eqn. (4.15), not because of reaction:

$$\frac{\partial(\rho Z)}{\partial t} + \frac{\partial(\rho Z u_i)}{\partial x_i} = \frac{\partial}{\partial x_i} \left(\rho D \frac{\partial Z}{\partial x_i} \right). \quad (4.19)$$

To ensure that the problem in the limit of pure fuel and pure oxidizer remains well-posed, the reaction progress approach has to be extended. According to [5] this can be realized in introducing the weighted reaction progress F_w , $F_w = Z_M \cdot (1 - c)$. A linear combination of the transport equation for Z_M and c yields the transport equation for F_w :

$$\frac{\partial(\rho F_w)}{\partial t} + \frac{\partial(\rho F_w u_i)}{\partial x_i} = \frac{\partial}{\partial x_i} \left(\rho D \frac{\partial F_w}{\partial x_i} \right) + 2(\rho D) \left(\frac{\partial Z_M}{\partial x_i} \frac{\partial c}{\partial x_i} \right) - Z_M \dot{\omega}_c. \quad (4.20)$$

³A unity Lewis number is assumed in the present work, which implies that the thermal diffusivity is equal to the mass diffusivity.

4.2.2 Practical premixed combustion model

Similar to Eqn. (4.6), (4.7), (4.8) a Reynolds averaged equation of the mixture fraction and the weighted reaction progress can be derived. For the weighted reaction progress this relation yields:

$$\begin{aligned} \frac{\partial(\bar{\rho} \tilde{F}_w)}{\partial t} + \frac{\partial(\bar{\rho} \tilde{F}_w \tilde{u}_i)}{\partial x_i} &= \frac{\partial}{\partial x_i} \left[\left(\bar{\rho} D + \frac{\mu_t}{Sc_{c,t}} \right) \frac{\partial \tilde{F}_w}{\partial x_i} \right] + \\ &2 \left(\bar{\rho} D + \frac{\mu_t}{Sc_{c,t}} \right) \left(\frac{\partial \tilde{Z}_M}{\partial x_i} \frac{\partial \tilde{c}}{\partial x_i} \right) - \tilde{Z}_M \bar{\omega}_c. \end{aligned} \quad (4.21)$$

The term $-\bar{\rho} \widetilde{c'' u_i''}$ was replaced analogous to Eqn. (4.11) by $\frac{\mu_t}{Sc_{c,t}}$, where $Sc_{c,t}$ denotes the turbulent Schmidt number, which is set by default to 0.9 [5]⁴. The source term $\bar{\omega}_c$ is defined as:

$$\bar{\omega}_c = \bar{S}_c - \frac{\partial}{\partial x_i} \left(\bar{\rho} D \frac{\partial \tilde{c}}{\partial x_i} \right). \quad (4.22)$$

To solve Eqn. (4.21), the *turbulent flame speed closure (TFC)* model is used for the unknown averaged reaction source term \bar{S}_c . The original idea of the TFC-model was presented by Zimont [138], whereas the complete formulation of the model was described by Zimont and Lipatnikov [136]. Furthermore, the TFC-model was improved and extended by Zimont et al. [137] and Polifke et al. [97].

The approach is based on the idea to represent the source term as a spatial progress of the flame front, which can be described as a function of the turbulent flame speed s_t :

$$\bar{S}_c = \rho_u s_t |\nabla \tilde{c}|. \quad (4.23)$$

$|\nabla \tilde{c}|$ is the magnitude of the gradient of the progress variable and ρ_u is the density of the unburnt gas. This approach has the advantage that, for a given

⁴Again, a unity Lewis number is assumed. In this case it follows that the Prandtl number $Pr = Sc$.

area, the integral over the source term matches the inflow of the fuel-air mass flow over the flame front. In addition the turbulent flame speed s_t , for which a closure has to be derived, varies in a given configuration typically by one order of magnitude compared to combustion models, which are based on molecular reaction rates⁵. Following Zimont, the closure for s_t is derived for the thickened-wrinkled flame regime, which is characterized by a Damköhler number of $Da > 1$ and a Karlowitz number of $1 < Ka < 100$. The Damköhler number describes the relation between the integral turbulent time scale τ_t and the chemical time scale τ_c . The Karlowitz number corresponds to the smallest eddies and is the ratio of the chemical time scale and the Kolmogorov time τ_k

$$Da = Da(l_t) = \frac{\tau_t}{\tau_c}, \quad Ka = \frac{1}{Da(\eta_k)} = \frac{\tau_c}{\tau_k} = \left(\frac{l_f}{\eta}\right)^2, \quad (4.24)$$

where l_t and η_k denote the turbulent integral length scale and the Kolmogorov length scale, respectively. l_f is the laminar flame thickness. In the range of $Ka > 1$ it is assumed, that the small turbulent eddies up to a certain size are able to enter the flame front and thus to thicken the flame. Assuming that the chemical time scale in the thickened flame front is the same as in the laminar case, the local flamelet velocity can be expressed, according to Zimont, in terms of the chemical time scale τ_c and local turbulent parameters u'' , τ_t and l_t . The evaluation of the average burning velocity s_t is based on the flamelet velocity and the average ratio of flamelet surfaces to the normal direction of propagation of the turbulent flame $\frac{\delta S}{\delta S_0}$ [138]. s_t can then be described by the following relation

$$s_t = 0.5 G u''^{3/4} s_L^{1/2} \chi_u^{-1/4} l_t^{1/4}, \quad (4.25)$$

where s_L represents the laminar flame speed and χ_u the thermal diffusivity. A stretch factor G is introduced in addition to the original formulation to account for the reduction of the flame speed at high turbulent intensities due to fluid dynamic strain and stretch. It is defined as the probability of unquenched flamelets. Local flamelet extinction takes place if the turbulent eddy dissipation ϵ is larger than a certain critical value $\epsilon_{crit} = 15\nu g_{crit}$, where ν is the kinematic viscosity of the fluid. The stretch factor can be obtained, assuming a

⁵The reaction rate of combustion models, which are based on molecular reaction rates, exhibit commonly large changes of several orders of magnitude in the computational domain.

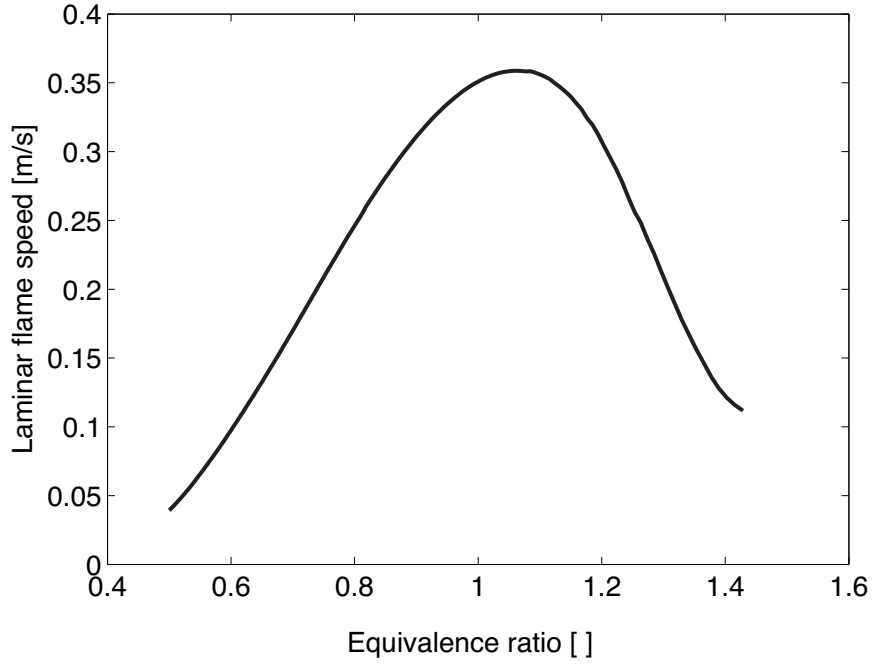


Figure 4.1: Laminar flame speed s_L as a function of equivalence ratio ϕ

log-normal distribution of ϵ , by:

$$G = \frac{1}{2} \operatorname{erfc} \left\{ -\sqrt{\frac{1}{2\sigma}} \left(\ln \frac{15\nu g_{\text{crit}}^2}{\epsilon} \right) \right\}. \quad (4.26)$$

σ denotes the standard deviation of the distribution of ϵ and is defined as $\sigma = 0.28 \ln(l_t/\eta)$. Following experiences of similar combustor configurations and recommendations given by Polifke et al. [97], the critical strain rate g_{crit} is set to 8500s^{-1} in the present work.

The laminar flame speed is a property of the fuel-air mixture. It depends on the equivalence ratio, the temperature of the unburnt mixture and pressure. In the present work the reference pressure is the atmospheric pressure. The inflow temperature of the simulations is 298K . To determine the correct value in dependence of the equivalence ratio a simulation of an one-dimensional laminar flame was performed using the solver *Chemkin*. Chemkin computes various laminar flame characteristics using a detailed chemical mechanism on the basis of elementary reactions, which are determined by Arrhenius ex-

pressions. The results of the computation in the range of $0.5016 < \phi < 1.429$ are shown in Fig. 4.1, where $\phi = 0.5016$ represents the lean extinction value.

An alternative correlation without performing any computations can be found in Metghalchi and Keck [80], Poinsoot and Veynante [94] or Turns [128].

5 System Identification

Flame transfer functions can in principle be obtained experimentally, analytically or numerically. To overcome limitations associated with experiments or analytical descriptions, the present study uses unsteady CFD computations and a system identification method to determine the flame transfer functions $F_u(\omega)$ and $F_\phi(\omega)$ over a wide range of frequencies.

The CFD/SI method based on digital signal processing was proposed and developed by Polifke et al. [98, 102] and Gentemann et al. [34] to identify SISO or MIMO systems. The method processes time series data generated by turbulent reactive flow simulation with broadband excitation. This makes it possible to determine frequency responses from a single CFD run, thus reducing the computational effort drastically. The presented routine is an extension of the basic approach and allows determining MISO model coefficients of a practical premixed flame. Identification of a MISO model is more difficult than identification of SISO model coefficients, especially in the presence of noise. Therefore it is explored how the quality of the identified model can be validated a posteriori. A simple Matlab/Simulink model that mimics qualitatively the behavior of a practical premixed combustion system with two fuel injector stages is used to establish the proof of concept for the proposed methodology. In contrast to a CFD simulation, the simple model allows a comparison between identified and predefined transfer functions as the exact values of the transfer functions are known. Furthermore, it is investigated which excitation signal type provides the best identification results in presence of noise.

In the next sections basic relations for identifying the flame dynamics are derived using theory of linear time-invariant systems, system identification and digital signal processing. The interested reader may refer to [51, 73, 85] for a more detailed explanation. Different types of excitation signal employed in this study are introduced. In addition, quality measures for a posteriori val-

validation of identification results are defined. Afterwards a numerical study of identification of a multiple-input single-output flame model is presented using the Matlab/Simulink model. Beside the proof of concept and the investigations of different excitation signal types the impact of the time series length on the identification results is analyzed. Furthermore, it is shown that identification fails if a SISO structure – inappropriate for the system investigated (see chapter 2.2.3) – is assumed.

5.1 Model structures and response filters

As non-linear effects are outside the scope of the present work, it is assumed that at sufficient small amplitudes the MISO system representing the flame dynamics can be regarded as a discrete, *linear time-invariant (LTI)* system. A system is said to be time invariant if the response to a input signal does not depend on absolute time. In addition, a system is a causal system, if the output signal depends only on present and past input signals. According to digital signal theory any linear, time-invariant, causal SISO system can be described by its *impulse response* or *weighting function* as follows:

$$y(t) = \int_{\tau=0}^{\infty} h(\tau)x(t-\tau)d\tau. \quad (5.1)$$

Here, y denotes the output or response of the system and x the input signal at time t . Knowing the impulse response $h(\tau)$ for every value $\tau = 0 \dots \infty$ and the present and past input signals the corresponding output can be determined for any input. The system is therefore completely characterized by its impulse response.

In most practical cases the output depends not only on the input, but also on disturbances in the system. Therefore an additive noise term e is introduced in the model. Depending on the signal to noise ratio, e can have a significant influence on the identification quality. For a discrete system, which is observed at the sampling instants $t_n = n\Delta t$, $n = 1, 2, \dots, n_{tot}$ with Δt being the sampling interval, Eqn. (5.1) becomes:

$$y_n = \sum_{k=0}^{\infty} h_k x_{n-k} + e_n. \quad (5.2)$$

To avoid infinite convolution sums, the first step is to choose a model structure and model size, which is capable of accurately representing the system with only a finite number of coefficients. In the field of system identification there exists a wide range of model classes for LTI systems.

A common description of a LTI system is, for example, the linear difference equation:

$$\begin{aligned}
 y_n &= -a_1 y_{n-1} - a_2 y_{n-2} - \dots - a_N y_{n-N} \\
 &\quad + b_0 x_n + \dots + b_M x_{n-M} + e_n \\
 &= -\sum_{k=1}^N a_k y_{n-k} + \sum_{k=0}^M b_k x_{n-k} + e_n.
 \end{aligned} \tag{5.3}$$

Here, the required output at time step n can be calculated using a finite amount of previous output values and the present and previous input values, which are weighted with model coefficients a and b . Eqn. (5.3) is also called an *equation error*, *infinite impulse response (IIR)* or an *ARX* model, where AR refers to the auto-regressive part $a_i y_{n-i}$ and X to the extra input $b_i x_{n-i}$. The advantage of the ARX model is the fact that its predictor defines a linear regression, which allows the use of powerful estimation methods to determine the unknown model coefficients.

To maintain the causal relationship between the input signal and the output response in the time-domain, the model is reduced to a discrete *finite impulse response (FIR)* description where $a_n = 0$, for $n = 1, 2, \dots, N$. The causal relationship has the advantage that a physical interpretation of the coefficients is straightforward¹.

In the following a practical premixed burner with two fuel injection stages is discussed, in which the flame is accordingly described as a MISO system as shown in Fig. 6.2. Treating the system as an open-loop, discrete time system without feedback, the output y_n (the normalized heat release rate fluctuation

¹A IIR description would reduce the required amount of model coefficients to achieve a desired accuracy. An undesirable consequence of an IIR model is, however, that a physical interpretation of the coefficients is rather difficult.

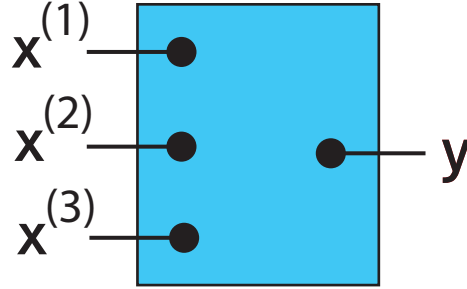


Figure 5.1: Sketch of a MISO system with two fuel injectors

\dot{Q}'/\bar{Q}) at time $n\Delta t$ can then be determined by the relation

$$y_n = \sum_{k=0}^M h_k^{(1)} x_{n-k}^{(1)} + \sum_{k=0}^M h_k^{(2)} x_{n-k}^{(2)} + \sum_{k=0}^M h_k^{(3)} x_{n-k}^{(3)} + e_n, \quad (5.4)$$

where $x^{(i)}$, $i = 1, 2, 3$ represent the three normalized input signals $u'_b/\bar{u}_b, \phi'_1/\bar{\phi}_1, \phi'_2/\bar{\phi}_2$. The parameters $h_k^{(1)}, h_k^{(2)}, h_k^{(3)}$ represent the unit impulse response vectors, which can be regarded as a causal, weighted, time-delayed distribution of the response to the different $x^{(i)}$'s.

The length M of the UIR vectors, which corresponds to the filter "memory", has to be chosen such that it accounts for the longest time lag of the system (usually a convective time scale [98]). The transfer functions of Eqn. (5.4) are computed as the z -transform of the UIRs:

$$F^{(i)}(\omega) = \sum_{k=0}^M h_k^{(i)} e^{-i\omega k\Delta t}, \quad i = 1, 2, 3. \quad (5.5)$$

The valid frequency range for the transfer functions depends on the time step Δt and the total simulation time $T = n_{tot}\Delta t$ and ranges from $f_{min} = 1/T$ to $f_{max} = f_n = 1/(2\Delta t)$. Here, f_n is denoted as the Nyquist frequency².

The UIR coefficients $h_k^{(i)}$ of Eqn. (5.5) describe the system as a so-called grey box with limited physical insight of the system. With the given model structure, the search for the optimum model reduces to the problem of identifying the unit impulse response vectors.

²The Nyquist frequency represents the maximum frequency at which a broadband signal can be exactly recovered from its sample values.

5.2 System Identification

To accomplish this task a routine based on a *non-recursive least square method* and the linear regression property are used (see [73] for more details). The predictor of Eqn. (5.4) can be described as

$$\hat{y}_{n|\theta} = \varphi_n^T \theta, \quad (5.6)$$

where θ denotes the unknown parameters

$$[h_0^{(1)} \ h_1^{(1)} \ \dots \ h_M^{(1)} \ h_0^{(2)} \ \dots \ h_M^{(2)} \ h_0^{(3)} \ \dots \ h_M^{(3)}]^T$$

and φ the *regression vector*

$$[x_n^{(1)} \ x_{n-1}^{(1)} \ \dots \ x_{n-M}^{(1)} \ x_n^{(2)} \ \dots \ x_{n-M}^{(2)} \ x_n^{(3)} \ \dots \ x_{n-M}^{(3)}]^T.$$

Using the predictor in Eqn. (5.6) the prediction error can be estimated:

$$\epsilon_{n,\theta} = y_n - \varphi_n^T \theta. \quad (5.7)$$

A *least-square criterion* for the linear regression can now be defined as

$$V(\theta) = \frac{1}{N - M + 1} \sum_{n=M}^N \frac{1}{2} [y_n - \varphi_n^T \theta]^2, \quad (5.8)$$

where N denotes the number of time steps considered. Eqn. (5.8) can be minimized analytically due to its quadratic characteristics in θ :

$$\hat{\theta} = \left[\frac{1}{N - M + 1} \sum_{n=M}^N \varphi_n \varphi_n^T \right]^{-1} \frac{1}{N - M + 1} \sum_{n=M}^N \varphi_n y_n. \quad (5.9)$$

The *least-square estimate* $\hat{\theta}$ can be calculated, if the inverse on the right side of the latter equation exists. The first sum of Eqn. (5.9) can be estimated as the $3M \times 3M$ auto-correlation matrix of the input signals:

$$\Gamma_{xx} = \frac{1}{N - M + 1} \sum_{n=M}^N x_n^{(i)} x_{n-k}^{(j)}; \quad k = 0, \dots, M; \quad i, j = 1, 2, 3. \quad (5.10)$$

The second term on the right hand side can be estimated as the cross-correlation vector of the input and output signals:

$$C_{xy} = \frac{1}{N - M + 1} \sum_{n=M}^N x_n^{(i)} y_{n-k}; \quad k = 0, \dots, M; \quad i = 1, 2, 3. \quad (5.11)$$

Compared to the basic CFD/SI method, which identifies SISO and MIMO models (see [34, 98, 102]), the auto-correlation matrix contains now as well non-diagonal entries as the input signals are correlated. This fact requires a discussion about the choice of excitation signals and the validation methods to judge the quality of the results obtained. Equation (5.9) can be rewritten as follows

$$\hat{\theta} = \Gamma_{xx}^{-1} C_{xy}, \quad (5.12)$$

which is the optimal *linear least square estimator* for the unit impulse response. It is also known as the Wiener-Hopf equation or rather the Wiener-Hopf inversion [40, 52, 73]. After the auto-correlations and cross-correlations are determined, the unknown parameters are solved using a method which is based on a least-square root algorithm for sparse linear equations [86].

5.3 Excitation signals

The identification method presented above processes data from simulations with broadband excitation. Several types of broadband excitation signals are known, and it is worthwhile to investigate how the signal type influences the results of the identification.

Insufficient excitation strength will yield poor identification results, especially in the presence of noise. On the other hand, because the identification procedure is limited to linear systems, it has to be assured that maximum signal amplitudes do not generate non-linear behavior. A maximum utilization of the amplitude limit over a wide range of frequencies is therefore beneficial. This can be judged in analyzing the so-called *crest factor* or *peak-to-average ratio*, proposed by Ljung [73]. The crest factor is a property of the waveform and is equal to the peak amplitude of the waveform divided by the mean square of

the zero mean signal:

$$C_r^2 = \frac{\max_n(x_n^2)}{\frac{1}{N} \sum_{n=1}^N x_n^2} \quad (5.13)$$

According to [73] a good signal waveform is one with a small crest factor. A similar definition can be found in Isermann [51]. In the next section, three different excitation signals are shortly explained as they are used in the following.

Overlaid multi-frequency signals

A broadband excitation signal x_{ex} can be generated by a superposition of sine waves (SINE):

$$x_{ex,n} = \sum_{v=0}^{NF} u_0 \sin(2\pi f_v(n\Delta t + \phi_v)), \quad (5.14)$$

where NF denotes the number of single frequencies, u_0 the basic amplitude and Δt is the sampling interval of the signal.

Broadband white noise (BBWN)

A broadband white noise signal can be generated from pseudo-random numbers "rand(n)" distributed uniformly between 0 and 1:

$$x_{ex,n} = \begin{cases} 2u_0(\text{rand}(m) - 0.5), & n = m T_c / \Delta t, \\ x_{ex,(n-1)}, & n \neq m T_c / \Delta t, \end{cases} \quad (5.15)$$

for $m = 0, 1, \dots, N\Delta t / T_c$. T_c represents the cycle time or rather the cut-off frequency $F_c = 1 / T_c$, which determines the frequency content of the signal.

Discrete random binary signal (DRBS)

A *discrete random binary signal* can take on only two values $\pm u_0$. The change between the two values takes place at a random multiple of the time step

$T_c = m\Delta t$, $m = 1, 2, \dots, N(\Delta t/T_c)$, which determines again the maximum frequency F_c of the signal:

$$x_{ex,n} = \begin{cases} u_0 \text{sign}((\text{rand}(m) - 0.5) 2), & n = m T_c / \Delta t, \\ x_{ex,(n-1)}, & n \neq m T_c / \Delta t. \end{cases} \quad (5.16)$$

"sign" is the sign function in this context which returns the value 1 or -1 depending on a positive or negative expression.

An example of the excitation signals in the time domain is shown in Fig. 5.2 to demonstrate the different utilization of the amplitude limit. The second line in Eqn. (5.15) and (5.16) represents a non-standard low-pass "filtering" operation that has been found useful in the present work. Its purpose is to preserve a maximum possible amplitude of the excitation signals. Using standard filter methods (e.g. low-pass Butterworth filter), the amplitudes in the time-domain and the power density spectrum are usually damped. This is demonstrated for the DRBS in Fig. 5.3. In principle rectangular or binary signals have the lowest crest factor and the highest power spectral density (signal amplitudes) for given limit amplitude. The power spectral density can be increased even further if the frequency content of the signal is reduced to a fraction of the sam-

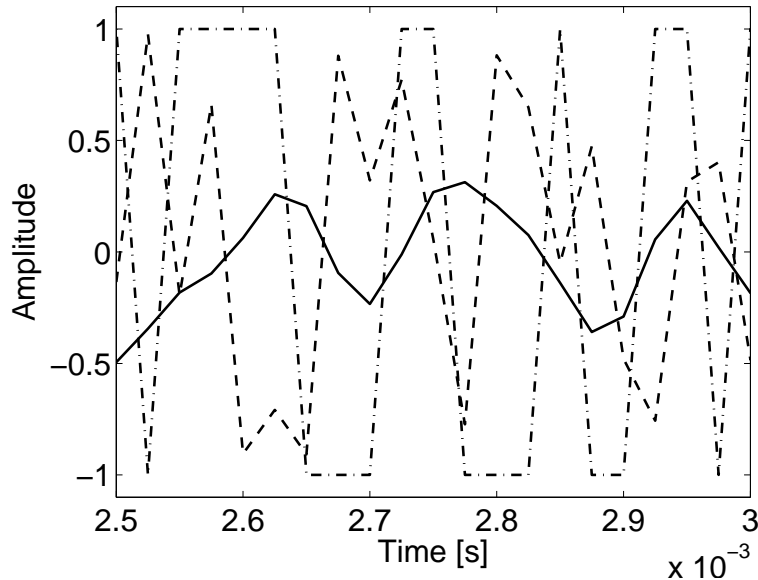


Figure 5.2: Excitation signals (— Sine, -- BBWN, -·- DRBS)

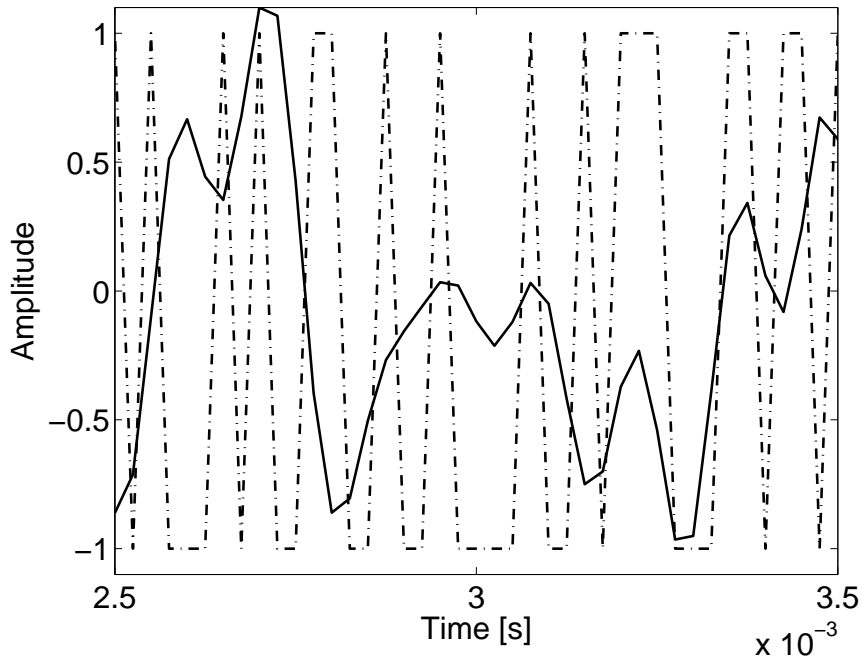


Figure 5.3: Filtered excitation signals (— Low-pass filtered DRBS, -- DRBS filtered acc. Eqn. (5.16))

pling frequency. This effect can be exploited especially in the present case, as the flame exhibits a low-pass behavior, i.e it does not respond to high frequencies.

5.4 A posteriori validation of identification results

In many cases it is difficult to judge whether the transfer function or the unit impulse response identified indeed describe the relationship between the measured signals and responses and thus the physics correctly. Especially in presence of noise the model size M and the length N of the signal have to be chosen in such a way that a proper identification is guaranteed. To accomplish this task, a posteriori "quality checks" are required, which are described in the following.

In some cases the transfer function or the unit impulse response vector has

to satisfy certain constraints or has to exhibit certain characteristic features. For example, constraints on the low-frequency limit of flame transfer functions can be derived from global conservation laws, as discussed by Polifke and Lawn [100]. According to their analysis, the flame transfer function F_u approaches unity for $\omega \rightarrow 0$. The same behavior holds for transfer functions F_ϕ in combustion systems with non-stiff fuel injection. The unit impulse response, on the other hand, has to reflect the physics of the system in showing a realistic mean time delay and time delay distribution of the response to the input signal.

Beside such qualitative evaluation two methods are used in the present work, which are described in system identification theory (e.g. [73]). In the first method, the measured³ input signals and the estimated parameters $h_k^{(i)}$ are used to determine the predicted response \hat{y} . The deviation between predicted and measured response y_n , the prediction error ϵ ($\epsilon_n = y_n - \hat{y}_n$), is then compared to the variations of the measured response by the following relation:

$$Q = 100 * \left(1 - \frac{\sqrt{\sum_{n=1}^N (y_n - \hat{y}_n)^2}}{\sqrt{\sum_{n=1}^N (y_n - \bar{y})^2}} \right) [\%]. \quad (5.17)$$

The numerator of the fraction term is the root mean squared prediction error. The denominator represents the standard deviation of the response measured, where \bar{y} denotes the mean value of y . Q represents the proportion of the total deviation of the measured response that is explained by the model. A value of 100% indicates that the response measured can be completely described by the input signals and the identified model parameters. $100\% - Q$ can therefore be related to the unexplained deviation and can be interpreted as the proportion of the error or white noise in the signal.

A better assessment of the quality of the model can be achieved in analyzing the correlation between the prediction error ϵ_n and the input signals $x^{(i)}$, $i = 1, 2, 3$

$$C_{\epsilon x^{(i)}}(k) = \frac{1}{N - O + 1} \sum_{n=O}^N \epsilon_n x_{n-k}^{(i)}, \quad k = 0, \dots, O; \quad i = 1, 2, 3. \quad (5.18)$$

³The terms "measured signal / response" represent in the present context the signals, which are obtained by the Matlab/Simulink model or the transient CFD simulation.

If the correlation values are rather large, it can be reasoned that there is still a part of the measured output y_n that originates from present and past input signals. In other words, the input-output relationship has not been properly identified by the model with order M . If the obtained correlation values are small, the model is probably independent of the input signal. The model can therefore also be applied to other input signals. As the least-square method determines the parameters $\hat{\theta}$ such that the correlation of the prediction error ϵ_n and the regressor vector φ is minimized, the analysis should be carried out with $O > M$. To judge whether a value is small or still acceptable, the correlation can be compared to a 99% confidence interval, which can be determined according to Ljung [73] to:

$$ci_{x^{(i)}} = \sqrt{\frac{\sum_{k=-O}^O \Gamma_{\epsilon,k} \Gamma_{x^{(i)},k}}{N-2O-1}} N_{\alpha}, \quad i = 1, 2, 3, \quad (5.19)$$

where Γ_{ϵ} and $\Gamma_{x^{(i)}}$ are the auto-correlation vectors of ϵ and $x^{(i)}$, $i = 1, 2, 3$ respectively. N_{α} represents the deviation of a normal distribution with expectation of $\mu = 0$ and a standard deviation of $\sigma = 1$. For a confidence value of 99%, N_{α} amounts to 2.58. It follows for the correlation that the relation

$$\left| \frac{1}{\sqrt{\Gamma_{\epsilon,k=0} \Gamma_{x,k=0}}} C_{\epsilon x,k} \right| \leq ci \quad (5.20)$$

has to be fulfilled.

Similar equations can be obtained for the auto-correlation of the prediction error. Large values of the auto-correlation are an indication that the prediction error does not exhibit white noise characteristics and may therefore still contain some dynamics of the system. An exception is the value at $k = 0$ which has to approach unity. If the prediction error exhibits, similar to the flame response, a low pass filter behavior with a cut-off frequency far below the sampling frequency the auto-correlation can contain large values for $k \leq 1/f_c/\Delta t$, where f_c denotes the cut-off frequency and Δt the sampling interval.

All methods mentioned above should be analyzed in combination to assess the quality of the identification.

5.5 Proof of concept for the identification of the MISO flame model

Until now, the CFD/SI method has not been applied to identify the flame dynamics, which are described by a MISO model. In this section, proof of concept for this approach is established by a comprehensive validation study. Both a priori and a posteriori quality criteria are employed. Furthermore, the impact of different excitation signals and of the signal time series length N in presence of noise on the quality of the identification results is assessed. Such a sensitivity study helps to determine the necessary conditions for a successful identification. The proof of concept is not based on CFD data – because with a CFD model, the exact values of the frequency response functions are not known a priori. Even, if highly accurate data can be obtained, it is not possible to distinguish whether discrepancies observed are due to inadequacies of the turbulent combustion model or due to the MISO identification scheme. Instead, a time-domain simulation of a linear, time-invariant dynamic system model, that is qualitatively representative of the dynamics of a practical

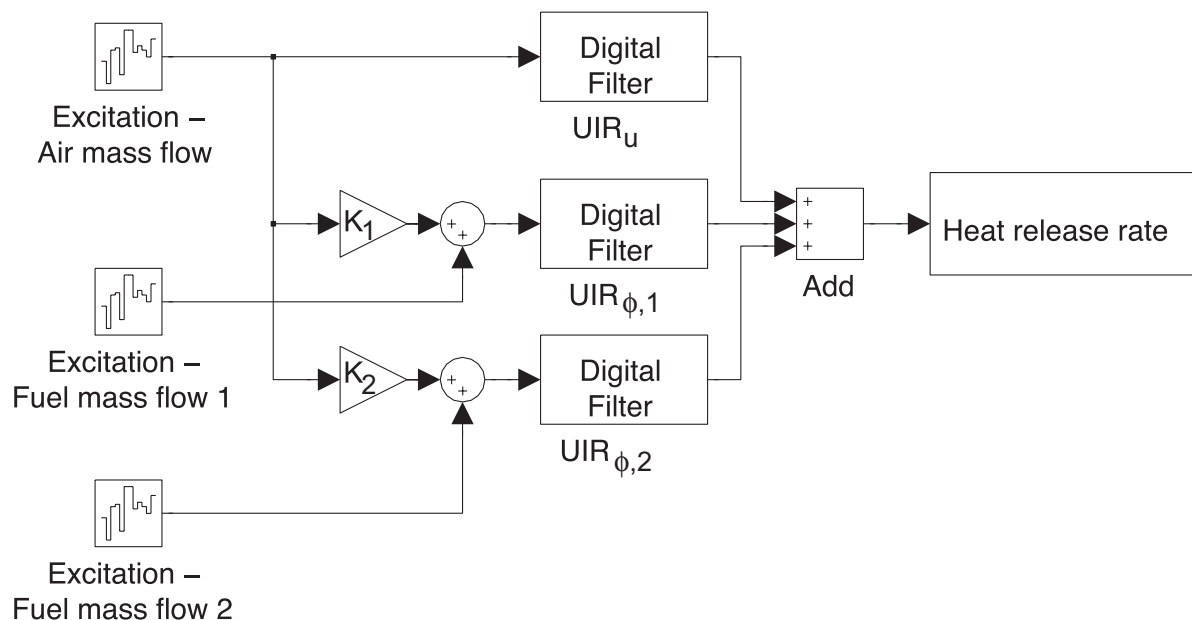


Figure 5.4: Sketch of the Matlab/Simulink test rig model

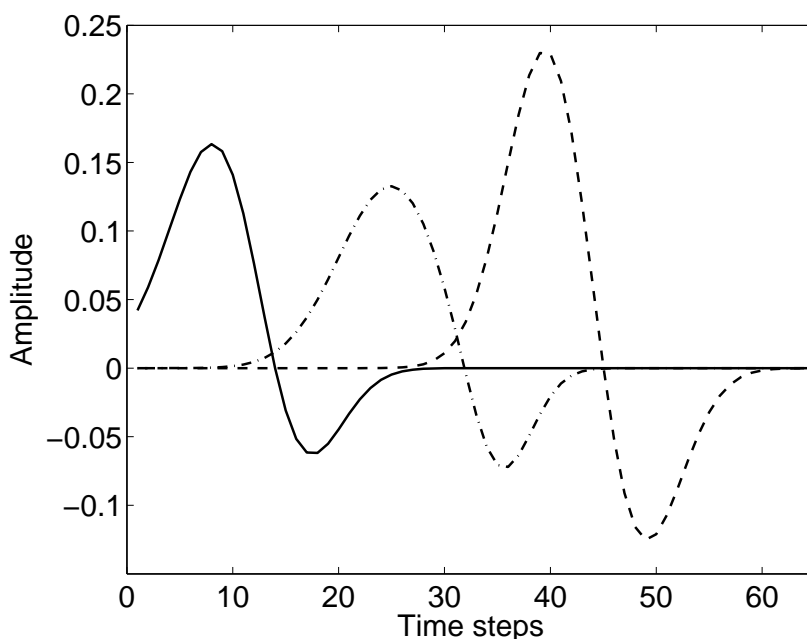


Figure 5.5: Predefined test UIRs of the model (— UIR_u , -- $UIR_{\phi,1}$, -·- $UIR_{\phi,2}$)

premixed combustor (see Fig. 1.2) is set up in Matlab/Simulink. A similar approach has been used by Yuen et al. [134] for validation of acoustic transfer matrix reconstruction. A block diagram of the model, which includes two fuel injectors at different locations, is shown in Fig. 5.4. The first disturbance represents the velocity fluctuation at the burner mouth. The second and the third one are fluctuations of the equivalence ratio, which arise from fluctuations of the velocity of the main stream and the fuel mass flow at the corresponding injection locations. Without essential loss of generality, zero acoustic boundary conditions and zero phase lags between velocity fluctuations at the injectors and the burner exit are assumed. Therefore, the velocity fluctuations at the injection locations are coupled directly to the fluctuations at the burner mouth, as indicated in Fig. 5.4. The flame dynamics is described by three unit impulse responses UIR_u , $UIR_{\phi,1}$, $UIR_{\phi,2}$, named "Digital filter" in Fig. 5.4. The amplitudes, mean time lags and time lag distributions of the three UIRs differ from each other as presented in Fig. 5.5. The UIRs are designed to correspond qualitatively with results of previous experimental and computational studies on premix flame dynamics, and also to the UIRs obtained in the CFD/SI study,

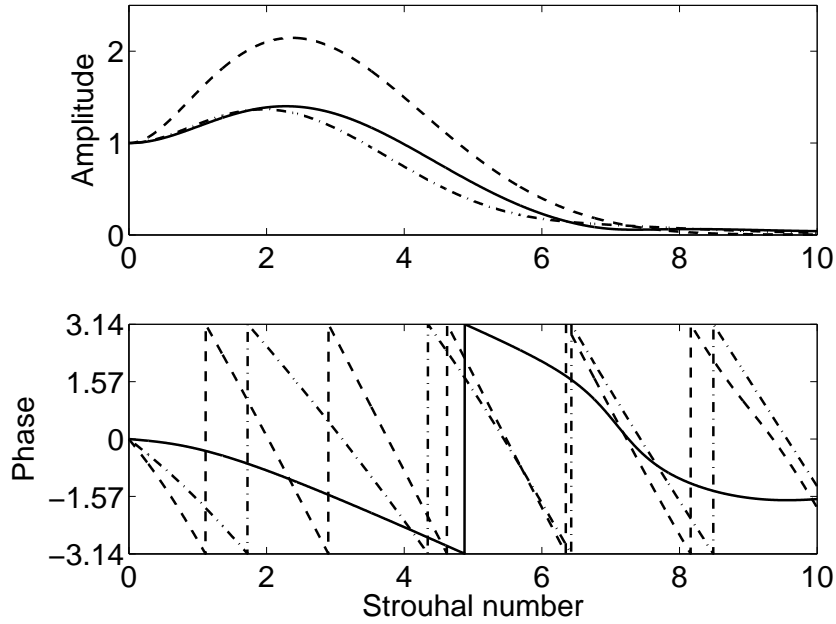


Figure 5.6: Predefined test FTFs of the model (— F_u , -- $F_{\phi,1}$, ·· $F_{\phi,2}$)

which are discussed in chapter 6.3. The corresponding transfer functions are presented in Fig. 5.6. For the present case 60% of the total amount of fuel is injected by the first fuel injection stage and the remaining 40% by the second one. The factor $K_i = \bar{m}_{F,i} / (\sum_{i=1}^N \bar{m}_{F,i})$ (see Eqn. 2.10) in the model is accordingly set to 0.6 for the first and 0.4 for the second fuel injection stage.

All excitation signals – see Fig. 5.2 for a sample – have the same amplitude in the following. The relevant signals were measured upstream of the flame, represented by the digital filters in Fig. 5.4. The amplitudes of the measured equivalence signals vary according to the sum of two excitation signals, which are weighted with factors K_1 and K_2 . The sum represents the correlation of the velocity fluctuations as described in Eqn. (2.10), (2.11). The crest factor of the

	DRBS	BBWN	SINE
C_r [-]	1,007	1,319	2,032

Table 5.1: Crest factor C_r of the measured signals.

measured signals are presented in table 5.1, confirming that the DRBS exhibits the best characteristics.

The simulations of the dynamic model were performed using a time step of $\Delta t = 2.5 \times 10^{-5}$ s. The total length of the simulations were equal to 10000 time steps, which corresponds to a minimum resolved frequency of $f_{\min} = 1/(10000 \Delta t) = 4$ Hz. In the first test series the used white noise signals are not limited in frequency ([0 40000 Hz]). The cycle time is thus the same as the sampling interval of the simulation. The sinus signal contains multiple sine waves with frequencies ranging up to 10000 Hz with a frequency step of 5 Hz.

5.5.1 Impact of model structure on identification results

In this sub-section results, which are obtained in the absence of noise, are presented. In this case the identification results obtained with the MISO model exhibit a perfect match for all excitation signals applied in terms of unit impulse responses or flame transfer functions. For example, the unit impulse response UIR_u is shown in Fig. 5.7. Equivalent results are achieved for $\text{UIR}_{\phi,1}$ and $\text{UIR}_{\phi,2}$, which are not presented here. This is a remarkable result, which demonstrates that the proposed method is capable to discern the impact of the different input signals variables on the overall flame response. For comparison, Fig. 5.7 shows also the identification result obtained if the flame response is represented by a SISO model structure taking the velocity fluctuation at the burner mouth as the only input signal. Here it is apparent, see Fig. 5.5 for comparison, that the identified UIR also includes spurious contributions of the correlated part of the equivalence ratio fluctuations. Fig. 5.8 shows in addition, that the predicted output signal using the UIR identified with the SISO model results in a huge prediction error. On the other hand, if the UIR identified with the MISO model is used, a perfect match between measured and predicted time series is achieved, see again Fig. 5.8. These observations indicate that, independent of the identification method chosen, an adequate model structure must be selected. In principle, simpler identification methods based e.g. on single frequency forcing and Fourier transforms of the signals could be applied. In that case a multi-load or multi-source strategy

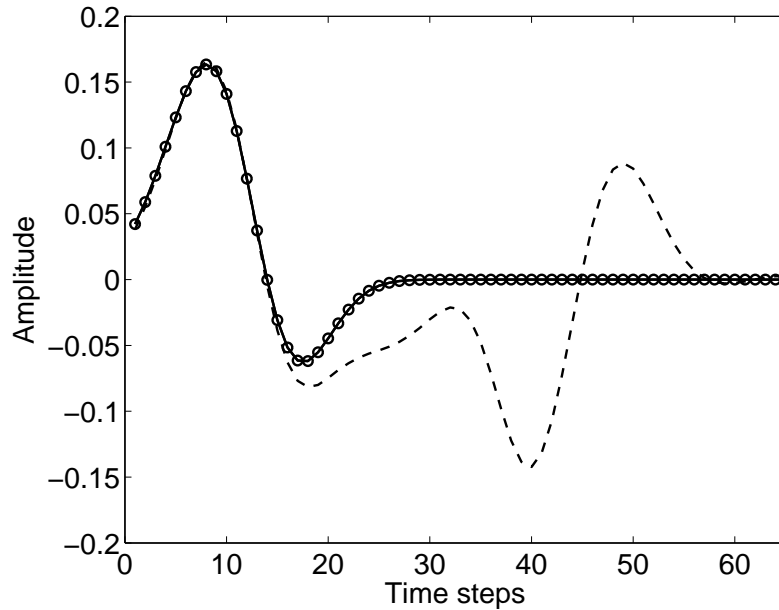


Figure 5.7: Comparison between predefined and identified unit impulse response UIR_u using MISO and SISO model structure (— Test UIR, -o MISO, -- SISO)

– an extension of the two-source method proposed by Åbom [2] – would have to be developed in order to separate the correlated effects of the signals on the response. This would, however, result in a several-fold increase in computational requirements.

5.5.2 Impact of excitation signal types in the presence of noise

In experiments or CFD simulations, measured signals as well as measured responses contain usually a certain amount of noise. To investigate the impact of noise on identification quality, the signals are overlaid with an uncorrelated, normally distributed white noise signal. A signal-to-noise ratio u_0/n_0 of about four was chosen in the present case, where n_0 denotes the basic amplitude of the white noise. Figure 5.9 and 5.10 show the result of the identification in the presence of noise in terms of the unit impulse responses UIR_u and $UIR_{\phi,2}$. The results for the third unit impulse response $UIR_{\phi,1}$, as well as the corre-

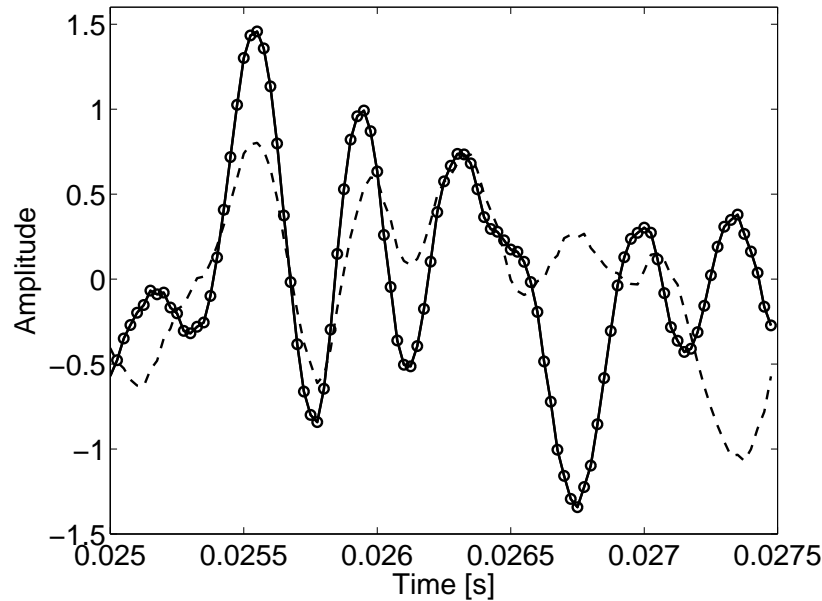


Figure 5.8: Comparison between measured and predicted heat release rate using MISO and SISO model structure (— measured, -o MISO, - - SISO)

sponding flame transfer functions exhibit similar trends and are omitted. The discrete random binary signal exhibits the best characteristics. The broadband white noise and the overlaid multiple sine signal result in noticeable deviations, especially in regions where the values of the predefined test UIRs are zero. However, compared to the sine signal the broadband white noise demonstrates a smoother behavior. A similar trend can be seen in Fig. 5.11 and 5.12, which show the identified flame transfer functions. The flame transfer functions are presented in form of amplitude and phase vs. Strouhal number (non-dimensional frequency):

$$Sr = \frac{\omega d}{2\pi u}. \quad (5.21)$$

d ($d = 0.04$ m) denotes the burner mouth diameter and u ($u = 19.4$ m/s) the mean flow velocity in the mixing section of the combustor test rig configuration, which is presented in the next chapter. Again the DRBS reveals, in terms of amplitude and phase, the best agreement with the target values. Analyzing

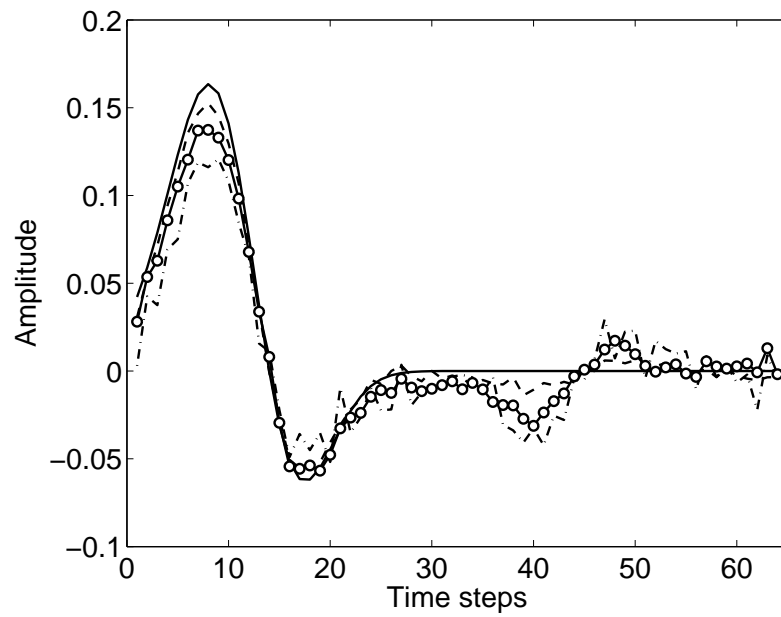


Figure 5.9: Unit impulse response UIR_u identified in the presence of noise (— Test UIR, -· Sine, -o BBWN, -- DRBS)

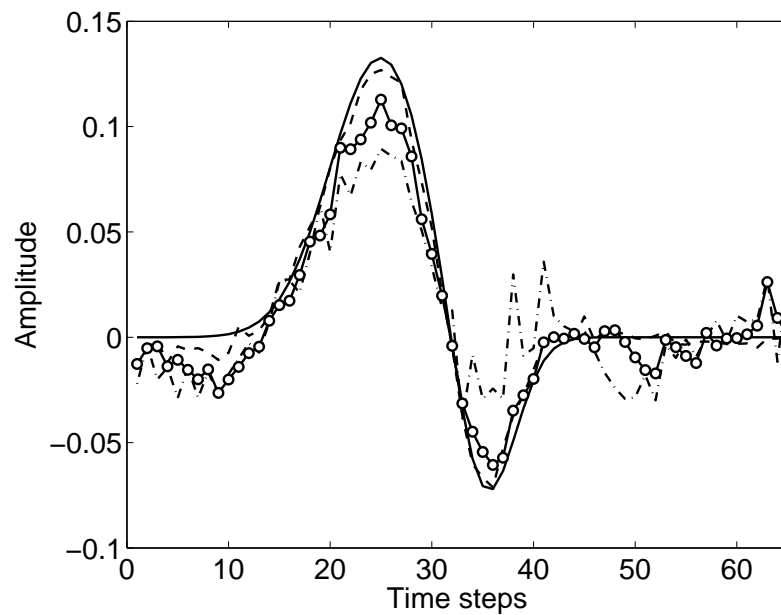


Figure 5.10: Unit impulse response $UIR_{\phi,2}$ identified in the presence of noise (— Test UIR, -· Sine, -o BBWN, -- DRBS)

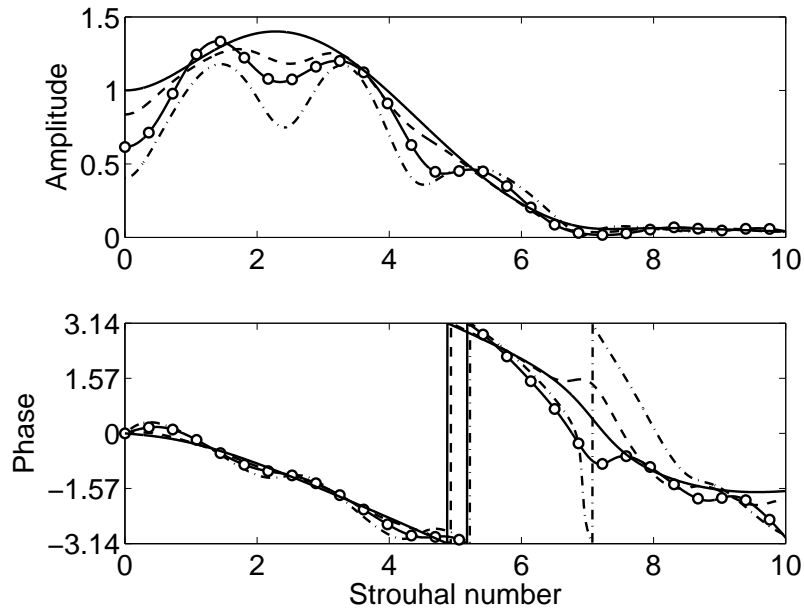


Figure 5.11: Flame transfer function F_u identified in the presence of noise (— Test FTF, -- Sine, -o BBWN, - - DRBS)

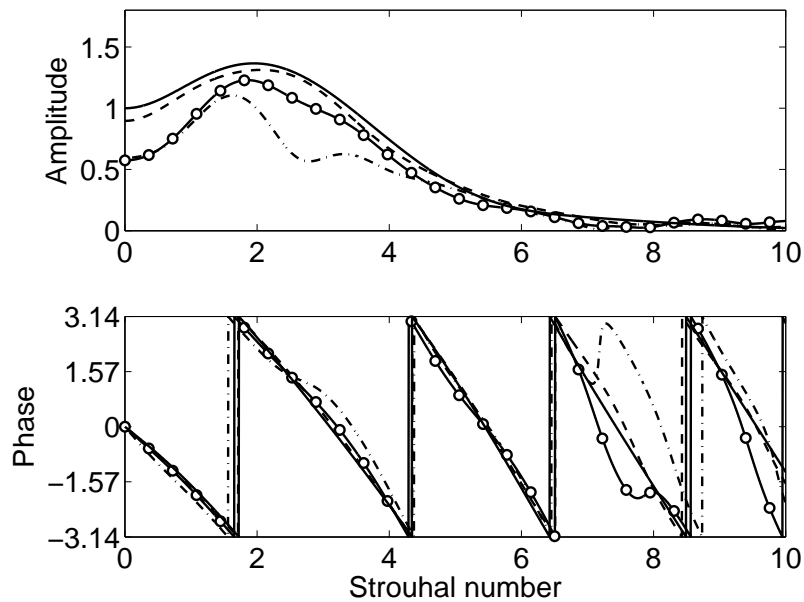


Figure 5.12: Flame transfer function $F_{\phi,2}$ identified in the presence of noise (— Test FTF, -- Sine, -o BBWN, - - DRBS)

the other two signals it can be confirmed that the BBWN is preferable to the SINE signal. Identification quality according to Eqn. (5.17) is listed in table 5.2. Figure 5.13 and 5.14 show the auto- and cross-correlations of error and measured DRBS and of the measured SINE signal, respectively, which have been defined in Eqn. (5.18) - (5.20). The confidence interval is marked by the two horizontal lines in the figures. The cross-correlation is determined between ϵ and u'_b and ϵ and ϕ'_2 . The correlation between ϵ and ϕ'_1 has similar characteristics and is again omitted. The length of the correlations was set to 120 time steps, which is almost twice the length of the UIRs. Except for a few cross-correlation values between the error and the SINE signal, which are located outside the border of the confidence interval, both figures indicate that the chosen model structure and number of model parameters are sufficient to properly describe the input-output relationships. The deviations in the auto-correlation signal for the first time steps are due to the limited frequency content of the response signal, which corresponds to the low-frequency behavior of the flame. Combining the information of table 5.2 and Fig. 5.13, 5.14, it can be concluded that the non-identified deviations (100% - Q) of the DRBS signal are completely due to the noise signal (which is equal to about 1/4 of the total signal level as mentioned before). In case of the SINE signal the same level of noise deteriorates the quality of the identification significantly. The BBWN lies between both extremes, but shows in total acceptable results.

In the second test case presented, two DRBS excitation signals with unlimited ([0 40000 Hz]) and limited frequency range ([0 8000 Hz]), respectively, were analyzed. A signal can be limited to a certain frequency range in setting a cycle time or cut-off frequency according to Eqn. (5.15), (5.16) or setting a maximal single frequency in case of a multi-frequency signal (Eqn. (5.14)). As a consequence the power spectrum density reaches a higher level in the limited fre-

	DRBS	BBWN	SINE
Q [%]	74,4	58,9	39,6

Table 5.2: Proportion of the explained deviation of the measured response according Eqn. (5.17)

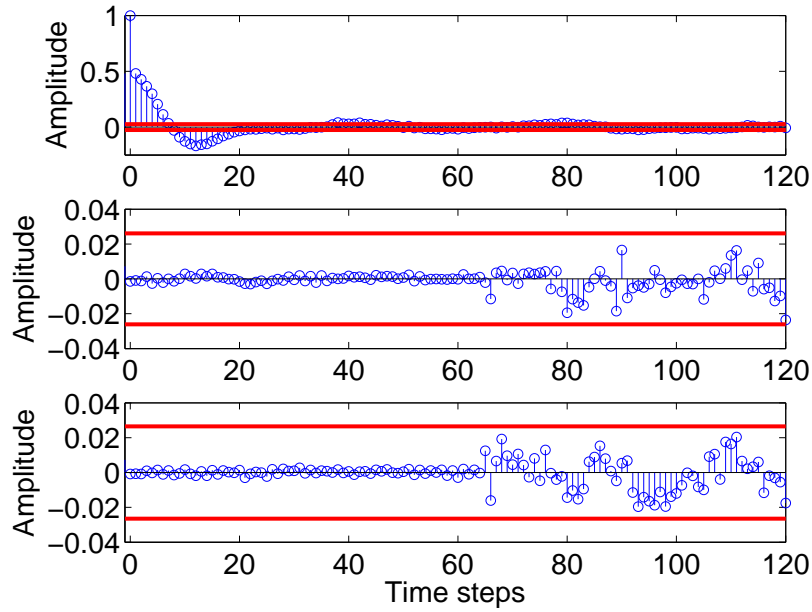


Figure 5.13: Auto- and cross-correlations of error and DRBS excitation signal (Top: Γ_ϵ , Middle: $C_{\epsilon u'_b}$, Bottom: $C_{\epsilon \phi'_2}$)

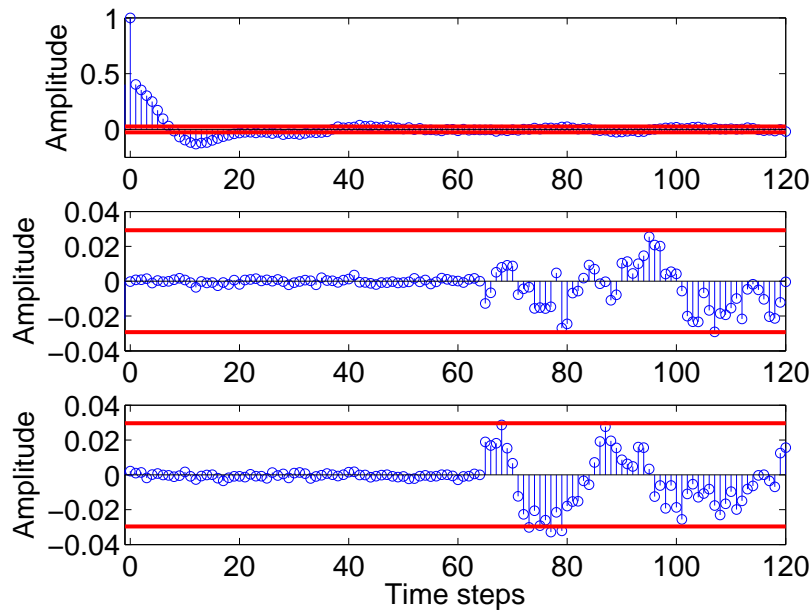


Figure 5.14: Auto- and cross-correlations of error and SINE excitation signal (Top: Γ_ϵ , middle: $C_{\epsilon u'_b}$, bottom: $C_{\epsilon \phi'_2}$)

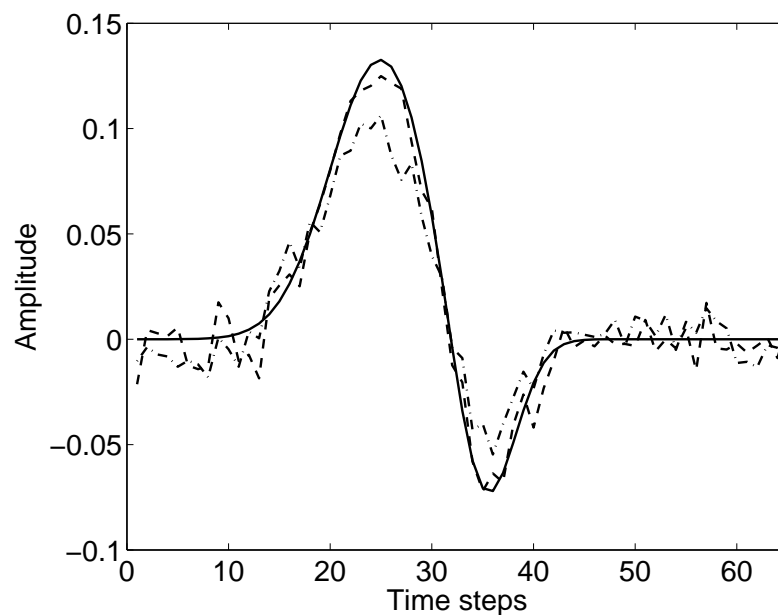


Figure 5.15: Unit impulse response $UIR_{\phi,2}$ identified in the presence of noise (— Test FTF, - - DRBS (limited frequency range), - · DRBS)

quency range. Such an excitation signal could therefore exhibit an even better characteristic regarding the identification process, especially in cases of significant noise amplitudes. The measured signals and responses are overlaid with white noise such that a signal to noise ratio of about two results. Fig. 5.15 and Fig. 5.16 show the identified UIR_u and the flame transfer function as an example. The impact of the noise is even further reduced in case of the signal with limited frequency content. Even with a high fraction of noise in the signal the identification results reveal only small deviations compared to the predefined flame transfer function.

5.5.3 Impact of the measured time series length

In further test series it was evaluated how many simulation time steps N of the signals are sufficient to guarantee a proper identification. As the total computational effort is proportional to the length of the time series, it is important to know under which circumstances shorter time series would not degrade

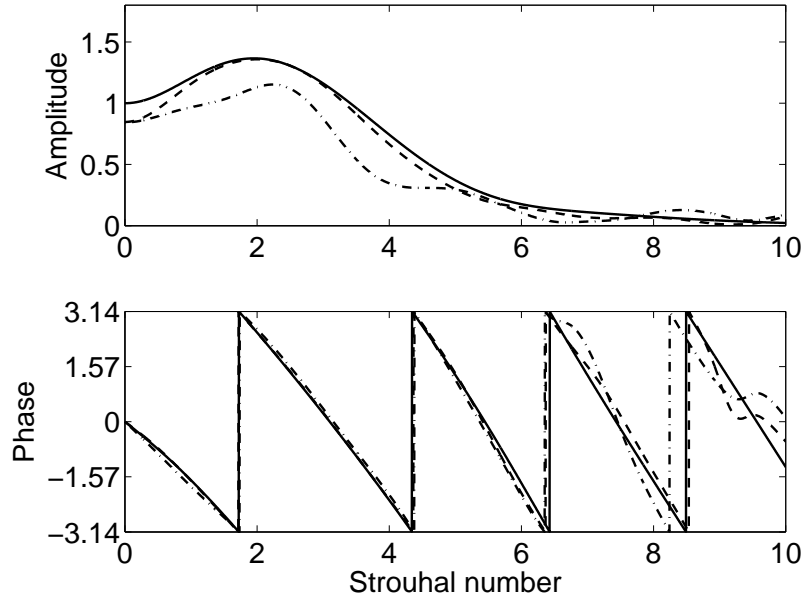


Figure 5.16: Flame transfer function $F_{\phi,2}$ identified in the presence of noise (— Test FTF, -- DRBS (limited frequency range), -· DRBS)

the identification quality. For the present case a DRBS signal with unlimited frequency range is used as a reference signal. Different numbers of time steps were evaluated ranging from $N = 3 \times M$ to $N = 150 \times M$, where M denotes again the number of UIR coefficients. Three different signal to noise ratios were analyzed (no noise, $S/N = 4$, $S/N = 10$). The results are presented in Fig. 5.17 in form of the "quality" Q/Q_0 over the time series length, which are shown as multiple of M . Q/Q_0 is determined using Eqn. (5.17), which is normalized by the maximum possible result of Q in presence of noise. Taking the case with a signal to noise ratio of 10, a value of 97% can be reached when the total simulation time is 15 times the length of the UIR or the longest time lag considered ($M\Delta t$).

The numerical study using the simplified model demonstrated that the proposed identification method based on correlation analysis and the Wiener-Hopf inversion is able to identify multiple-input single-output (MISO) systems. Furthermore, it is capable to separate the impact of the different input signals on the response, even if the input signals are correlated to a certain

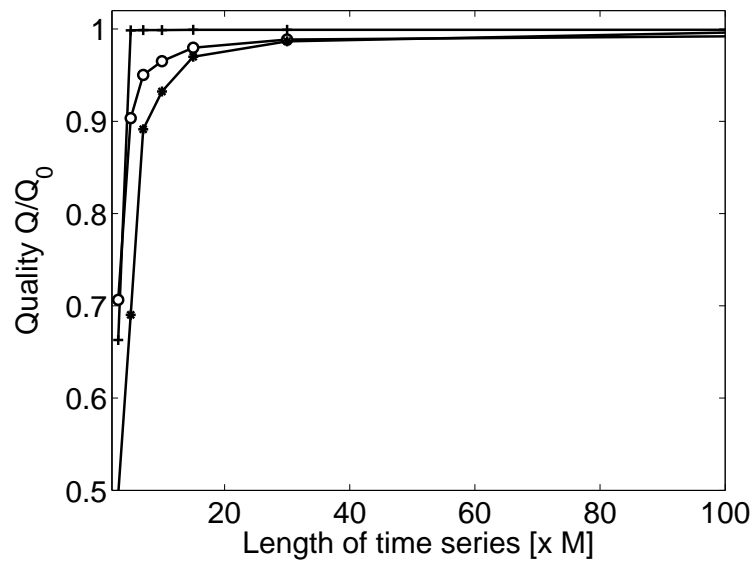


Figure 5.17: Quality Q/Q_0 of identification as a function of time series length (-+ W/O NOISE, -o S/N = 10, -* S/N = 4)

degree. In the present case the correlation amounted to 50%. In the presence of noise it becomes apparent that the discrete random binary signal showed the best performance compared to broadband white noise or a sine overlay. Therefore the DRBS is used in the following to apply the identification method to the measured signals and responses, which are obtained by a transient CFD simulation. As the method itself has proven to work properly, the physical quality of the identification just depends on the numerical models (turbulence, combustion) used in the CFD simulation and the amount of noise in the signals.

6 Numerical simulation

MISO model identification is now applied to a generic practical premixed swirl burner with a multi-stage fuel injection system. The purpose is to show that the method proposed can be applied successfully to complex configurations, like the turbulent reacting flow of a practical premixed combustor, and to demonstrate that relevant information on flame dynamics can be deduced from unit impulse and frequency responses.

In the next section the combustor configurations with two stage and three stage fuel injection will be described in more detail, followed by a summary of the CFD model setup. Then the results of steady-state and transient simulations are presented, including a physics-based interpretation of the flame dynamics. As the acoustic characteristics of the axial swirler are not known and can not be derived analytically, the transfer matrix of the swirler is identified in addition to the flame transfer functions. The results obtained are implemented into an acoustic network model of the combustion system, as described in chapter 7.

6.1 Practical premixed combustor configuration

The configuration investigated in this study is representative of a combustor with practical premixing. The layout is similar to a combustion test rig investigated by Komarek et al. [56, 57] and comprises a plenum, an axial swirler and bluff-body flame holder mounted in an annular duct, and the combustion chamber. The axial swirler comprises in total eight blades with an angle of attack of 45° . The theoretical swirl number of the flow is 0.74. The plenum has a length of $L = 0.095$ m with a cross-section area of $A = 0.0312$ m². The length of the combustion chamber is equal to $L = 0.3$ m, with a cross-section of $A =$

0.00816 m². An orifice plate is used as termination of the combustion chamber through which the hot products leave the chamber into the atmosphere. In the experiments of Komarek et al. [56, 57], natural gas was injected upstream of a choked cross section, such that the fuel/air mixture was perfectly homogeneous even in the presence of combustion oscillations. The computational model investigated in this work, however, incorporates additional fuel injection stages, which inject fuel through a number of small holes into the annular duct upstream of the axial swirler. A sketch of the entire combustion system including the fuel supply system is shown in Fig. 6.1. As in many industrial combustion systems, the distances between the fuel injectors and the flame are too short to allow for perfect premixing. More important in the present content is the fact that the fuel injection system is acoustically non-stiff, i.e. the pressure drop between fuel plenum and mixing section is not sufficient to decouple the acoustics of the fuel injection system from the acoustics of the entire combustion system. Therefore, the fuel concentration at the flame will be influenced by acoustic perturbations in the annular mixing duct and in the fuel injectors.

In the present work two different configurations with two and with three injection stages, respectively, are studied with the CFD/SI approach. The main focus in the first case lies on the analysis of the impact of fuel injector impedance

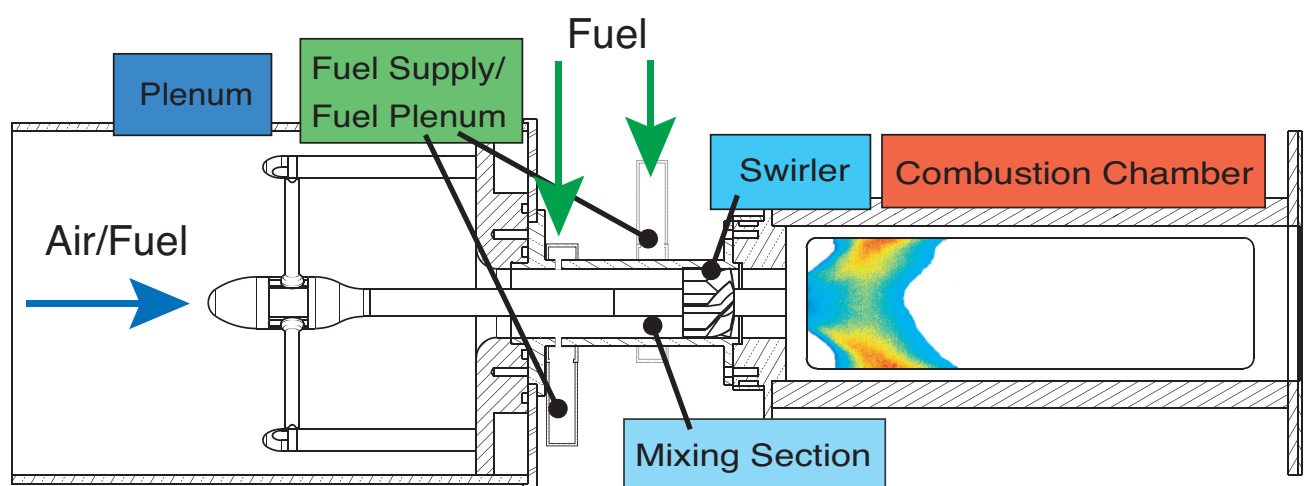


Figure 6.1: Sketch of the combustion test rig

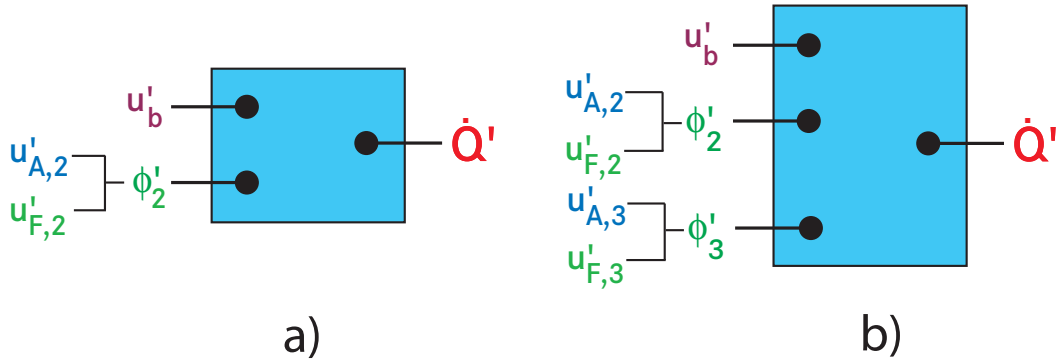


Figure 6.2: MISO systems representing practical premixed combustion configurations: a) case A and b) case B

on the thermo-acoustic stability. The second one explores possible implementation strategies of fuel staging as a means of passive control. Note that the first fuel injection stage is not resolved in the computational model. Instead, a lean premixture of fuel and air is imposed at the inlet boundary of the computational domain at the upstream side of the plenum.

In the first case, denoted as case A, 50% of the fuel is already premixed in the first stage before it enters the plenum. The remaining fuel is injected through the second fuel injector. The axial distance from the injection to the burner is $L_{F2} = 0.125$ m.

The second case, named case B in the following, is an extension of the first one. A third fuel injection stage is placed at a location of $L_{F3} = 0.085$ m upstream of the burner mouth, indicated as a grey shadow in Fig. 6.3. A part of the fuel, namely 10%, is premixed before it enters the mixing section. 36% of the fuel is injected via the second injection stage and the remaining 54% are supplied to the third one.

In all cases methane (CH_4) is used as fuel. The thermal power is set to 50 kW and the overall nominal equivalence ratio to $\phi = 0.77$. The MISO model structures for the configurations are shown in Fig. 6.2, where u'_b represents the velocity fluctuation at the burner exit and \dot{Q}' the fluctuations of heat release rate. The variables ϕ'_i denote the nominal equivalence ratio fluctuations at injec-

tors $i = 2$ for the second injector and $i = 3$ for the third injector¹. As discussed in chapter 2.2.2, the nominal fluctuations of equivalence ratio at the injectors can in turn be expressed in terms of the velocity fluctuations of the fuel mass flow $u'_{F,i}$ and the main mass flow $u'_{A,i}$ at the location of injection i , see Eqn. (2.10).

6.1.1 Design of the fuel injector

The fuel supply nozzle is designed similar to the one described in Richards and Robey [108]. The fuel plenum is arranged as an annulus of rectangular cross section around the mixing section. In addition, a resonator tube with variable length L_R is attached to the fuel plenum to change the acoustic impedance of the fuel injection system. A sketch of the fuel supply dimensions is shown in Fig. 6.3. From the fuel plenum, fuel is injected radially inward through eight holes, which are equally distributed around the circumference. The injection holes have a diameter of $d_j = 1.2$ mm. The choice of the number of holes, the diameter of the holes and chosen fuel mass flow is a trade-off between the acoustic characteristics and the premixing quality of the air and fuel: For the present purposes the pressure drop over the fuel injection nozzles has, on the one hand, to be small enough to ensure an acoustically coupled fuel injection system. On the other hand the impulse ratio of the fuel and main stream has to be high enough to ensure a sufficient penetration and mixing of the fuel.

The pressure loss coefficients from the fuel plenum to the injection tube (ζ_1) and from the tube to the mixing section (ζ_2) were determined with a steady-state CFD simulation and are equal to 0.73 and 0.84. The coefficient is, in general, defined as (see also Eqn. (3.42)):

$$\zeta \equiv \frac{2\Delta p}{\rho u^2}. \quad (6.1)$$

In both cases the pressure loss coefficients depend on the velocity u in the injection tube. In case A, for example, the pressure loss over the fuel injection

¹As the first injector is acoustically decoupled the equivalence ratio fluctuations at injector $i = 1$ are zero ($\phi'_1 = 0$)

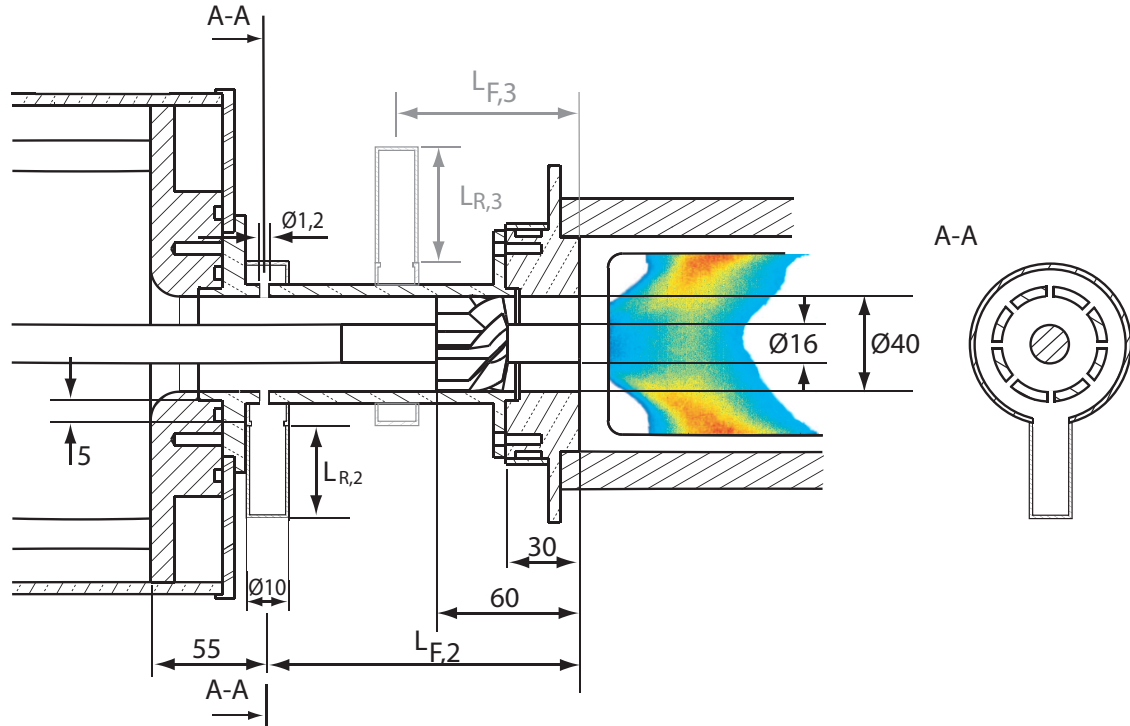


Figure 6.3: Dimensions of fuel supply and mixing section (mm)

system is $\Delta p_1 = 3794 \text{ Pa}$ or $\Delta p_1 = 0.037 p_{atm}$, where p_{atm} denotes the standard atmospheric pressure.

Beside the relatively low pressure loss, the mixing quality between air and fuel should be adequate. The impulse of the fuel stream in relation to the main stream should be high enough that the fuel jet penetrates to a radial position near the middle of the mixing section. Various estimations of the penetration depth exist in the literature and can be found in e.g. Lefebvre [69]. Many of these estimates are validated for liners in combustion chambers. The diameter of the liner holes is commonly an order of magnitude larger than the one used in the present work. Therefore, these relations can only be used as a first starting point. In contrast to the cases described in literature, the configuration analyzed exhibits a rather low distance between the injection and the burner center body. According to [69] a penetration depth of

$$Y_{max} = 1.15 d_j \sqrt{J} \quad (6.2)$$

can be calculated for a single jet injected into a circular duct. J represents the impulse ratio of the fuel and main stream and is defined as:

$$J = \frac{\rho_F u_F^2}{\rho_A u_A^2}. \quad (6.3)$$

The subscripts F and A represent again the fuel and main stream, respectively. In configuration A, for example, the main flow velocity is equal to $u_A = 18.6$ m/s. The density has a value of $\rho_A = 1.167$ kg/m³. With the properties for the fuel stream ($u_F = 85.6$ m/s, $\rho_F = 0.66$ kg/m³) an impulse ratio of $J = 12.0$ is computed for the present case. The fuel injection including stream lines and the fuel mass fraction at a downstream location are presented exemplarily for the configuration A in Fig. 6.4. The legend refers to the plane presented whereas the colors of the streamlines indicate the amplitude of the velocity. The fuel is distributed well over the radial direction, with the main part of the fuel located in the middle between the outer wall and the center body. The maximum depth according to Eqn. (6.2) would be 0.005 m, which is slightly too low. The optimum number of circumferential holes was estimated according to Holdeman et al. [45] and lies in the range between 6.1 and 10.2 for the configuration analyzed (see appendix A.2 for more details). CFD simulations with different numbers of holes showed that the configuration with eight injection holes exhibits adequate mixing characteristics.

6.1.2 Numerical setup of the combustion system

To determine the flame transfer functions, a three-dimensional unsteady RANS computation of the compressible turbulent reacting flow in the combustor has been performed using the software package ANSYS-CFX. According to the discussion in chapter 2.3.2, the computational domain can be reduced to the mixing section, the fuel injection holes, the axial swirler and the combustion chamber. A sketch of the computational domain including the "measurement" planes for case A, at which the time series of the required velocity fluctuations are recorded, is shown in Fig. 6.5. To save computational time only a 90° segment is simulated using periodic boundary conditions. A *second order backward Euler scheme* and the *high-resolution scheme* were

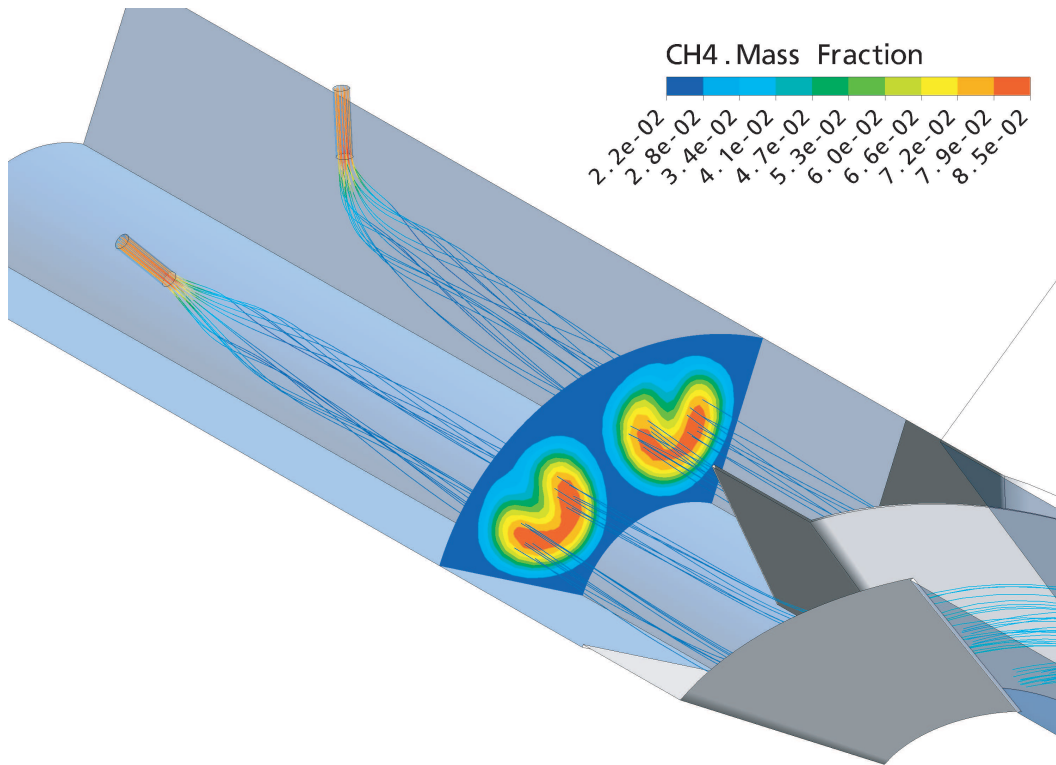


Figure 6.4: Streamlines of the injected fuel and fuel mass fraction of combustion configuration, case A

used in time and space discretization, respectively. More details about the numerical methods can be found in [5]. The simulations were performed with the *Shear Stress Transport turbulence model* and the *partially burning velocity combustion model* of CFX. Both models are described in chapter 4.1.2 and 4.2.2. For simplicity all walls are assumed to be adiabatic. The chosen time step is $\Delta t = 2.5 \times 10^{-5}$ s. The main inlet flow parameters of the two simulation cases are shown in Table 6.1. The temperature for all inlets was set to $T = 298$ K. The inlet turbulence intensity, which is defined as the ratio of turbulent velocity fluctuations to the mean flow velocity, has a value of 5%. CFX non-reflecting boundary conditions are used for the inlets and the outlet to prevent resonant amplification with high amplitudes in the vicinity of eigenfrequencies, which deteriorates the quality of identification results. This condition is realized using a modified algorithm on the basis of the Navier-Stokes charac-

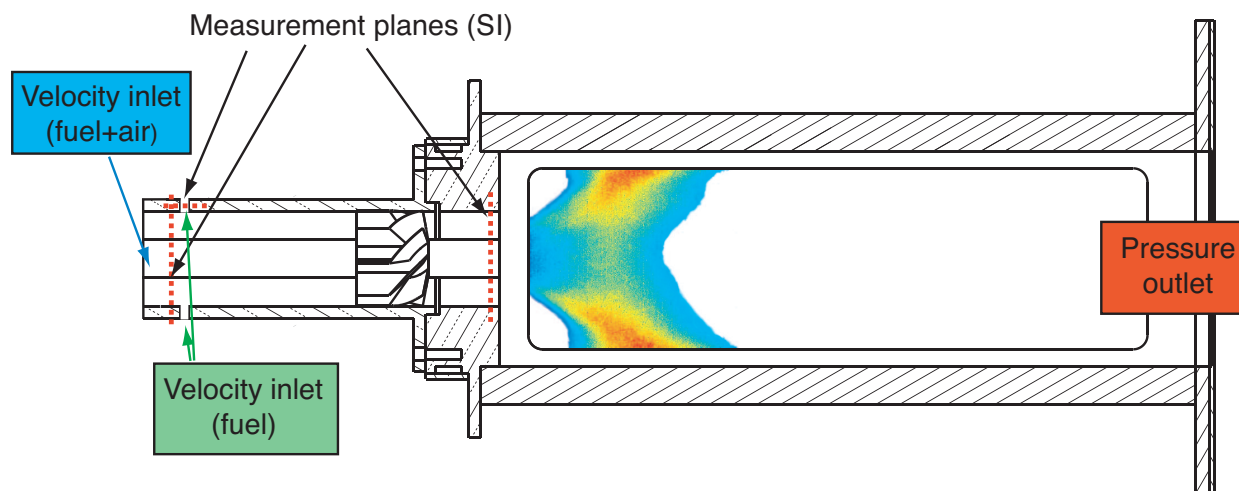


Figure 6.5: Sketch of the computational domain and location of "measurement" planes (case A) for the SI-method

teristic boundary conditions (NSCBC) of Poinso and Lele [95], which was implemented in the CFX environment by Widenhorn [130]. The inlet boundary conditions of the main air-fuel and the fuel stream(s) are overlaid by acoustic velocity excitation. As the discrete random binary signal with limited frequency content led to heat release fluctuations, which can not be described completely by a linear relationship and might be due to non-linearities, the unlimited signal ($f_{max} = 1/\Delta t$) was used in the following. These unexplained deviations, which are also present at low level using the unlimited signal, are described in more detail in chapter 6.3. The excitation amplitude at the inlet

Inlet, case A:	Main stream	Fuel stream
Velocity u [m/s]	18.6	85.6
Density ρ [kg/m ³]	1.167	0.66
Fuel mass fraction Y_{CH_4} [-]	0.0218	1

Inlet, case B:	Main stream	Fuel stream 1	Fuel stream 2
Velocity u [m/s]	18.02	61.84	93.01
Density ρ [kg/m ³]	1.18	0.66	0.66
Fuel mass fraction Y_{CH_4} [-]	0.0044	1	1

Table 6.1: Inlet flow parameters.

boundary conditions equals 4% of the mean flow velocity in the combustion configuration with two fuel injection stages and 3% for the one with three fuel injection stages. The velocity fluctuations and the volume integrated heat release rate, which are the signals used for the identification of the flame dynamics, are recorded at the "measurement" planes at every time step of the simulation. To suppress possible turbulent contributions and to account for density fluctuations of the fuel-air mixture, mass flow rate fluctuations were exported instead of the velocity fluctuations. The "measurement" plane at the burner mouth was placed 5 mm upstream of the burner exit to minimize errors due to the fluctuating flame front, which is able to travel slightly inside the burner. At the point of injection the "measurement" planes in the fuel line and in the mixing section were placed 2.5 mm upstream of the stream crossing point. The "measurement" planes are also shown in Fig. 6.5.

The size of the grid is a compromise between computational effort and a sufficient resolution of the flow structures and acoustics. Especially in the vicinity of the swirler a fine grid was necessary to realize the flow separation at the swirler blade and the secondary flow. The secondary flow further enhances the mixing quality due to the additional imposed turbulence. It develops from the point of flow separation and is due to the pressure gradient, which drives the fluid to the middle of the swirler passage. The chosen grid predicts a slightly higher strength of the passage vortex compared to a simulation case where the boundary layer is fully resolved as described in Hoffmann [44]. Figure 6.6 shows the critical area of the swirler with the passage vortex, which is highlighted by stream lines.

In the present work the propagation of acoustic waves up to 2000 Hz are resolved in the unsteady RANS context, reflecting the amplitude and the phase of an acoustic wave correctly. The quality of an acoustic wave traveling through the CFD domain can be judged by mainly two parameters: the grid size or length of a grid cell Δx and the time step Δt of the simulation. Both parameters can be combined into one parameter, the acoustic Courant-Friedrichs-Lewy (aCFL) number, which is defined as:

$$\text{aCFL} = (u + c) \frac{\Delta t}{\Delta x}. \quad (6.4)$$

It is an extension of the CFL number, which is based on the mean flow velocity. The CFL number determines the number of grid cells through which a flow disturbance is convected in one time step. In terms of computational fluid dynamics it is a condition for the algorithms for solving partial differential equations to be convergent. An explicit method becomes unstable if the CFL value exceeds one. However, a fully implicit discretization method allows CFL values over one, although the accuracy of the discrete schemes diminishes. It has been shown that for $\text{aCFL} \gg 1$ the propagation of an acoustic wave could be resolved adequately. The important criteria to minimize the numerical dispersion effects are the number of grid cells per wavelength and time steps per

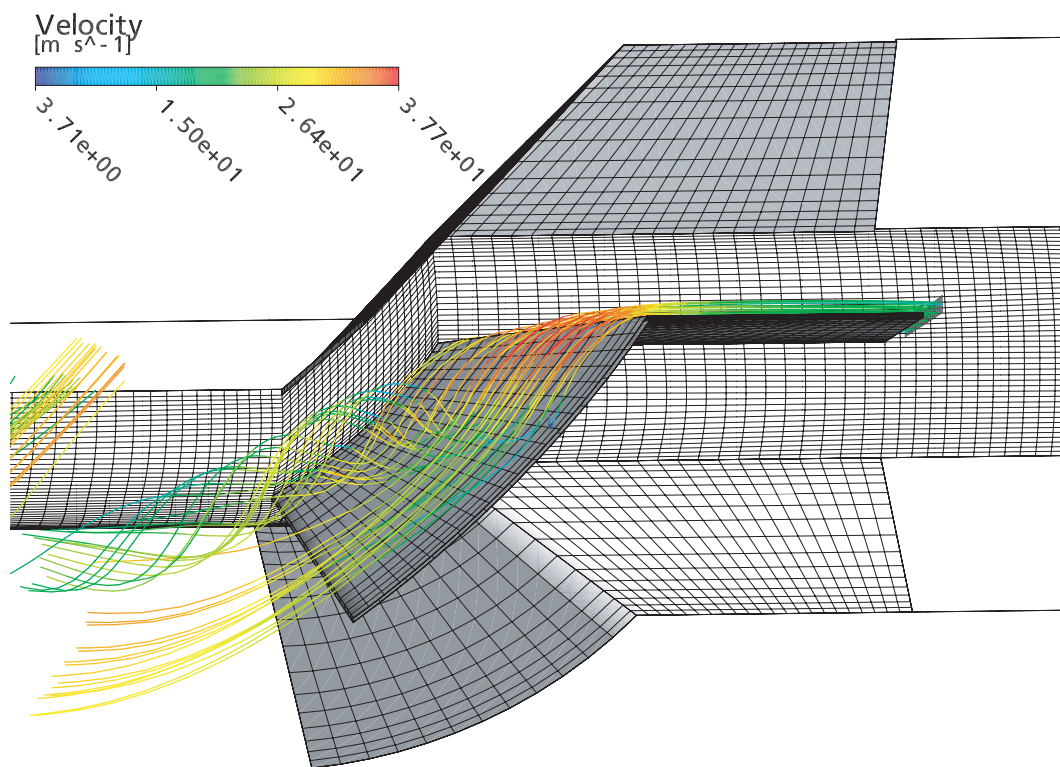


Figure 6.6: Streamlines around a swirler blade showing the flow separation and the resulting secondary flow

period. In the present simulations a minimum of 100 grid cells and 20 time steps per period was ensured for an acoustic wave with a frequency of 2000 Hz. Details about a numerical test case, in which the propagation of a plane acoustic wave in a simple duct was analyzed, can be found in Hoffmann [44].

6.2 Steady-state simulations of the combustor configurations

As a starting point for the transient simulations to determine the flame transfer functions, steady-state simulations were performed. They are required to obtain the main characteristics of the two combustion configurations regarding mixing quality and axial heat release distribution. The heat release distribution is necessary to define an appropriate axial location of the flame in the acoustic network models.

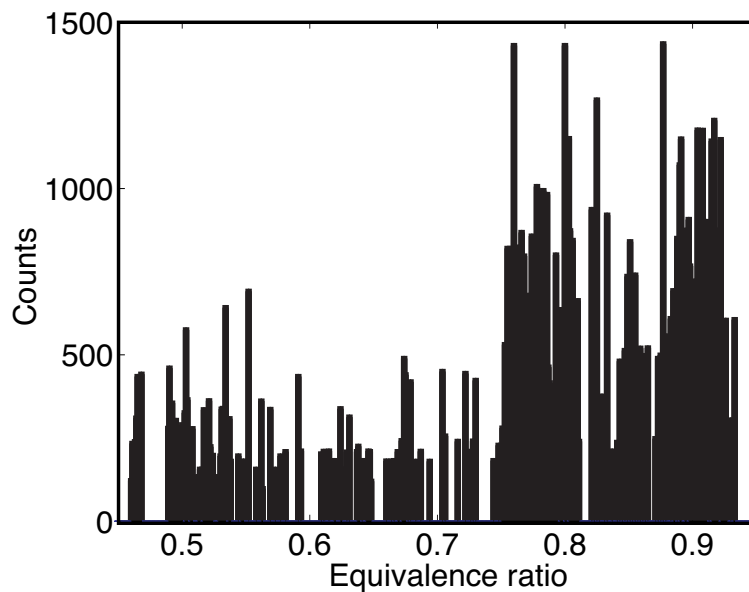


Figure 6.7: Equivalence ratio distribution upstream of the burner mouth, case A

To judge the air-fuel mixing quality the grid cell value of the equivalence ratio measured on a cut through the mixing section were exported and analyzed. The cut was placed slightly in front of the burner mouth. As each cell exhibits a

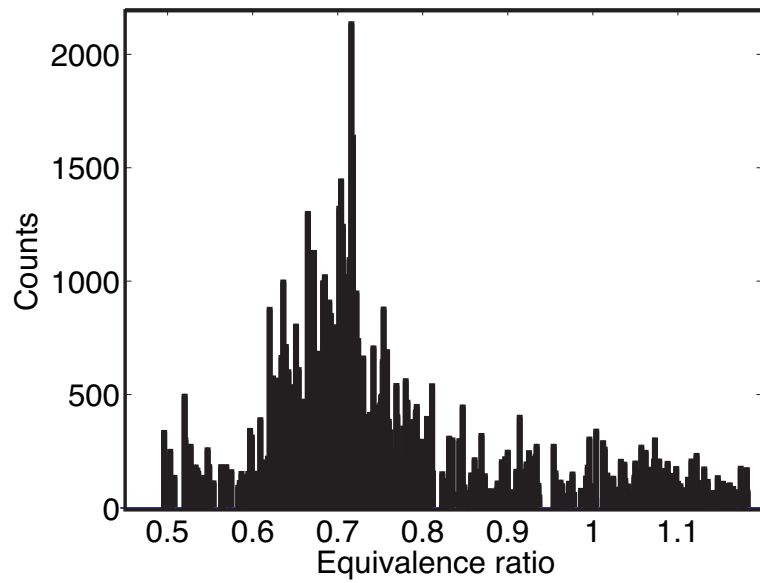


Figure 6.8: Equivalence ratio distribution upstream of the burner mouth, case B

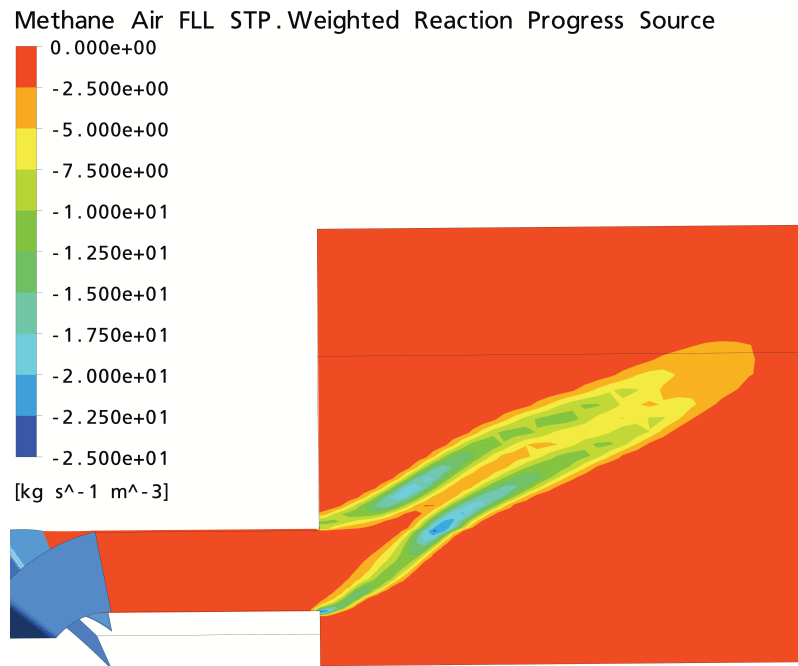


Figure 6.9: Weighted reaction progress source, case A

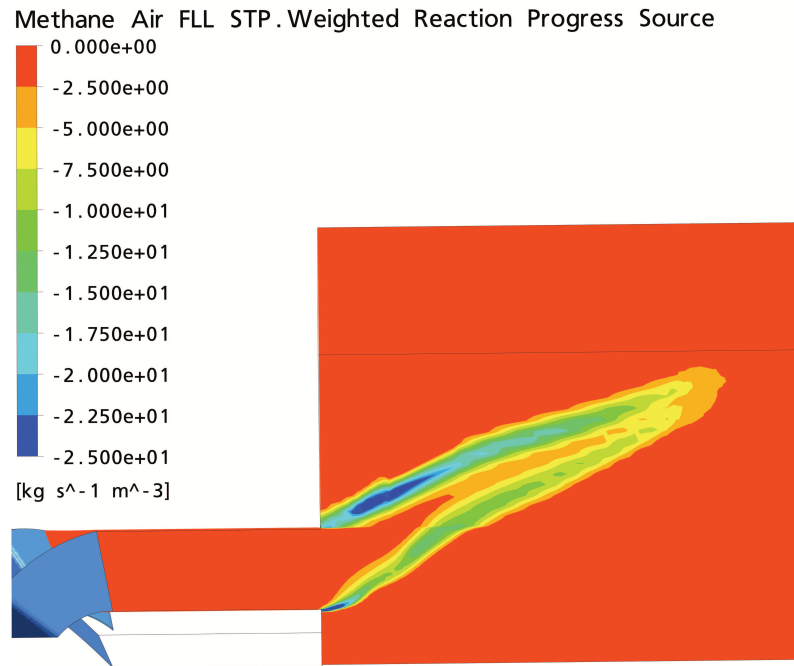


Figure 6.10: Weighted reaction progress source, case B

different area, the values obtained are area weighted. The results are presented in form of a histogram, showing the counts for different equivalence ratio values. In configuration A (Fig. 6.7) the equivalence ratio is mainly distributed between 0.75 and 0.92 (the mean value of both cases is about $\phi = 0.77$). The second case (Fig. 6.8) has a wider distribution, which ranges up to 1.18. Here, regions with a rich fuel mixture still exist. The mixing quality is, however, significantly better than in case A with a peak around $\phi = 0.72$.

The heat release rate of both cases is presented in terms of the weighted reaction progress source $Z_M \dot{\omega}_c$ (see chapter 4.2.2) in Fig. 6.9 and 6.10, which show the downstream end of the mixing section and the upstream part of the combustion chamber. In case A the heat release rate is more or less equally distributed between the inner and outer burning shear layer. Case B shows that the combustion process is shifted towards the outer region. The reason is the upstream injection location, where 36% of the fuel is injected. This injector possesses a lower impulse ratio and therefore, in comparison to case A, a decreased penetration depth. The consequence is a richer mixture close

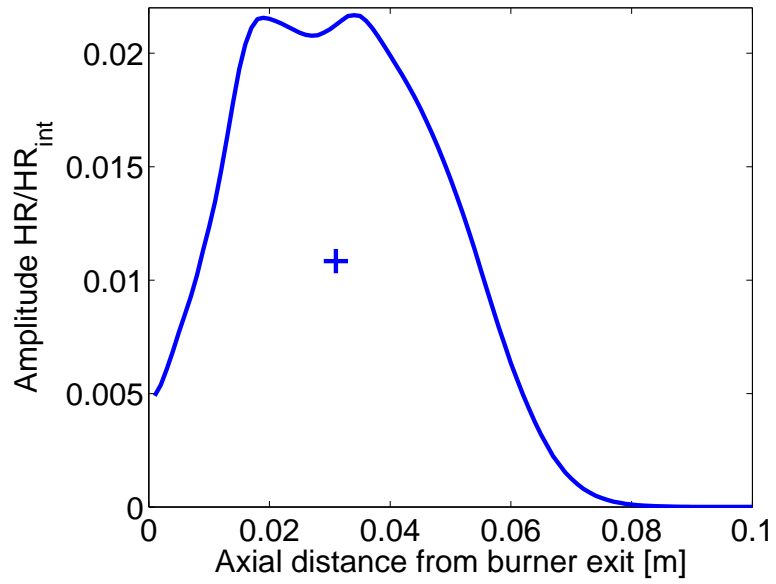


Figure 6.11: Axial heat release rate distribution, case A

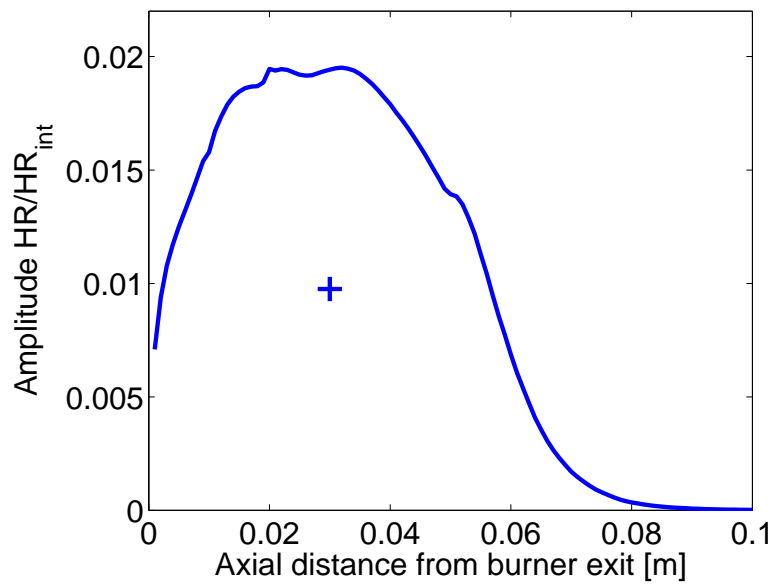


Figure 6.12: Axial heat release rate distribution, case B

to the outer wall of the annulus and the outer shear layer, which explains the high heat release rate close to the burner exit. The corresponding axial distribution of the heat release rate can be found in Fig. 6.11 and 6.12. The heat release rate distribution is normalized by the area integral over the axial direction HR_{int} . Both curves show a similar overall trend. In contrast to case A, case B exhibits an overall slightly lower amplitude but a wider heat release rate peak. The center of the heat release rate area is located in both cases 0.03 m downstream of the burner exit, which is marked as a cross in the figures. It is defined as the ratio of the local area integral of the heat release rate weighted with its axial position and the overall heat release rate. In the acoustic network models (see chapter 3.3.1.2 or 7.1) the flame is treated as a discontinuity of negligible thickness. Therefore this location is used as the location where the combustion process takes place.

6.3 Identification of the flame transfer functions

From the time series of the CFD simulations, the unit impulse response vectors can be determined using the system identification relations derived in chapter 5. The corresponding flame transfer functions can be obtained from the UIR by z -transformation. As the simulations with broadband excitation only allow a limited physical insight into the flame behavior, additional transient simulations have been performed using impulse forcing. The results of such simulations, although not quantitatively accurate, are very helpful in developing a physics-based interpretation of the flame dynamics. In this way the changes in flame shape, position, heat release rate, etc. in response to the impulse perturbation can be visualized easily.

At first the results of both combustion configurations, case A and case B, are discussed. Furthermore, the flame response to velocity and equivalence ratio fluctuations obtained are analyzed and interpreted using the results of the impulse forcing simulations.

6.3.1 Combustor configuration with two fuel injection stages

The simulation of the combustor configuration with two fuel injection stages was performed using DRBS broadband excitation with an excitation amplitude of 4%. With a 50 / 50 % fuel split between the injection stages, the factor K_1 , required to calculate the nominal equivalence ratio fluctuations from the mass flow rate fluctuations, was set to 0.5. The simulation was continued for 7600 time steps, corresponding to a total simulation time of $T_t = 0.19$ s and a minimum resolved frequency $f_{\min} = 5.33$ Hz. The length of the UIR vectors was set to 520 time steps, which is more than 50% longer than the mean time interval required for a convective disturbance to travel from the point of injection to the center of the heat release rate of the flame. As discussed in chapter 5.5.3, this modest length of the time series is in comparison to the length of the UIR sufficiently large for accurate identification, provided that the signal-to-noise-ratio is equal to or higher than 10.

The unit impulse responses of the heat release rate fluctuations caused by velocity fluctuations at the burner exit and equivalence ratio fluctuations at the fuel injection location, respectively, are presented in Fig. 6.13. The flame responds to the two signals with different time delays: A response to equivalence ratio fluctuations $\text{UIR}_{\phi,2}$ is visible after about 250 time steps, which corresponds roughly to the convective transport time from the point of fuel injection to the flame. The peak response is reached at about 300 time steps, when the fuel arrives at the center of the flame. At later times, the UIR shows an "undershoot", i.e. a range of coefficients $h_k < 0$. This is a remarkable feature, which has to the author's knowledge not been observed previously in studies on the response of premix flames to equivalence ratio fluctuations. A discussion of the interpretation of this observation is the main focus of chapter 6.3.3.

The response UIR_u to velocity fluctuations at the burner exit, which starts after a shorter delay, exhibits two positive peaks. The first peak at 60 time steps corresponds to fluctuations at the burner exit, whereas the second one at about 100 time steps is the response to fluctuations of velocity at the axial swirler, which in turn generate fluctuations in swirl number. This point is discussed extensively by Komarek and Polifke [56]. The flame kinematic response UIR_u

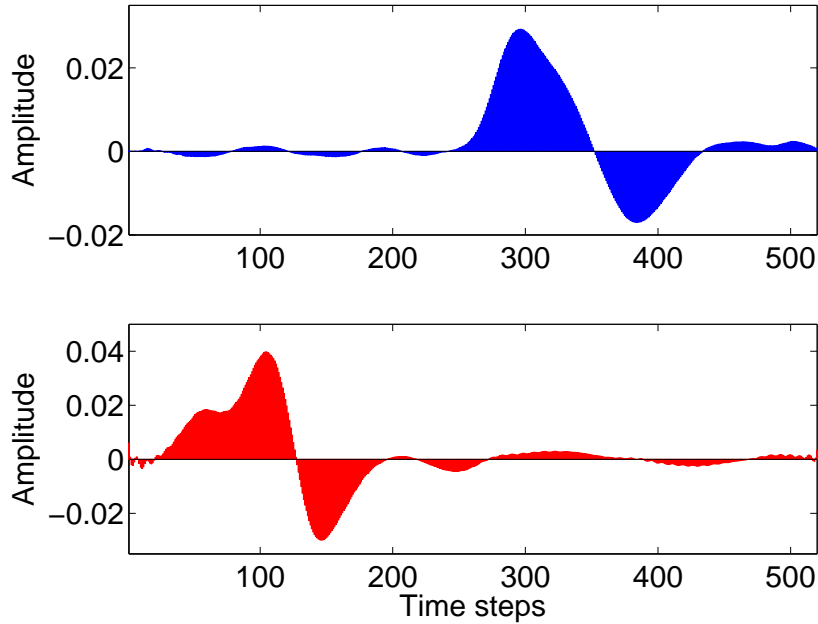


Figure 6.13: Unit impulse response, case A (Top: $\text{UIR}_{\phi,2}$, Bottom: UIR_u)

also shows an undershoot.

The corresponding flame transfer functions are presented in Fig. 6.14. The frequency is normalized by the Strouhal number ($\text{Sr} = \omega d / (2\pi u)$), with mean velocity $u = 19.4$ m/s and burner exit diameter $d = 0.04$ m. The phase information of F_u shows the aforementioned influence of the different time lags between the axial swirler and the flame and the burner exit and the flame. The mean time delay is approximately $\tau \approx 7.5$ ms for the response to equivalence ratio fluctuations and $\tau \approx 2.1$ ms for velocity fluctuations. Both flame transfer functions computed from the UIRs show the correct behavior in the limit of low frequencies. As mentioned in chapter 5.4, conservation of mass and energy requires that both flame transfer functions have to approach unity for $\omega \rightarrow 0$ (see [100] for more details). At higher frequencies – Strouhal numbers in the range 0.3 to 0.5 – both transfer functions show a gain significantly larger than unity, $|F| \approx 2$. This has been observed before for the front-kinematic response F_u , see e.g. [35, 121]. However, for the response F_ϕ to equivalence ratio fluctuations, previous work has always assumed that a dispersion of convec-

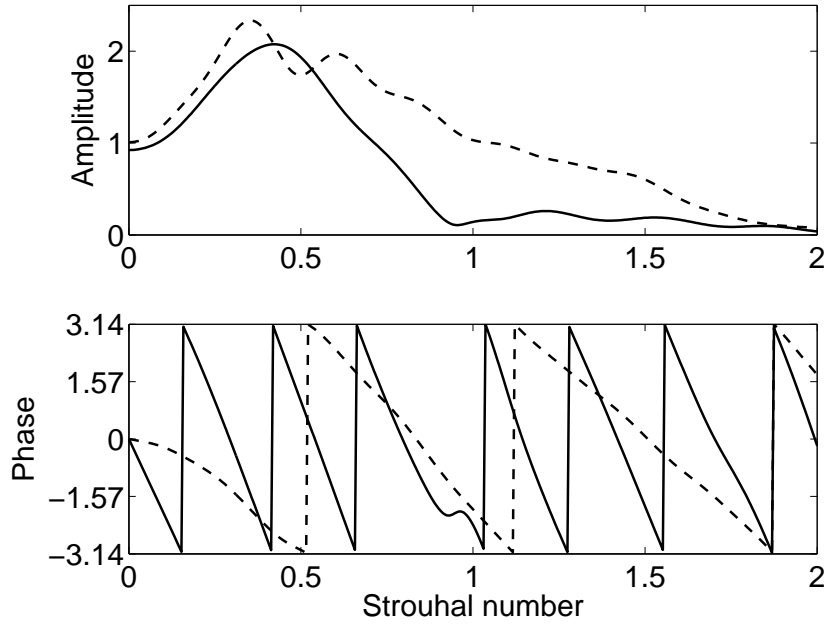


Figure 6.14: Flame transfer function, case A (— $F_{\phi,2}$, -- F_u)

tive time delays will result in a low-pass filter behaviour with $|F_\phi| < 1$ for frequencies $\omega > 0$ [31, 60, 99, 112]. An explanation of the present result is developed in chapter 6.3.3.

The high quality of the identification is demonstrated by the achieved Q -value (see Eqn. (5.17)) of 92.7%. The Q -value obtained indicate that 92.7% of the heat release rate fluctuations are properly described by the unit impulse responses identified. The auto-correlations of the prediction error ϵ and the error-input signal cross-correlations (between ϵ , equivalence ratio fluctuations ϕ'_2 and velocity fluctuations at the burner exit u'_b) are presented in Fig. 6.15. The correlation analysis was performed with a length of two times the length of the UIRs. The correlations are below the confidence interval, which are marked by the two horizontal lines. Therefore the unpredicted deviations (100%- Q) of the output heat release rate signal can not be related to the input velocity signals. This verifies that the chosen number of UIR coefficients is sufficient to completely describe the impact of the input signals. The auto-correlation of the prediction error is for most of the time steps inside or close

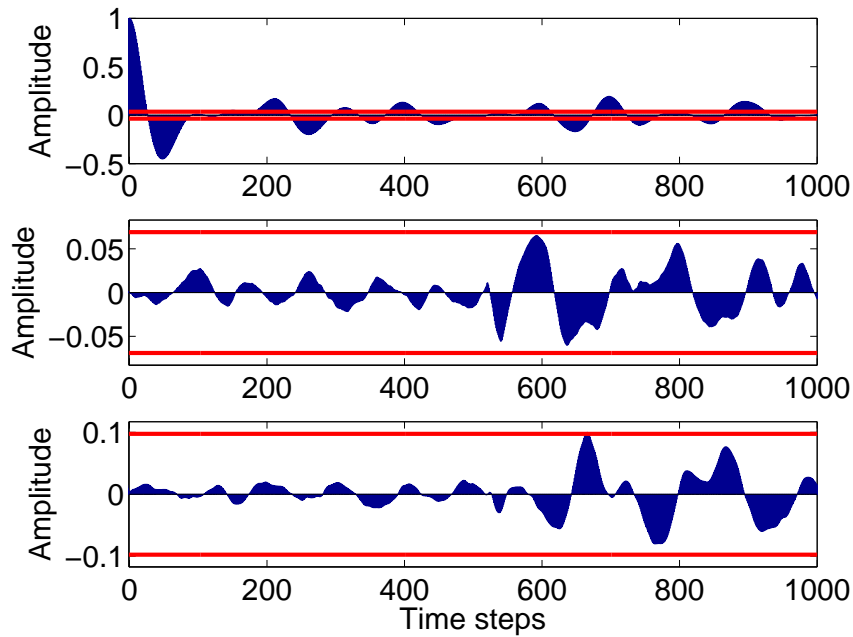


Figure 6.15: Auto- and cross-correlations of error and signals, case A (Top: Γ_ϵ , middle: $C_{\epsilon\phi'_2}$, bottom: $C_{\epsilon u'_b}$)

to the confidence interval. It has almost the characteristics of a white noise signal. The deviations at time steps close to zero are due to the low-pass filtering behavior of the flame. The reason for the further deviations is not clear.

To analyze the unpredicted deviations (100%-Q) and the ones observed in the auto-correlations of the prediction error the predicted heat release rate fluctuations are compared to the ones computed in the CFD simulation. The prediction of the heat release rate fluctuations is done using the input signals obtained by the CFD simulation and the identified UIR coefficients. A segment of both signals is shown in Fig. 6.16. The phase is perfectly reproduced by the identified model. However, the amplitude of the signal predicted shows some small deviations mainly at higher absolute values. As the deviations do not correlate with the input signals (see Fig. 6.15) they might be due to nonlinearities or reflections at the boundaries. This should be clarified in detail in the future.

However, the results obtained demonstrate that the model structure and the

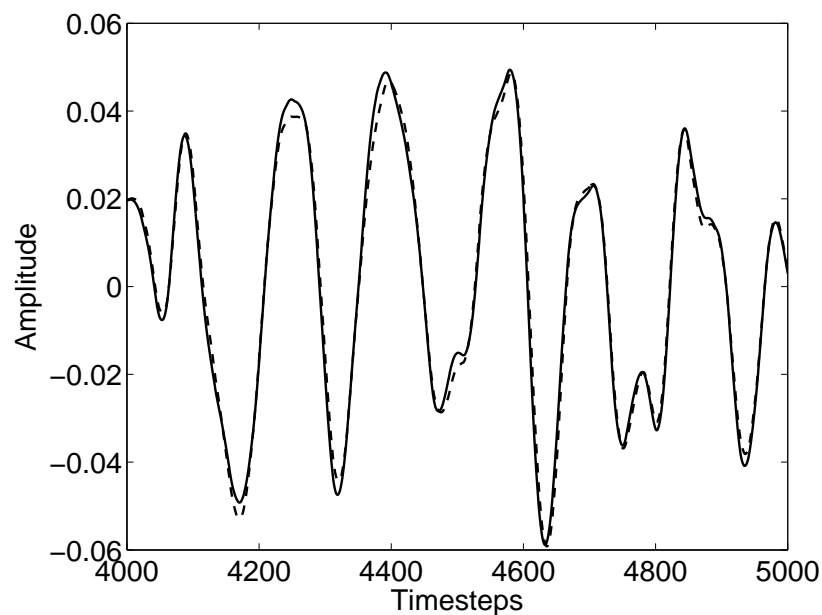


Figure 6.16: Comparison between heat release rate signals, case A (— measured, -- predicted)

estimations made regarding the total simulation time and model order enable a proper identification of the flame dynamics in the present case.

Please note that a validation of the results obtained can only be done with the methods used above. A validation against experimental data can not be done, as to the author's knowledge no such data exist at the time of writing. A generation of such data, however, is rather difficult as discussed in chapter 1.4.

6.3.2 Combustor configuration with three fuel injection stages

In the second CFD/SI simulation the combustion configuration containing three separate fuel injection stages were analyzed. Ten percent of the fuel is already homogeneously premixed with air as they enter the mixing section at the upstream boundary of the computational domain. 36% of the total fuel is injected at the second and 54% at the third injector. Therefore K_2 and K_3 equal 0.36 and 0.54, respectively. Similar to the first case the total simulation

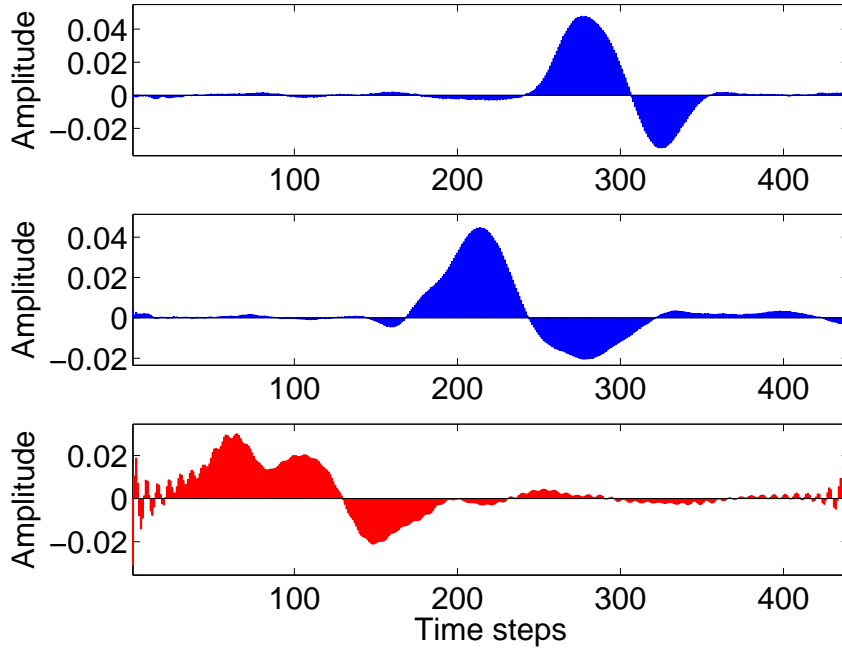


Figure 6.17: Unit impulse response, case B (Top: $\text{UIR}_{\phi,2}$, Middle: $\text{UIR}_{\phi,3}$, Bottom: UIR_u)

time was $T_t = 0.2$ s, which is equivalent to 8000 time steps. The overall considered time delay of the UIRs were set to 440 time steps. The unit impulse response vectors and the corresponding flame transfer functions are presented in Fig. 6.17 and Fig. 6.18. The results demonstrate that the method is able to separate the impact of three different input excitation signals, although they are correlated significantly. The location of the UIR peaks as well as the low-frequency behavior characteristics of the flame transfer functions indicate a proper identification and thus affirm the potential of the proposed identification method. Compared to case A, the UIR of the equivalence ratio fluctuations ϕ'_2 at the second injector shows a similar trend, but exhibits a narrower time delay distribution. The result can be explained by analyzing the heat release rate distribution (see Fig. 6.10). The upstream fuel injection, which supplies 36% of the total amount of fuel, induces a region of a rich mixture and thus high reaction rates in the outer shear layer close to the burner exit. Indeed, a substantial part of the fuel injected at the upstream fuel injector is

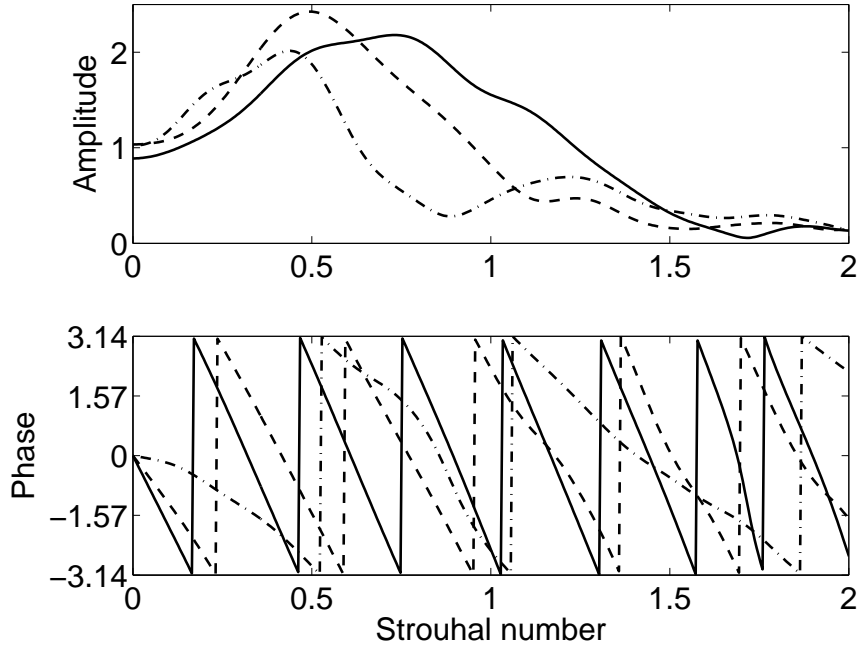


Figure 6.18: Flame transfer function, case B ($— F_{\phi,2}$, $-- F_{\phi,3}$, $- \cdot F_u$)

consumed in this region. This influence can also be observed in the flame response to velocity fluctuations. As the velocity increases with increasing radial distance and taking into account the slightly changed flow field, the impact of the velocity fluctuations at the burner exit results in a strong response of the outer flame region, see again Fig. 6.17. In contrast to the two fuel injection stage configuration the first peak of the UIR_u has a higher amplitude than the second one, indicating that the flame in this case responds stronger to velocity fluctuations at the burner exit than to those at the swirler. The response $UIR_{\phi,3}$ starts about 170 time steps and reaches its positive maximum at 220 time steps. It exhibits a time-shifted, but comparable time delay distribution as $UIR_{\phi,2}$ in the first configuration. The mean time delay of the different impacts is $\tau \approx 6.2$ ms for the upstream fuel injection, $\tau \approx 4.5$ ms for the downstream fuel injection and $\tau \approx 2$ ms for the velocity fluctuations at the burner exit. Compared to case A, the shortened time delays are mainly due to the slightly changed heat release rate distribution and to the fact that the mean inlet velocity of case B is about 0.5 m/s less than in case A. Similar to the first

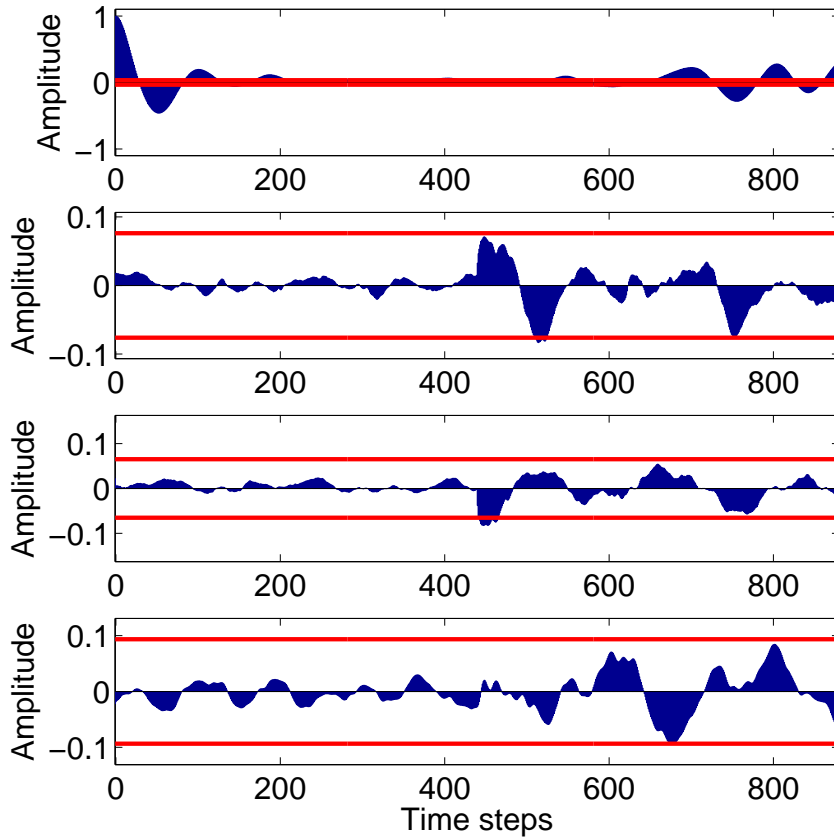


Figure 6.19: Auto- and cross-correlation of error and signals, case B. (From top to bottom: Γ_ϵ , $C_{\epsilon\phi'_2}$, $C_{\epsilon\phi'_3}$, $C_{\epsilon u'_b}$)

configuration, the deviations between the predicted and measured heat release rate signal is rather low. The quality parameter Q equals 90.4%. Fig. 6.19 shows the auto- and cross-correlation analysis of the prediction error and the input signals ϕ'_2 , ϕ'_3 and u'_b . Again the cross-correlation values stay for nearly all considered time delays within the 99% confidence interval. Only a few values are located slightly at or outside the border. The auto-correlation shows unexpected deviations at large delay times, which are again probably due to non-linearities.

6.3.3 Analysis and interpretation of identification results

The unit impulse responses and flame transfer functions identified show some remarkable results, which are analyzed in more detail in this section. The unit impulse responses exhibit an undershoot $h_k < 0$ for a range of time lags $k\Delta t$, whereas the gain of the flame transfer functions exceeds one ($|F(\omega)| > 1$) for a range of frequencies ω . Both phenomena are strongly related to each other, which is described in the following. Furthermore a physics-based interpretation of the impulse responses to velocity and equivalence ratio fluctuations will be developed on the basis of results obtained with impulse forcing imposed on transient CFD simulations.

The flame transfer function is determined by the z -transform of the unit impulse response (see chapter 5):

$$F(\omega) = \sum_{k=0}^M h_k e^{-i\omega k\Delta t}. \quad (6.5)$$

The conservation equations of mass and energy requires that the flame transfer functions $F_{\phi,i}$ and F_u have to approach unity for $\omega \rightarrow 0$ (see [100]). To realize the correct low frequency limit the sum over all unit impulse response coefficients has also to approach unity:

$$\lim_{\omega \rightarrow 0} F(\omega) = \lim_{\omega \rightarrow 0} \sum_{k=0}^M h_k e^{-i\omega k\Delta t} = \sum_{k=0}^M h_k = 1. \quad (6.6)$$

If all coefficients h_k of a unit impulse response vector are positive, the gain of the flame transfer function decreases with increasing frequency. The reason is due to the index k in the phase factor $\exp(-i\omega k\Delta t)$ of the z -transform, which is responsible for a phase difference between the contributions of the individual coefficients. These phase differences lead with increasing frequencies to an increasing destructive superposition of the contributions. The result is a reduction of the sum over all weighted UIR coefficients. The flame acts therefore as a low pass filter with a maximum gain of unity at zero frequency.

An UIR with positive and negative values, however, can result in a gain $|F(\omega)| > 1$ for a range of frequencies as the phase factors can, in this case, lead to

constructive superposition between the contributions of the individual coefficients.

To further analyze the relevant physical mechanism of the behavior observed, simulations of the configuration with two fuel injection stages were carried out using impulse forcing.

Flame response to impulse forcing of velocity at the burner exit

The first transient CFD simulation with impulse forcing was performed with excitation of only the main air-fuel velocity inlet. The fuel mass flow rate at fuel injector "2" was kept constant. The amplitude of the impulse in flow velocity was set to 10% of the mean value. As it is not possible to numerically resolve an impulse that is enforced during only one time step, a impulse duration of 20 time steps is chosen. The results obtained are normalized according to the excitation level of the CFD/SI simulation.

The response of the flame should exhibit a similar behavior as the UIR_u obtained with broadband forcing. A comparison between the CFD/SI unit impulse response and the UIR determined with impulse forcing is presented in Fig. 6.20. For the first time delays both response vectors match very well. For later times, the result of the impulse forcing shows oscillations, caused by partial reflection of the impulse signal at the boundaries of the computational domain. These spurious features are not representative of the response of the flame to the impulse excitation. To explain the undershoot of the UIR, the temporal development of flame front surface area and heat release rate are tracked, which is presented in Fig. 6.21. The flame front is defined as an iso-surface of the progress variable with $c = 0.5$. In addition a cut through the flame in a meridional plane at several instances in time is presented in Fig. 6.22 and 6.23. The undisturbed flame front is shown in Fig. 6.21 and 6.22 and is denoted as state "A". When the increased mass flow reaches the burner exit, the flame is first pushed downstream resulting in a stretched flame front at the burner exit, especially in the inner shear layer. After a short time delay the flame is reacting to the disturbance with an increased flame speed and heat release rate. As a consequence, the flame moves again

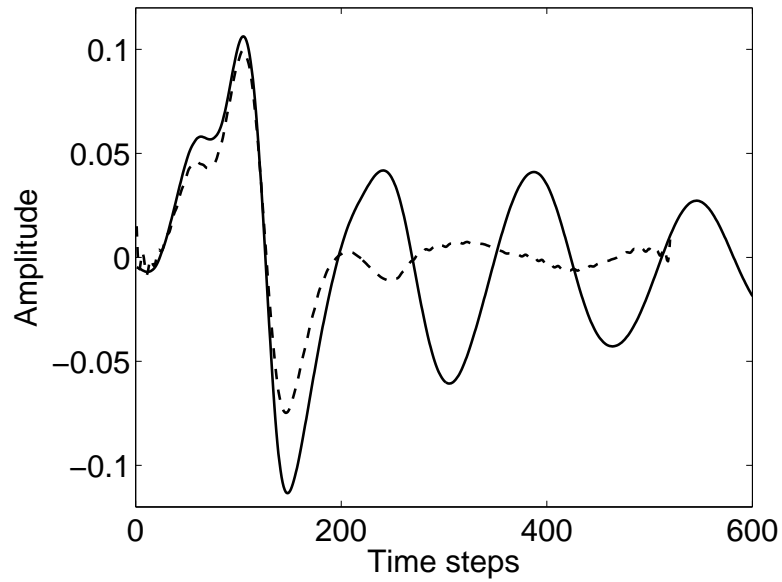


Figure 6.20: UIR_u computed with DRBS (- -) and impulse forcing of mass flow rate of premixture (—)

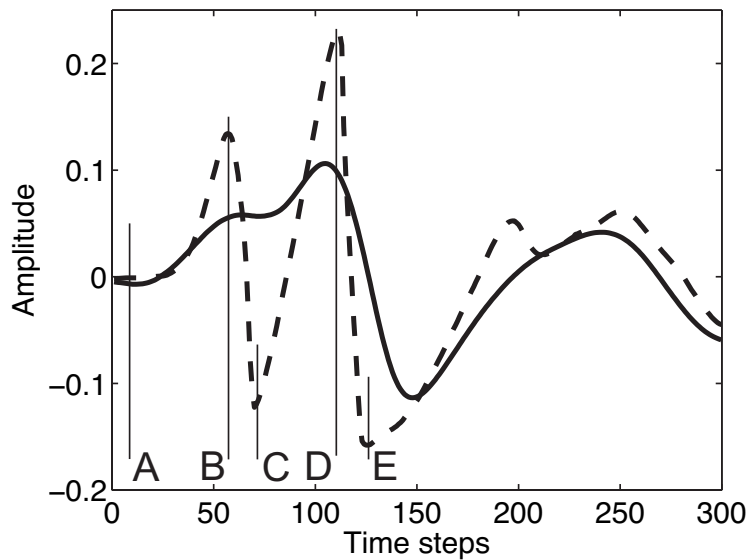


Figure 6.21: Response of flame surface area (- -) and heat release rate (—) to impulse forcing of mass flow rate of premixture

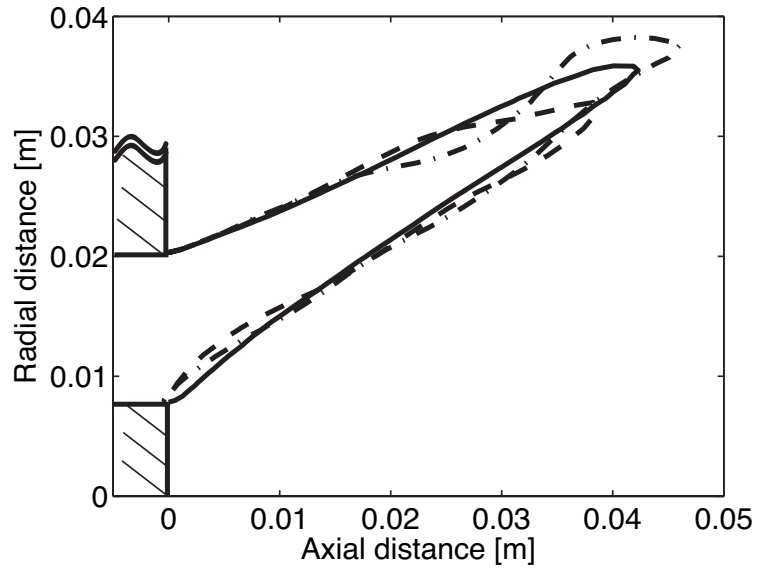


Figure 6.22: Response of flame front to impulse forcing of mass flow rate of premixture at time A (—), B (-·) and C (- -)

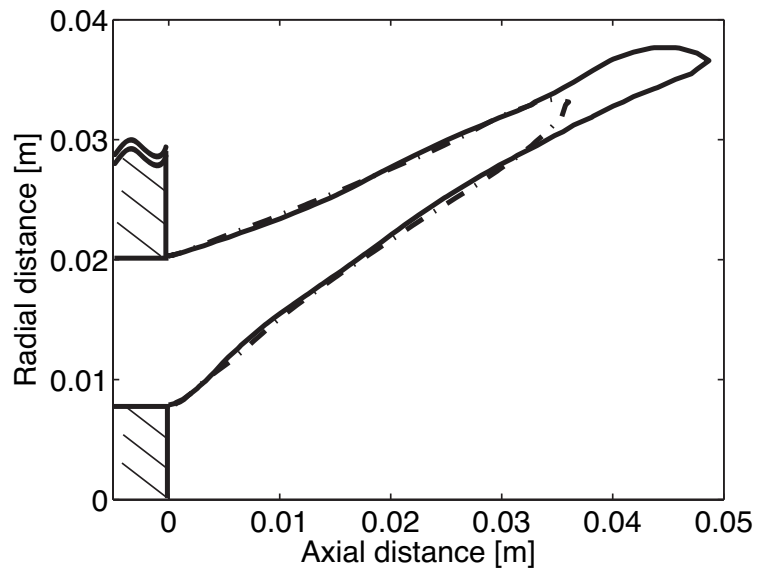


Figure 6.23: Response of flame front to impulse forcing of mass flow rate of premixture at time D (—) and E (-·)

towards the burner and at the inner shear layer even into the mixing section. This undulating motion, generated at the burner exit in the outer and inner flame front, is then convected along the entire flame, leading to an increase of the overall flame surface area and heat release rate (state "B"). Close to the downstream end of the flame the outer and the inner flame front merge, separating the remaining downstream fuel from the main combustion zone. The downstream end of the flame extinguishes, which is denoted as status "C". At this time the disturbance produced at the axial swirler reaches the burner exit where it results in a similar response (state "D", "E"). A similar behavior (states "A", "B", "C") was described by Schuller et. al. [120]. In their work they investigated a laminar premixed flame and observed as well a sudden decrease of the flame surface due to the interaction of neighboring flame fronts at the tip of the flame.

Flame response to equivalence ratio fluctuations at the burner exit

In a second simulation, impulse forcing was applied to the fuel mass flow rate at injector "2" without perturbation of the main flow. Unit impulse responses of the flame, obtained from impulse and DRBS broadband excitation, respectively, are compared in Fig. 6.24. The basic trend matches again. However, the amplitude of the impulse response is only 60% of the UIR computed from broadband forcing with SI. This is due to the small impact of the fuel mass flow added at injector "2" compared to the overall mass flow. An alternating sign of the impulse UIRs for larger time delays is also clearly seen.

As above the impulse response of the flame surface area and the heat release rate are investigated. As mentioned in chapter 1.2 the overall rate of heat release \dot{Q} of a premixed flame may be expressed as a function of the unburnt gas density ρ_u , the flame surface per unit volume Σ , the (turbulent) burning velocity s_t and the heat of reaction per unit mass of premixture ΔH . Once the richer fuel-air mixture arrives at the flame front, the heat released per unit mass of premixture ΔH and therefore the overall heat release rate \dot{Q} increases as shown in Fig. 6.25. As the turbulent burning velocity s_t also increases, the flame propagates upstream, resulting in a reduction of total flame surface

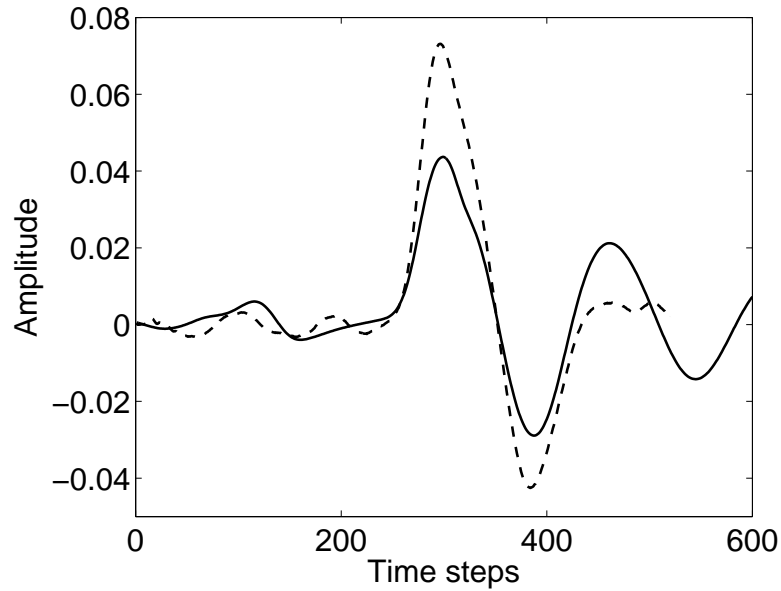


Figure 6.24: $UIR_{\phi,2}$ computed with DRBS (- -) and impulse forcing of mass flow rate of fuel at injector "2" (—)

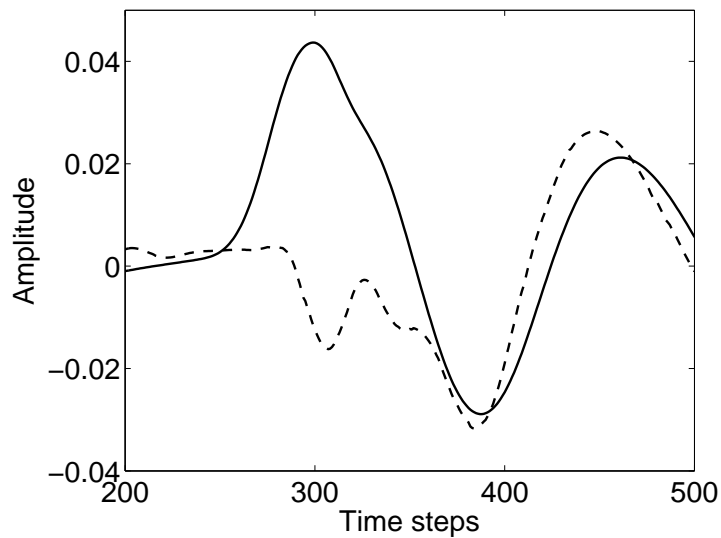


Figure 6.25: Response of flame surface area (- -) and heat release rate (—) to impulse forcing of mass flow rate of fuel at injector "2"

area, which is shown in Fig. 6.25. Although the total flame surface is reduced the overall heat release rate increases in the beginning due to the strong increased release of heat per unit mass of premixture and the increased burning velocity. However, once the additional fuel injected by the impulse forcing is consumed, the equivalence ratio returns along with ΔH and s_t to its original value. As the flame surface is still smaller compared to the undisturbed case, \dot{Q}' decreases and attains finally negative values. With the burning velocity s_t restored to its original value, the flame surface area is now too small to burn the arriving fresh premixture. The flame is thus convected downstream to its original area and position.

In summary, the overall shape of UIR_ϕ and in particular the undershoot can be explained by an interaction of changes in the heat released per mass of premixture and burning velocity with perturbations of flame position and surface area. Methods using steady state CFD simulation and a Eulerian or Lagrangian approach to model the convective transport of fuel to the flame front are therefore not able to capture this effect. These methods can only determine F_ϕ simply as "fuel transport time lag distributions" [30,31,59,60,99] assuming a fixed position of the flame and therefore a constant flame surface area. The reduction in flame surface due to "front kinematics", which is responsible for the undershoot in the UIR_ϕ and therefore also for the excess gain of F_ϕ , can not be properly described with such modeling strategies.

6.4 Identification of the acoustic characteristics of the swirler

The acoustic characteristics of the axial swirler are also not known a priori and no analytical solution exists. Therefore the acoustic transfer matrix of this element has to be determined separately. This is accomplished in a similar way as the identification of the flame transfer functions in the last section using the CFD/SI method. With the properties of the swirler an acoustic model of the entire combustion system can be built up, because all other elements can be described by the relations derived in chapter 3.3 and by the results obtained in the last section. The computational domain was reduced for the present analysis to a shortened mixing section with the axial swirler and the combustion

chamber. The fuel injection tubes are not included. The simulation was performed with air as the only fluid and a mean flow velocity of 20 m/s. In contrast to the identification of the flame transfer functions, it is necessary to excite the inlet and the outlet conditions to obtain a physical meaningful transfer matrix. The velocity fluctuation of the inlet condition was set to $u' = 5\%$ of the mean value. The pressure outlet condition with zero mean pressure was overlaid with an acoustic fluctuation in the same order of the velocity fluctuation: $p' = \rho c u'$. As the present investigation focuses on the pure acoustic characteristics over a relatively short distance, the time step of the simulation was reduced to $\Delta t = 0.5 \times 10^{-5}$ s to capture the acoustic waves accurately.

The velocity fluctuations were exported 5 mm upstream and 20 mm downstream of the swirler. 15000 time steps were simulated, which leads to a total simulation time and minimum resolved frequency of $T_t = 0.075$ s and $f_{\min} = 13.33$ Hz, respectively. The scattering matrix in form of amplitude and phase is shown in Fig. 6.26 and 6.27. The amplitudes of the diagonal elements S_{11} and S_{22} represent the transmission, whereas the non-diagonal elements

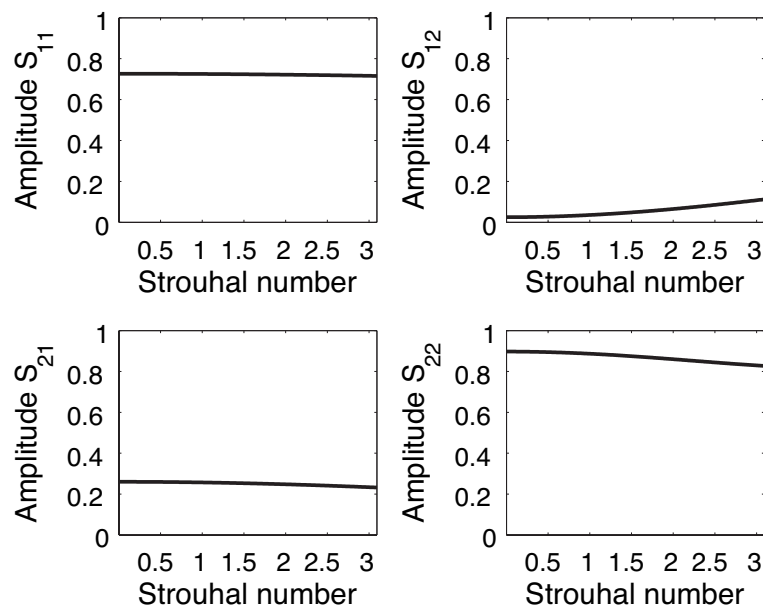


Figure 6.26: Scattering matrix of the axial swirler (amplitude)

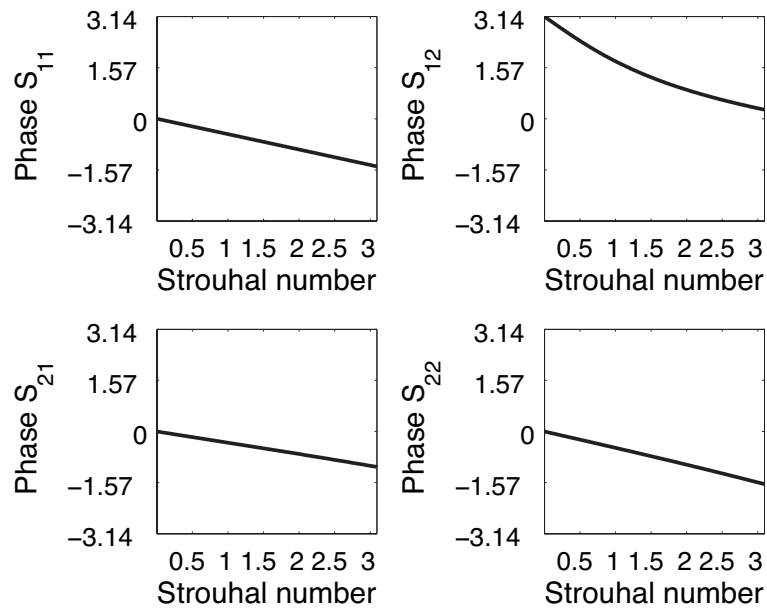


Figure 6.27: Scattering matrix of the axial swirler (phase)

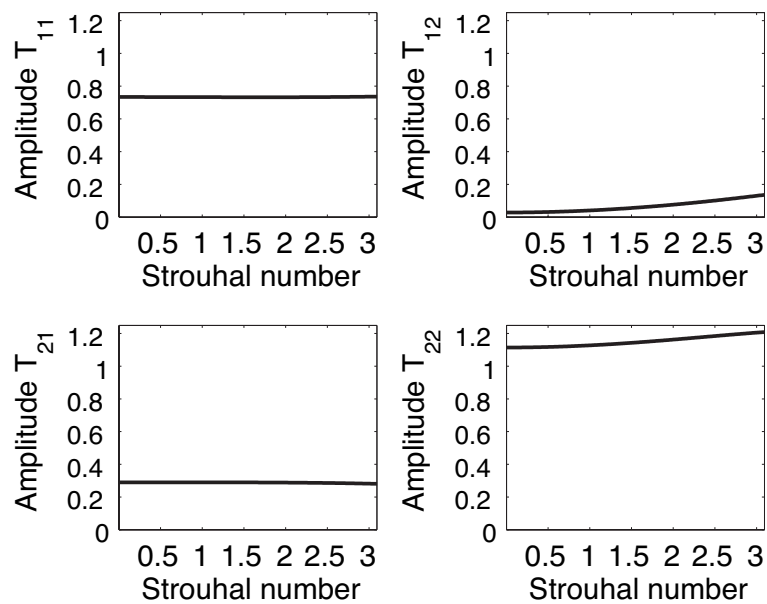


Figure 6.28: Transfer matrix $T_{fg,center}$ of the axial swirler (amplitude)

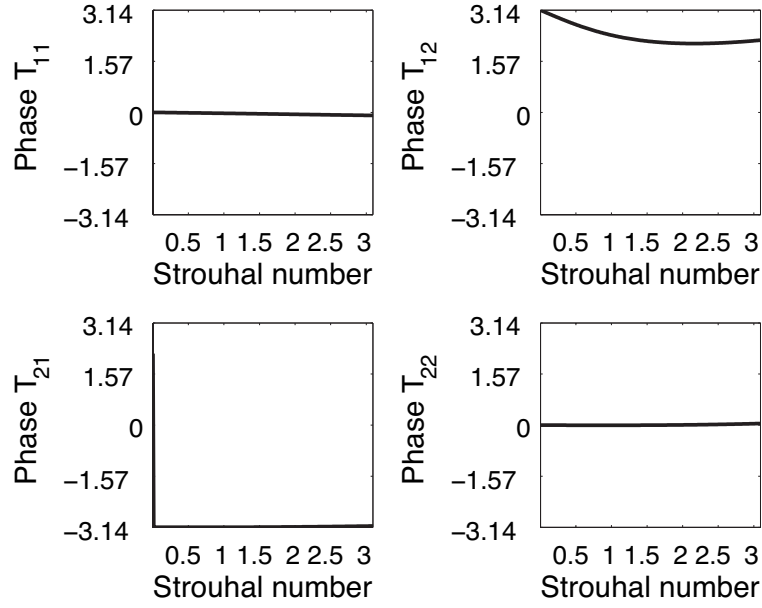


Figure 6.29: Transfer matrix $T_{fg\text{center}}$ of the axial swirler (phase)

represent the reflection of acoustic waves. The phase of S_{11} and S_{22} determines the time, which an acoustic wave needs to travel between the two export planes. The results show that the reflection of the downstream side is rather low. The reflection of the upstream side reaches a value of over 20%. The acoustic waves are also slightly damped as they pass the swirler. The reflections of the swirler indicate that the acoustic characteristics are comparable to the one of an area change. This comparison seems to be quite reasonable as the area of the swirler passage, which is perpendicular to the blades, is smaller than the inlet and outlet area. For the acoustic network model, the scattering matrix has to be transformed into a transfer matrix described by f and g (see appendix A.1). In addition, the acoustic characteristics between the two export planes obtained are exchanged by a description, which is related to the axial center of the swirler. This is done in changing the phase of the matrix elements, which is equivalent to the subtraction of two ducts with a specific length from both sides:

$$T_{fg\text{center}} = \begin{bmatrix} e^{-ik_+L_d} & 0 \\ 0 & e^{-ik_-L_d} \end{bmatrix}^{-1} T_{fg} \begin{bmatrix} e^{-ik_+L_u} & 0 \\ 0 & e^{-ik_-L_u} \end{bmatrix}^{-1}. \quad (6.7)$$

The length of the ducts are the distances from the upstream plane and from the downstream plane to the center and are equal to $L_u = 0.02$ m and $L_d = 0.035$ m, respectively. The resulting transfer matrix $T_{fg\text{center}}$ is represented in Fig. 6.28 and 6.29

7 Acoustic analysis

Once the acoustic characteristics of the flame dynamics and the axial swirler are determined with the CFD/SI method, an acoustic network model of the combustion configuration can be set up. The setup of the model is part of the next section. With the network model the impact of the acoustic impedance on the thermo-acoustic stability is analyzed. Furthermore, it is shown how the location of the fuel injection nozzles influences the acoustics of the entire system, followed by the investigation of the impact of multiple fuel injection stages. From the results obtained, design guidelines are derived.

7.1 Setup of the acoustic network model

The acoustic network model consists of the plenum, the mixing section, the fuel supply, the axial swirler and the combustion chamber. The acoustic characteristics of the combustor parts, like plenum or fuel supply, are represented by acoustic elements, e.g. acoustic boundary conditions, simple ducts, area changes and "T-junctions". The analytic relations of the acoustic elements were derived in chapter 3.3. The flame dynamics obtained by CFD/SI is implemented using the practical premixed flame element (chapter 3.3). The acoustic characteristics of the axial swirler are represented by a transfer matrix, which was also determined by CFD/SI as shown in chapter 6.4. As in the numerical analysis, two basic configurations are considered with two and three fuel injection stages, respectively. They are denoted again as case A and B. The structure of the acoustic network model of the combustion test rig with two fuel injection stages is presented in Fig. 7.1. Here, the names, e.g. "Plenum", "AC I", "Mixing section I" are the names of the individual elements of the combustor network model, whereas their colors (see legend in Fig. 7.1) define the types of the acoustic elements, e.g. simple duct, area change, etc. The network

model of the configuration containing three fuel supply stages is built up in a similar way with an additional "T-junction" and fuel injection stage as shown in appendix A.3.

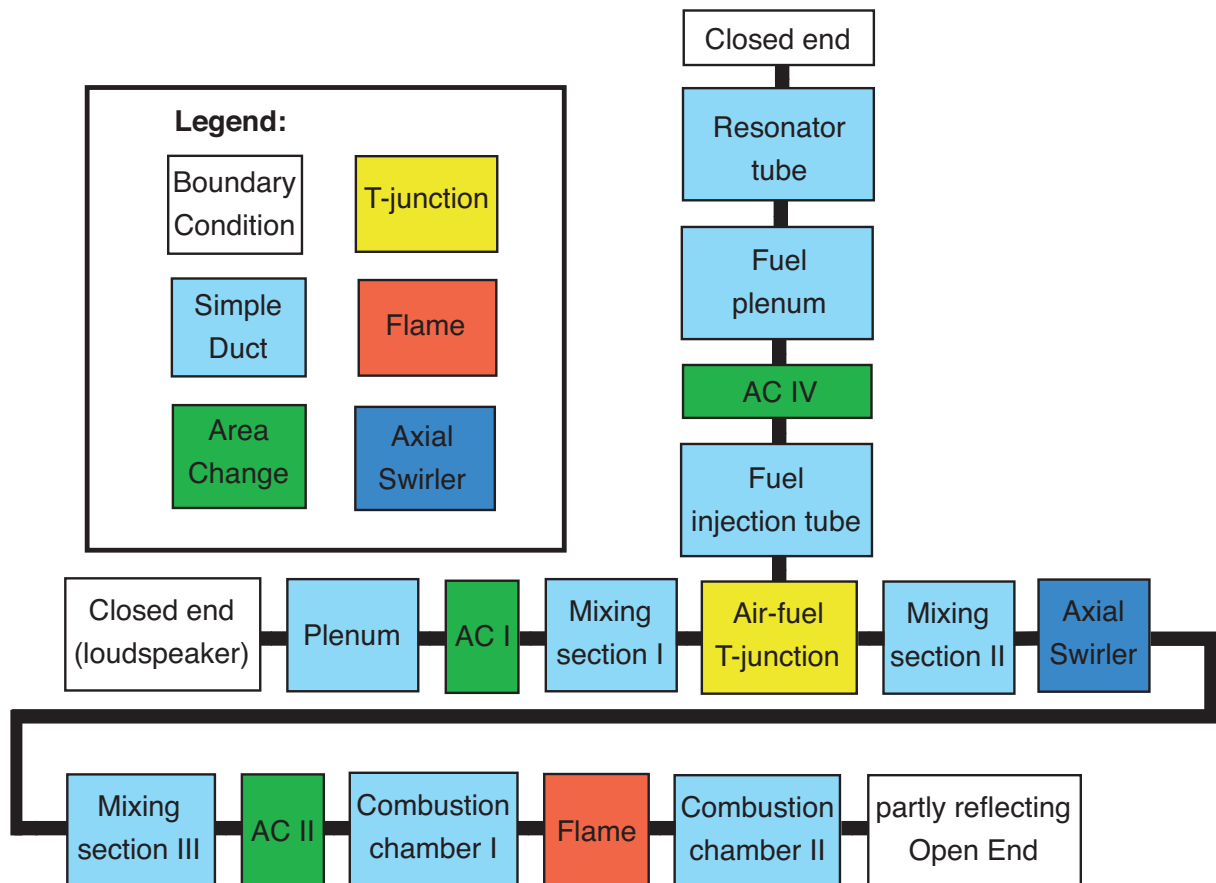


Figure 7.1: Sketch of the acoustic network model of the combustion test rig with two fuel injection stages (configuration A)

The fuel supply stage including the fuel injection tubes, the fuel plenum and the resonator tube are substituted by a simplified model to reduce the computational effort associated with the search routine to find the complex eigenfrequencies of the system. Because only plane waves can travel through the combustion system in the frequency range considered, all fuel injection holes face the same acoustic conditions. Therefore, they are combined into one injection slot for simplicity. In addition, the fuel plenum and the resonator tube,

which have the same cross-section, are merged into one duct. Finally the network model of the fuel injection stage contains a "Closed end", a simple duct representing the "Resonator tube" and "Fuel plenum", an area change ("AC IV") between fuel plenum and the "Fuel injection tube" (simple duct), which is connected by the "Air-fuel T-junction" ("T-junction") to the mixing section of the combustor. To estimate the error, which is made with the simplified model, a finite element-based acoustic model was set up using the commercial software package COMSOL. The model consists of the fuel injector including the single injection tubes. An open end boundary condition ($p' = 0$) is used as the termination on the injection tube side. The opposite side, the resonator end, is realized as a rigid wall ($u' = 0$). The length of the resonator tube was set exemplarily to $L_R = 0.3$ m. As the finite element method solves the homogeneous wave equation, mean flow effects and pressure losses are not considered. Fig. 7.2 shows the first two eigenmodes of the fuel injector. The scale of the legend is arbitrary and indicates the maximum and minimum pressure fluctuations. The first eigenmode of the finite element model exhibits nearly a $\lambda/4$ mode, whereas the second one approximates a $3\lambda/4$ eigenmode. The overall length corresponding to the $\lambda/4$ modes can be composed of the geometrical length of the resonator and half of the circumference of the fuel plenum. The acoustic field inside the fuel plenum ring is almost constant. The acoustic characteristics of the fuel supply changes with increasing frequency as the acoustics of the fuel plenum becomes more complex. This is shown in table 7.1, in which the eigenfrequencies of the finite element-based model are compared against the simplified network model with and without the effect of mean flow and pressure losses. Here and in the following, the eigenfrequencies are normalized with the Strouhal number, where the reference speed is the mean axial velocity in the mixing section of case A. In the network model the length of the fuel supply tube was set to $L_R = 0.355$ m. This length is slightly less than the one considered above, but results in a more accurate match in terms of the first and second eigenfrequency. The mean flow and the pressure loss have in general only a small effect on the eigenfrequencies. The deviation of the first eigenfrequency between the network and finite element model is rather low. As mentioned before, the error increases as the frequency increases. Nevertheless, in the Strouhal range up to $Sr = 2$ the simplified net-

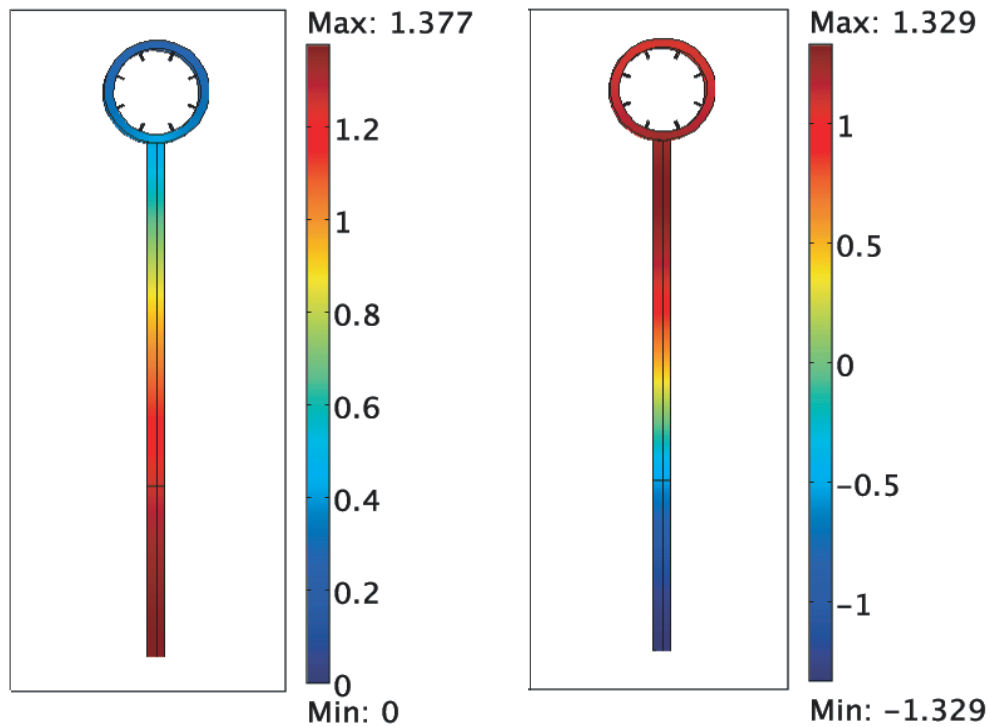


Figure 7.2: Finite element analysis of the fuel injection system (left: first eigenmode, right: second eigenmode)

work model represents the acoustic behavior of the fuel injector quite well. However, the impact of the acoustic impedance should be shown in general. Therefore, small deviations, like the ones presented, can be neglected. In the following L_R , as the length of the resonator tube, is exclusively taken as the length of the combined tube in the simplified network model.

The termination of the combustion chamber through which the hot products

Eigenfrequencies:	1st	2nd	3rd
Finite element-based model	0.61	1.71	2.62
Simplified network model w/o mean flow and pressure loss	0.59	1.79	2.99
Simplified network model with mean flow and pressure loss	0.57	1.75	2.98

Table 7.1: Eigenfrequencies of the finite element-based model and simplified network model of the fuel supply

leave the chamber into the atmosphere is acoustically described by a partly reflecting open end with a reflection coefficient of $R_f = 0.5$ [55]. The further combustion test rig elements are modeled according to their dimensions described in chapter 6.1 and Fig. 6.3. The acoustic behavior of the flame and the axial swirler are implemented using the identified time domain information in form of the unit impulse response. The UIR can be transformed in the real or complex frequency domain using Eqn. (5.5), which is repeated here for completeness:

$$F(\omega_{\text{real}}, \omega_{\text{im}}) = \sum_{k=0}^M h_k e^{-i(\omega_{\text{real}} + i\omega_{\text{im}})k\Delta t}. \quad (7.1)$$

In this way it is possible to use the eigenfrequency search method described in chapter 3.3.2. The main flow parameters of the acoustic network models, case A and case B, can be found in appendix A.3.

7.2 Acoustic network model results

With the acoustic network models of the two combustion configurations, the impact of acoustic impedance, fuel injection location and fuel staging on the thermo-acoustic stability of the entire combustion system can be analyzed in detail. The eigenfrequencies and thereby the linear stability of the eigenmodes are determined as the roots of the determinant of the system matrix. To gain further insight into the complex system, frequency responses of the acoustic variables to a velocity excitation (loudspeaker) at the plenum are calculated in solving the inhomogeneous matrix equation. The excitation amplitude was set to 10%. Both methods are described in more detail in chapter 3.3.2. The three different design options influence predominantly the amplitude of the heat release rate fluctuations and the phase relationship between fluctuations of pressure and heat release rate (see also the discussion in chapter 1.2). The parameters, which are affected, can therefore be found in the relation, which describes the heat release rate fluctuations (see also Eqn. (2.11)):

$$\frac{\dot{Q}'(\omega)}{\bar{Q}} = F_u(\omega) \frac{u'_b(\omega)}{\bar{u}_b} + \sum_{k=1}^N F_{\phi,k} \frac{\phi'_k(\omega)}{\bar{\phi}}$$

$$= F_u(\omega) \frac{u'_b(\omega)}{\bar{u}_b} + \sum_{i=1}^N F_{\phi,i}(\omega) \left(\frac{u'_{F,i}(\omega)}{\bar{u}_{F,i}} - \frac{u'_{A,i}(\omega)}{\bar{u}_{A,i}} \right) \frac{\bar{m}_{F,i}}{\sum_{i=1}^N \bar{m}_{F,i}}. \quad (7.2)$$

This equation is used in the next sections to explain and emphasize the various interdependencies between the acoustic variables and the heat release rate. Figure 7.3 clarifies the acoustic variables and main parameters, which are used in the analysis.

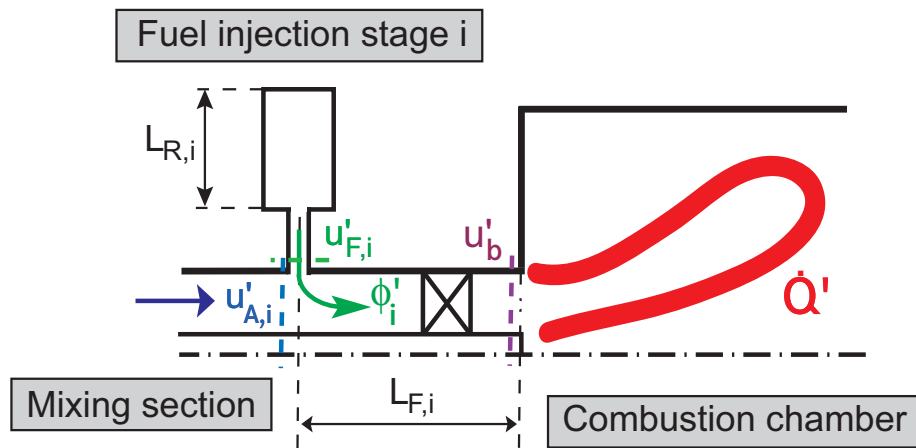


Figure 7.3: Acoustic variables and main parameters used in the acoustic analysis

The design proposals and results derived are based on the operating condition (see chapter 6.1) at which the flame transfer functions were determined. The results are therefore only valid at and close to these conditions. To analyze operating conditions far off the current one, additional flame transfer functions are required. However, the basic design guidelines are independent of the design.

7.2.1 Impact of the fuel injection stage impedance

The acoustic impedance and the eigenfrequencies of the fuel injection stage are changed in adjusting the length of the resonator tube $L_{R,i}$, which is mounted on the fuel plenum as described in the previous section. The fuel

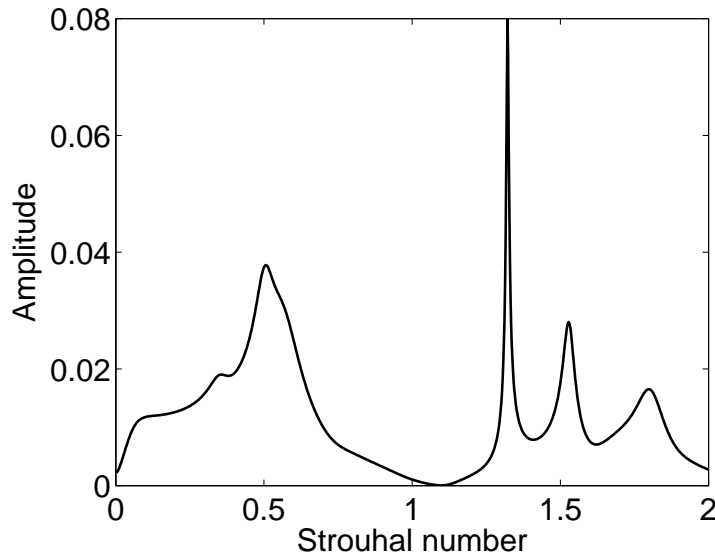


Figure 7.4: Amplitude and phase of the velocity fluctuations u'_F in the fuel line of an acoustically coupled fuel injector ($\zeta = 0.2$) with resonator length $L_R = 0.42$ m

injection stage exhibits nearly the acoustic characteristics of a $\lambda/4$ tube. The amplitude of the velocity fluctuations at the injector nozzle i , $u'_{F,i}$, reaches therefore a maximum around the eigenfrequencies of the fuel supply system. This fact can be exploited to modify the fluctuations of the fuel mass flow and thus the fluctuations of equivalence ratio. Between two eigenfrequencies the amplitude of $u'_{F,i}$ is minimized. In that case the fuel supply has no active influence – the equivalence ratio fluctuations are mainly driven by the acoustics of the mixing section. An example of the amplitude of u'_F is shown in Fig. 7.4 for a coupled fuel injection stage with resonator length $L_R = 0.42$ m. The eigenfrequencies of the fuel injection stage are around $Sr = 0.5$ and $Sr = 1.5$. As the fuel injector is coupled acoustically to the combustion system, the influence of the combustor acoustics can also be seen in the region of the second eigenfrequency around $Sr = 1.3$ and $Sr = 1.8$.

The effect of the fuel supply impedance on the system stability was already described with a similar setup of the fuel injector by Richards et al. [106]. They demonstrated that a change in the acoustic impedance of the fuel sup-

ply could change the phase and amplitude of the equivalence ratio fluctuations. In their study the phase of the equivalence ratio fluctuations modified the phase relationship between pressure and heat release rate fluctuations and led finally to a significant reduction of pressure oscillations. This can also be confirmed by the considerations derived above: As the the amplitude and phase of the velocity fluctuations in the fuel line $u'_{F,i}$ is directly driven by the impedance of the fuel injection stage i , it follows from

$$\frac{\phi'_i(\omega)}{\bar{\phi}} \sim \left(\frac{u'_{F,i}(\omega)}{\bar{u}_{F,i}} - \frac{u'_{A,i}(\omega)}{\bar{u}_{A,i}} \right), \quad (7.3)$$

that the amplitude and phase of the equivalence ratio is also modified. If now the phase change is sufficient to influence the phase of the heat release rate fluctuations (see Eqn. (7.2)) in such a way that the heat release rate fluctuations and the acoustic pressure at the flame are out of phase, the system becomes stable.

Scarinci et. al. [116] suggested that minimizing the overall amplitude of equivalence ratio fluctuations can be useful to reduce the heat release rate fluctuations and thus to realize a low-oscillation combustion chamber. They developed a new mixing strategy, which is based on multiple injection stages injecting air instead of fuel. In this way the fuel-air mixing process is decoupled from pressure pulsations in the combustion chamber as the local equivalence ratio fluctuations are damped on the way through the premixer. In the present context using fuel injection stages a reduction of heat release rate fluctuations can be achieved in changing the velocity fluctuation $u'_{F,i}$ such that it is in phase with $u'_{A,i}$. If both fluctuations have the same amplitude the resulting equivalence ratio fluctuations are reduced to zero:

$$\frac{\phi'_i(\omega)}{\bar{\phi}} \sim \left(\frac{u'_{F,i}(\omega)}{\bar{u}_{F,i}} - \frac{u'_{A,i}(\omega)}{\bar{u}_{A,i}} \right) \rightarrow 0. \quad (7.4)$$

The consequence is a reduction of heat release rate fluctuations. The reduction leads to a decrease in growth rate and results therefore in a more stable system.

Both studies mentioned have shown that influencing the equivalence ratio

fluctuations can lead to lower thermo-acoustic oscillations in combustion systems. However, the models derived only account for the impact of equivalence fluctuations on the heat release rate. As the heat release rate fluctuation in a practical premixed system is also driven by the kinematic response of the flame, tuning of the amplitude and phase of equivalence ratio fluctuations alone will in general not be sufficient to achieve a stable system. In the worst case it may lead also to a more unstable system, which is explained in the following.

Taking into account both contributions ($F_u u'_b / \bar{u}_b$, $F_{\phi,i} \phi'_i / \bar{\phi}$) to fluctuations of heat release rate, a reduction of the heat release rate fluctuation can also be achieved if the phase difference between both equals π . This implies that both contributions are out of phase with respect to each other and lead to a destructive interference:

$$F_u(\omega) \frac{u'_b(\omega)}{\bar{u}_b} + F_{\phi,i}(\omega) \frac{\phi'_i(\omega)}{\bar{\phi}} \rightarrow 0. \quad (7.5)$$

The superposition of both contributions equals zero if the corresponding amplitudes have the same order of magnitude. Returning to the argument above, such a constellation would be affected in a negative way if the amplitude of the equivalence ratio fluctuations is reduced. The result would be an undesired increase of the heat release rate fluctuations.

To analyze the conceptual considerations the combustion configuration A is used in the following, in which the fuel supply is located, as in the CFD simulation, 0.125 m upstream the burner exit. In the baseline configuration the pressure loss coefficient between fuel injection tube and mixing section is set to a large value ($\zeta \gg 1$) to decouple the acoustic field of the fuel supply from the remaining system. The stability map ($\det(S(\omega))$) of the baseline configuration is shown in Fig. 7.5 in the range of $Sr = [0 \ 2]$. The ordinate is plotted using the cycle increment $CI - 1$. The figure includes all possible stable or unstable eigenfrequencies of the system in the frequency range considered. The stability border is marked as a solid line with $CI - 1 = 0$. As discussed in chapter 3.3.2 a value below zero corresponds to a stable eigenfrequency, whereas a value greater zero indicates an acoustically unstable system.

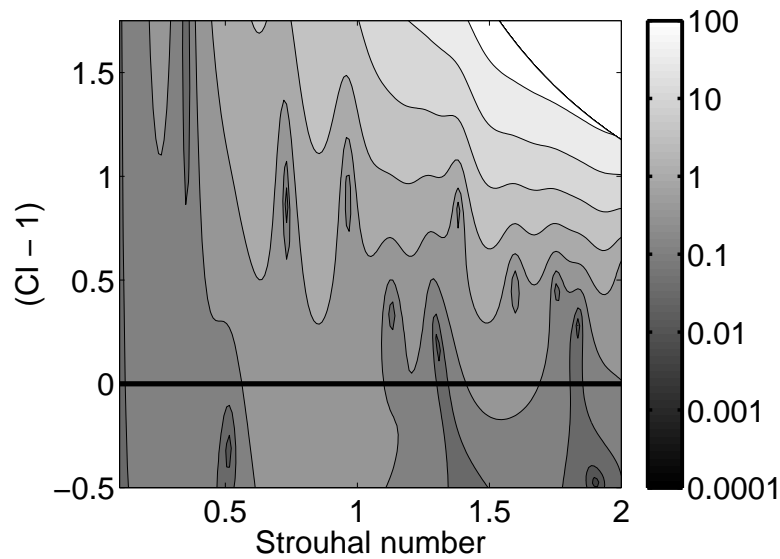


Figure 7.5: Stability map of the baseline configuration, case A with acoustically decoupled fuel supply ($\zeta \gg 1$)

In the following three eigenfrequencies of the baseline configuration are exemplarily analyzed in more detail: two unstable eigenmodes around $Sr = 1.13$ and $Sr = 1.32$ and one stable eigenmode at $Sr = 0.51$. The eigenfrequencies and their corresponding cycle increments can be found in Fig. 7.6. In tuning the impedance of the fuel injector it is demonstrated how the three eigenfrequencies can be influenced in applying the different approaches presented above. To acoustically couple the fuel injection stage to the combustion system the pressure loss coefficients are set in the following to zero between the fuel plenum and the injection tube and to 0.2 between the injection tube and the mixing section. The values are lower than the ones obtained by steady state CFD simulations. They are chosen to enhance the demonstration of the stabilizing potential of the tuned fuel injector impedances ¹.

In the first example the combined length of the resonator tube and the fuel

¹The values obtained by CFD are in some demonstration cases too high to realize a stable combustion system. A reduction of the pressure loss can be realized, for example, in using injection holes with a higher diameter. The resulting lower fuel velocity leads to a lower impulse of the fuel, which can lead to lower mixing qualities. To obtain similar mixing qualities the fuel has to be injected closer to the middle of the mixing section, e.g. by extending the injection tubes into the mixing section.

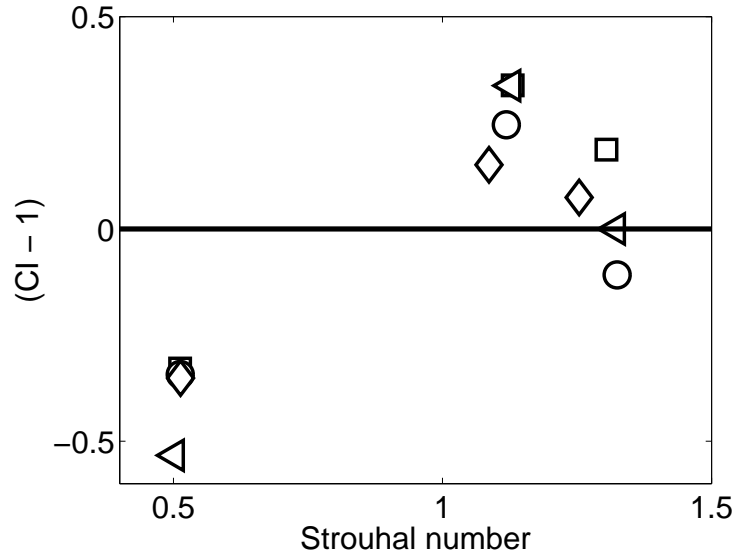


Figure 7.6: Influence of the injector impedance on the eigenfrequencies and cycle increments – comparison between baseline configuration ($\zeta \gg 1$) (\square) and configurations with resonator length $L_{R,2} = 0.12$ m (\circ), $L_{R,2} = 0.42$ m (\triangleleft), and $L_{R,2} = 0.18$ m (\diamond)

plenum is set to $L_{R,2} = 0.12$ m. The corresponding eigenfrequency of this fuel injection stage affects mainly the eigenfrequency at $Sr = 1.32$ of the baseline configuration. Here, the phase of the equivalence ratio fluctuations ϕ'_2 at the fuel injection stage is shifted by nearly π . In addition also the phase of the velocity fluctuations at the burner mouth u'_b is changed. Both are shown in Fig. 7.7. In consequence the phase of the heat release rate contributions $F_{\phi,2} \phi'_2 / \bar{\phi}$ and $F_u u'_b / \bar{u}_b$ and thus of the heat release rate fluctuations are changed by about 1.1π , see Fig. 7.8. This change leads to a favorable phase relationship between pressure fluctuations and heat release rate fluctuations and turns finally the unstable eigenfrequency ($CI - 1 = 0.19$) into a stable one ($CI - 1 = -0.1$). The amplitude of the equivalence ratio fluctuation, however, is increased by the increase of the fuel velocity fluctuation $u'_{F,2}$ and the fact that $u'_{F,2}$ and the velocity of the main stream $u'_{A,2}$ are out of phase, see Fig. 7.9 and Fig. 7.10. Here and in the following all amplitudes are normalized with their mean values. Higher equivalence ratio fluctuations increase the amplitude of the heat release rate contribution $F_{\phi,2} \phi'_2 / \bar{\phi}$. The amplitude of the heat release

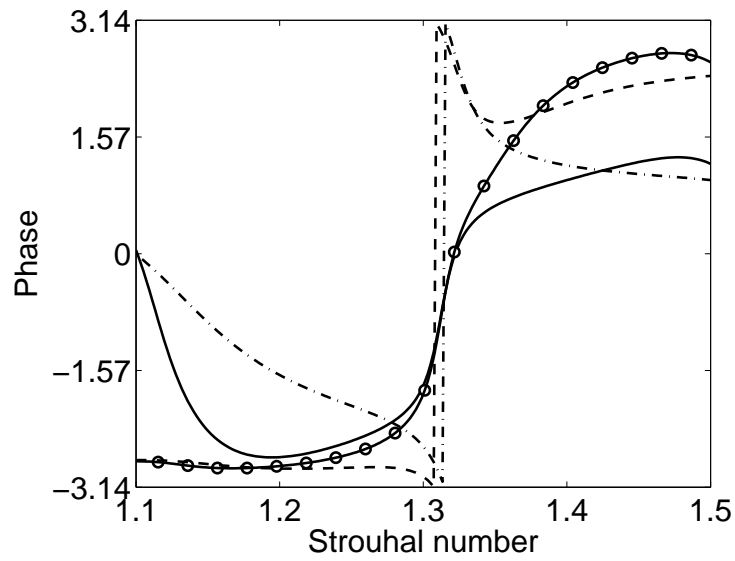


Figure 7.7: Phase of equivalence ratio and velocity fluctuations at the burner mouth of the baseline configuration ($\zeta \gg 1$) ($-- \phi'_2, -- u'_b$) and configuration with resonator length $L_{R,2} = 0.12$ m ($— \phi'_2, -\circ u'_b$)

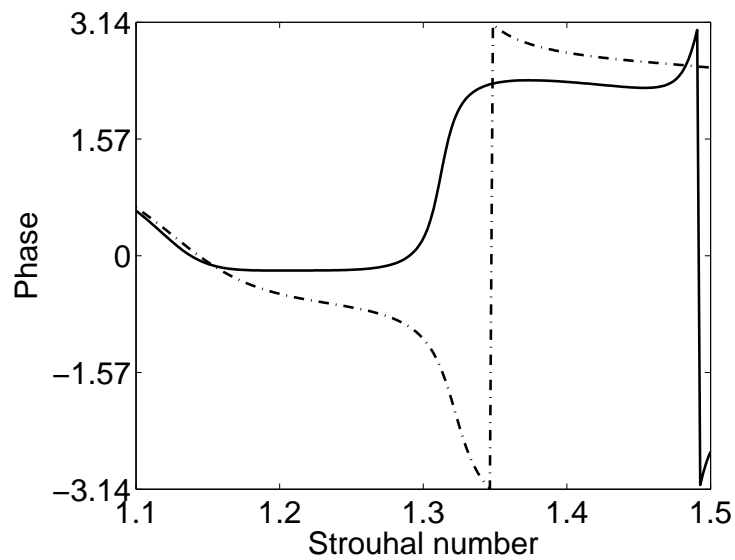


Figure 7.8: Phase of the heat release rate fluctuations \dot{Q}'/\bar{Q} of the baseline configuration ($\zeta \gg 1$) ($--$) and configuration with resonator length $L_{R,2} = 0.12$ m ($—$)

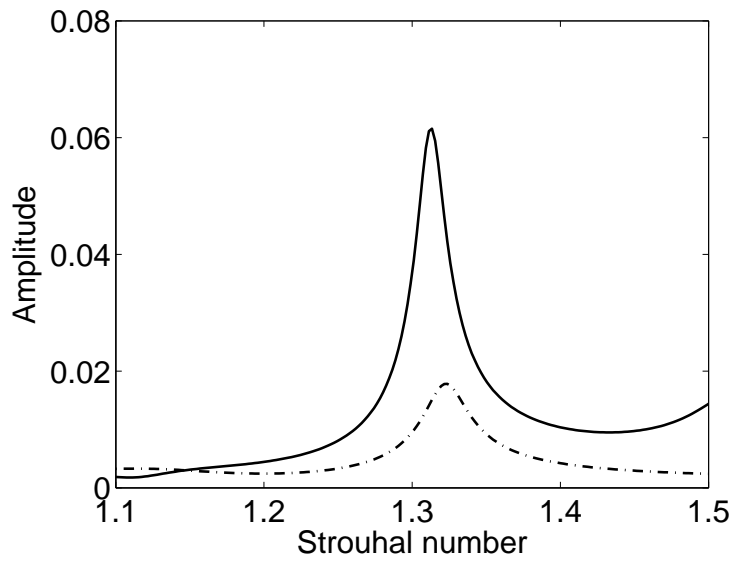


Figure 7.9: Amplitude of the equivalence ratio fluctuations ϕ'_2 of the baseline configuration ($\zeta \gg 1$) (---) and configuration with resonator length $L_{R,2} = 0.12$ m (—)

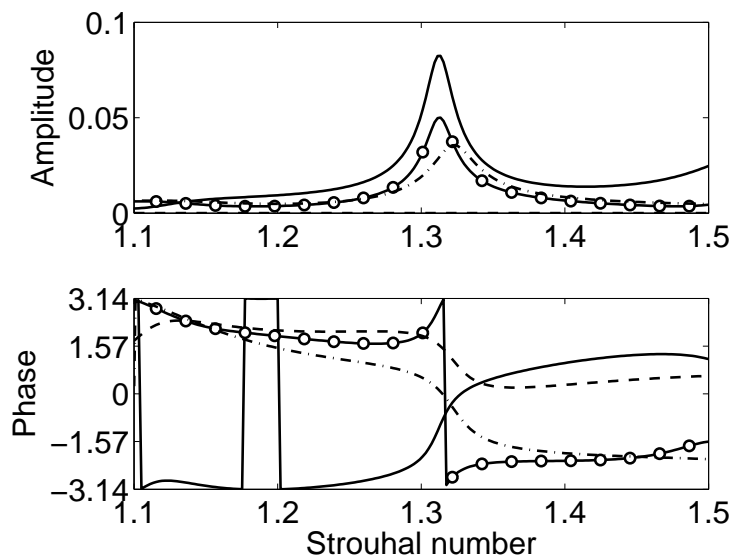


Figure 7.10: Velocity fluctuations at the fuel injection location of baseline configuration ($\zeta \gg 1$) (--- $u'_{A,2}$, -- $u'_{F,2}$) and configuration with resonator length $L_{R,2} = 0.12$ m (-o $u'_{A,2}$, — $u'_{F,2}$)

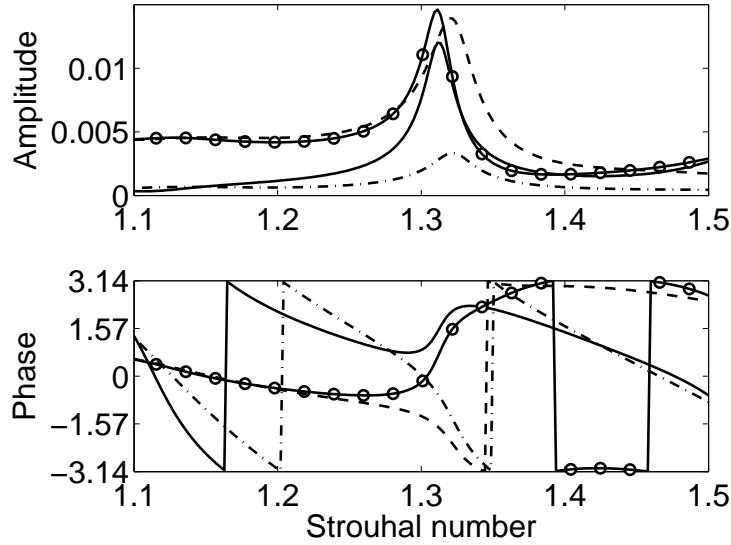


Figure 7.11: Amplitude and phase of heat release rate contributions of the baseline configuration ($\zeta \gg 1$) ($\cdots F_{\phi,2} \phi'_2 / \bar{\phi}$, $\cdots F_u u'_b / \bar{u}_b$) and configuration with resonator length $L_{R,2} = 0.12$ m ($\circ F_{\phi,2} \phi'_2 / \bar{\phi}$, $\circ F_u u'_b / \bar{u}_b$)

rate fluctuations is also increased as the heat release rate contributions are almost in phase, which is presented in Fig. 7.11. As the heat release rate fluctuations and the pressure fluctuations are certainly out of phase, the increase could even strengthen the stabilizing effect. The observations confirm the fact that the main driving parameter is the phase of the equivalence ratio fluctuations, which influences the phase of the heat release rate fluctuations and thus the stability of the system. The amplitude of the equivalence ratio fluctuations, however, determines the absolute value of the cycle increment.

A length of the resonator tube of $L_{R,2} = 0.42$ m results in a reduction of equivalence ratio fluctuations ϕ'_2 at a Strouhal number of about $Sr = 0.51$. At this frequency the amplitude of the fuel velocity fluctuation $u'_{F,2}$ is increased. Compared to the last case the phase difference between $u'_{F,2}$ and the velocity fluctuation of the main stream $u'_{A,2}$ is now roughly zero as it is demonstrated in Fig. 7.12.

As both velocity fluctuations have almost the same amplitude at this fre-

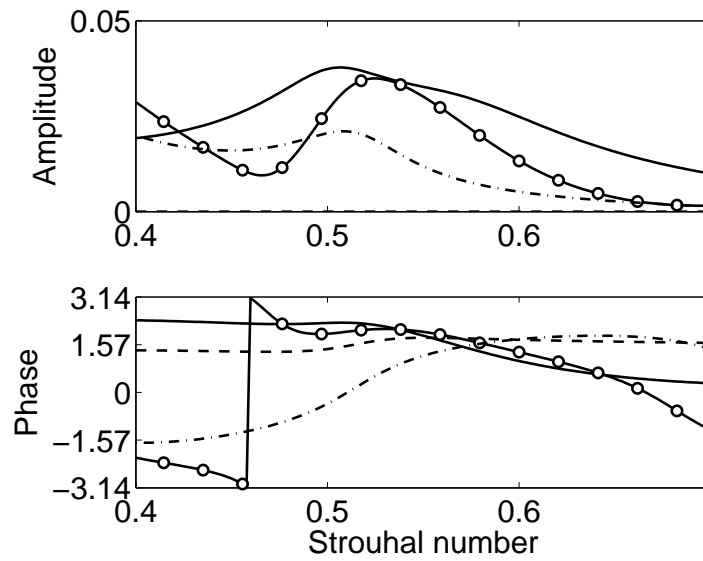


Figure 7.12: Velocity fluctuations at the fuel injection location of the baseline configuration ($\zeta \gg 1$) ($\cdots u'_{A,2}$, $\cdots u'_{F,2}$) and configuration with resonator length $L_{R,2} = 0.42$ m ($\circ u'_{A,2}$, $— u'_{F,2}$)

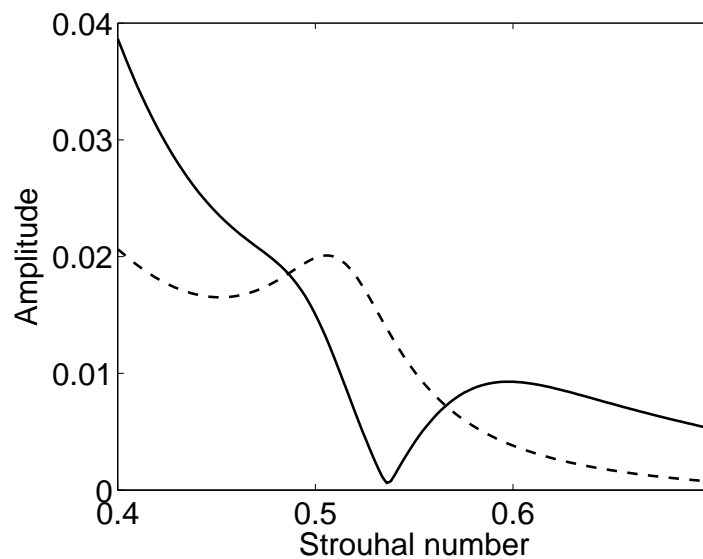


Figure 7.13: Heat release rate fluctuations caused by equivalence ratio fluctuations ($F_{\phi,2} \phi'_2 / \bar{\phi}$) of the baseline configuration ($\zeta \gg 1$) (\cdots) and configuration with resonator length $L_{R,2} = 0.42$ m ($—$)

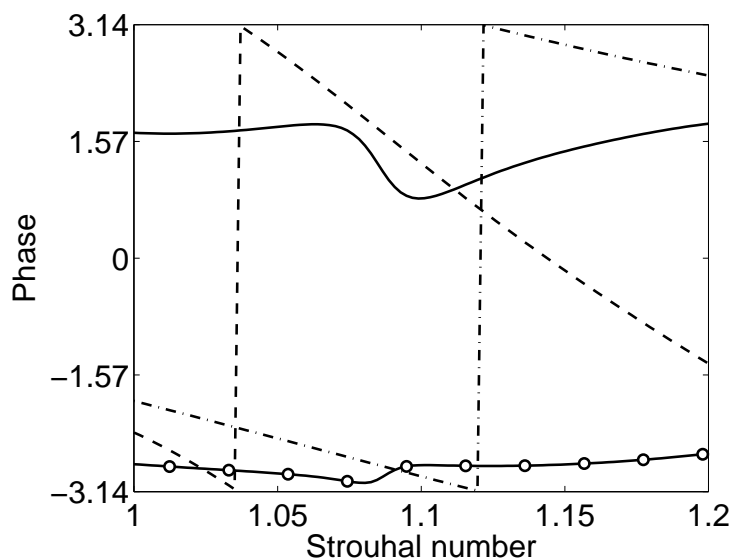


Figure 7.14: Phase of the flame transfer functions and their corresponding fluctuating variables of configuration with resonator length $L_{R,2} = 0.18$ m (— ϕ' , -○ u'_b , -- $F_{\phi,2}$, ·· F_u)

quency, the equivalence ratio fluctuations vanish almost completely. The resulting heat release fluctuation caused by the equivalence ratio fluctuation, which is shown in Fig. 7.13, decreases strongly leading to a lower cycle increment (from $CI - 1 = -0.33$ to $CI - 1 = -0.54$) and thus to a more stable system.

To demonstrate the possibility where the contributions ($F_u u'_b / \bar{u}_b$, $F_{\phi,2} \phi'_2 / \bar{\phi}$) to fluctuations of heat release rate are out of phase the length of the resonator is set to $L_{R,2} = 0.18$ m. At $Sr = 1.08$ the flame transfer functions and the corresponding fluctuating variable $F_{\phi,2}$ and ϕ'_2 as well as F_u and u'_b are almost in phase at $\pi/2$ and π , which is shown in Fig. 7.14. The sum of the two phases² is equal to π and 2π . Using a pressure loss value of $\zeta = 0.1$ between the injection tube and the mixing section both heat release rate contributions have, at this frequency, roughly the same amplitude (see Fig. 7.15). As discussed above this finally leads to a destructive interference of the heat release rate contributions. For the chosen pressure loss value a reduction in total heat release rate fluctuations of 75% can be achieved as shown in Fig. 7.16. As the phase of the

² $A_1 \exp^{-i\varphi_1} \cdot A_2 \exp^{-i\varphi_2} = A_1 A_2 \exp^{-i(\varphi_1 + \varphi_2)}$

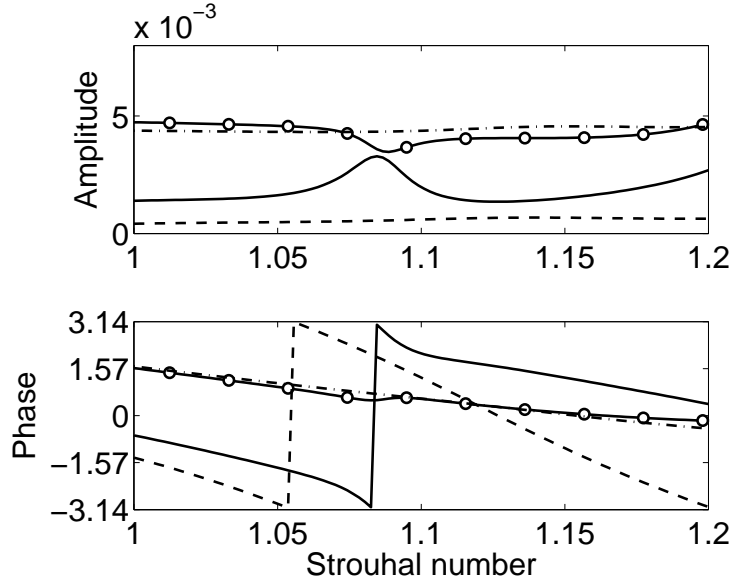


Figure 7.15: Contributions to heat release rate fluctuations of the baseline configuration ($\zeta \gg 1$) ($-- F_{\phi,2} \phi'_2 / \bar{\phi}$, $- \cdot F_u u'_b / \bar{u}'_b$) and configuration with resonator length $L_{R,2} = 0.18$ m ($— F_{\phi,2} \phi'_2 / \bar{\phi}$, $- \circ F_u u'_b / \bar{u}'_b$)

heat release rate fluctuations is only changed slightly, the eigenfrequency is damped but remains unstable. Here, the cycle increment is finally decreased by almost 0.2 to $CI - 1 = 0.15$.

Another example of a destructive interference of the two heat release rate contributions can already be observed at the baseline configuration ($\zeta \gg 1$). At the unstable eigenfrequency at $Sr = 0.37$ (see Fig. 7.5) both flame transfer functions are in phase. In that case the equivalence ratio and the velocity fluctuations at the burner mouth have to be influenced in such a way that their phase difference equals π . For the baseline configuration this is already the case as shown in Fig. 7.17 and Fig. 7.18. As in the last example the phase relationship between total heat release rate and pressure fluctuations is unfavorable. This is another good example that the phase relationship is the main key in influencing the stability of a system.

The analyzed cases confirm that the fuel injector impedance influences the acoustics of the entire system mainly in the range of eigenfrequencies of the

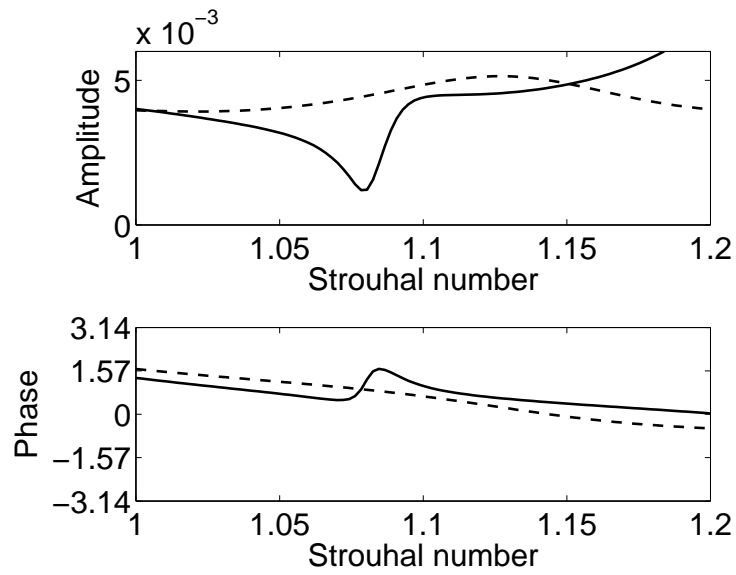


Figure 7.16: Heat release rate fluctuations \dot{Q}'/\bar{Q} of the baseline configuration ($\zeta \gg 1$) (---) and configuration with resonator length $L_{R,2} = 0.18$ m (—)

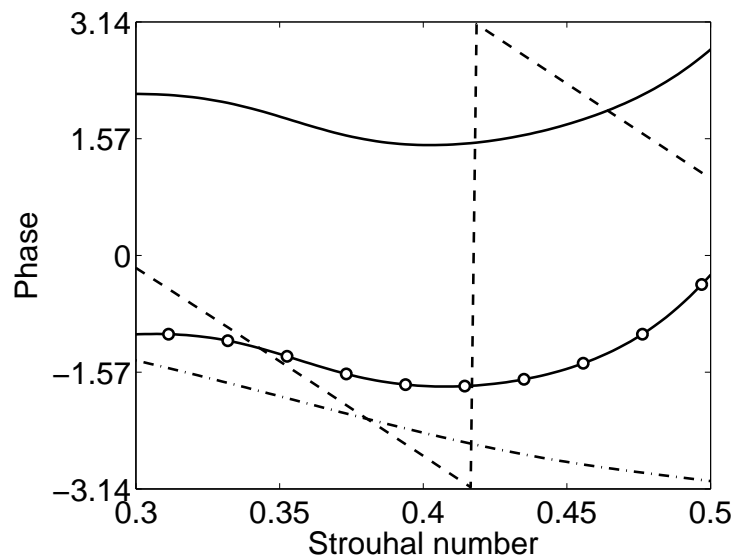


Figure 7.17: Phase of the flame transfer functions and their corresponding fluctuating variables of the baseline configuration ($\zeta \gg 1$) (— ϕ_2' , -o u_b' , -- $F_{\phi,2}$, ··· F_u)

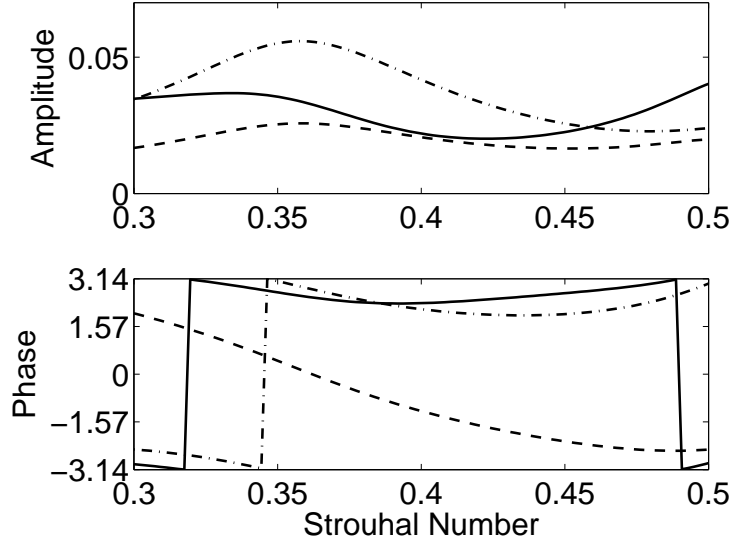


Figure 7.18: Contributions to heat release rate fluctuations and total heat release rate fluctuations of the baseline configuration ($\zeta \gg 1$) (--- $F_{\phi,2} \phi'_2 / \bar{\phi}$, -·- $F_u u'_b / \bar{u}'_b$, — \dot{Q}' / \bar{Q})

fuel injector (see subsection 7.1 and Fig. 7.6). The fuel injector with a resonator length of $L_{R,2} = 0.18$ acts at the first injector eigenfrequency near $Sr = 1.1$. The eigenfrequency of the system at $Sr = 0.51$ is, as expected, not affected. The configuration with a resonator length with $L_{R,2} = 0.42$ interacts with the system acoustics at the first and second injector eigenfrequency ($Sr = 0.51, 1.54$). The effect of the second injector eigenfrequency can also be observed at the eigenfrequency of the system at $Sr = 1.32$, where the cycle increment can be reduced to $CR - 1 = 0$. An exception is the fuel supply system with a resonator length of $L_{R,2} = 0.12$. Here, the frequency range of influence is quite wide, acting as well at the injector eigenfrequency at around $Sr = 1.56$ (not shown here) and at the eigenfrequencies of the system at $Sr = 1.08$ and $Sr = 1.32$.

Whereas the eigenfrequencies of the fuel supply can be changed by the length of the resonator tube, the strength of the influence of the fuel injection stage impedance on the system stability is mainly driven by the injector pressure loss. A lower pressure loss results in a higher impact on the system. This effect is demonstrated using the configuration with a resonator length of $L_{R,2} = 0.12$,

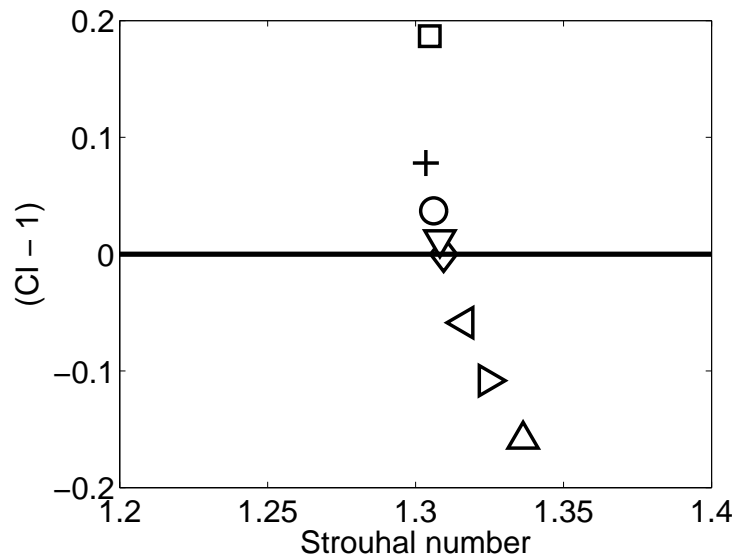


Figure 7.19: Influence of injector pressure loss ζ on eigenfrequencies and cycle increments of configuration with resonator length $L_{R,2} = 0.12$ m ($\zeta = 0.1$ Δ , $\zeta = 0.2$ \triangleright , $\zeta = 0.3$ \triangleleft , $\zeta = 0.4$ \diamond , $\zeta = 0.5$ ∇ , $\zeta = 0.6$ \circ , $\zeta = 0.84$ $+$, $\zeta \gg 1$ \square)

see Fig. 7.19. The pressure loss coefficient between the fuel injection tube and the mixing section is varied in the following between $\zeta = 0.1$ and $\zeta = 0.84$. The cycle increment changes for these cases from $CI - 1 = -0.16$ ($\zeta = 0.1$) to $CI - 1 = 0.078$ ($\zeta = 0.84$). The border between a stable eigenfrequency and the unstable one is reached near $\zeta = 0.4$. For comparison the cycle increment of the baseline configuration ($\zeta \gg 1$) is also shown in Fig. 7.19.

7.2.2 Impact of the fuel injection nozzle location

If the distance of the fuel injection location to the burner mouth can be adjusted within a certain range in the early design stage³, the fuel injection can be placed such that the acoustic stability of the combustion system is improved. The location of the fuel injection determines the time for convective

³Of course, considering the impact of the location in terms of auto-ignition or flash-back, mixing quality and NOx.

transport of the fuel from the injection point to the flame and thus the phase of the corresponding flame transfer function F_ϕ . Taking again the combustion configuration case A, the phase of $F_{\phi,2}$ can influence the phase of the overall heat release rate fluctuations as shown by the following equation:

$$\frac{\dot{Q}'(\omega)}{\bar{Q}} = F_u(\omega) \frac{u'_b(\omega)}{\bar{u}_b} + F_{\phi,2}(\omega) \frac{\phi'_2(\omega)}{\bar{\phi}}. \quad (7.6)$$

The impact of the location of the fuel injection nozzles is comparable to the impact of the fuel injector impedance. The distance between the fuel injection location and the flame replaces in this case the length of the resonator tube $L_{R,2}$ as the design variable. The different possibilities to change the stability of the entire system are the same as discussed and demonstrated before.

In the following the baseline configuration is the combustion system, case A, with the same flame response to velocity fluctuations F_u as before, but without the contributions due to the equivalence ratio fluctuations ($|F_{\phi,2}| = 0$). The fuel supply is acoustically decoupled from the combustion system ($\zeta \gg 1$). The corresponding stability map over the complex frequency plane is presented in Fig. 7.20.

Here, the two unstable eigenfrequencies at $Sr = 0.487$ and $Sr = 0.489$ will be influenced by placing the fuel injector to a favorable location. By reducing the distance between fuel injection location and flame to $L_{F,2} = 0.101$ the cycle increment of both eigenfrequencies can be reduced below zero. Compared to the basic configuration the two eigenfrequencies are shifted to a lower ($Sr = 0.41$) and higher ($Sr = 0.55$) frequency, respectively. The change in the fuel injection location corresponds to a mean time delay change of 1.25 ms compared to the configuration where the flame transfer function was originally determined (basic configuration: $L_{F,2} = 0.125$ m). The slope of the phase of the new flame transfer function is therefore adjusted to match the desired location. The amplitude is kept constant. Here, it is assumed that the slight change of the fuel injection position does not change the mixing process nor the flame, so that the new flame transfer function still represents the flame response correctly. The eigenfrequencies of the baseline configuration and the configuration with $L_{F,2} = 0.101$ can be found in Fig. 7.21. The stabilizing ef-

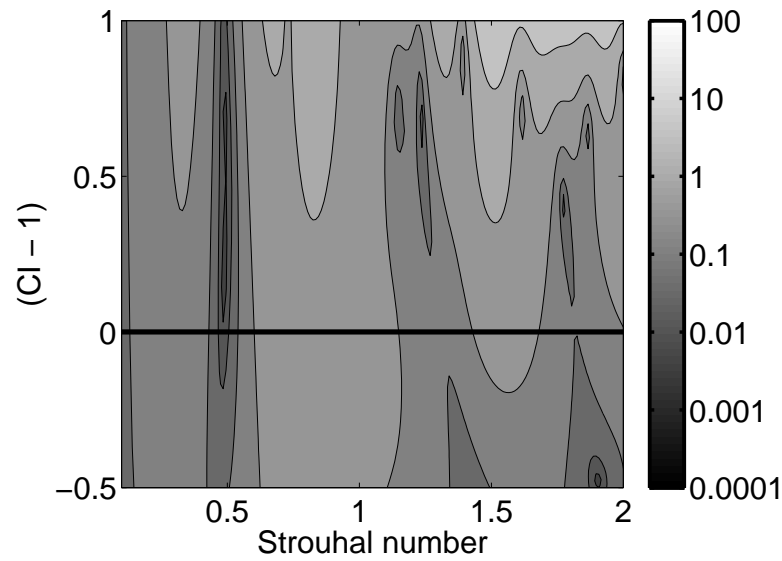


Figure 7.20: Stability map of the baseline configuration without equivalence ratio fluctuations (case A, $\zeta \gg 1$, $|F_{\phi,2}| = 0$)

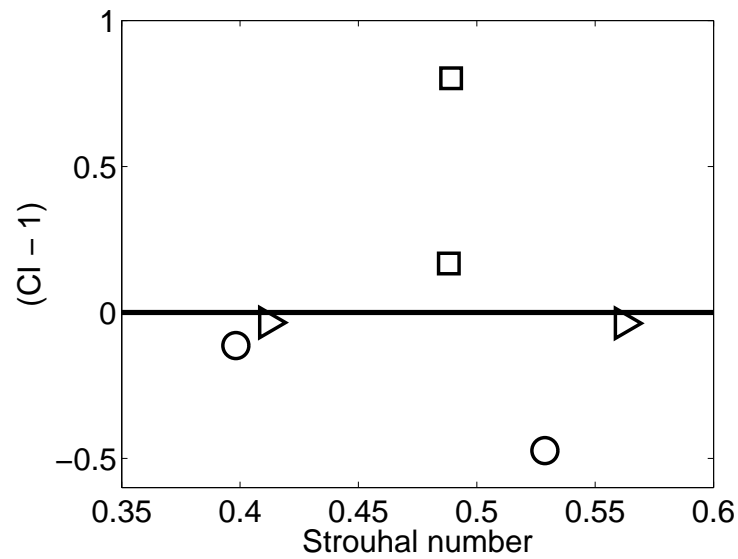


Figure 7.21: Influence of the injector location on the eigenfrequencies and cycle increments – comparison between baseline configuration ($\zeta \gg 1$, $|F_{\phi,2}| = 0$) (\square), and configuration with $L_{F,2} = 0.101$ m and decoupled ($\zeta \gg 1$) (\triangleright) and coupled fuel injection system ($L_{R,2} = 0.42$ m) (\circ)

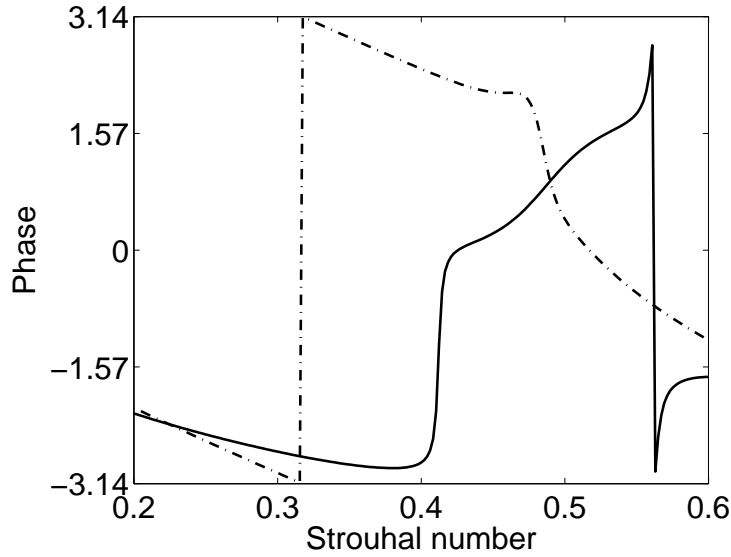


Figure 7.22: Phase of the heat release rate fluctuations \dot{Q}'/\bar{Q} of the baseline configuration ($\zeta \gg 1$, $|F_{\phi,2}| = 0$) (---) and configuration with injector location $L_{F,2} = 0.101$ m ($\zeta \gg 1$) (—)

fect is due to the changed phase of the heat release rate fluctuations in relation to the acoustic pressure at the flame. As demonstrated in Fig. 7.22 the phase of the heat release rate fluctuations is changed at both eigenfrequencies ($Sr = 0.41, 0.55$) by about π . To further decrease the cycle increment of the two eigenfrequencies of the new configuration, which are close to the stability limit, the fuel supply was coupled to the system in setting the pressure loss coefficient between the fuel injection tube and the mixing section as in the former analysis to $\zeta = 0.2$. The resonator tube was adjusted to a length of $L_{R,2} = 0.42$ m, which exhibits an eigenfrequency around $Sr = 0.5$. In this frequency range the phase of the heat release rate contribution due to equivalence ratio fluctuations ($F_{\phi,2} \phi'_2/\bar{\phi}$) is out of phase compared to the one due to velocity fluctuations at the burner mouth ($F_u u'_b/\bar{u}_b$). The destructive interference reduces strongly the overall heat release rate fluctuations \dot{Q}'/\bar{Q} especially near $Sr = 0.57$ as shown in Fig. 7.23. The stability of the system is further improved. As shown in Fig. 7.21 the cycle increment at the eigenfrequency at $Sr = 0.53$ is reduced from $C - 1 = -0.04$ to $C - 1 = -0.47$.

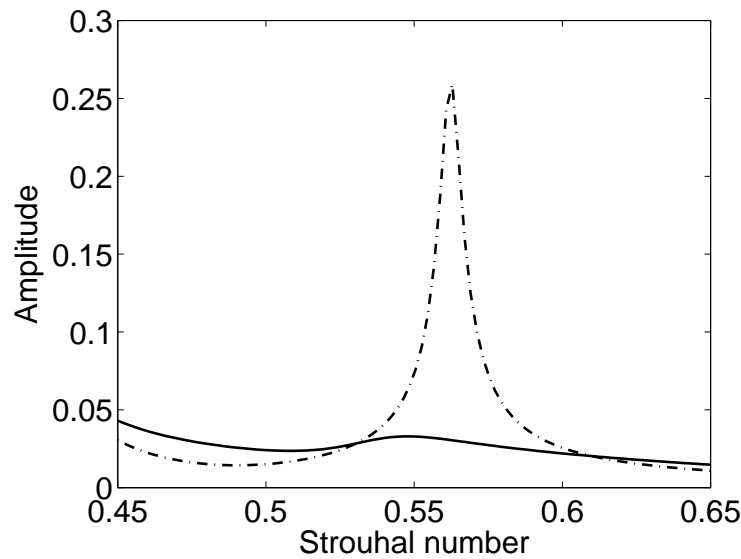


Figure 7.23: Amplitude of the heat release rate fluctuations \dot{Q}'/\bar{Q} of configuration with injector location $L_{F,2} = 0.101$ m with uncoupled ($\zeta \gg 1$) (---) and coupled injection system with $L_{R,2} = 0.42$ m (—)

7.2.3 Impact of fuel staging

According to the discussion in the last sections and to Eqn. (7.2) all possible options to reduce the heat release rate fluctuations and thus to enhance the thermo-acoustic stability of the entire combustion system have been mentioned. The opportunity of implementing a staged fuel supply, meaning that the fuel is injected at different locations, increases the number of degrees of freedom. Therefore, one has to be quite careful that an additional fuel injection stage, which is placed into the system, does not affect the overall stability in a negative way.

One case is demonstrated in the next section with the overall focus to design a combustion system with three fuel injection stages, which is stable over a wide range of frequencies. The basis is now configuration B with three different flame transfer functions as presented in chapter 6.3. The baseline configuration is the combustion system without the impact of the equivalence ratio flame transfer functions ($|F_{\phi,2} = 0|$, $|F_{\phi,3} = 0|$). Initially the fuel injector is, as in

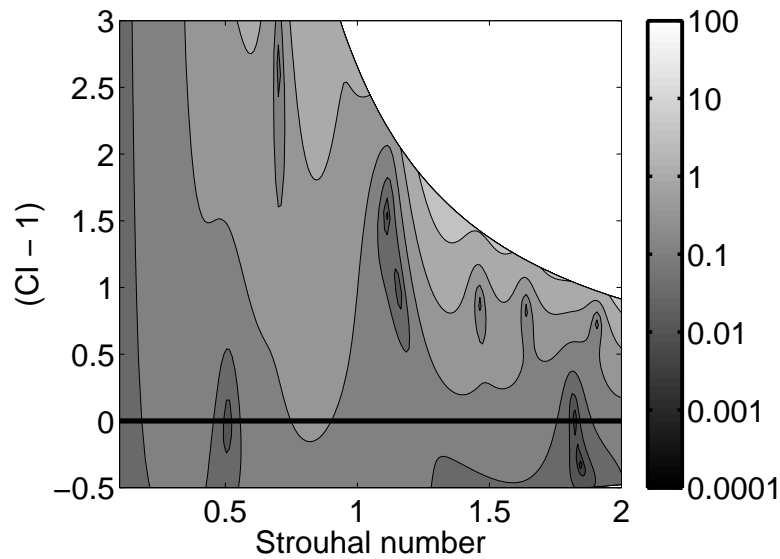


Figure 7.24: Stability map of the baseline configuration without equivalence ratio fluctuations (case B, $\zeta \gg 1$, $|F_{\phi,2}|, |F_{\phi,3}| = 0$)

the latter case, acoustically decoupled from the remaining combustion system ($\zeta \gg 1$). Starting from this point, the flame transfer functions of the individual fuel injection stages are implemented step by step. At the end the fuel supply impedance is adjusted to further optimize the acoustics of the entire system. The stability map of the baseline configuration is shown in Fig. 7.24.

The system contains mostly unstable eigenfrequencies in the frequency range analyzed except two modes at $Sr = 0.51$ and 1.8 , which are close to the stability limit. Similar to the last case the first unstable eigenmode can be damped in placing the downstream fuel injection stage at a favorable location. Here, L_{F3} was set to 0.0714 m upstream of the burner exit, which is again slightly downstream of the original CFD/SI location at $L_{F3} = 0.085$ m. Therefore the mean time delay of the corresponding flame transfer function was reduced by about 0.7 ms. In this case the impact of the second or upstream fuel injection still remains zero ($|F_{\phi,2}| = 0$). The result of this configuration can be found in Fig. 7.25, showing that the stability of almost all eigenfrequencies is improved. The cycle increment of the eigenfrequency at $Sr = 0.7$ was reduced from $CI - 1 = 2.7$ to a value slightly below zero and is now stable. Now the second fuel

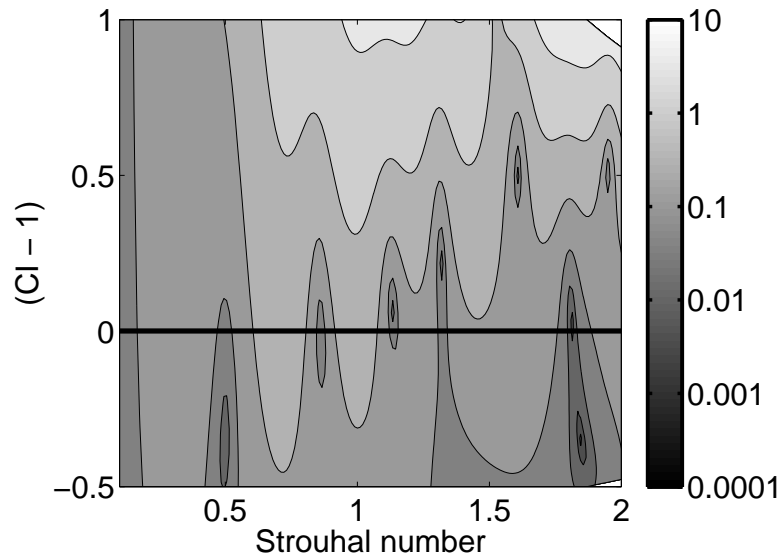


Figure 7.25: Stability map of the combustion configuration (case B) without equivalence ratio fluctuations at injector 2 ($\zeta \gg 1$, $|F_{\phi,2} = 0|$, $L_{F,3} = 0.0714$ m)

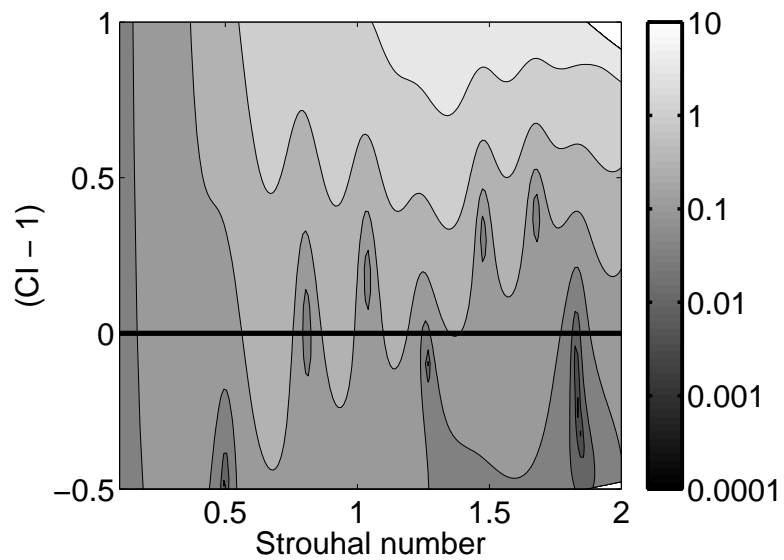


Figure 7.26: Stability map of the combustion configuration (case B) with acoustically uncoupled fuel injectors ($\zeta \gg 1$, $L_{F,2} = 0.132$ m, $L_{F,3} = 0.0714$ m)

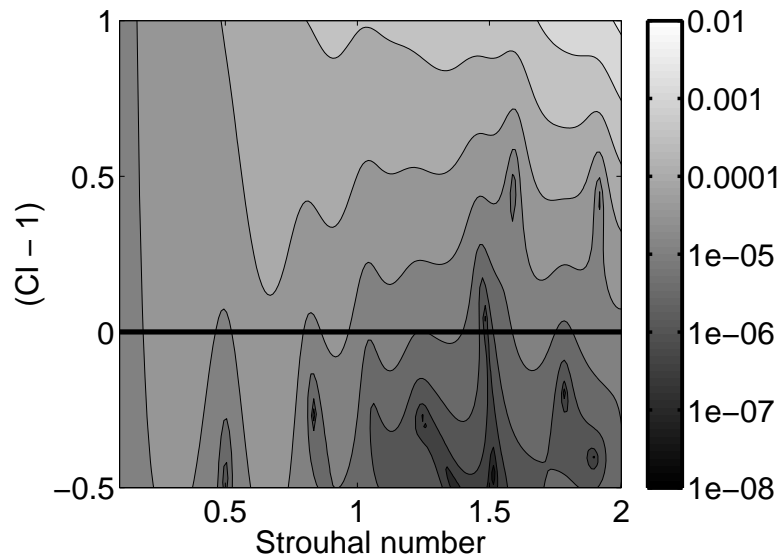


Figure 7.27: Stability map of the combustion configuration (case B) with acoustically coupled fuel injectors ($L_{F,2} = 0.132$ m, $L_{R,2} = 0.18$ m, $L_{F,3} = 0.0714$ m, $L_{R,3} = 0.12$ m)

injection is placed into the system. The distance was set according to the options mentioned to $L_{F,2} = 0.132$ m. The mean time delay of the corresponding flame transfer function was increased slightly by 0.4 ms. The impact of the second fuel supply system is presented in Fig. 7.26. The cycle increment of the eigenfrequencies above $Sr = 1.2$ and below $Sr = 0.7$ is further decreased, with two eigenfrequencies at $Sr = 1.27$ and $Sr = 1.81$ crossing the stability border. For the eigenfrequencies at $Sr = 0.86$ and $Sr = 1.14$ the stability is, on the other hand, slightly reduced.

To finally stabilize the entire combustion system in the range between $Sr = 0.8$ and $Sr = 1.5$ the resonator length of the two fuel injection stages were set to $L_{R,2} = 0.18$ m and $L_{R,3} = 0.12$ m. The results of the last example can be found in Fig. 7.27. The eigenfrequencies up to $Sr = 1.5$ are all stable with an adequate stability margin. The eigenfrequency at $Sr = 1.5$ is shifted close to the stability limit, but remains unstable. The last two unstable eigenfrequencies at $Sr = 1.62$ and $Sr = 1.9$ are hardly affected by the design modifications. Comparing the basic configuration (Fig. 7.24) with the last case (Fig. 7.27), it becomes clear

how effective it is to tune the fuel injector impedance and to choose favorable locations for the fuel injection stages.

The last remaining parameter, which could be adjusted during the design process in a system with fuel staging, is the amount of fuel, which is injected at a certain fuel injection stage. Similar to the pressure loss coefficient, which determines the amplitude of the acoustic velocity fluctuation in the fuel injection tube, the mass flow split between the mean fuel mass flow at injection i (\bar{m}_i) and the total fuel mass flow ($\sum_{i=1}^N \bar{m}_{F,i}$) defines the strength of the impact, which was already explained in chapter 2.2:

$$F_{\phi,i}(\omega) \frac{\phi'_i(\omega)}{\bar{\phi}} = F_{\phi,i}(\omega) \left(\frac{u'_{F,i}(\omega)}{\bar{u}_{F,i}} - \frac{u'_{A,i}(\omega)}{\bar{u}_{A,i}} \right) \frac{\bar{m}_{F,i}}{\sum_{i=1}^N \bar{m}_{F,i}}.$$

Here, N denotes again the number of fuel injection stages. Thus the fuel split can be seen as a fine-tuning parameter to adjust the impact distribution between the different fuel injection stages. It should be noted that each fuel injection stage should, in general, be placed at a location and designed in a way that it has a positive influence on the acoustics of the entire combustion system.

8 Summary and Conclusions

In the present work a numerical design method was developed to analyze the impact of fuel injector impedance, fuel injector location and fuel staging on the thermo-acoustic stability of practical premixed combustion systems. Fuel staging denotes in this context, that the fuel is injected at multiple locations into the mixing section of the combustion system.

In terms of thermo-acoustic stability analysis a physical understanding and an accurate description of the flame dynamics is essential. In practical premixed combustion systems the flame responds to acoustic disturbances of the velocity at the flame holder and of the equivalence ratio, which are the result of acoustic velocity fluctuations of the air and fuel stream at the location of fuel injection. In such a system, a physically meaningful, consistent and unambiguous description of the overall flame dynamics can in general only be obtained if the flame response is described as a multiple-input single-output (MISO) model with two or more flame transfer functions, which relate the heat release rate of the flame to the various disturbances.

In order to determine the flame transfer functions for such a model structure, a system identification method was developed, which is based on correlation analysis of time series data and the inversion of the Wiener-Hopf equation. As the identification of a MISO model is, because of partly correlated input signals, a challenging task, quality criteria were implemented to analyze how accurately an identified model reproduces the system dynamics. The method was validated successfully against test data generated with a time domain model, designed to qualitatively represent a practical premixed combustion system. To obtain the flame dynamics for the present purpose the MISO identification was applied to data generated by a transient computational fluid dynamics (CFD) simulation of a generic configuration of a practical premixed combustor with two and three fuel injection stages. The CFD

simulations were performed with only about 8000 time steps and a broadband, discrete-random-binary excitation. The results achieved demonstrate that the approach is very well able to separate the impact of up to three different signals on the response and to identify the corresponding unit impulse response (UIR) vectors and flame transfer functions. The high quality of the results was also affirmed by the implemented quality criteria. A validation of the results against experimental data is not possible, as to the knowledge of the author no such data exists at the time of writing. The experimental determination of such practical premixed flame transfer functions is, however, rather difficult.

All unit impulse response functions obtained exhibit after an initial peak a pronounced undershoot of the flame response, i.e. a range of delay times with negative UIR coefficients. The observation is strongly related to the corresponding flame transfer functions, which exhibit in consequence an excess gain in a range of frequencies. Such behavior has been reported for the flame kinematic response, but to the knowledge of the author it has not been observed previously for the response to equivalence ratio fluctuations. To analyze and interpret the results in detail, transient simulations with impulse forcing were performed. The additional data generated revealed that fluctuations of equivalence ratio or velocity at the flame holder induce a flame movement, which accounts for the observed undershoot. In terms of the equivalence ratio fluctuations, the flame movement is due to the interaction of changes in the heat released per mass of premixture and burning velocity with perturbations of flame position and shape. Other approaches, which determine the flame transfer function simply by steady state CFD measuring the fuel transport time lag distributions, are not able to capture this effect, as they assume a fixed position of the flame. Here, the flame exhibits a low-pass filter behavior, which corresponds to purely positive UIR coefficients.

The flame information obtained is implemented into an acoustic network model, which represents the acoustic characteristics of the entire combustion system. The acoustic network model technique allows a fast, flexible and robust investigation of the impact of fuel injector impedance, fuel injector location and fuel staging on the stability characteristics of the combustion system.

The flame element of the network accounts for the acoustics at the flame location as well as for the acoustics at the flame holder and fuel injection stages. The network model is based on linear acoustic relations, derived from the wave equation and the Bernoulli equation. To analyze the acoustic behavior of the combustion system two mathematical techniques have been applied: The calculation of the response of the inhomogeneous system, which is excited over a certain range of frequencies and the determination of the eigenfrequencies of the unexcited homogeneous system. In the present work the following impacts on the thermo-acoustic stability were investigated in detail:

- The impedance of a fuel injection stage at a predefined location, which was controlled by the length of a resonator tube and the pressure loss over the injector. The resonator tube was placed upon the fuel plenum, which was arranged as an annulus of rectangular cross section around the mixing section.
- The distance of the fuel injection stage to the flame.
- The application of up to two fuel injection stages at two different locations, in which the positions and the acoustic impedances have been adjusted.

The results of the analysis confirm the conceptual considerations derived to suppress unwanted pressure oscillations and to improve the thermo-acoustic stability of combustion systems: The main key to influence the stability is the phase relationship between the acoustic pressure at the flame and the heat release rate fluctuations. In tuning the acoustic impedance or the location of the fuel injection stage the phase of the heat release rate fluctuations and thus the relationship mentioned is changed directly. In addition the stability can be further improved in

- damping the equivalence ratio fluctuations, which can be achieved by adjusting the fuel injector impedance and thus the velocity fluctuation in the fuel injection tube.

As the velocity fluctuations in the fuel injection tube and in the mixing section upstream the location of injection determine the equivalence

ratio fluctuations, the latter can be damped if both fluctuations are in phase. The damping effect leads to a reduction of the corresponding heat release rate contribution term ($F_{\phi,i} \phi'_i / \bar{\phi}$) and thus reduces the amplitude of the heat release rate fluctuations.

- changing the phase delay between the heat release rate contributions ($F_u u'_b / \bar{u}_b, F_{\phi,i} \phi'_i / \bar{\phi}$) to π .

This can again be performed in influencing the fuel injector impedance and the acoustic velocity in the fuel injection tube or in adjusting the position of the fuel injection and the corresponding flame transfer function. This implies finally that both contributions are out of phase and lead to a destructive interference.

The pressure loss over the injection tubes and the amount of fuel, which is distributed to the individual fuel injection stages, can be used in addition to control the impact of each fuel injection stage.

The considerations, derived in the present work, can be taken as rough design guidelines to judge the impact of acoustic impedance, the location and number of the fuel injection stages. The present work has also shown that the hybrid design method consisting of transient CFD, system identification and acoustic network modeling can be successfully used to support the design of an acoustically stable combustion system.

Bibliography

- [1] Verband der Elektrizitätswirtschaft - VDEW - e.V. <http://www.bdew.de>.
- [2] M. Åbom. A note on the experimental determination of acoustical two-port matrices. *Journal of Sound and Vibration*, 155(1):185–188, 1991.
- [3] International Energy Agency. World energy outlook 2006. Technical report, Organisation of Economic Co-operation and Development (OECD), 2006.
- [4] C. Angelberger, D. Veynante, F. Egolfopoulos, and T. Poinso. Large eddy simulation of combustion instabilities in premixed flames. In *Proceedings of the Summer Program 1998*, pages 61–82. Center for Turbulence Research, 1998.
- [5] ANSYS, Inc., Canonsburg, USA. *ANSYS CFX-Solver Theory Guide*, 2006.
- [6] C.A. Armitage, R.S. Cant, A.P. Dowling, and T.P. Hynes. Linearised theory for LPP combustion dynamics. Number GT2003-38670 in Proceedings of ASME Turbo Expo 2003: Power for Land, Sea and Air, June 16-19, 2003, Atlanta, USA, 2003.
- [7] C.A. Armitage, A.J. Riley, R.S. Cant, A.P. Dowling, and S.R. Stow. Flame transfer function for swirled LPP combustion from experiments and CFD. Number GT2004-53820 in Proceedings of ASME Turbo Expo 2004: Power for Land, Sea and Air, June 14-17, 2004, Vienna, Austria, 2004.
- [8] V. Bellucci, C.O. Paschereit, P. Flohr, and F. Magni. On the use of Helmholtz resonators for damping acoustic pulsations in industrial gas turbines. Number 2001-GT-0039 in Proceedings of ASME Turbo Expo

- 2001: Power for Land, Sea and Air, June 4-7, 2001, New Orleans, USA, 2001.
- [9] P. Berenbrink and S. Hoffmann. Suppression of dynamic combustion instabilities by passive and active means. Number 2000-GT-0079 in Proceedings of ASME Turbo Expo 2000: Power for Land, Sea and Air, May 8-11, 2000, Munich, Germany, 2000.
- [10] G.J. Bloxsidge, A.P. Dowling, and P.J. Langhorne. Reheat buzz: an acoustically coupled combustion instability. Part 2. Theory. *Journal of Fluid Mechanics*, 193:445–473, 1988.
- [11] D. Bohn and E. Deucker. An acoustical model to predict combustion driven oscillations. 20th International Congress on Combustion Engines, 1993.
- [12] D. Bohn, G. Deutsch, and U. Krüger. Numerical prediction of the dynamic behavior of turbulent diffusion flames. *ASME Journal of Engineering for Gas Turbines and Power*, 120(4):713–720, 1998.
- [13] L. Boyer and J. Quinard. On the dynamics of anchored flames. *Combustion and Flame*, 82:51–65, 1990.
- [14] J.H. Cho and T. Lieuwen. Laminar premixed flame response to equivalence ratio oscillations. *Combustion and Flame*, 140:116–129, 2005.
- [15] J.H. Cho and T.C. Lieuwen. Modeling the response of premixed flames to mixture ratio perturbations. Number GT2003-38089 in Proceedings of ASME Turbo Expo 2003: Power for Land, Sea and Air, June 16-19, 2003, Atlanta, USA, 2003.
- [16] B.T. Chu. On the generation of pressure waves at a plane flame front. *4th Intl. Symposium on Combustion*, pages 603–612, 1953.
- [17] A. Coker, Y. Neumeier, B.T. Zinn, S. Menon, and T. Lieuwen. Active instability control effectiveness in a liquid fueled combustor. *Combustion Science and Technology*, 178:1251–1261, 2006.

- [18] L. Crocco. Theoretical studies on liquid-propellant rocket instability. In *Tenth Symposium (International) on Combustion*, pages 1101–1128. The Combustion Institute, Pittsburgh, 1965.
- [19] L. Crocco and S. Cheng. *Theory of combustion instability in liquid propellant rocket motors*. AGARDOGRAPH No. 8. Butterworths Science Publication, 1956.
- [20] E. Deuker. *Ein Beitrag zur Vorausberechnung des akustischen Stabilitätsverhaltens von Gasturbinen-Brennkammern mittels theoretischer und experimenteller Analyse von Brennkammerschwingungen*. PhD thesis, RWTH Aachen, 1994. VDI Verlag: Fortschrittsberichte, Reihe 6: Energietechnik.
- [21] A.P. Dowling. The calculation of thermoacoustic oscillations. *Journal of Sound and Vibration*, 180(4):557–581, 1995.
- [22] A.P. Dowling. A kinematic model of a ducted flame. *Journal of Fluid Mechanics*, 394:51–72, 1999.
- [23] A.P. Dowling. Thermoacoustics instability. Sixth International Congress on Sound and Vibration, 1999.
- [24] A.P. Dowling and J.E. Ffowcs Williams. *Sound and Sources of Sound*. Ellis Horwood Limited, Chichester, 1983.
- [25] A.P. Dowling and A.S. Morgans. Feedback control of combustion oscillations. *Annual Revision of Fluid Mechanics*, 37:151–182, 2005.
- [26] A.P. Dowling and S.R. Stow. Acoustic analysis of gas turbine combustors. *Journal of Propulsion and Power*, 19:751–764, 2003.
- [27] S. Ducruix, D. Durox, and S. Candel. Theoretical and experimental determinations of the transfer function of a laminar premixed flame. In *Proceedings of the Combustion Institute*, volume 28, pages 765–773, 2000.

- [28] S. Evesque and W. Polifke. Low-order acoustic modelling for annular combustors. Validation and inclusion of modal coupling. Number GT-2002-30064 in Proceedings of ASME Turbo Expo 2002: Power for Land, Sea and Air, 2002, Amsterdam, Netherlands, 2002.
- [29] M. Fleifil, A.M. Annaswamy, Z.A. Ghoneim, and A.F. Ghoniem. Response of a laminar premixed flame to flow oscillations: A kinematic model and thermoacoustic instability results. *Combustion and Flame*, 106:487–510, 1996.
- [30] P. Flohr, C.O. Paschereit, and V. Bellucci. Steady CFD analysis for gas turbine burner transfer functions. Number AIAA 2003-1346 in 41st AIAA Aerospace Sciences Meeting and Exhibit, January 6-9, 2003, Reno, NV, 2003.
- [31] P. Flohr, C.O. Paschereit, B. van Roon, and B. Schuermans. Using CFD for time-delay modeling of premix flames. Number 2001-GT-0376 in Proceedings of ASME Turbo Expo 2001: Power for Land, Sea and Air, June 4-7, 2001, New Orleans, USA, 2001.
- [32] R.O. Fox. *Computational models for turbulent reacting flows*. Cambridge University Press, 2003.
- [33] R. Friedrich. *Kompressible Strömungen mit Reibung und Wärmeverluste*. Fachgebiet Strömungsmechanik, Technische Universität München, version 2004.
- [34] A. Gentemann, A. Fischer, S. Evesque, and W. Polifke. Acoustic transfer matrix reconstruction and analysis for ducts with sudden change of area. Number AIAA-2003-3142 in 9th AIAA/CEAS Aeroacoustics Conference and Exhibit, 2003, Hilton Head, USA, 2003.
- [35] A. Gentemann, C. Hirsch, K. Kunze, F. Kiesewetter, T. Sattelmayer, and W. Polifke. Validation of flame transfer function reconstruction for perfectly premixed swirl flames. Number GT2004-53776 in Proceedings of ASME Turbo Expo 2004: Power for Land, Sea and Air, June 14-17, 2004, Vienna, Austria, 2004.

- [36] A. Giaque, L. Selle, T. Poinso, H. Büchner, P. Kaufmann, and W. Krebs. System identification of a large-scale swirled partially premixed combustor using LES and measurements. *Journal of Turbulence*, 6(21), November 2005.
- [37] J. Goldmeer, S. Sanderson, G. Myers, J. Stewart, and M. D’Ercole. Passive control of dynamic pressure in a dry, low NO_x combustion system using fuel gas circuit impedance optimization. Number GT2005-68605 in Proceedings of ASME Turbo Expo 2005: Power for Land, Sea and Air, June 6-9, 2005, Reno-Tahoe, Nevada, USA, 2005.
- [38] M.E. Goldstein. *Aeroacoustics*. McGraw-Hill, New York, 1976.
- [39] C.-C. Hantschk and D. Vortmeyer. Numerical simulation of self-excited combustion oscillations in a non-premixed burner. *Combustion Science and Technology*, 174:189–204, 2002.
- [40] S. Haykin. *Adaptive Filter Theory*. Prentice-Hall, Upper Saddle River, NJ, 2002.
- [41] U.G. Hedge, D. Reuter, and B.T. Zinn. Sound generation by ducted flames. *American Institute of Aeronautics and Astronautics Journal*, 26:532–537, 1988.
- [42] M. Hettel, M. Habisreuther, H. Bockhorn, and N. Zarzalis. URANS modelling of flame transfer functions of turbulent premixed jet flames. Number GT2004-53808 in Proceedings of ASME Turbo Expo 2004: Power for Land, Sea and Air, June 14-17, 2004, Vienna, Austria, 2004.
- [43] D.E. Hobson, J.E. Fackrell, and G. Hewitt. Combustion instabilities in industrial gas turbines - measurements on operating plant and thermoacoustic modelling. *ASME Journal of Engineering for Gas Turbines and Power*, 122:420–428, July 2000.
- [44] F. Hoffmann. Akustische und strömungsphysikalische Analyse von Gasturbinenkomponenten mittels CFD-Simulation und Systemidentifikation. Technical report, Lehrstuhl für Thermodynamik, Technische Universität München, 2007.

- [45] J.D. Holdemann, D.S. Liscinsky, and D.B. Bain. Mixing of multiple jets with a confined subsonic crossflow: Part I - cylindrical duct. *ASME Journal of Engineering for Gas Turbines and Power*, 119:852–862, 1997.
- [46] G.C. Hsiao, R.P. Pandalai, H.S. Hura, and H.C. Mongia. Investigation of combustion dynamics in dry-low-emission (DLE) gas turbine engine. Number AIAA 98-3381 in 34th AIAA/ASME/SAE/ASEE Joint Propulsion Conference and Exhibit, Cleveland, USA, July 13-15, 1998.
- [47] S. Hubbard and A.P. Dowling. Acoustic instabilities in premix burners. In *4th AIAA/CEAS Aeroacoustics Conference, June, 1998, Toulouse, France*, 1998.
- [48] S. Hubbard and A.P. Dowling. Acoustic resonances of an industrial gas turbine combustion system. Number 2000-GT-94 in Proceedings of ASME Turbo Expo 2000: Power for Land, Sea and Air, May 8-11, 2000, Munich, Germany, 2000.
- [49] A. Huber and W. Polifke. Impact of fuel supply impedance on system stability of gas turbines. Number GT2008-51193 in Proceedings of ASME Turbo Expo 2008: Power for Land, Sea and Air, June 11-13, 2008, Berlin, Germany, 2008.
- [50] A. Huber, P. Romann, and W. Polifke. Filter-based time-domain impedance boundary conditions for CFD applications. Number GT2008-51195 in Proceedings of ASME Turbo Expo 2008: Power for Land, Sea and Air, June 11-13, 2008, Berlin, Germany, 2008.
- [51] R. Isermann. *Identifikation dynamischer Systeme 1*. Springer Verlag Berlin Heidelberg, 2nd edition, 1992.
- [52] T. Kailath, A.H. Sayed, and B. Hassibi. *Linear Estimation*. Prentice-Hall, Upper Saddle River, NJ, 2000.
- [53] J.J. Keller. Thermoacoustic oscillations in combustion chambers of gas turbines. *AIAA Journal*, 33(12):2280–2287, 1995.

- [54] J.J. Keller, W. Egli, and J. Hellat. Thermally induced low frequency oscillations. *Journal of Applied Mathematics and Physics*, 36:250–274, March 1985.
- [55] T. Komarek. private communication. 2008.
- [56] T. Komarek and W. Polifke. Impact of swirl fluctuations on the flame response of a perfectly premixed swirl burner. Number GT2009-60100 in Int'l Gas Turbine and Aeroengine Congress & Exposition, Jun 8-12, 2009, Orlando, FL, USA, 2009.
- [57] T. Komarek, L. Tay Wo Chong, M. Zellhuber, A. Huber, and W. Polifke. Modeling of the effect of heat loss on flame stabilization in shear layers. International Conference on Jets, Wakes and Separated Flows (ICJWSF), September 16-19, 2008, Berlin, Germany, 2008.
- [58] J. Kopitz, A. Huber, T. Sattelmayer, and W. Polifke. Thermoacoustic stability analysis of an annular combustion chamber with acoustic low order modeling and validation against experiment. Number GT2005-68797 in Proceedings of ASME Turbo Expo 2005 Power for Land, Sea and Air, June 6-9, 2005, Reno-Tahoe, USA, 2005.
- [59] W. Krebs, P. Flohr, B. Prade, and S. Hoffmann. Thermoacoustic stability chart for high-intensity gas turbine combustion systems. *Combustion Science & Technology*, 174(7):99–128, 2002.
- [60] W. Krebs, S. Hoffmann, B. Prade, M. Lohrmann, and H. Büchner. Thermoacoustic flame response of swirl flames. Number GT-2002-30065 in Proceedings of ASME Turbo Expo 2002: Power for Land, Sea and Air, June 3-6, 2002, Amsterdam, Netherlands, 2002.
- [61] U. Krüger, J. Hüren, S. Hoffmann, W. Krebs, P. Flohr, and D. Bohn. Prediction and measurement of thermoacoustic improvements in gas turbines with annular combustion systems. Number 2000-GT-0095 in Proceedings of ASME Turbo Expo 2000: Power for Land, Sea and Air, June 8-11, 2000, Munich, Germany, 2000.

- [62] Klaas Kunze. *Untersuchung des thermoakustischen Flammenübertragungsverhaltens in einer Ringbrennkammer*. PhD thesis, Lehrstuhl für Thermodynamik, Technische Universität München, 2004.
- [63] J.C. Lagarias, J.A. Reeds, M.H. Wright, and P.E. Wright. Convergence properties of the nelder-mead simplex method in low dimensions. *SIAM J. Optim.*, 9(1):112–147, 1998.
- [64] M. Lauer and T. Sattelmayer. On the adequacy of chemiluminescence as a measure for heat release in turbulent flames with mixture gradients. Number GT2009-59631 in Proceedings of ASME Turbo Expo 2009: Power for Land, Sea and Air, June 8-12, 2009, Orlando, Florida, USA, 2009.
- [65] C.J. Lawn and W. Polifke. A model for the thermoacoustic response of a premixed swirl burner, part II: The flame response. *Combustion Science and Technology*, 176:1359–1390, 2004.
- [66] C. Lechner and J. Seume, editors. *Stationäre Gasturbinen*. Springer Verlag Berlin Heidelberg, 2003.
- [67] J. LeConte. On the influence of musical sounds on the flame of a jet of coal gas. *American Journal of Science and Arts*, 23(2):62–67, 1858.
- [68] D.-H. Lee and T. Lieuwen. Acoustic near-field characteristics of a conical, premixed flame. *Journal of the Acoustical Society of America*, 113(1):167–177, 2003.
- [69] A.H. Lefebvre. *Gas turbine combustion*. McGraw Hill, 1983.
- [70] J. Lepers, W. Krebs, B. Prade, P. Flohr, G. Pollarolo, and A. Ferrante. Investigation of thermoacoustic stability limits of an annular gas turbine combustor test rig with and without Helmholtz resonators. Number GT-2005-68246 in Proceedings of ASME Turbo Expo 2005: Power for Land, Sea and Air, June 6-9, 2005, Nevada, USA, 2005.
- [71] T. Lieuwen and B.T. Zinn. The role of equivalence ratio oscillations in driving combustion instabilities in low NO_x gas turbines. In *Proceedings of the 27th Symposium (International) on Combustion, Pittsburgh, USA*, 1998.

- [72] T. Lieuwen and B.T. Zinn. Theoretical investigation of combustion instability mechanisms in lean premixed gas turbines. Number AIAA 98-0641 in AIAA 36th Aerospace Sciences Meeting and Exhibit, January 12-15, 1998, Reno, NV, 1998.
- [73] L. Ljung. *System Identification: Theory for the User*. Prentice-Hall, Englewood Cliffs, NJ, 2nd edition, 1999.
- [74] J.A. Lovett and K.T. Uznanski. Prediction of combustion dynamics in a staged premixed combustor. Number GT-2002-30646 in Proceedings of ASME Turbo Expo 2002: Power for Land, Sea and Air, June 3-6, 2002, Amsterdam, Netherlands, 2002.
- [75] K. McManus, F. Han, W. Dunstan, C. Barbu, and M. Shah. Modeling and control of combustion dynamics in industrial gas turbines. Number GT2004-53872 in Proceedings of ASME Turbo Expo 2004: Power for Land, Sea and Air, June 14-17, 2004, Vienna, Austria, 2004.
- [76] K. McManus, T. Poinsot, and S.M. Candel. A review of active control of combustion instabilities. *Progress in Energy and Combustion Science*, 19:1–29, 1993.
- [77] E.R. Menter. Multiscale model for turbulent flows. 24th Fluid Dynamics Conference, American Institute of Aeronautics and Astronautics, 1993.
- [78] E.R. Menter. Two-equation eddy-viscosity turbulence models for engineering applications. *AIAA-Journal*, 32(8):1598–1605, 1994.
- [79] H.J. Merk. Analysis of heat-driven oscillations of gas flows, I. General consideration. *Applied scientific Research, Section A*, 6:317–335, 1956/57.
- [80] M. Metghalchi and J.C. Keck. Burning velocities of mixtures of air with methanol, iso-octane and indolene at high pressure and temperature. *Combustion and Flame*, 48:191–210, 1982.
- [81] P.M. Morse and U.I. Ingard. *Theoretical Acoustics*. Princeton University Press, 1986.

- [82] M.L. Munjal. *Acoustics of ducts and mufflers*. John Wiley & Sons, 1987.
- [83] T. Murota and M. Ohtsuka. Large-eddy simulation of combustion oscillations in the premixed combustor. Number 99-GT-274 in Proceedings of ASME Turbo Expo 1999: Power for Land, Sea and Air, June 7-10, Indianapolis, USA. ASME Turbo Expo, 1999.
- [84] F. Nicoud, L. Benoit, C. Sensiau, and T. Poinso. Acoustic modes in combustors with complex impedances and multidimensional active flames. *AIAA Journal*, 45(2):426–441, 2007.
- [85] A.V. Oppenheim and R.W. Schaffer. *Discrete time signal processing*. Prentice-Hall, Upper Saddle River, NJ, 2. edition, 1999.
- [86] C.C. Paige and M.A. Saunders. Lsqr: An algorithm for sparse linear equations and sparse least squares. *ACM Transactions on Mathematical Software*, 8(1):43–71, 1982.
- [87] C. Pankiewicz and T. Sattelmayer. Hybrid methods for modelling combustion instabilities. 10th International Congress on Sound and Vibration, Stockholm, Sweden, 2003.
- [88] C. Pankiewicz and T. Sattelmayer. Time domain simulation of combustion instabilities in annular combustors. *Journal of Engineering for Gas Turbines and Power*, 125:677–685, 2003.
- [89] C.O. Paschereit and E. Gutmark. The effectiveness of passive combustion control methods. Number GT2004-53587 in Proceedings of ASME Turbo Expo 2004: Power for Land, Sea and Air, June 14-17, 2004, Vienna, Austria, 2004.
- [90] C.O. Paschereit, W. Weisenstein, and E.J. Gutmark. Role of coherent structures in acoustic combustion control. Number A98-32792 in 29th AIAA Fluid Dynamics Conference, Albuquerque, New Mexico, June 15-18 1998.
- [91] A.A. Peracchio and W.M. Proscia. Nonlinear heat-release/acoustic model for thermoacoustic instability in lean premixed combustors.

- Number 98-GT-269 in International Gas Turbine and Aeroengine Congress and Exhibition, 1998.
- [92] N. Peters. *Turbulent Combustion*. Cambridge University Press, 2000.
- [93] A.D. Pierce. *Acoustics*. McGraw-Hill, Inc., 1981.
- [94] T. Poinso and D. Veynante. *Theoretical and Numerical Combustion*. R.T. Edwards, Inc., 2nd edition edition, 2005.
- [95] T.J. Poinso and S.K. Lele. Boundary conditions for direct simulation of compressible viscous flows. *Journal of Computational Physics*, 101:104–129, 1992.
- [96] W. Polifke. System modelling and stability analysis. In *Basics of Aero-Acoustics and Thermo-Acoustics*, VKI LS 2007-02, Brussels, BE, Dec 3-7 2007. Von Karman Institute.
- [97] W. Polifke, P. Flohr, and M. Brandt. Modeling of inhomogeneously premixed combustion with an extended TFC model. *ASME Journal of Engineering for Gas Turbines and Power*, 124(1):58–65, 2002.
- [98] W. Polifke and A. Gentemann. Order and realizability of impulse response filters for accurate identification of acoustic multi-ports from transient CFD. *Int. J. of Acoustics and Vibration*, 9(3):139–148, July 7-10 2004.
- [99] W. Polifke, J. Kopitz, and A. Serbanovic. Impact of the fuel time lag distribution in elliptical premix nozzles on combustion stability. Number AIAA 2001-2104 in 7th AIAA/CEAS Aeroacoustics Conference, 2001, Maastricht, Netherlands, 2001.
- [100] W. Polifke and C. Lawn. On the low-frequency limit of flame transfer functions. *Combustion and Flame*, 151(3):437–451, 2007.
- [101] W. Polifke, C.O. Paschereit, and K. Döbbeling. Constructive and destructive interference of acoustic and entropy waves in a premixed combustor with a choked exit. *Int. J. of Acoustics and Vibration*, 6(3):135–146, 2001.

- [102] W. Polifke, A. Poncet, C.O. Paschereit, and K. Döbbeling. Reconstruction of acoustic transfer matrices by instationary computational fluid dynamics. *Journal of Sound and Vibration*, 245(3):483–510, 2001.
- [103] W. Polifke, J. van der Hoek, and B. Verhaar. Basic equations and numerical tools for linear acoustics in gas turbines. Technical report, ABB Corporate Research, Baden, Switzerland, 1997.
- [104] S.B. Pope. *Turbulent Flows*. Cambridge University Press, 2000.
- [105] J.W.S. Rayleigh. The explanation of certain acoustical phenomena. *Nature*, 18:319–321, 1878.
- [106] G. Richards, D. Straub, and E. Robey. Control of combustion dynamics using fuel system impedance. Number GT2003-38521 in Proceedings of ASME Turbo Expo 2003: Power for Land, Sea and Air, June 16-19, Atlanta, USA, 2003.
- [107] G.A. Richards and M.C. Janus. Characterization of oscillations during premix gas turbine combustion. *J. Eng. for Gas Turbines and Power*, 120:294 – 302, 1998.
- [108] G.A. Richards and E.H. Robey. Effect of fuel system impedance mismatch on combustion dynamics. Proceedings of ASME Turbo Expo 2005: Power for Land, Sea and Air, June 6-9, 2005, Nevada, USA, 2005.
- [109] G.A. Richards, D.L. Straub, and E.H. Robey. Passive control of combustion dynamics in stationary gas turbines. *Journal of Propulsion and Power*, 19(5):795–810, 2003.
- [110] S.W. Rienstra and A. Hirschberg. *An introduction to acoustics*. Eindhoven University of Technology, 2006.
- [111] S. Roux, G. Lartigue, T. Poinso, U. Meier, and C. Bérat. Studies of mean and unsteady flow in a swirled combustor using experiments, acoustic analysis, and large eddy simulations. *Combustion and Flame*, 141(1-2):40–54, 2005.

- [112] T. Sattelmayer. Influence of the combustor aerodynamics on combustion instabilities from equivalence ratio fluctuations. *Journal of Engineering for Gas Turbines and Power*, 125:11–19, Januar 2003.
- [113] T. Sattelmayer and W. Polifke. Assessments of methods for the computation of the linear stability of combustors. *Combustion Science and Technology*, 175(3):453–476, 2003.
- [114] T. Sattelmayer and W. Polifke. A novel method for the computation of the linear stability of combustors. *Combustion Science and Technology*, 175(3):477–497, 2003.
- [115] T. Scarinci and C. Freeman. The propagation of a fuel-air ratio disturbance in a simple premixer and its influence on pressure wave amplification. Number 2000-GT-0106 in Proceedings of ASME Turbo Expo 2000 Power for Land, Sea and Air, May 8-11, 2000, Munich, Germany, 2000.
- [116] T. Scarinci, C. Freeman, and I. Day. Passive control of combustion instability in a low emissions aeroderivative gas turbine. Number GT 2004-53767 in Proceedings of ASME Turbo Expo 2004: Power for Land, Sea and Air, June 14-17, 2004, Vienna, Austria, 2004.
- [117] T. Scarinci and J.L. Halpin. Industrial trend combustor - combustion noise characteristics. *ASME Journal of Engineering For Gas Turbines and Power*, 122(98-GT-9):280–286, 2000.
- [118] T. Schönfeld and T. Poinso. Influence of boundary conditions in LES of premixed combustion instabilities. *Center for Turbulence Research, Annular Research Briefs*, pages 73–84, 1999.
- [119] B. Schuermans, V. Bellucci, G. Felix, F. Meili, P. Flohr, and C.O. Paschereit. A detailed analysis of thermoacoustic interaction mechanisms in a turbulent premixed flame. Number GT2004-53831 in Proceedings of ASME Turbo Expo 2004: Power for Land, Sea and Air, June 14-17, 2004, Vienna, Austria, 2004.
- [120] T. Schuller, D. Durox, and S. Candel. Self-induced combustion oscillations of laminar premixed flames stabilized on annular burners. *Combustion and Flame*, 135:525–537, 2003.

- [121] T. Schuller, D. Durox, and S. Candel. A unified model for the prediction of laminar flame transfer functions: Comparisons between conical and V-flame dynamics. *Combustion and Flame*, 134:21–34, 2003.
- [122] J.R. Seume, N. Vortmeyer, W. Krause, J. Hermann, C.-C. Hantschk, P. Zangl, S. Gleis, D. Vortmeyer, and A. Orthmann. Application of active combustion instability control to a heavy duty gas turbine. *ASME Journal of Engineering for Gas Turbines and Power*, 120:721–726, 1998.
- [123] D. Shcherbik, E. Lubarsky, Y. Neumeier, B.T. Zinn, K. McManus, T.F. Fric, and S. Srinivasan. Suppression of instabilities in gaseous fuel high-pressure combustor using non-coherent oscillatory fuel injection. Number GT2003-38103 in Proceedings of ASME Turbo Expo 2003: Power for Land, Sea and Air, June 16-19, 2003, Atlanta, USA, 2003.
- [124] R.C. Steele, L.H. Cowell, S.M. Cannon, and C.E. Smith. Passive control of combustion instability in lean premixed combustors. *ASME Journal of Engineering for Gas Turbines and Power*, 122(3):412–419, 2000.
- [125] D.L. Straub and G.A. Richards. Effect of fuel nozzle configuration on premix combustion dynamics. Number 98-GT-492 in International Gas Turbine and Aeroengine Congress and Exhibition, June 2-5, 1998, Stockholm, Sweden, 1998.
- [126] H. Tennekes and J.L. Lumley. *A first course in turbulence*. MIT Press, Cambridge, USA, 1972.
- [127] K. Truffin and T. Poinso. Comparison and extension of methods for acoustic identification of burners. *Combustion and Flame*, 142:388–400, 2005.
- [128] S.R. Turns. *An introduction to combustion: concepts and applications*. McGraw-Hill, 2nd edition, 2000.
- [129] J. van Kampen, J.B.W. Kok, and T.H. van der Meer. Efficient retrieval of a flame transfer function from a steady state CFD simulation. 12th International Congress on Sound and Vibration, July 11-14, 2005, Lisbon, Portugal, 2005.

- [130] A. Widenhorn. private communication. 2007.
- [131] D.C. Wilcox. Multiscale model for turbulent flows. AIAA 24th Aerospace Sciences Meeting, American Institute of Aeronautics and Astronautics, 1986.
- [132] F.A. Williams. *Combustion Theory*. The Benjamin-Cummings Publishing Inc., California, USA, 2nd edition, 1985.
- [133] D. You, Y. Huang, and V. Yang. A generalized model of acoustic response of turbulent premixed flame and its application to gas-turbine combustion instability analysis. *Combustion Science and Technology*, 177(5 - 6):1109–1150, 2005.
- [134] S.W. Yuen, A. Gentemann, and W. Polifke. Investigation of the influence of boundary conditions on system identifiability using real time system modeling. 11th International Congress on Sound and Vibration, July 5-8, 2004, St. Petersburg, Russia, pages 3501–3508, 2004.
- [135] M. Zhu, A.P. Dowling, and K.N.C. Bray. Transfer function calculations for aeroengine combustion oscillations. *ASME Journal of Engineering For Gas Turbines and Power*, 127(2001-GT-0374):18–26, 2005.
- [136] V. Zimont and A. Lipatnikov. A numerical model of premixed turbulent combustion of gases. *Chemical Physics Reports*, 14(7):993–1025, 1995.
- [137] V. Zimont, W. Polifke, M. Bettelini, and W. Weisenstein. An efficient computational model for premixed turbulent combustion at high Reynolds numbers based on a turbulent flame speed closure. *ASME Transactions Journal of Fluids Engineering*, 120(3):526 – 532, 1997.
- [138] V. L. Zimont. Theory of turbulent combustion of a homogeneous fuel mixture at high Reynolds numbers. *Combust. Expl. and Shock Waves*, 15:305–311, 1979.

A Appendix

A.1 Transformation of pu , fg transfer matrix and scattering (sr) matrix notation

The following relations show the necessary operations to transform a transfer or scattering matrix from one notation into another:

$$T_{pu} = Z T_{fg} Z^{-1} \quad (\text{A.1})$$

$$T_{fg} = Z^{-1} T_{pu} Z \quad (\text{A.2})$$

where

$$Z \equiv \begin{pmatrix} 1 & 1 \\ -1 & 1 \end{pmatrix}. \quad (\text{A.3})$$

With

$$T_{fg} \equiv \begin{pmatrix} A & B \\ C & D \end{pmatrix} \quad (\text{A.4})$$

the scattering matrix can be obtained:

$$S_{sr} = \begin{pmatrix} A - B \frac{C}{D} & \frac{B}{D} \\ -\frac{C}{D} & \frac{1}{D} \end{pmatrix}. \quad (\text{A.5})$$

A.2 Estimation of the optimum number of circumferential injection holes

The optimum number of circumferential holes was estimated according to Holdeman et al. [45] using the relation

$$C = \frac{S}{H} \sqrt{J}, \quad (\text{A.6})$$

where S denotes the spacing of the holes and H corresponds to the height of rectangular duct. C represents a constant with an optimum value of 2.5. For a cylindrical duct the spacing amounts to $S = 2\pi R/n$ with n being the number of holes. Therefore the number of holes can be calculated by the following equation:

$$n = \frac{2\pi R}{H} \sqrt{J}. \quad (\text{A.7})$$

In case of a cylindrical duct the height can be substituted by the radius using the relation $R = H/\sqrt{2}$. For the analyzed case the radius can be determined by the outer radius or the difference between the outer radius and the inner radius of the mixing section. The optimum number of injection holes can then be calculated and lies in the range between 6.1 and 10.2.

A.3 Main flow parameters and structure of the acoustic network models

The following tables represent the basic flow parameters which are required as an input for the acoustic network models used in the present work. In addition Fig. A.1 shows the network structure of the combustion configuration with three fuel injection systems (configuration B).

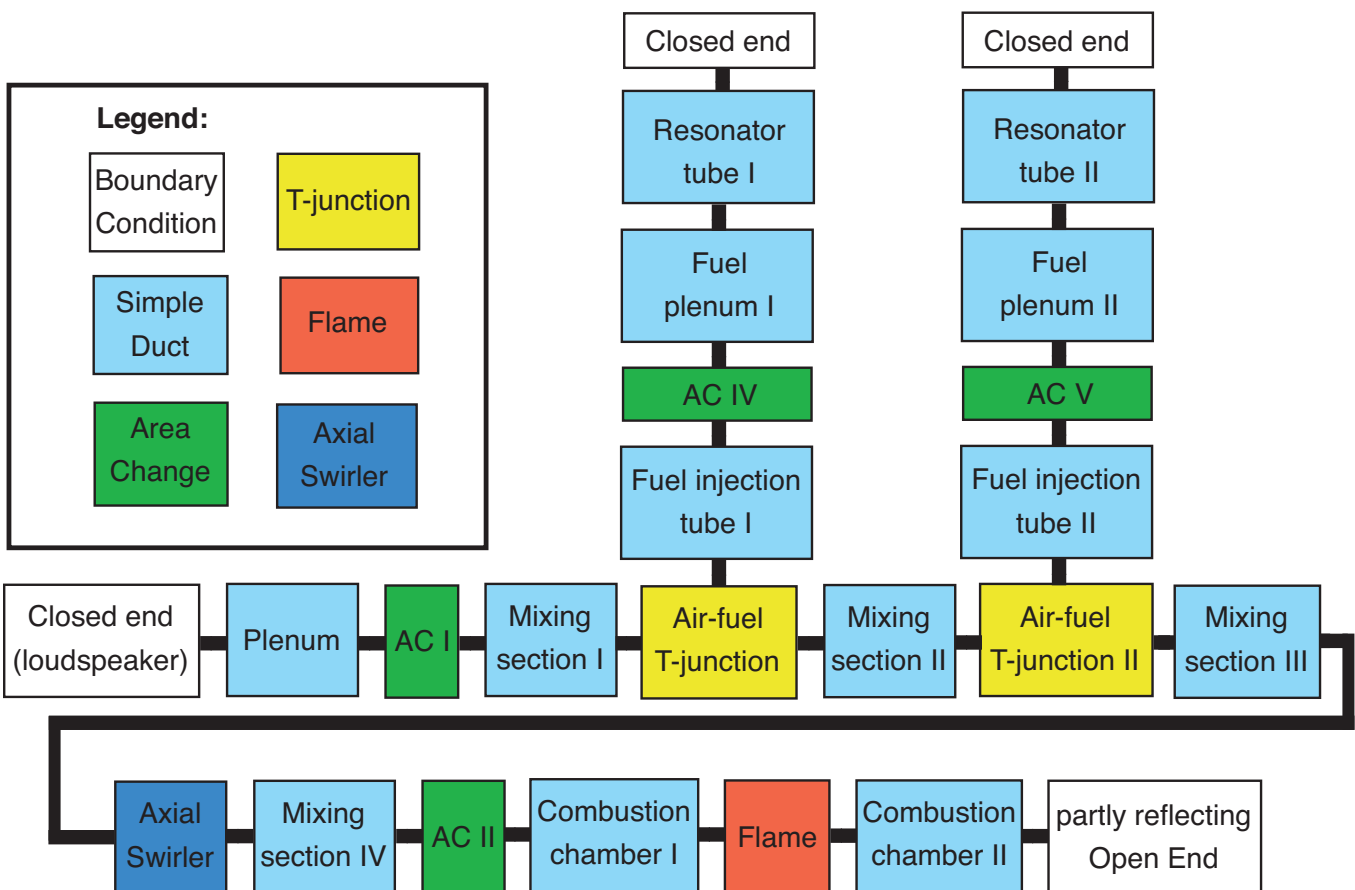


Figure A.1: Sketch of the acoustic network model of the combustion configuration with three injection stages, case B.

Simple ducts	l [m]	M [-]	ρ [kg/m ³]	c [m/s]
Plenum	0.095	0.0018	1.166	349
Mixing section I	0.055	0.053	1.166	349
Mixing section II	0.08	0.055	1.14	350.6
Mixing section III	0.045	0.055	1.14	350.6
Combustion chamber I	0.03	0.018	1.14	350.6
Combustion chamber II	0.27	0.019	0.176	851.4
Fuel injection tube	0.005	0.191	0.66	448
Fuel plenum and resonator tube	$L_{R,2}$	0.0173	0.66	448

Table A.1: Main flow parameters of the simple ducts (configuration A).

Simple ducts	l [m]	M [-]	ρ [kg/m ³]	c [m/s]
Plenum	0.095	0.00176	1.182	346
Mixing section I	0.055	0.052	1.182	346
Mixing section II	0.04	0.053	1.168	349
Mixing section III	0.04	0.056	1.13	350.6
Mixing section IV	0.045	0.056	1.13	350.6
Combustion chamber I	0.03	0.0186	1.13	350.6
Combustion chamber II	0.27	0.019	0.176	851.4
Fuel injection tube I	0.005	0.138	0.66	448
Fuel plenum and resonator tube I	$L_{R,2}$	0.0125	0.66	448
Fuel injection tube II	0.005	0.208	0.66	448
Fuel plenum and resonator tube II	$L_{R,3}$	0.0185	0.66	448

Table A.2: Main flow parameters of the simple ducts (configuration B).

Area changes	A_i [m ²]	A_j [m ²]	ζ [-]
Plenum - mixing section (AC I)	0.312	0.00106	0.27
Mixing section II - combustion chamber I (AC II)	0.00106	0.00816	8.5
Fuel plenum I - fuel injection tube I (AC IV)	0.00005	0.000009	0 / 0.73
Fuel plenum II - fuel injection tube II (AC IV)	0.00005	0.000009	0 / 0.73

Table A.3: Main flow parameters of the area changes (configuration A, B).

T-junctions	A_i [m ²]	A_j [m ²]	A_k [m ²]	ζ_i [-]	ζ_j [-]
T-junction I, II	0.000009	0.00106	0.00106	0.1 - 0.84	0.11

Table A.4: Main flow parameters of the T-junction (configuration A, B).

Flame	γ [-]	T_i [K]	T_m [K]
Flame	1.39	298	1930

Table A.5: Main flow parameters of the flame (configuration A, B).